8& %HUNHOH\

8& %HUNHOH\ (OHFWURQLF 7KHVHV DQG 'LVVHUWDWL

7LWOH
5HDFWLRQ RI 3OXWRQLXP 9, ZLWK WKH 0DQJDQHVH 6XEVWLWXWHG

3HUPDOLQN
KWWSV HVFKRODUVKLS RUJ XF LWHP WG K

$XWKRU
+X <XQJ -LQ +X

3XEOLFDWLRQ 'DWH

3HHU UHYLHZHG_7KHVLV GLVVHUWDWLRQ

Reaction of Plutonium(VI) with the Manganese-Substituted Iron Oxide Mineral Goethite

by

Yung-Jin Hu

A dissertation submitted in partial satisfaction of the
requirements for the degree of
Doctor of Philosophy

in

Chemistry

in the

Graduate Division
of the
University of California, Berkeley

Committee in charge:
Professor Heino Nitsche, Chair
Professor Darleane Hoffman
Professor Joonhong Ahn

Spring 2011

Reaction of Plutonium(VI) with the Manganese-Substituted Iron Oxide Mineral Goethite

Abstract

Reaction of Plutonium(VI) with the Manganese-Substituted Iron Oxide Mineral Goethite

by

Yung-Jin Hu

Doctor of Philosophy in Chemistry

University of California, Berkeley

Professor Heino Nitsche, Chair

More than 60 years of nuclear power and weapons production in the United States has left this country with a large burden of radioactive legacy waste containing long-lived transactinide elements, as well as highly radioactive fission products. To face the challenge of contaminated site remediation, a solid understanding of the fundamental chemical processes behind the transport and migration of actinides in the environment is necessary. Especially important is the elucidation of interfacial reactions at the boundary between aqueous radionuclide solutions and minerals. This knowledge will allow us to more accurately model and predict the ultimate fate of radionuclides in the geosphere.

The work presented in this thesis focuses on understanding the binding mechanisms and structure of plutonium on the surface of metal oxide minerals. Plutonium(VI) sorption on the surface of well-characterized synthetic manganese-substituted goethite minerals ($Fe_{1-x}Mn_xOOH$) was studied using X-ray absorption spectroscopy. Because manganese is often found in the environment as a minor component associated with major mineral components, such as goethite, understanding the molecular-level interactions of plutonium with such substituted-mineral phases is important for risk assessment purposes at radioactively contaminated sites and long-term underground radioactive waste repositories.

The first chapter of this thesis is an introduction and motivation to the work presented in the following chapters. The second chapter describes fundamental aqueous solution chemistry and covers the calculation of species in solution including methods for handling statistical errors. The third chapter provides an overview of the fundamental interactions that occur at the interface between aqueous solution and the surface of a mineral. The fourth chapter presents the methods and characterization techniques used in synthesizing goethite (α-FeOOH) and manganese-substituted goethite ($Fe_{1-x}Mn_xOOH$) minerals. The fifth chapter presents an overview of the plutonium chemistry needed to conduct and understand the experiments. The sixth chapter presents a fundamental overview of X-ray absorption spectroscopy methods used in this study, including X-ray absorption near-edge structure spectroscopy, extended X-ray absorption fine-structure spectroscopy, micro X-ray absorption spectroscopy, and synchrotron X-ray fluorescence spectroscopy. The seventh chapter presents the data and discussion of experiments with plutonium sorbed on the surface of manganese-substituted goethite minerals. Work relating to the modeling of stochastic noise in extended X-ray absorption fine-structure spectra and synchrotron X-ray beam-induced

chemistry on plutonium are also presented. The eighth chapter gives an overview of the work and offers suggestions for future work on this topic. The appendices at the end of this thesis are a collection of methods, instructions, suggestions, and computer code that was helpful when conducting experiments.

For my Mother and Father

Contents

List of Figures vi

List of Tables xii

1 Introduction 1

2 Aqueous Solution Chemistry 5
2.1 Ionic Strength and Activity . . . 5
2.2 Acid-Base Chemistry . . . 6
2.3 Complexation and Speciation . . . 7
2.3.1 Equilibrium Constants . . . 7
2.3.2 Speciation and Statistical Error in Speciation Diagrams . . . 9
2.4 Oxidation and Reduction Reactions . . . 12
2.5 Carbonate Equilibrium in Aqueous Systems . . . 14

3 Surface Chemistry 20
3.1 Ion Exchange . . . 20
3.2 Point of Zero Charge . . . 21
3.2.1 Introduction . . . 21
3.2.2 Potentiometric Titration . . . 21
3.2.3 Mass Titration . . . 22
3.2.4 Powder Addition . . . 24
3.3 Sorption of Trace Metals . . . 24

4 Goethite and Manganese-Substituted Goethite 27
4.1 Introduction . . . 27
4.2 Goethite . . . 29
4.2.1 Synthesis . . . 29
4.2.2 Sample Characterization . . . 29
4.3 Manganese-Substituted Goethite . . . 32
4.3.1 Synthesis . . . 32
4.3.2 Sample Characterization . . . 32

5 The Chemistry of Plutonium 38
5.1 Introduction . . . 38
5.2 Nuclear Reactions . . . 39

5.3 Aqueous Plutonium Chemistry . . . 42
5.3.1 Hydrolysis and Carbonate Complexes of Plutonium(VI) . . . 42
5.3.2 Plutonium Solubility . . . 44
5.3.3 Redox Chemistry of Plutonium . . . 45
5.4 Detection and Measurement of Plutonium Oxidation States . . . 47
5.4.1 UV-Vis Spectroscopy . . . 47
5.4.2 X-ray Absorption Near Edge Structure Spectroscopy . . . 48

6 X-ray Absorption Spectroscopy **54**
6.1 Introduction . . . 54
6.2 Synchrotron Radiation . . . 54
6.2.1 Introduction . . . 54
6.2.2 Theory . . . 55
6.2.3 Radiation Characteristics . . . 57
6.2.4 XAS Beamline Setup . . . 60
6.2.5 Detector Systems . . . 62
6.3 XANES . . . 67
6.3.1 Introduction . . . 67
6.3.2 Theory . . . 68
6.3.3 Data Analysis . . . 70
6.4 EXAFS . . . 70
6.4.1 Introduction . . . 70
6.4.2 Theory . . . 71
6.4.3 Data Analysis . . . 75
6.5 Micro-SXRF . . . 85
6.5.1 Introduction . . . 85
6.5.2 Theory . . . 86
6.5.3 Micro-SXRF Beamline Setup . . . 86
6.5.4 Data Analysis . . . 87
6.6 Micro-XANES . . . 87
6.6.1 Introduction . . . 87
6.6.2 Theory . . . 87
6.6.3 Micro-XANES Beamline Setup . . . 87
6.6.4 Data Analysis . . . 88

7 Experiments **89**
7.1 Introduction . . . 89
7.2 Predetermining Acceptable EXAFS Spectral Noise in the Limit of Stochastic Noise . . . 89
7.2.1 Overview . . . 89
7.2.2 Simulation Method . . . 90
7.2.3 Discussion . . . 94
7.3 Synchrotron X-ray Beam-Induced Chemistry on Plutonium Sorbed on Various Substrates . . . 95
7.3.1 Overview . . . 95

7.3.2 Materials and Methods . . . 96
7.3.3 Evidence of X-ray Beam-Induced Chemistry on Pu(VI) . . . 97
7.3.4 Discussion and Conclusions . . . 103
7.4 Plutonium(VI) Sorption on Manganese-Substituted Goethite . . . 111
7.4.1 Overview . . . 111
7.4.2 Materials and Methods . . . 112
7.4.3 Evidence of Plutonium Reduction at the Surface of Manganese-Substituted Goethite . . . 113
7.4.4 Conclusions . . . 119
7.5 Interactions of Plutonium(VI) with Samples Containing Mixed Goethite / Manganese-Substituted Goethite using Microprobe X-ray Analysis . . . 119
7.5.1 Overview . . . 119
7.5.2 Materials and Methods . . . 120
7.5.3 Results and Discussion . . . 121
7.5.4 Conclusions . . . 132

8 Conclusions and Future Work **133**
8.1 Conclusions . . . 133
8.2 Future Work . . . 134

Bibliography **136**

A Perchloric Acid and Perchlorates **148**
A.1 Introduction . . . 148
A.2 Aqueous Perchloric Acid . . . 148
A.3 Anhydrous Perchloric Acid . . . 149
A.4 Perchloric Anhydrite . . . 150
A.5 Perchlorate Toxicology . . . 150

B Silver/Silver Chloride Electrodes **151**
B.1 Making Ag/AgCl Electrodes . . . 151
B.2 Electrochemical Reactions . . . 152

C Chemical and Electrochemical Preparation of Plutonium Oxidation States in Aqueous Solution **155**
C.1 Introduction . . . 155
C.2 The Three-Electrode Cell . . . 155
C.3 Preparation of Pu(III) . . . 156
C.4 Preparation of Pu(IV) . . . 157
C.5 Preparation of Pu(VI) . . . 157
C.6 Preparation and Removal of Pu(IV) Polymer . . . 158

D Lanthanum Fluoride Precipitation **159**
D.1 Introduction . . . 159
D.2 Lanthanum Fluoride Co-Precipitation of Plutonium . . . 159

E Anion Exchange of Plutonium **161**
E.1 Column Preparation . . . 161
E.2 HI Distillation . . . 161
E.3 Pu Anion Exchange . . . 162

F Scientific Computing **164**
F.1 Introduction . . . 164
F.2 Fortran . . . 165
F.3 Python . . . 167
F.3.1 The Core Python Programming Language . . . 167
F.3.2 SciPy . . . 168
F.3.3 NumPy . . . 168
F.3.4 Matplotlib . . . 168
F.3.5 wxPython . . . 168
F.4 Code Listings . . . 169
F.4.1 Introduction . . . 169
F.4.2 SIMERAD . . . 169
F.4.3 SPECIATE . . . 174
F.4.4 GFITES . . . 181

G Tips and Tricks **204**
G.1 Introduction . . . 204
G.2 A Liquid Helium Cryostat for Bulk XAS Measurements . . . 204
G.3 Packaging Transuranic Samples for Bulk XAS and Micro-XAS Measurements 207
G.3.1 Introduction . . . 207
G.3.2 Bulk XAS Sample Loading . . . 207
G.3.3 Micro XAS Sample Loading . . . 209
G.4 A Sample Mount for Transuranic Micro XAS . . . 209
G.5 Running Beamtime Experiments . . . 209
G.5.1 Introduction . . . 209
G.5.2 Logging In and Preparing for Runs . . . 213
G.5.3 Working with X-ray Mirrors . . . 214
G.5.4 Common Rookie Mistakes . . . 215
G.5.5 Transferring Data Back to the Ranch . . . 217
G.5.6 Temperature Controlling Notes . . . 219
G.5.7 Data Collection Notes . . . 219

List of Figures

1.1 Molecular-scale processes in environmental science, from Brown *et al.* [1]. . 2
1.2 Subset of molecular interactions investigated in this work. Adapted from Brown *et al.* [1]. 2
1.3 (a) Photomicrograph of the manganese and iron oxide phases in the sample under reflected light. The silver-colored structure in the upper left corner is hematite, the center area is a manganese oxide, and the surrounding features are highly zeolitic. Complementary micro-SXRF elemental map images show spatially localized (b) Fe, (c) Mn, and (d) Pu. From Duff *et al.* [19]. 4

2.1 Speciation diagram of acetic acid and its conjugate base as a function of pH. 10
2.2 Plot of the yearly average partial pressure of CO_2 in the atmosphere over Mauna Loa, Hawaii from 1959 to 2009. Error bars for individual measurements fall within the plotted data point. 15
2.3 Log-plot of carbonate concentration as a function of pH. 18
2.4 Speciation plot of carbonate species as a function of pH. 19

3.1 The molecular structure of the active site of the synthetic cation exchange material Kayexalate [55]. 20
3.2 pH dependent protonation and deprotonation of hydroxyl groups on the mineral surface. Adapted from Tourinho *et al.* [62]. 23
3.3 Three-dimensional schematic of three possible surface complex structures for a cation approaching a surface. The ion can reside as a diffuse ion in solution, form an electrostatic outer-sphere complex, or form an inner-sphere complex containing direct chemical bonds to the surface. From Sposito [63]. 25
3.4 Two-dimensional schematic of possible surface complex structures. Depth into the surface, normal to the surface, increases from right to left. Vertical lines define planes parallel to the surface associated with different types of bonding. "s" represents the surface, "a" defines the boundry for inner-sphere complexes, "β" defines the boundary for outer-sphere complexes, and "d" defines the boundary for ions in the diffuse layer. Adapted from Sposito [65]. 26

4.1 Structure of goethite. Eight unit cells plotted down the principle crystallographic axes and isometrically, from data in [73]. Iron = brown, oxygen = red, hydrogen = white. 28

4.2 Powder XRD spectra of commercial goethite, synthesized goethite, and the calculated goethite powder XRD spectra. 30
4.3 Scanning electron micrograph image of the 63-212 μm size fraction of synthesized goethite. Upon inspection of the micrograph (in the 1 μm range) round rod-like morphologies are seen for goethite. 31
4.4 Manganese K-edge XANES spectra for Mn-substituted goethite (MG-1.0 and MG-0.5) and reference compounds. Reference scan for $Mn^{II}SO_4$, $LaMn^{III}O_3$, and $CaMn^{IV}O_3$ taken from Alvarez *et al.* [81]. A dashed line is drawn at the peak position of the $LaMn^{III}O_3$ reference compound and shows that manganese in the Mn-substituted goethite is incorporated into the mineral structure as Mn(III). 33
4.5 Powder XRD spectra of commercial goethite and Mn-substituted goethite. . 35
4.6 Scanning electron micrograph images of the 63-212 μm size fraction of (a) goethite and (b) MG-1.0. Upon inspection of the micrographs (in the 1 μm range) the following morphologies are seen: round rod-like structures for pure goethite and an increase in the length-to-width ratio in crystal growth for Mn-substituted goethite as compared to pure goethite. 36
4.7 Room temperature Mössbauer spectra (a) and the modeled hyperfine field distribution (b) for Mn-substituted goethite samples. 37

5.1 Log-log plot of neutron on $^{239}_{94}Pu$ fission cross section. Adapted from the OECD Nuclear Energy Agency [88]. 40
5.2 Log plot of the distribution of fission product nuclei of atomic number (A) versus percent fission yield for the neutron-induced fission of $^{239}_{94}Pu$. Adapted from Friedlander [93]. 41
5.3 Pu(VI) speciation diagram calculated using the in-house code SPECIATE. Solid middle bands represent the average species. Upper and lower dashed bands represent error propagated into the speciation diagram at the 1σ level. Thermodynamic data used to calculate this diagram is shown in table 5.2 and taken from Guillaumont *et al.* [41]. The plutonium species $(PuO_2)_2(OH)_2$ did not exceeded 1% of the total solution species and was not plotted for the sake of clarity. 43
5.4 Formal reduction potentials presented in a Latimer diagram for the four environmentally available plutonium species and plutonium metal. Potentials were measured in 1 M $HClO_4$ at 25 C° [94]. 46
5.5 Overlay of UV-Vis spectra of Pu(III), Pu(IV), Pu(V), and Pu(VI) in 1 M $HClO_4$. Notice the large differences in the absorption spectra and sharp absorption features caused by the dipole forbidden f-f electronic transitions. Adapted from Cohen [101]. 49
5.6 UV-Vis spectra of Pu(III) in 1 M $HClO_4$. Adapted from Cohen [101]. . . . 49
5.7 UV-Vis spectra of Pu(IV) in 1 M $HClO_4$. The steady increase in absorption beginning at 600 nm, and increasing as the photon wavelength gets smaller, has been historically attributed to light scattering in the solution. Adapted from Cohen [101]. 50

5.8 UV-Vis spectra of Pu(V) in 1 M $HClO_4$. Note that Pu(V) has the smallest molar extinction coefficients of any of the plutonium ions shown. Adapted from Cohen [101]. 50
5.9 UV-Vis spectra of Pu(VI) in 1 M $HClO_4$. The very large peak at approximately 830 nm has an extinction coefficient of ∼550 $M^{-1}cm^{-1}$. Adapted from Cohen [101]. 51
5.10 Plot of normalized XANES spectra as a function of energy for Pu(IV), Pu(V), and Pu(VI) in aqueous acidic solution. Note the reduced intensity in the white-line and associated high-energy shoulder for the plutonyl ($Pu^{V}O_2^+$ and $Pu^{VI}O_2^{2+}$) species. 52
5.11 Ball and stick models of (a) Pu^{4+}, (b) $Pu^{V}O_2^+$, and (c) $Pu^{VI}O_2^{2+}$. Plutonium = blue and oxygen = red. Relative bond distances are drawn accurately, but atomic radii are not. Notice the slightly shorter plutonyl bond distance for $Pu^{VI}O_2^{2+}$ due to the higher cationic charge on the plutonium atom. . . . 53

6.1 Schematic of a bending magnet [111]. 56
6.2 Schematic of a wiggler/undulator [111]. 56
6.3 Reflected photon energy as a function of incident X-ray angle for various silicon monochromator crystal cuts. 58
6.4 Photon energy resolution as a function of selected photon energy for various silicon monochromator crystal cuts. 59
6.5 Photon energy resolution as a function of selected photon energy for for a Si 220 monochromator with 0.025 mrad and 0.050 mrad slit size. 59
6.6 Schematic of a typical experimental beamline set-up for XAS collection in transmission mode. 60
6.7 Schematic of a typical experimental beamline set-up for XAS collection in fluorescence mode. 61
6.8 Schematic of an ion chamber. From Knoll [114]. 63
6.9 p-n junction without applied voltage (left) and with applied voltage (right) [47]. 66
6.10 p-n junction acting as a detector. Here x_o defines the active detector area where charge separation occurs as the measured photon interacts with the detector material [47]. 67
6.11 Log plot of absorption cross-section as a function of photon energy for elemental plutonium . The L_I-edge, L_{II}-edge, and L_{III}-edge positions are labeled for clarity. Data from McMaster X-ray cross-section tables [80]. 68
6.12 XAS spectra of the PuO_2 L_{III}-edge with the XANES region labeled. 69
6.13 XAS spectra of the PuO_2 L_{III}-edge with the EXAFS region labeled. 71
6.14 Schematic of the photoexcitation of the 2p core-electron into the continuum by an incident photon of energy $h\nu$. 72
6.15 Schematic of the photoexcitation of the 2p core-electron into the continuum by an incident photon of energy $h\nu$ and the subsequent decay of a higher energy electron into the core-hole with emission of fluorescence photon $h\nu'$. 73
6.16 Plot of the photoelectron wavevector, k, as a function of energy above the photoionization energy, E_o, as defined in equation 6.21. 78

6.17 Plot of the extracted EXAFS oscillations for PuO_2 in (a) k-space and Fourier transformed into (b) r-space. 78

7.1 $k^3\chi(k)$ verses k plots of (a) 15 experimental scans of plutonium sorbed on pyrolusite. (b) The average and standard deviation of the mean for the 15 scans. Red error bars show the error at 1σ. 90
7.2 Molecular model of plutonium (magenta) sorbed on the surface of pyrolusite with associated first hydration shell of waters. Manganese = brown, oxygen = red, hydrogen = gray. Metrics used for the simulation are found in table 7.1. 91
7.3 r-space fits to simulated data using (a) both Pu-Mn and Pu-O paths and (b) only Pu-O paths. 92
7.4 Surface plot of the α surface as a function of simulated EXAFS scans and fit k-range in $Å^{-1}$. 93
7.5 Contour plot of the α surface as a function of simulated EXAFS scans and fit k-range in $Å^{-1}$. 94
7.6 Chemical structure of acetamide phosphonate (Ac-Phos) silane grafted to the mesoporous silica substrate SBA-15, represented as a box labeled SiO_2. . . 96
7.7 L_{III}-edge XANES spectra of plutonium on goethite in a pH 8.0 mineral solution at 300 K. 12 scans at approximately 40 minutes per scan are overlaid and show the effect of beam-induced reduction on the XANES spectra of plutonium [37]. 98
7.8 Least-squares fit of L_{III}-edge XANES spectra of plutonium on goethite in a pH 8.0 mineral solution at 300 K (shown in figure 7.7) plotted against the time exposed to the X-ray beam. 99
7.9 L_{III}-edge XANES spectra of plutonium on goethite in a pH 7.5 mineral solution at 20 K. 11 scans at approximately 40 minutes per scan show no beam-induced reduction occurring at low temperature [37]. 100
7.10 Least-squares fit of L_{III}-edge XANES spectra of plutonium on goethite in a pH 7.5 mineral solution at 20 K (shown in figure 7.9) plotted against the time exposed to the X-ray beam. 101
7.11 L_{III}-edge XANES spectra of plutonium on 0.5 % manganese-substituted goethite in a pH 7.63 mineral solution at 50 K. 16 scans at approximately 25 minutes per scan are overlaid and show no beam-induced reduction occurring at low temperature. 102
7.12 Least-squares fit of XANES spectra of plutonium on 0.5 % manganese-substituted goethite in a pH 7.63 mineral solution at 50 K (shown in figure 7.11) plotted against the time exposed to the X-ray beam. 103
7.13 XANES spectra of plutonium on Ac-Phos (see figure 7.6) bound to a mesoporous silica substrate in a pH 4.4 solution at 30 K. 20 scans at approximately 25 minutes per scan are overlaid and show the effect of beam-induced reduction on the L_{III}-edge XANES spectra of plutonium. 104
7.14 Least-squares fit of XANES spectra of plutonium on Ac-Phos bound to a mesoporous silica substrate in a pH 4.4 solution at 30 K (shown in figure 7.13) plotted against the time exposed to the X-ray beam. 105

7.15 Least-squares fit of 5 XANES spectra of plutonium on Ac-Phos bound to a mesoporous silica substrate in a pH 4.4 solution at 300 K (XANES spectra not shown) plotted against the time exposed to the X-ray beam. Each scan took approximately 5 minutes. 105
7.16 Composite plot of figures 7.14 and 7.15 above, showing the full beam exposure time for the sample of plutonium on Ac-Phos bound to a mesoporous silica substrate in a pH 4.4 solution. After 8 hours of X-ray beam exposure at 30 K the sample was warmed to and left at 300 K for approximately 42 hours before being exposed to the X-ray beam again while 5 additional XANES spectra were collected at 300 K. Notice the split x-axis and different x-axis scaling on this plot. 106
7.17 OceanOptics fiber-optic UV-Vis spectrum of Pu(VI). Note that the sharp peak at approximately 830 nm is partially truncated due to the resolution of the spectrometer. 112
7.18 Representative plutonium L_{III}-edge XANES spectra for Pu(VI) sorbed on Mn-substituted goethite. The energy was calibrated by setting the first inflection point of the Pu L_{III}-edge of a PuO_2 reference sample to be 18062.3 eV [123]. Approximately 35% of the plutonium was Pu(IV) and 65% was Pu(V). Error in the fit at 1σ confidence is 3%. 114
7.19 EXAFS spectra fits in k^3-weighted $\chi(k)$ vs. k, the photoelectron wave vector (left column, blue line) and the corresponding Fourier transform magnitude verses $r + \Delta$, the pseudo-radial distribution function (right column, red line). Dashed black lines are the associated fits. The position of the Pu-Fe scattering path is at roughly 3.0 $r + \Delta$. 117
7.20 Percent sorption of Pu(VI) on the surface of goethite (red open circles and triangles) [37] and manganese-substituted goethite (black squares) as a function of solution pH at an ionic strength of 0.1 M and open to air. 122
7.21 Sorption of Pu(VI) on the surface of goethite (red open triangles) [37] and manganese-substituted goethite (black squares) normalized to mineral surface area as a function of solution pH at an ionic strength of 0.1 M and open to air. 123
7.22 Sorption of Pu(VI) on the surface of 1 % manganese-substituted goethite in units of mg Pu per m^2 of mineral (left axis) open to air. Fractional Pu(VI) solution species (see figure 5.3) unlikely to sorb to the mineral surface are overlayed (right axis). 124
7.23 Sorption of Pu(VI) on the surface of 1 % manganese-substituted goethite in units of mg Pu per m^2 of mineral (left axis) open to air. Fractional Pu(VI) solution species (see figure 5.3) likely to sorb to the mineral surface are overlayed (right axis). 125
7.24 Elemental heat maps for mixed goethite / 1 % manganese-substituted goethite sample in a mineral solution at pH 5.32. 126
7.25 Tri-color plot of iron, manganese, and plutonium for mixed goethite / 1 % manganese-substituted goethite sample in a mineral solution at pH 5.32. White squares with accompanying numbers show positions where Pu-L_{III} edge μ-XANES spectra were collected. μ-XANES fit results are shown in table 7.5. 128

7.26 Elemental heat maps for mixed goethite / 1 % manganese-substituted goethite sample in a mineral solution at pH 6.87. 129
7.27 Tri-color plot of iron, manganese, and plutonium for mixed goethite / 1 % manganese-substituted goethite sample in a mineral solution at pH 6.87. 130
7.28 Elemental heat maps for mixed goethite / 1 % manganese-substituted goethite sample in a mineral solution at pH 8.56. 131
7.29 Tri-color plot of iron, manganese, and plutonium for mixed goethite / 1 % manganese-substituted goethite sample in a mineral solution at pH 8.56. White squares with accompanying numbers show positions where Pu L_{III} edge μ-XANES spectra were collected (see figure 7.25). μ-XANES fit results are shown in table 7.6. 132

B.1 Schematic of the Ag/AgCl electrode. 152
B.2 Schematic of the galvanic Ag/AgCl plating cell. 153
B.3 E_R is the potential required for the reaction to occur and E_W is the potential the working electrode is set at, both with respect to the reference electrode. Figure adapted from [42]. 154

C.1 A schematic of the three-electrode cell. 156
C.2 Plutonium current-voltage diagram adapted from [94, 204]. Potentials referenced with respect to both the standard hydrogen and silver/silver chloride electrodes. 157

E.1 Flow chart of plutonium separation in an anion exchange column. 163

F.1 Flow chart of the programming process for compiled languages and interpreted languages. 166

G.1 Manufacturing drawing of the Janus liquid helium cryostat transfer line. . . 205
G.2 Manufacturing drawing of the Janus liquid helium cryostat. 206
G.3 Sample loader schematics for bulk XAS samples. 208
G.4 Schematic of the first containment layer of the X-ray microprobe sample holder. 210
G.5 Schematic of the second and third containment layers of the X-ray microprobe sample holder. 211
G.6 Photographs of the (a) front and (b) back of the X-ray microprobe sample holder for radioactive samples. 211
G.7 Manufacturing drawing of the sample mount for transuranic μ-XAS samples. 212

List of Tables

4.1 Characterization data for synthesized pure goethite and two synthesized Mn-substituted goethite minerals. Error bars are presented at the 1σ confidence level. . . . 29

5.1 Half-lifes, α decay energies, and α decay intensities for selected isotopes of plutonium [92]. . . . 40
5.2 Thermodynamic data for the hydrolysis and formation of carbonate species in aqueous solution for Pu(VI). Error bars are representative of the 95% confidence interval. . . . 42
5.3 Available experimentally determined standard solubility products, $\log_{10}(K^{\circ}_{sp})$, for plutonium oxides, hydroxides, and carbonate complexes in aqueous solution. Error bars are representative of the 95% confidence interval. . . . 44

6.1 Silicon crystal d-spacings between adjacent crystal planes for different crystal cuts. . . . 57
6.2 W_{gas} values for common gases used in ion chambers [115]. Values listed in bold are commonly used for ion chambers in XAS experiments. . . . 65
6.3 Constants and conversion factors for converting from units of eV to SI units. 76
6.4 Constants and conversion factors for converting from units of eV to atomic units. . . . 77

7.1 Proposed EXAFS model for plutonium sorbed at the mineral-water interface of pyrolusite in solution. Note the subscripts next to O in the paths column are indices for different plutonium-oxygen paths. . . . 91
7.2 Selected standard reduction potentials relative to the S.H.E. related to reactions involving plutonium and radiolytically generated species. . . . 108
7.3 Least-squares fits of Pu L_{III}-edge XANES data to Pu(IV), Pu(V), and Pu(VI) standard spectra. Fits consistently returned zero fit contribution from the Pu(VI) standard spectra. Error bars are presented at the 1σ confidence level. 114
7.4 Fit parameter results from Pu L_{III}-edge EXAFS fits. Symmetric and asymmetric error bars are presented at the 1σ confidence level. . . . 116
7.5 Least-squares fits of Pu L_{III}-edge μ-XANES data at the indicated spatial position (see figure 7.25). Error bars are presented at the 1σ confidence level. . . . 127

7.6 Least-squares fits of Pu L_{III}-edge μ-XANES data at the indicated spatial position (see figure 7.29). Error bars are presented at the 1σ confidence level. 131

B.1 Selected standard reduction potentials relative to the standard hydrogen electrode [39]. 153

C.1 Selected standard reduction potentials for plutonium relative to the standard hydrogen electrode [204]. 156

C.2 Boiling points of common chemicals used in plutonium oxidation state augmentation [39]. 158

Acknowledgments

Acknowledgements have always read kinda funny to me. Towards the end they always seem to deteriorate into an endless list of names with no context given as to why these people are being acknowledged in the first place. Believe me, I'm tempted to follow suit because after almost 10 years at Berkeley (only 5 years in grad school, mind you) the last thing I'm short of is people to thank.

My parents get top billing for their endless love and support throughout both college and graduate school. I've tended to follow my own path, but they've always been there for me when I needed them. I hope to continue to make them proud in the coming years.

I'm lucky to have had such wonderful friends during my time here. Terra and Albert, you two have been the best roommate / weekend roommate a guy could ever hope for. They say friends should never live together, but I think we did pretty well for ourselves. Terra, I'm glad I talked you into drinking martinis, and the invention of the "pint-o-wine" is nothing short of miraculous.

Dr. Prell, you are an inspiration to us all. Never too drunk to talk shop intelligibly and never too proud to make a "...that's what she said!" joke. I've appreciated your frank honesty throughout the years.

To Nick, Ryan, Westin, and Will: you four are grade-A, first-class jerks, and I'm proud to call you my friends. The only thing that made first year quantum tolerable was sitting in the back making snarky remarks. Will, being the late comer to our group never got the chance to take classes with the rest of us, but you and Nick always welcomed me to your guys' apartment and although you never brought down the top-shelf beer, I appreciated all the delicious middle-shelf beer we've drank over the years.

Jason, Tim, and Monica: thank you for being such great friends. We've come a long way since that year in Japan, but I know I can always count on you guys.

The Nitsche Group has been quite kind to me these last 10 years. In that time I've had the great pleasure of meeting quite the rag-tag band of misfits that make up the past and present of our group. Thanks Sam for showing me how to run the laser and being a good friend during those early undergraduate years. The same thanks also goes out to Herbie. Have you taught your 7 year-olds calculus yet? Phil, you taught me the most important lesson of all: going to college is about learning *how* to learn. I remember once when I was a freshman undergrad you asked me why synchrotron radiation is focused like a spotlight tangent to the curvature of the storage ring. I'm honored that you thought so highly of me that you thought I would know the answer back then (incidentally, it's a result of the Lorentz contraction in the laboratory frame of reference). Good luck with that new wife of yours. Ken and Jackie, you always asked the questions that I feared the most because they were always the most poignant and fundamental ones. When I did have an answer to your questions, it usually made my day. Thanks to Liv and Zuzana for great scientific discussions. Thanks Maz for showing me how to etch, Joe (A.K.A. Joey II, New Joey) for enlightening discussions on statistics, and Carolina because she's apparently collecting thank-yous.

Kestrel, Tashi, Deborah, Oliver, Jennifer, Nick, and Erin, the future of the Nitsche group has never looked so bright (I'm serious... Well, OK Oliver might be bringing you guys down a little). I'm glad I got a chance to give back a little before checking out. Kestrel gets a double thank you here for proof reading this whole thing. Any sense of readability in this

thesis is probably her doing.

Thanks goes out to my qualifying exam committee members. Professor Ahn, you've been a wonderful fellowship coordinator these past few years. Professor Cerny, I'll be sure to brush up on the topic of "The History of Chemistry." Also, sorry about that whole mid-term thing. Professor Head-Gordon, thanks for being such a good sport. I know I work with elements that have about 2.36 orders of magnitude more nucleons than you're used to (although it's really the number of electrons that matter), but it was still great to have you on my committee. I only thing I regret was not getting the chance to whip out the spin-orbit coupling term to the Hamiltonian. Here you go, just in case:

$$\sum_j \xi(r_j)\mathbf{l}_j \cdot \mathbf{s}_j$$

Darleane, thank you for all of the kind words, helpful discussions, and support you've given me throughout the years.

Wayne, thanks for knowing everything about everything (and not being a jerk about it). David, thank you for setting me straight about vacuum systems and being the only guy I could ever count on to be at lab bright and early at 8 A.M. on Saturday mornings. Justin, thanks for coming into my office to talk shop. Science is always more fun when you have someone to talk to about it.

Thank you John, Joe R., and Sam W. down at SSRL. Your hard work made my experiments so much easier. I'm glad to have been a small part of the SSRL family during my time here.

It's also important to remember that getting science done requires more than the will of scientists. Thank you John V. and Naomi for all the pass-outs, surveys, assays, and making the HERL a more entertaining place to work. Also, thank you to the radiation protection group down at SSRL, especially Carol for going above and beyond the call of duty to make sure that I was able to measure my samples safely.

I've had many mentors along the way, but three in particular stand out: Richard, Corwin, and Heino. Now when I say Richard I don't mean the happy-go-lucky Richard of today. I'm talking about Richard circa 2001-2005. I'm talking about mean, bitter, jaded Richard. The guy who, on multiple occasions, made other graduate students cry using only his words. That guy was awesome! Without Richard, I'm not sure what kind of grad student I would have become. There, I said it. It's out there. On two separate occasions he asked me the questions that would set me on my grad student path: "Hey, do you know how to program?" and, "Hey, want to fit my EXAFS data for me?". The guy says "hey" a lot.

Of course, without the help of Corwin I don't think I would have gotten very far. As I write this, I find myself thinking, "What kind of scientist is Corwin Booth?" The answer to that question of course is that he's like any other scientist ... only more so. He's sort of the XAS Yoda, only less green and taller. His patience, assistance, and mentorship has made my experience in grad school better.

Finally, there's Heino. Heino, Heino, Heino ... what can I say? I still remember meeting you for the first time in the chemistry research seminar series C96 back in 2001. What kind of professor drinks out of the sink faucet in front of 150 freshmen? Probably the same kind of professor who lights his arm on fire during a class demo, or stands up to a rowdy bus rider by picking a fight with him. I knew back then that I wanted to work for you. You gave that

naive, starry-eyed 17-year-old a chance to do real science at one of the greatest universities in the world. For that I am forever grateful. The same goes for helping me get into grad school. Of all the lessons I've learned during my time here the two most important lessons are the ability to think independently and the fact that the donkey always puts himself first. *I* thank you Heino.

Chapter 1

Introduction

In recent years the scientific community and the world have seen mounting evidence pointing to anthropogenic global warming. This has resulted in a tremendous drive towards utilizing methods of energy production that do not release significant amounts of CO_2 and other greenhouse gases. Nuclear energy is currently the only feasible, non-CO_2 emitting, secure peak-power source of electricity that is able to meet the energy demands of our nation and the rest of the world and must be adopted more widely if we hope to curb our reliance on fossil fuels.

Unfortunately, nuclear power and weapons production results in highly radiologically and chemically toxic byproducts that need to be properly handled and isolated from human contact. To face the challenge of radioactive waste storage and contaminated site remediation, a solid understanding of the fundamental molecular-level chemical processes behind the transport and migration of actinides in the environment is necessary. The elucidation of interfacial reactions/interactions at the boundary between aqueous radionuclide solutions and minerals is particularly important when trying to understand how these contaminants move in the environment. However, measurements on this type of sample is often hindered by their low concentrations and absence of long-range molecular order. To mitigate these issues we take advantage of advanced synchrotron based X-ray spectroscopies that allow use to probe non-crystalline materials on an atom-specific level with a reasonably low limit of detection. The knowledge acquired from these experiments will allow us to more accurately model and predict the ultimate fate of radionuclides in the geosphere.

The study of environmental processes includes solubility and speciation [2, 3, 4, 5, 6, 7, 8], solution complexation (organic [9, 10] and inorganic ligands [11, 12, 13, 14, 15]), surface complexation (organic [16] and inorganic substrates [17, 18, 19, 20, 21, 22, 23, 24, 25, 26]), reduction-oxidation reactions [27, 28, 29, 30], interactions with microorganisms [31, 32, 33, 34], and many other processes [35, 36]. Figure 1.1 shows a schematic of some selected processes in environmental science. Here we can see that even a simple representation of natural systems is characterized by a level of complexity that is difficult, if not impossible, to study as a whole in a laboratory setting. In an attempt to recast this problem in a tractable form, we concentrate our studies on only a subset of all possible environmental processes. In this way we formulate idealized model interactions to those that occur in nature in order to probe and understand which variables are the key driving forces in these environmental processes. Figure 1.2 shows a schematic of the interactions studied in this work.

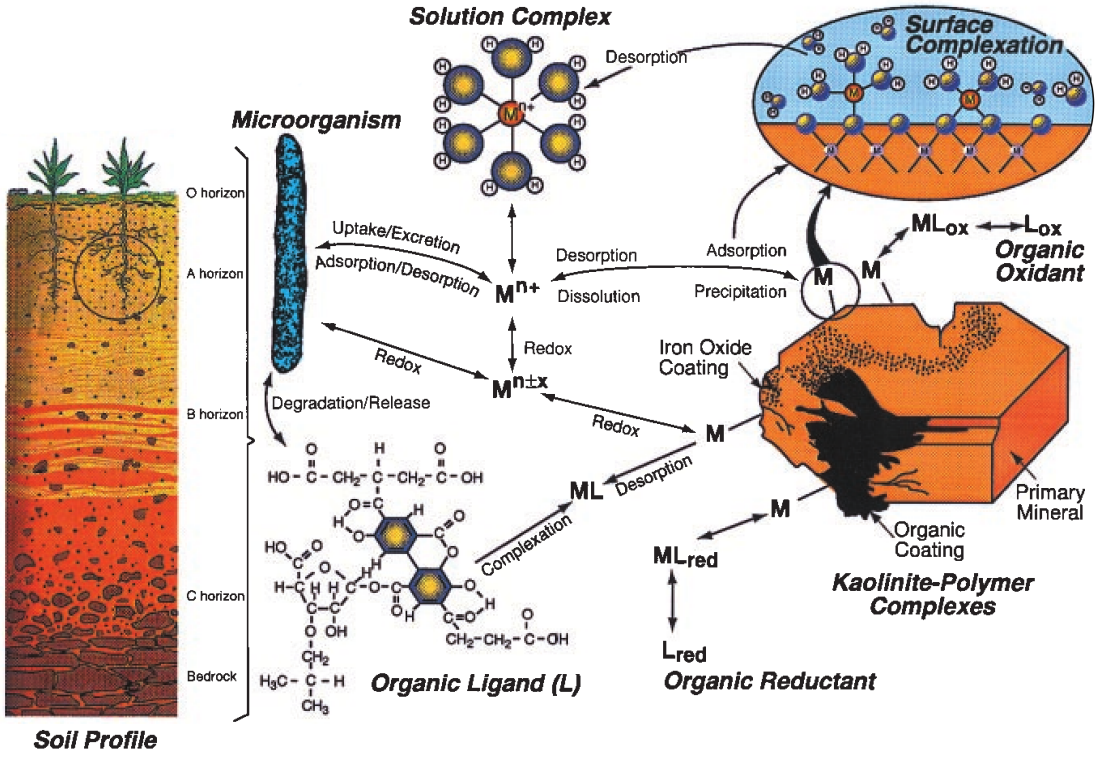

Figure 1.1: Molecular-scale processes in environmental science, from Brown *et al.* [1].

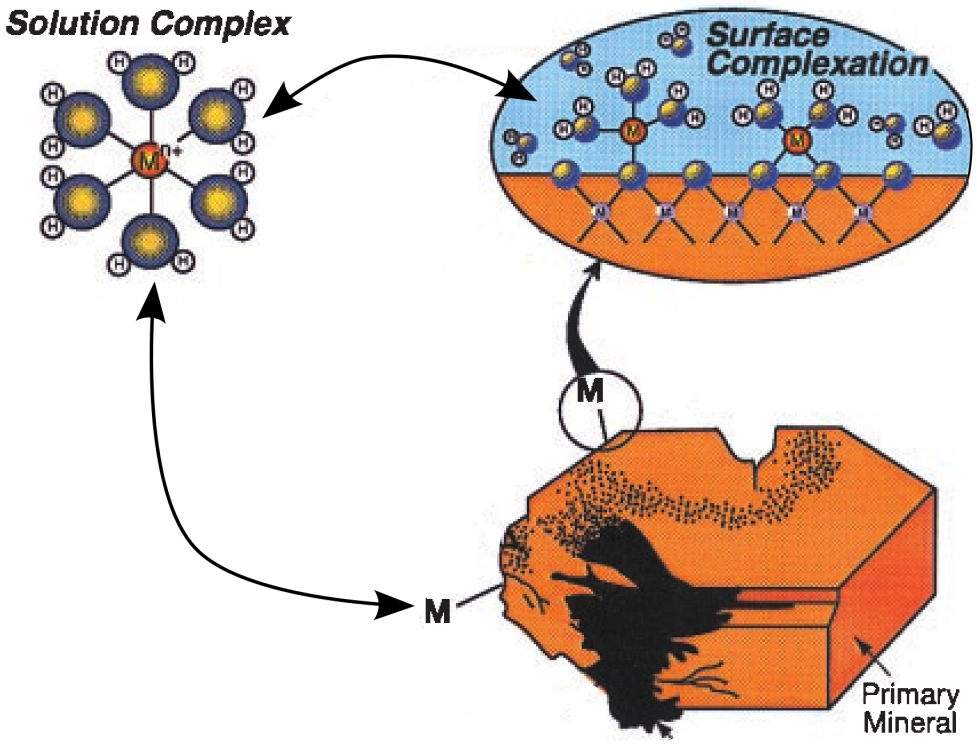

Figure 1.2: Subset of molecular interactions investigated in this work. Adapted from Brown *et al.* [1].

The goal of this study is to understand the interaction of plutonium(VI) at the surface of a well-characterized synthetic manganese-substituted goethite mineral ($Fe_{1-x}Mn_xOOH$). This work presents molecular-level information acquired through the use of advanced synchrotron-based X-ray techniques including: X-ray absorption near-edge structure (XANES) spectroscopy, extended X-ray absorption fine-structure (EXAFS) spectroscopy, micro synchrotron X-ray fluorescence (μ-SXRF) spectroscopy, and micro X-ray absorption near-edge structure (μ-XANES) spectroscopy.

This line of research is a continuation of work previously conducted by Wilson [37], on goethite (α-FeOOH) and Shaughnessy *et al.* [20] on various manganese oxide minerals. Wilson showed that Pu(VI) sorption on pure goethite resulted in reduction of Pu(VI) to Pu(V), but not to the more insoluble Pu(IV) oxidation state (see subsection 5.3.2), and showed evidence suggesting that plutonium was bound to the surface of goethite as an inner-sphere complex (see section 3.3). Shaughnessy *et al.* showed reduction of Pu(VI) to Pu(IV) on the surface of various manganese oxide minerals, with spectroscopic evidence suggesting that plutonium was bound to the mineral surface as an inner-sphere complex (see chapter 6). This previous work, along with results from a paper by Duff *et al.* [19] showing plutonium association with manganese, but not iron containing minerals in Yucca Mountain tuff, inspired us to look into the interaction of plutonium(VI) with synthetic manganese-substituted goethite minerals to see the effect of a minor substitution of Mn for Fe on the redox chemistry and binding characteristics of plutonium at the mineral-solution interface. We chose to study the influence of manganese as a minor component in goethite because goethite rarely exists as a pure phase in nature. In the process of conducting these experiments, we encountered and overcame certain challenges involving sample preparation and data collection. Quantitative understanding of these limitations is discussed in this work and allows for the design of better experiments.

The use of advanced synchrotron-based X-ray techniques allows us to directly and unambiguously measure the oxidation state, coordination number, and nearest neighbor identity of plutonium *in-situ* at the mineral surface and spatially resolve plutonium associations with different mineral phases. Because manganese is often found in the environment as a minor component associated with major minerals, such as goethite, understanding the molecular-level interactions of plutonium with such manganese-substituted goethite mineral phases is important for risk assessment purposes at radioactively contaminated sites and long-term underground radioactive waste repositories.

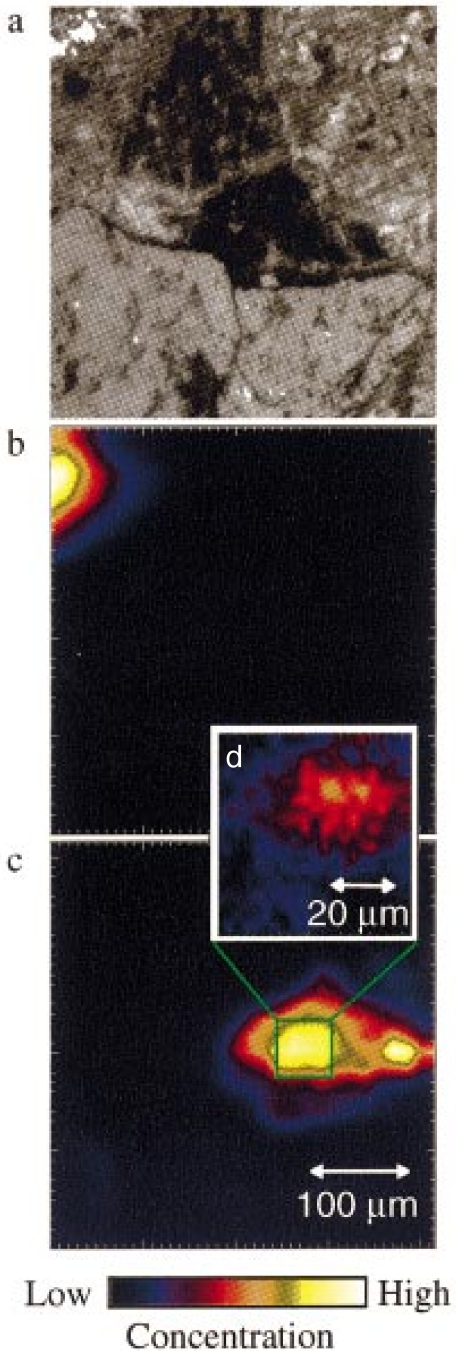

Figure 1.3: (a) Photomicrograph of the manganese and iron oxide phases in the sample under reflected light. The silver-colored structure in the upper left corner is hematite, the center area is a manganese oxide, and the surrounding features are highly zeolitic. Complementary micro-SXRF elemental map images show spatially localized (b) Fe, (c) Mn, and (d) Pu. From Duff *et al.* [19].

Chapter 2

Aqueous Solution Chemistry

> Once, during Prohibition, I was forced to live for days on nothing but food and water.
>
> *W. C. Fields*

2.1 Ionic Strength and Activity

Water is the ubiquitous solvent in environmental systems. Therefore, to understand species of interest in solution it is important to understand the characteristics of water as a solvent. Ions in aqueous solutions are found surrounded by a layer of water molecules attracted to the ion by ion-dipole forces. The greater the ionic charge, the more water molecules are attached. For ions of the same charge, the smaller the ionic radius (the more charge density around the ion) the more water molecules are attracted. Therefore, a highly charged ion with small ionic radius has a large hydrated radius in aqueous solution.

When inert salts, such as $NaClO_4$, are added to solution the hydrated radius of the species of interest changes, despite the fact that the added salts do not complex with the species of interest. These inert ions instead change the structure of the hydrated radius. To understand how this effect ultimately changes the solution chemistry, the so-called ionic strength of the solution must be defined. The ionic strength of a solution is a measure of the total ion concentration, where more highly charged species are weighted more. The equation to calculate the ionic strength is:

$$\mu = \frac{1}{2} \sum_i c_i z_i^2 \tag{2.1}$$

where c_i is the concentration of species i in solution, z_i is the charge of species i in solution, and μ is the ionic strength of the solution in units of molarity.

The ionic strength of the solution can then be used to calculate the activity coefficient

for a specific ion using the extended Debye-Hückel equation [38]:

$$\log\gamma_i = -\frac{0.51 z_i^2 \mu^{1/2}}{1 + \frac{\alpha_i \mu^{1/2}}{305}} \tag{2.2}$$

where z_i is the charge on the ion and α_i is the size parameter of the ion at 25 °C in a solution of ionic strength μ. Equation 2.2 works well for aqueous solutions where $\mu \leq 0.1$ M. The activity coefficient of a species is the correction to the concentration of a species in aqueous solution with non-zero ionic strength. Together with the concentration of a species, the activity coefficient defines the activity of a species in solution:

$$\mathcal{A}_i = [i]\gamma_i \tag{2.3}$$

The rigorous definition of equilibrium constants (subsection 2.3.1) requires the use of species activities, as opposed to species concentrations. However, under certain conditions, such as dilute solutions or constant ionic strength, the activity coefficient remains constant and often cancels out.

2.2 Acid-Base Chemistry

At common environmental temperatures and pressures, water exists predominantly in the form H_2O. However, a small fraction of water molecules in a pure solution of water will undergo auto-dissociation according to the equation:

$$H_2O \rightleftharpoons H^+ + OH^- \tag{2.4}$$

We can define a thermodynamic constant, K_w, that represents the extent to which reaction 2.4 occurs.

$$K_w(2.4) = [H^+][OH^-] \tag{2.5}$$

The numerical value of K_w is temperature dependent, and is not, in the strictest sense, constant. At 25 °C and atmospheric pressure $K_w = 10^{-13.995}$ [39]. More rigorously, the equation that defines K_w should be written using the activity, $\mathcal{A}$, of the proton and hydroxide ions. For equation 2.5 above, we can correct for activities by multiplying the concentration of each ion with its respective activity coefficient, γ:

$$K_w(2.4) = [H^+]\gamma_{H^+}[OH^-]\gamma_{OH^-} \tag{2.6}$$

The activity coefficient, γ, varies as a function of the ionic strength of the solution. However, since the ionic strength of a solution of pure water is exceedingly small, equation 2.5 is an excellent approximation for equation 2.6.

The acidity of an aqueous solution is conventionally measured in units of pH, defined to be the negative logarithm of the hydrogen ion activity.

$$\mathrm{pH} = -\log\left([H^+]\gamma_{H^+}\right) \tag{2.7}$$

Although the term pOH is similarly defined for the basicity of a solution, pH is still often used because pOH can easily be calculated from this value. Rearranging equation 2.7 and the similarly defined pOH equation, and substituting into equation 2.6 gives:

$$K_w = 10^{-13.995} = 10^{-pH}10^{-pOH} = 10^{-(pH+pOH)}$$

implying that

$$pH + pOH = 13.995 \tag{2.8}$$

at 25 °C. Note that equation 2.8 does not restrict pH values to be between 1 and 14. However, it is often used within this range, whereas units of concentration are used when the pH falls outside of this range.

Many compounds, including organic molecules and metal oxide surfaces in aqueous solution, can undergo dissociation reactions similar to water (equation 2.4). If a proton is donated during the reaction then the species is defined to be a Brønsted acid, while if a proton is accepted during the reaction the species is defined as a Brønsted base.

$$AH \rightleftharpoons A^- + H^+ \tag{2.9}$$

$$B + H_2O \rightleftharpoons BH^+ + OH^- \tag{2.10}$$

Using these two equations we can define two thermodynamic stability constants K_a and K_b to be:

$$K_a(2.9) = \frac{[A^-][H^+]}{[AH]} \tag{2.11}$$

$$K_b(2.10) = \frac{[BH^+][OH^-]}{[B]} \tag{2.12}$$

To simplify equations, the concentration of a species is used interchangeably with the activity of the species. However, it is important to realize when it is necessary to use species activities and account for solution ionic strength. Notice that in equations 2.11 and 2.12, AH and BH^+ are both Brønsted acids, and A^- and B are both Brønsted bases. If the chemical form of A and B are the same then,

$$K_a \cdot K_b = K_w \tag{2.13}$$

In chapter 3 these equations are expanded on and applied to metal oxide surfaces to help describe the chemistry occurring at the solution/mineral interface.

2.3 Complexation and Speciation

2.3.1 Equilibrium Constants

Thermodynamic equilibria of chemical species is essential to understanding the long-term fate of radionuclides in the environment. In aqueous solutions, various species or

combinations of species may form depending on the available elements and the chemical reactions these elements can undergo. For the general chemical equation

$$\mathrm{aA} + \mathrm{bB} \rightleftharpoons \mathrm{cC} + \mathrm{dD} \tag{2.14}$$

we can define a term called the equilibrium constant, K, to be approximately:

$$\mathrm{K} = \frac{[\mathrm{C}]^{\mathrm{c}}[\mathrm{D}]^{\mathrm{d}}}{[\mathrm{A}]^{\mathrm{a}}[\mathrm{B}]^{\mathrm{b}}} \tag{2.15}$$

It is important to realize that the exact equilibrium constant is defined using the activities of the reaction species and not the concentrations. This formalism is the same as the one used in section 2.2 to define the water dissociation constant (equation 2.5), $\mathrm{K_w}$, and the acid and base dissociation constants (equations 2.11 and 2.12), $\mathrm{K_a}$ and $\mathrm{K_b}$. We define a reaction as being "favorable" in the direction written if $\mathrm{K} > 1$.

The equilibrium constant is related to the free energy of the system by the equation:

$$K = e^{-\Delta G^\circ / RT} \tag{2.16}$$

where ΔG° is the free energy of the system where all species are in their standard states, R is the gas constant, and T is temperature in units of Kelvin. Inspection of equation 2.16 shows that for K to be greater than one it is necessary that ΔG° be negative, implying that the forward reaction is favored as was defined above. It is also important to note that the equilibrium constant is a function of temperature. Free energy is defined by the equation:

$$\Delta G^\circ = \Delta H^\circ - T\Delta S^\circ \tag{2.17}$$

where ΔG° is again the free energy of the system at standard state, ΔH° is the enthalpy of the reaction at standard state, T is the temperature in units of Kelvin, and ΔS° is the entropy of the reaction at standard state. Substituting equation 2.17 into equation 2.16 and rearranging gives:

$$K = e^{-(\Delta H^\circ - T\Delta S^\circ)/RT} = e^{-\Delta H^\circ/RT + \Delta S^\circ/R} = e^{-\Delta H^\circ/RT} \cdot e^{\Delta S^\circ/R} \tag{2.18}$$

The second term in the final result of equation 2.18 shows no dependence on T. The first term states that the equilibrium constant will increase with increasing temperature if ΔH° is positive (the reaction is endothermic), and decrease with increasing temperature if ΔH° is negative (reaction is exothermic). This result is expected from Le Châtelier's principle.

For reactions where multiple ligands form around a coordination center, the convention is that K is used for the stepwise formation constant and β is used for the overall formation constant. The following ligand protonation equations illustrate this convention:

$$\mathrm{H^+} + \mathrm{H_{x-1}L} \rightleftharpoons \mathrm{H_xL} \tag{2.19}$$

$$K(2.19) = \frac{[\mathrm{H_xL}]}{[\mathrm{H^+}][\mathrm{H_{x-1}L}]} \tag{2.20}$$

$$\mathrm{xH^+} + \mathrm{L} \rightleftharpoons \mathrm{H_xL} \tag{2.21}$$

$$\beta(2.21) = \frac{[\mathrm{H_xL}]}{[\mathrm{H^+}]^{\mathrm{x}}[\mathrm{L}]} \tag{2.22}$$

Notice that we reference the number of the reaction directly when writing equilibrium constants, as suggested by [40, 41]. The decision to do this is partially fueled by the fact that the IUPAC has not explicitly defined a standardized way to present equilibrium constants. There are therefore a multitude of ways to properly subscript the equilibrium constant, many of which are confusing and contradictory. In this way there is no need to guess as to which equation the stability constant expression is referring to, nor is there a need to decipher cryptic subscripts.

2.3.2 Speciation and Statistical Error in Speciation Diagrams

A speciation diagram is a plot of solution complexes as a function of some variable physical parameter (usually pH). These types of plots give insight into the chemical species in solution that are available to possibly undergo further chemistry. For simple systems, it is possible to analytically calculate a speciation diagram. This is done below for the acid dissociation of acetic acid. Acetic acid loses a proton to solution through the following reaction:

$$\mathrm{CH_3CO_2H} \rightleftharpoons \mathrm{CH_3CO_2^-} + \mathrm{H^+} \tag{2.23}$$

Given this reaction we can write a thermodynamic acid dissociation constant having the following functional form:

$$\mathrm{K_a}(2.23) = \frac{[\mathrm{CH_3CO_2^-}][\mathrm{H^+}]}{[\mathrm{CH_3CO_2H}]} \tag{2.24}$$

Again, we approximate the species activities with the species concentrations. This equilibrium constant has been measured in the past and has a value of $\mathrm{K_a}(2.23) = 1.75 \times 10^{-5}$ [42]. For equation 2.23, mass action clearly shows that the sum of the acetic acid ($\mathrm{CH_3CO_2H}$) and its conjugate base ($\mathrm{CH_3CO_2^-}$) must be constant as a function of pH. We can therefore substitute in the variable x for the concentration of acetic acid and 1-x for the concentration of the conjugate base. Equation 2.24 then becomes:

$$\mathrm{K_a}(2.23) = \frac{(1-x)[\mathrm{H^+}]}{x} = \frac{[\mathrm{H^+}]}{x} - [\mathrm{H^+}] \tag{2.25}$$

rearranging the equation to solve for x gives:

$$x = \frac{[\mathrm{H^+}]}{\mathrm{K_a}(2.23) + [\mathrm{H^+}]} \tag{2.26}$$

Next we rearrange equation 2.7, assuming that the activity coefficient ($\gamma_{\mathrm{H^+}}$) is equal to one, and substitute into equation 2.26 to give:

$$x = \frac{10^{-\mathrm{pH}}}{\mathrm{K_a}(2.23) + 10^{-\mathrm{pH}}} \tag{2.27}$$

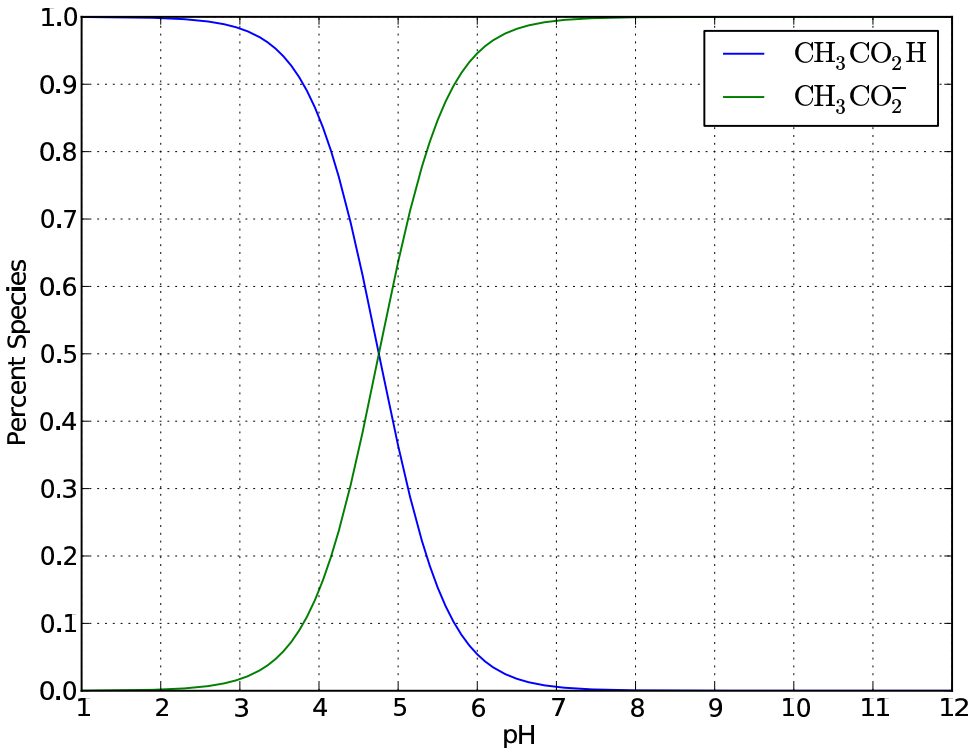

Figure 2.1: Speciation diagram of acetic acid and its conjugate base as a function of pH.

Figure 2.1 shows a speciation plot of acetic acid and its conjugate base as a function of pH, plotted from the analytic function derived in equation 2.27. The calculation of the error associated with this speciation diagram is fairly straightforward for simple systems such as this and involves calculating the derivative of equation 2.27 with respect to K_a(2.23). However, in general this calculation is not trivial.

As the number of potential species increases, it becomes more difficult to analytically solve the system of equations necessary to plot the speciation diagram. However, modern computers are well suited for this type of problem and numerical solutions can be achieved to any level of accuracy desired. Many computer programs are available to assist in this type of calculation, including PHREEQC [43], MINEQL+ [44], and The Geochemist's Workbench [45]. For this work PHREEQC is used to calculate speciation diagrams because it is a free and open source program that is fairly easy to couple to scripting/programming languages. However, very few programs properly address the issue of error propagation in speciation diagrams.

The understanding and proper application of errors in the physical sciences is of utmost importance when trying to understand the impact and validity of a measured physical property in an experiment. Many excellent books and chapters of books on the subject of error analysis and propagation have been written [42, 46, 47, 48, 49, 50]. Some of these books, such as "Statistics for Nuclear and Particle Physicists" by Lyon, are written with a particular audience in mind. However, the field of statistics is all encompassing in relation to the physical sciences, and application to one's own field is simply a matter of understanding which proper nouns to exchange out while reading.

Thermodynamic formation constants, like other measured physical constants, are often taken from various sources, resulting in a mean value and associated error bars. Often these error bars are presented symmetrically with the assumption that the value is distributed according to the normal, or Gaussian, distribution. This choice is made by many authors in the absence of a better alternative [41]. When preparing speciation diagrams it is very rare to see the use of proper error propagation from the thermodynamic data into the speciation diagram itself. Often practitioners use the mean value of the thermodynamic constant, even for values that have exorbitantly large error bars.

At this point, it is important to recall from elementary statistics that the mean value of a measurement is not necessarily the "true" value of the property being measured. Specifically, when we present data with some confidence interval (usually 68% or 95%, corresponding to $1\sigma/\sqrt{n}$ and $1.95\sigma/\sqrt{n}$, respectively, where n is the number of independent measurements) it should be noted that the probability of the true value to be anywhere within the cited interval is exactly the same. It is not any more likely to be found at the center of the interval than it is at the extremes [50]. That is to say, once we define a confidence interval for our measurement and reduce our measured distribution to a set of two to three numbers we lose specific information about the original distribution. The authors of "Chemical Thermodynamics: Update on the Chemical Thermodynamics of Uranium, Neptunium, Plutonium, Americium and Technetium" [41] make the assumption that the collected thermodynamic constants from the literature are distributed according to the Gaussian distribution. It turns out that in most cases this is approximation is valid.

Given the need for confidence in speciation calculations it is worth the effort to propagate thermodynamic data error through to the speciation diagram. The difficulty in this process

arises from the fact that even if analytical solutions were possible, they would become increasingly complex as the number of solution complexes increased. In an attempt to side-step this difficulty we resort to a brute-force process using the Monte Carlo method where thermodynamic data is randomly chosen within the confidence interval given, and a speciation diagram is calculated from these random values. This process is repeated many times, and through this effort we recover the speciation distribution (error) of the speciation diagram at a particular pH value. These diagrams, a function of species percentage verses pH, show possible solution species available for binding onto the mineral surface. Unfortunately, it is often the case that thermodynamic data contains values with such large error bars that we are unable to acquire any useful information from them in the form of speciation diagrams. It is especially important under such conditions to calculate the speciation diagram with error bars, because only then will one be able to make a quantitative judgement as to how reliable a speciation diagram is.

Issues with the Monte Carlo method include the extremely large amount of calculation time that is required to properly sample the various stability constant distributions and give reliable error bars. However, these calculations are easily automated on modern computers. Previous work has been done on the subject of propagating errors into speciation diagrams using both Monte Carlo and Latin hypercube sampling methods, resulting in LJUNGSKILE [51, 52], a freely available program for the Windows operating system.

Our in-house code SPECIATE (see section F.4) borrows heavily from LJUNGSKILE's basic internal design, but has been written from scratch to take advantage of parallel computer processing, and allows for more direct interaction with the underlying speciation calculation engine, PHREEQC. The code automates the calculation of solution species at one pH value and loops through a large set of pH values to calculate the full speciation diagram. It then randomly chooses a new set of thermodynamic constants and calculates another speciation diagram. This is done repeatedly until the species distribution (error) at all pH values is recovered. The exact number of calculations this takes depends on the number of species in the speciation diagram and the size of the error in the thermodynamic formation constant for each species. The final recovered distribution is then integrated to yield the error bars at the confidence level of interest. Individual speciation calculations are calculated using the freely-available program PHREEQC from the United States Geological Survey (USGS). An example of such a speciation diagram calculated using SPECIATE can be found in section 5.3.

2.4 Oxidation and Reduction Reactions

Another class of important aqueous solution reactions are oxidation and reduction reactions. These types of reactions occur when electrons are transfered from one species to another in solution. Such reactions can vastly change the chemistry of solution species since the transfer of electrons is accompanied by a change in oxidation state for both species. Depending on the solution species, oxidation state changes can result in vastly different chemistries. The generic redox half-reaction is shown below:

$$\mathrm{Ox}^{n+} + \mathrm{e}^{-} \rightleftharpoons \mathrm{Re}^{(n-1)+} \tag{2.28}$$

where Ox is an oxidized species, and Re is a reduced species. Obviously, whether a species is oxidized or reduced depends on the other species it is being compared to. Half-reactions are conventionally written as reduction half-reactions where the oxidized species and electrons are on the left and the reduced species is on the right. Each half-reaction is characterized by a potential for the process to occur in the direction that the reaction is written. These reduction potentials are characteristic of the chemical half-reaction. The value E° is defined as the standard reduction potential. Since potential values only make sense relative to a reference point, electrochemists have set the standard reduction reaction of H^+ to hydrogen gas to be exactly 0.00 V.

$$2\,H^+ + 2\,e^- \rightleftharpoons H_{2\,(g)} \qquad E^\circ = 0.00\ V \tag{2.29}$$

The electrode that can produce this half-reaction is referred to as the standard hydrogen electrode (SHE). Other half-reactions are measured relative to the SHE. The reduction of O_2 and H^+ to form water has a positive standard reduction potential and is therefore favored in the direction it is written relative to the SHE.

$$O_{2\,(g)} + 4\,H^+ + 4\,e^- \rightleftharpoons 2\,H_2O \qquad E^\circ = 1.23\ V \tag{2.30}$$

The standard reduction potential is related to the free energy of the system by the amount of work that the reaction is able to do. This is represented by the equation:

$$-\Delta G^\circ = nE^\circ F \tag{2.31}$$

Equation 2.31 confirms that reactions with positive E° are spontaneous in the direction they are written, while reactions that have negative E° are spontaneous in the opposite direction. Substitution of equation 2.31 into equation 2.16 yields the functional relation between the thermodynamic constant, K, for the redox reaction and the standard reduction potential for that reaction.

$$K = e^{-nE^\circ F/RT} \tag{2.32}$$

For reactions with species that are not at standard state, it becomes necessary to calculate the reduction potential (E) using the standard reduction potential (E°) and the Nernst equation. For the half-reaction:

$$aA + ne^- \rightleftharpoons bB \tag{2.33}$$

the Nernst equation is defined as:

$$E = E^\circ - \frac{RT}{nF}\ln\left(\frac{\mathcal{A}_B^b}{\mathcal{A}_A^a}\right) \tag{2.34}$$

where E° is the half-reaction potential at standard state, R is the universal gas constant, T is the temperature in units of Kelvin, n is the number of electrons transfered in the reaction, F is Faraday's constant, and $\mathcal{A}_A^a$ and $\mathcal{A}_B^b$ are the activities of species A and B to the power of their coefficients, respectively. At 25 °C collecting all constant terms and converting from the natural logarithm to base-10 logarithm, the Nernst equation becomes:

$$E = E^\circ - \frac{0.05916\ V}{n}\log\left(\frac{\mathcal{A}_B^b}{\mathcal{A}_A^a}\right) \tag{2.35}$$

Appendix B contains an example of utilizing the Nernst equation to calculate the necessary driving potential to plate silver chloride on a silver wire for preparing Ag/AgCl reference electrodes.

2.5 Carbonate Equilibrium in Aqueous Systems

In nature, aqueous systems are often open to and in equilibrium with air. When this is the case, it is important to understand the effect of CO_2 on the solution chemistry of the sample. When CO_2 gas dissolves in water the gas comes into equilibrium with carbonic acid, which can then change the pH of the aqueous solution. Carbonic acid in aqueous solution will undergo acid dissociation reactions to form carbonate anions (CO_3^{2-}), which can form metal-ligand complexes of the form:

$$M^{n+} + xCO_3^{2-} \rightleftharpoons M(CO_3)_x^{n-2x} \tag{2.36}$$

These complexes can interact with the environment differently than the bare metal cation originally would. Therefore, it is important to understand the availability and concentration of carbonate in solution as a function of pH. First, the equilibrium equations concerning gaseous CO_2 dissolution into aqueous solution will be discussed, then this equilibrium knowledge will be applied to the preparation of sample solutions.

The chemical equations controlling CO_2 dissolution and carbonate formation in aqueous solution are:

$$pCO_{2(g)} \quad CO_{2(aq)} \tag{2.37a}$$

$$CO_{2(aq)} + H_2O \quad H_2CO_3 \tag{2.37b}$$

$$H_2CO_3 \quad H^+ + HCO_3^- \tag{2.37c}$$

$$HCO_3^- \quad H^+ + CO_3^{2-} \tag{2.37d}$$

where $pCO_{2(g)}$ is the partial pressure of CO_2 in the atmosphere. Most texts cite the partial pressure of CO_2 in the atmosphere to be $10^{-3.5}$ atm, or approximately 316 ppm by volume [53]. Data from the National Oceanic & Atmospheric Administration (NOAA) shows that this value was most likely measured in the early 1960's. As of October 2010, the average partial pressure of CO_2 in the atmosphere is $10^{-3.41}$ atm, or approximately 388 ppm by volume [54]. Figure 2.2 shows a plot of the yearly average partial pressure of CO_2 as measured at Mauna Loa, Hawaii. Monthly averages would show seasonal oscillations in CO_2, but the increasing trend is still evident and widely believed to be caused by anthropogenic CO_2 production from the use of fossil fuels.

Equations 2.37a and 2.37b are often combined into a single equation (equation 2.38) because it is difficult to measure the equilibrium constant of absorbed CO_2 in the absence of carbonic acid.

$$pCO_{2(g)} + H_2O \quad H_2CO_3^* \tag{2.38}$$

where $H_2CO_3^*$ represents the available doubly protonated carbonic acid in the sample solution. As Henry's law states, at constant temperature and volume the concentration of a dissolved gas in solution is directly proportional to the partial pressure of that gas in contact

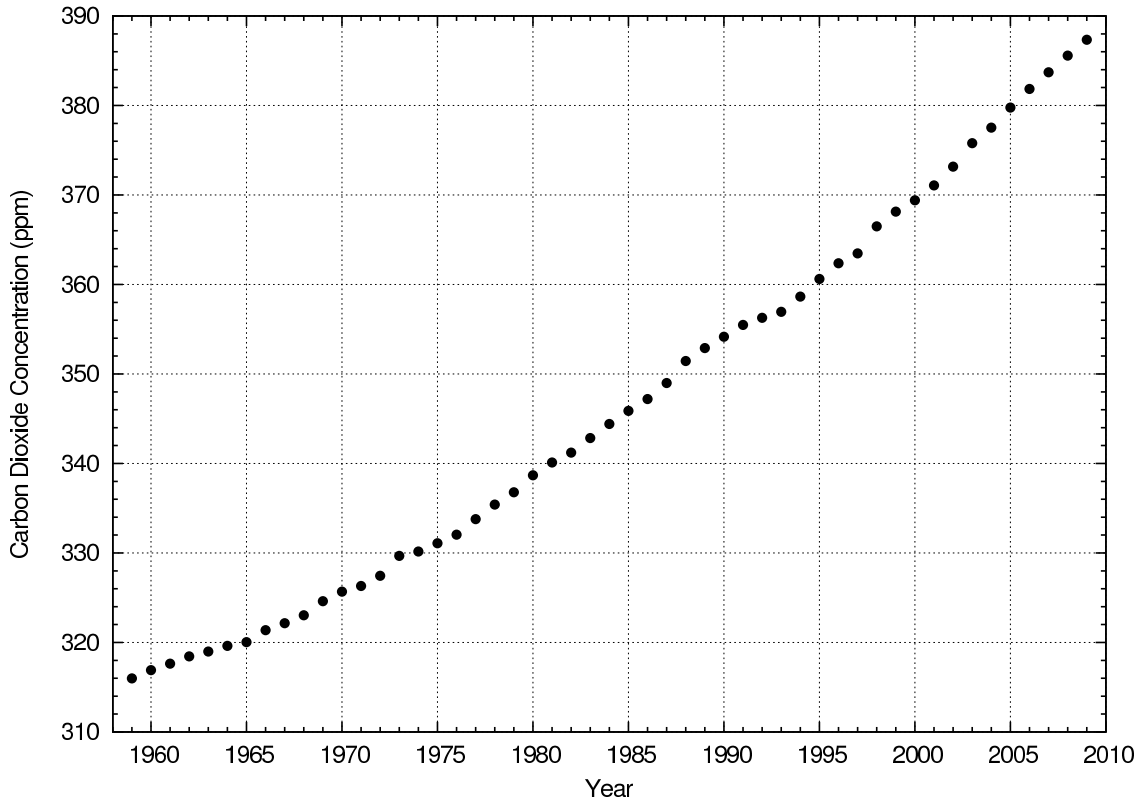

Figure 2.2: Plot of the yearly average partial pressure of CO_2 in the atmosphere over Mauna Loa, Hawaii from 1959 to 2009. Error bars for individual measurements fall within the plotted data point.

with the solution. This proportionality constant is known as the Henry's law constant for a specific gas. Given equation 2.38 we can then write the equilibrium constant equation:

$$k_H = \frac{[H_2CO_3^*]}{pCO_{2(g)}} \tag{2.39}$$

where k_H is the Henry's law constant for CO_2. The value of k_H can be calculated from equation 2.39 and CO_2 gas solubility experiments. At 298.15 K and a partial pressure of 1 atm, the aqueous solubility of CO_2 is 1.501 g/L [39]. Dividing by the molecular weight of CO_2 we find k_H to be 0.03411 M/atm. Henry's law constants, along with other equilibrium constants, are often given as $\log(k)$ to simplify comparison of constants that differ by many orders of magnitude. Here $\log(k_H)$ is -1.467 M/atm. It is important to note that by taking the logarithm of k_H we can no longer say anything about the units of k_H, so defining $\log(k_H)$ as having units of M/atm is not exactly correct. However, since Henry's law constants can be defined in a number of ways with many different units, we continue to display the units of k_H with the $\log(k_H)$ value to minimize confusion as to how $\log(k_H)$ was originally calculated.

From equations 2.37c and 2.37d above we can form the equilibrium equations:

$$k_1 = \frac{[H^+][HCO_3^-]}{[H_2CO_3^*]}$$

$$k_2 = \frac{[H^+][CO_3^{2-}]}{[HCO_3^-]}$$

These equations are often easier to deal with in logarithmic form:

$$\log(k_H) = \log[H_2CO_3^*] - \log(pCO_{2(g)}) \tag{2.40}$$

$$\log(k_1) = \log[H^+] + \log[HCO_3^-] - \log[H_2CO_3^*] \tag{2.41}$$

$$\log(k_2) = \log[H^+] + \log[CO_3^{2-}] - \log[HCO_3^-] \tag{2.42}$$

Adding together equations 2.40 through 2.42 yields:

$$\log(k_H) + \log(k_1) + \log(k_2) = -\log(pCO_{2(g)}) + \log[H^+] + \log[H^+] + \log[CO_3^{2-}]$$

Solving for $\log[CO_3^{2-}]$ gives:

$$\log[CO_3^{2-}] = \log(k_H) + \log(k_1) + \log(k_2) + \log(pCO_{2(g)}) - 2\log[H^+]$$

$$\log[CO_3^{2-}] = \log(k_H) + \log(k_1) + \log(k_2) + \log(pCO_{2(g)}) + 2\text{pH}$$

$$[CO_3^{2-}] = k_H \cdot k_1 \cdot k_2 \cdot pCO_{2g} \cdot 10^{2\text{pH}} \tag{2.43}$$

where $-\log[H^+]$ is replaced with pH (equation 2.7).

Equation 2.43 can be used to calculate the concentration of CO_3^{2-} in solution as a function of pH given the Henry's law constant for CO_2, the first and second dissociation constants for carbonic acid, and the partial pressure of CO_2 in the atmosphere.

Knowing the concentration of CO_3^{2-} in solution, equation 2.42 can be rearranged and solved for the concentration of HCO_3^-:

$$\log(k_2) = \log[H^+] + \log[CO_3^{2-}] - \log[HCO_3^-]$$

$$\log[HCO_3^-] = -\log(k_2) + \log[H^+] + \log[CO_3^{2-}]$$

Replacing $-\log[H^+]$ with pH (equation 2.7) gives:

$$[HCO_3^-] = \frac{[CO_3^{2-}]}{k_2 \cdot 10^{\mathrm{pH}}} \tag{2.44}$$

an equation to calculate the concentration of HCO_3^- in solution as a function of pH and CO_3^{2-}.

Finally, rearranging equation 2.40 yields:

$$\log(k_H) = \log[H_2CO_3{}^*] - \log(pCO_{2_g})$$

$$[H_2CO_3{}^*] = k_H \cdot pCO_{2_g} \tag{2.45}$$

Equations 2.43 through 2.45 can be used to calculate the concentrations of the different carbonate species as a function of pH. A plot of these data are shown in figure 2.3. Dividing by the total carbon concentration gives a speciation diagram for carbonate in solution as a function of pH (figure 2.4). It is important to note that the log plot of carbonate concentration begins to approach very high levels above a pH of approximately 10. Normally in the environment, the reaction of carbonate with Ca^{2+} forms insoluble calcium carbonate ($CaCO_3$) that precipitates out of solution. Since this was not taken into account in our calculation, carbonate concentration will simply increase as pH increases. At some point above pH 10 the initial assumption about species solution activity being comparable to solution concentration begins to break down and the plot no longer represents what one would expect to see in an actual physical solution.

When preparing sample solutions representing environmental solutions open to air, it is necessary to take into account the presence of carbonate in solution. One option is to prepare samples and leave them open to air, allowing the dissolution of $CO_{2(g)}$ from the atmosphere to come to equilibrium with the sample and then adjust the pH until the target pH is reached. This equilibrium process is slow and iterative since the pH adjustment at the end will cause the equilibrium to shift and the sample will have to re-equilibrate. The second option is to prepare pH solutions and "rapidly equilibrate" these solutions by introducing the correct amount of HCO_3^- and CO_3^{2-} into the solution in the form of $NaHCO_3$ and Na_2CO_3; this process is preferred.

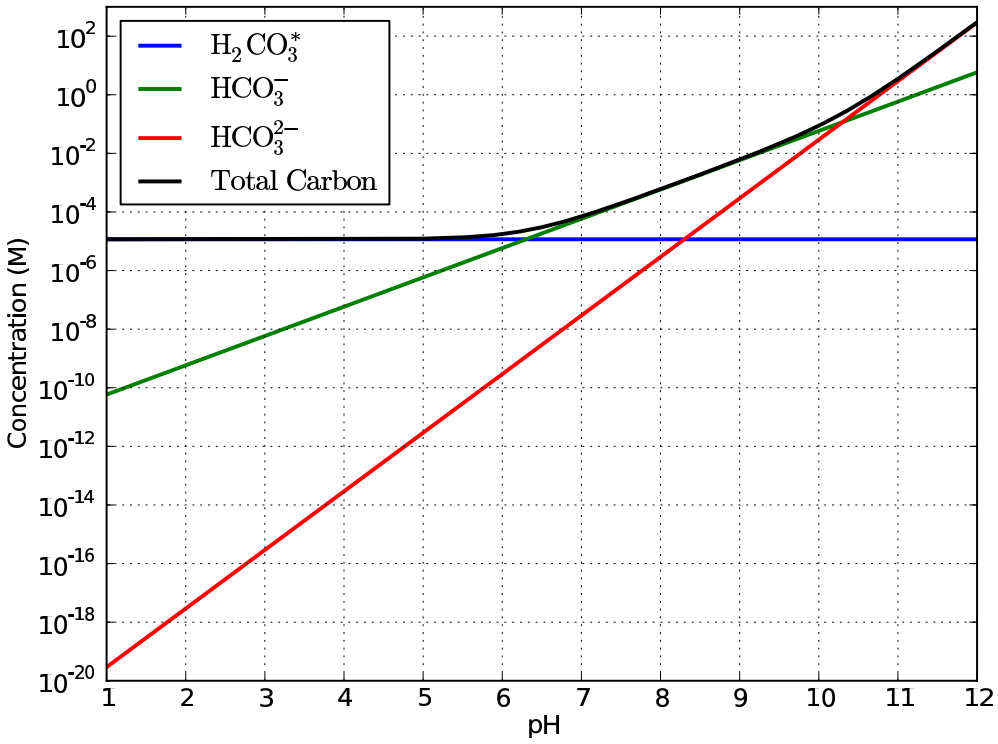

Figure 2.3: Log-plot of carbonate concentration as a function of pH.

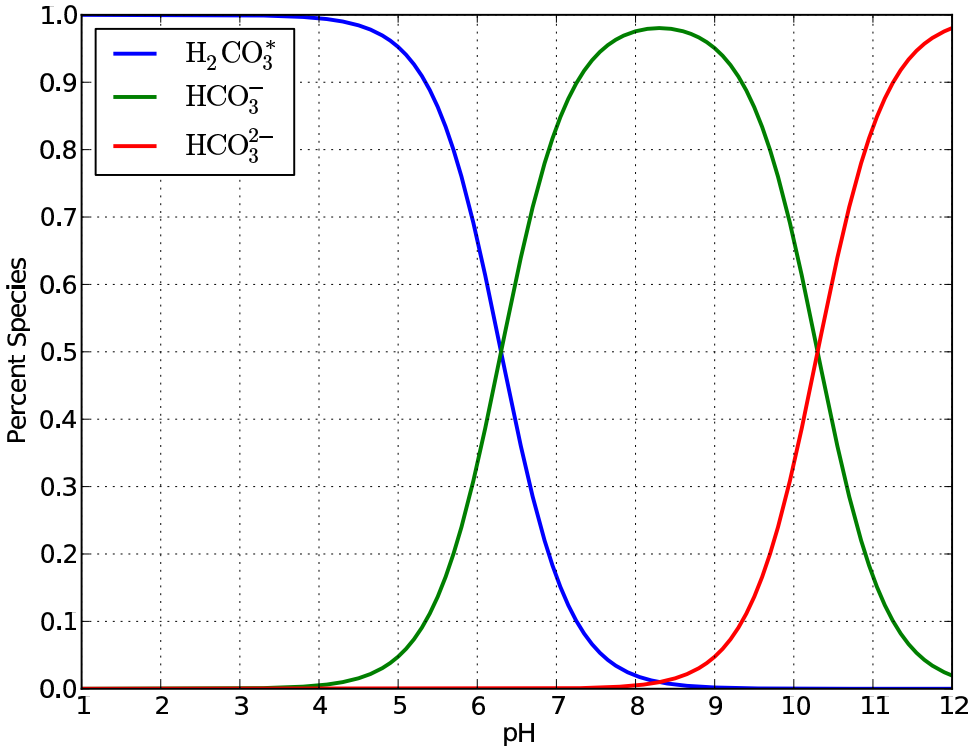

Figure 2.4: Speciation plot of carbonate species as a function of pH.

Chapter 3

Surface Chemistry

3.1 Ion Exchange

The process of ion exchange, or the exchange of ionic species at the heterogeneous boundary at the solution/solid interface, occurs both naturally and in man-made materials. The field of ion-exchange chromatography was greatly developed during the Manhattan project as a means of chemically separating similar rare-earth elements using cation-exchange columns. Since then ion-exchange methods have been used to separate various charged species in solution, such as amino acids. Appendix E presents the complete procedure of separating plutonium from fission products and other actinide contaminants using anion exchange methods.

Ion exchange resins have the capacity to reversibly exchange ions and are often named for the type of ion that is exchanged. Figure 3.1 shows the molecular structure of the active site of a cation exchanger. In this example, SO_3^- is bound to a robust and stable lattice structure that is part of a larger superstructure. Depending on solution conditions, cations in solution are attracted to these anionic sites and bind to them according to the exchange reaction below:

$$(RSO_3)^-H^+ + M^+ \rightleftharpoons (RSO_3)^-M^+ + H^+ \tag{3.1}$$

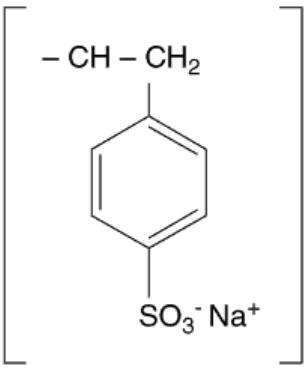

Figure 3.1: The molecular structure of the active site of the synthetic cation exchange material Kayexalate [55].

How tightly a resin binds an ion is dependent on the total charge and charge density of the ion. In general, highly charged ions with smaller hydrated radii and larger polarizability bind better to ion-exchange resins. We characterize the effectiveness of a separation between the solution and the exchange resin by calculating the distribution constant:

$$K_d = \frac{\text{Activity (per gram solid)}}{\text{Activity (per mL liquid)}} \tag{3.2}$$

Notice that the units of K_d in this case should be g/mL. However, the units for this value may be different depending on how the above equation is defined. Additionally, since the ratio of two numbers is being taken we do not need to worry about the background or efficiency of the detector because these terms will cancel out. Working with radioactive material allows us to conveniently measure the concentration of a particular isotope of an element both in solution and attached to the ion exchange resin since the activity of the isotope is directly proportional to the concentration.

By carefully controlling the solution chemistry of the solution in contact with an ion exchange resin, we can change the distribution constant, allowing us to control when species will bind or unbind to the solid phase exchange resin. In nature, such reactions also occur on the surface of mineral oxides. There, the solution pH and the point of zero charge (section 3.2) of the mineral often control the interaction with the mineral surface.

3.2 Point of Zero Charge

3.2.1 Introduction

The point of zero charge (PZC) can generally be considered as the point of zero net charge, i.e., the pH where the total positive charges are equal to the total negative charges. The protonation and deprotonation of the surface hydroxyl groups can be represented as [56]:

$$\mathrm{MOH_2^+} \rightleftharpoons \mathrm{MO^-} + 2\,\mathrm{H^+} \tag{3.3}$$

where $\mathrm{MOH_2^+}$ and $\mathrm{MO^-}$ represent the positive and negative surface sites, respectively. A small change in the pH can lead to a large increase or decrease of the electrostatic interaction between the ions and the ionizable surface sites of the material of interest. Therefore, knowledge of the PZC plays a crucial role in understanding ion sorption processes at the mineral/solution interface.

If the PZC is determined by measuring the pH where the difference between $\mathrm{H^+}$ and $\mathrm{OH^-}$ adsorbed on the mineral surface is zero, it is called the point of zero net proton charge (PZNPC). This quantity is commonly obtained by acid/base potentiometric titration [53]. Alternative methods to measure the PZNPC include mass titration [57] and powder addition [58, 59, 60].

3.2.2 Potentiometric Titration

In potentiometric titration [61], the mineral acts as a weak diprotic acid or base [56]. It can therefore be titrated by adding small amounts of a strong acid or base in the presence

of a background electrolyte. The PZC is estimated as the average between the measured values for pK_1 and pK_2 (figure 3.2). The potentiometric titrations are performed both on a blank and on the mineral suspension with a minimum of three different background electrolyte ionic strengths. The blank curve is then subtracted from the mineral curves and the common intersection point (CIP) among the three resulting curves, also known as the point of zero salt effect (PZSE), is considered to be the PZC.

It has been shown by Sposito [63] that the PZSE does not necessarily coincide with a zero surface charge. PZSE is simply an invariant point for all the curves where the mineral surface is uninfluenced by the ionic strength of the solution. The PZC and PZSE therefore coincide only when: a) the mineral is pure, b) no inner-sphere adsorption occurs, and c) zero net contribution exists for outer-sphere complexation by non-determining ions. If such conditions cannot be met, or if one is not sure that the mineral system under study fulfills these conditions, it may be prudent to measure the PZC using multiple methods. Other disadvantages of the potentiometric titration technique are that curves must be collected at a minimum of three different background electrolyte concentrations, the background electrolyte added can be adsorbed to a certain degree on the mineral surface, and the mineral must have a sufficiently large surface area.

3.2.3 Mass Titration

The mass titration technique was developed by Noh and Schwarz (1989) to estimate the PZC of simple oxides. The dry oxide must be a pure mineral phase and is assumed to be uncharged. When it is put into pure water, the pH of the suspension changes and the final pH value depends on the oxide concentration. The suspension reaches a constant value after the addition of an excess of solid. This limiting pH value can be interpreted as a function of the solid concentration according to:

$$N_t = \frac{(C_{OH^-} - C_{H^+}) \cdot ([MOH] + [MOH_2^+] + [MO^-])}{[MOH_2^+] - [MO^-]} \tag{3.4}$$

where N_t is the total number of ionizable sites on the mineral surface (representative of the mass of the solid); $(C_{OH^-} - C_{H^+})$ is the difference between the concentration of OH^- and H^+ in the mineral suspension, and is therefore representative of the pH of the suspension; and $[MOH_2^+]$, $[MOH]$, and $[MO^-]$ are the concentrations of positive, neutral, and negative sites, respectively.

From equation 3.4 it can be shown that as N_t approaches infinity and if $(C_{OH^-} - C_{H^+}) \neq 0$ (the case when the suspension pH is not equal to 7), $[MOH_2^+] - [MO^-]$ approaches 0. Under these conditions, the net surface charge of the solid is zero and the PZC value is reached. If the PZC of the oxide is 7 (as is the initial pH of pure water) the suspension pH will not change with increasing mineral mass. In this case $(C_{OH^-} - C_{H^+}) = 0$ and the pH is independent of the mass (N_t).

Limitations to this technique include the need for the mineral solid to be insoluble in solution and restriction of the ratio of oxide to water by weight to below 20% (above this value the solution becomes too dense for a proper pH measurement due to the limitation of the liquid-junction potential). One of the great advantages of this method is that it can be performed in pure water, without the risk of specific sorption by background electrolytes.

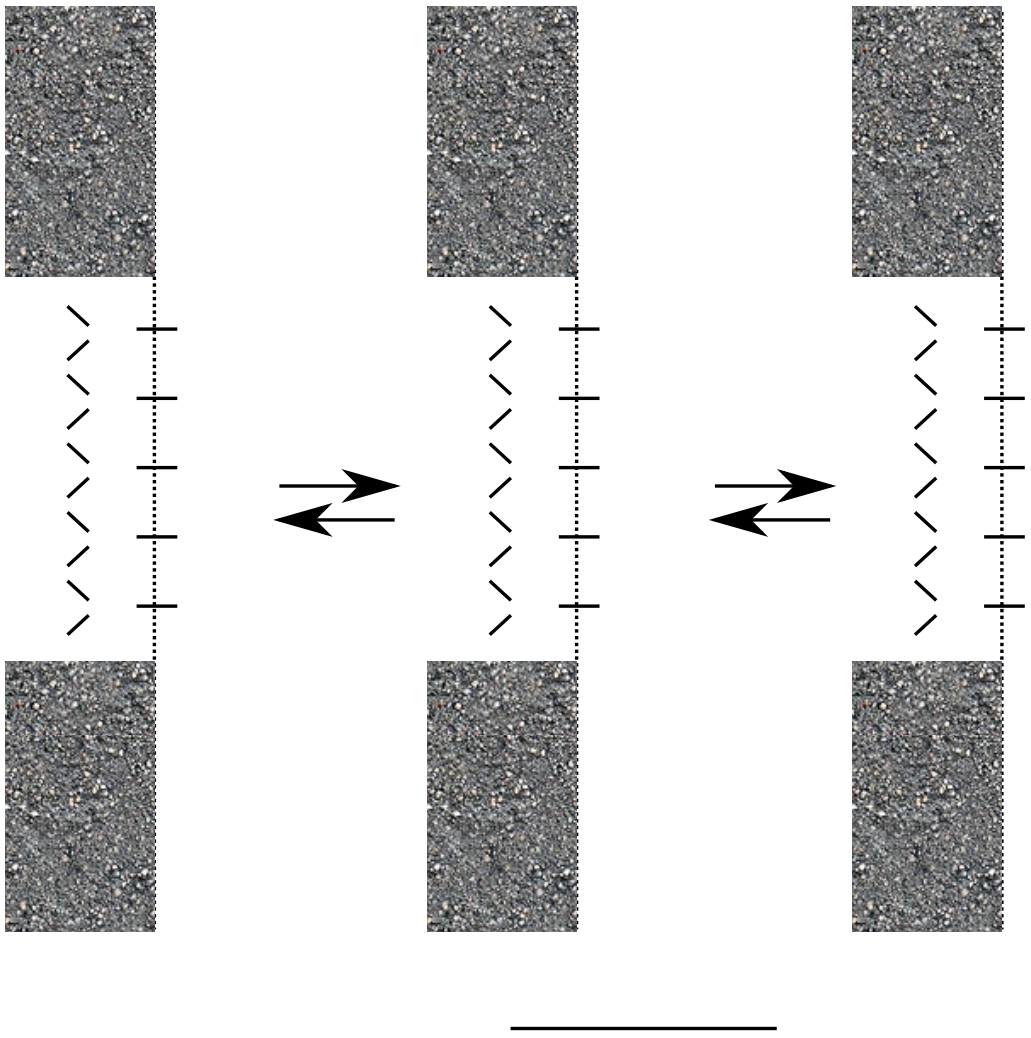

Figure 3.2: pH dependent protonation and deprotonation of hydroxyl groups on the mineral surface. Adapted from Tourinho *et al.* [62].

3.2.4 Powder Addition

The powder addition technique is performed by adding identical amounts of mineral to a set of solutions of the same ionic strength at different pH values [58, 59, 60]. The added mineral changes the solution pH. If the initial pH (pH_i) is lower than the PZC of the solid, the mineral surface adsorbs protons and the final pH (pH_f) will be higher. The reverse is true if the initial pH is higher than the PZC, and the mineral surface desorbs protons, resulting in a lower final pH. The final pH values are usually measured 24 h after addition of the solid. The final pH minus the initial pH (ΔpH) is plotted versus pH_i. The PZC occurs at the point where $pH_f - pH_i = 0$.

This technique can be compared to a potentiometric titration performed at only one ionic strength value. The advantages of powder addition over potentiometric titration are that the powder addition method is faster, and can be used with minerals that do not have a sufficiently large surface area to be measured by potentiometric titration.

3.3 Sorption of Trace Metals

The field of heavy metal sorption in the environment is quite a vast one, encompassing elements from across the periodic table. The major elements that make up the earth's crust are O, Si, Al, Fe, Ca, Na, K, Mg, Ti, and P [64]. The remaining elements are considered to be trace elements in the environment and often only accumulate in the vicinity of ore veins where enrichment of certain elements relative to the major elements occurs. Within this field is the subfield concerning the study of actinide interactions with the environment. Understanding the sorption of trace actinide elements in environmental systems is of utmost importance in modeling/estimating the ultimate fate of radioisotopes in the event of contamination or in the planning of contaminated site remediation.

The term sorption is used as an all-encompassing descriptor of a physical process when more specific knowledge of whether the reaction undergoes adsorption or absorption is unknown. Absorption implies that the species being absorbed is being taken up and incorporated into the structure of the material that is doing the absorbing. Adsorption refers to the process by which a species approaches and adheres to the surface of a material.

Figure 3.3 shows a three-dimensional schematic of a diffuse ion floating in solution and two types of adsorption to the surface, outer-sphere and inner-sphere adsorption. Figure 3.4 shows a two-dimensional depth profile with vertical lines designating specific planes, parallel to the surface, defining the areas where certain types of surface complexes form.

Outer-sphere complexes are formed when an ion, and associated hydration sphere, of opposite charge to the surface charge approaches and electrostatically interacts with the surface. Such complexes are defined by the ion and surface being separated by one or more water molecules, and are not strongly bound to the surface. Often, an increase in the ionic strength of the solution will cause ions bound in this fashion to become unbound and released back into solution because the increased ionic strength will disrupt the outer-sphere binding by shielding the charged surface.

In the case of metal-oxide surfaces interacting with metal ions in solution, it is possible for inner-sphere complexes to form. Inner-sphere complexes are formed when solution ions

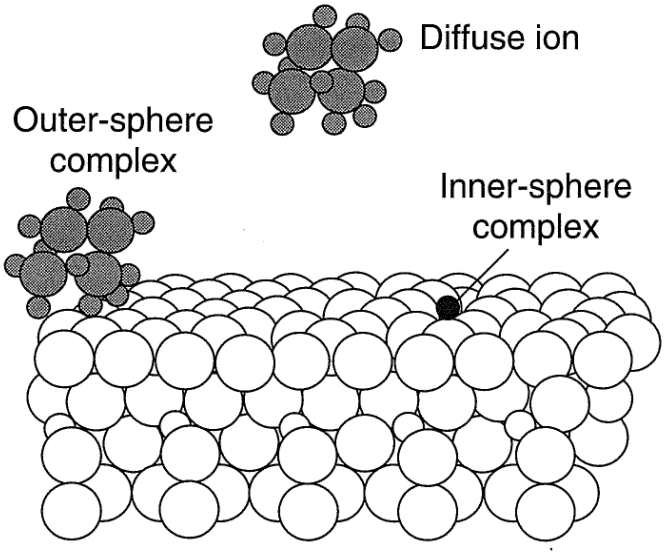

Figure 3.3: Three-dimensional schematic of three possible surface complex structures for a cation approaching a surface. The ion can reside as a diffuse ion in solution, form an electrostatic outer-sphere complex, or form an inner-sphere complex containing direct chemical bonds to the surface. From Sposito [63].

interact with the surface oxygens in a way where electron density is donated from the oxygen to the ion. This formation of a covalent chemical bond involves an increase in electron density around the coordinated metal ion and produces a strong interaction between the adsorbed ion and the surface.

Understanding the way in which actinide ions are bound to the surface, particularly if they are bound as outer-sphere or inner-sphere species, is important in understanding the long-term thermodynamic stability of these adsorbed species. Furthermore, the mechanism of most surface controlled processes depends on the coordinative environment at the solid-water interface [53]. Unfortunately, there exist very few direct experimental probes that will allow the experimenter to differentiate between outer-sphere and inner-sphere complex formation. This problem is compounded by the fact that sorption onto mineral surfaces does not exhibit long-range order, making it difficult to probe samples for structural information using conventional X-ray diffraction techniques.

Chapter 6 presents an overview of X-ray absorption spectroscopy, a synchrotron-based spectroscopic method for determining the coordination environment of a specific element in non-crystalline materials. This method allows us to unequivocally assign the type of surface coordination that is occurring and elucidates binding structure at the solution/solid interface. Chapter 7 presents work using these and associated techniques to investigate the binding of plutonium(VI) on the surface of a synthetic manganese-substituted goethite (see chapter 4), and mixtures of goethite and manganese-substituted goethite.

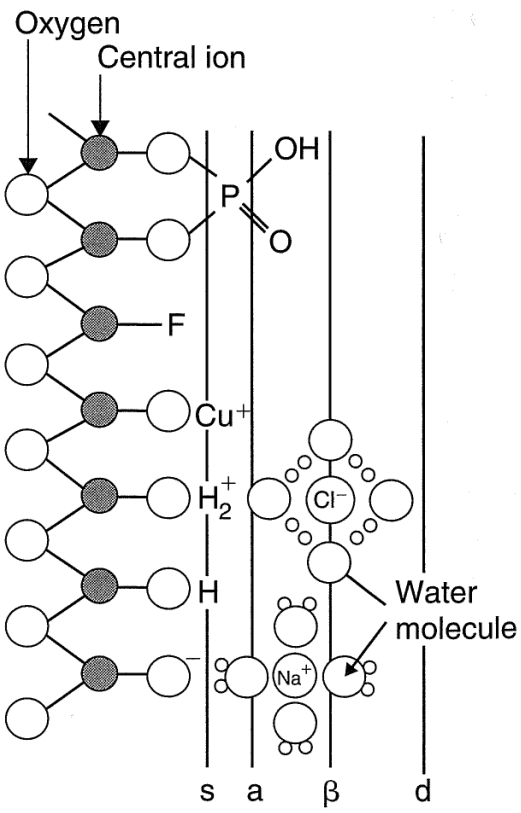

Figure 3.4: Two-dimensional schematic of possible surface complex structures. Depth into the surface, normal to the surface, increases from right to left. Vertical lines define planes parallel to the surface associated with different types of bonding. "s" represents the surface, "a" defines the boundry for inner-sphere complexes, "β" defines the boundary for outer-sphere complexes, and "d" defines the boundary for ions in the diffuse layer. Adapted from Sposito [65].

Chapter 4

Goethite and Manganese-Substituted Goethite

> If you see a whole thing - it seems that it's always beautiful. Planets, lives... But up close a world's all dirt and rocks.
>
> *Ursula K. Le Guin*

4.1 Introduction

Iron and manganese oxyhydroxides and oxides are an important class of minerals due to their abundance in the environment. Their low solubility within environmental pH ranges results in their ubiquitous presence in well-aerated soils and sediments. Furthermore, these minerals have been shown to sorb high concentrations of contaminants with respect to their total mass [66, 67, 68, 69, 24, 70, 20, 37].

Among iron oxyhydroxides and oxides, goethite (α-FeOOH) is one of the most prevalent minerals in soils, and is involved in the uptake of several toxic elements commonly found in the environment [71, 72]. Figure 4.1 shows the crystal structure of pure goethite along the three principle crystallographic axes and one isometric view. In this study we have synthesized goethite to compare to other substituted goethite samples and for use in experiments described in chapter 7.

In nature, manganese is rarely encountered as a pure mineral phase. It is often found as a minor component associated with major mineral phases, such as goethite. As a model to these environmental minerals, we have synthesized and extensively characterized manganese-substituted goethite with a small mole-fraction of manganese substituted into the goethite crystal structure. These substituted goethite minerals are also used in experiments described in chapter 7.

Sections of this chapter have been published in the peer reviewed journal "Radiochimica Acta" [68], while other sections have been prepared and submitted for publication to the peer reviewed journal "Clays and Clay Minerals" [74].

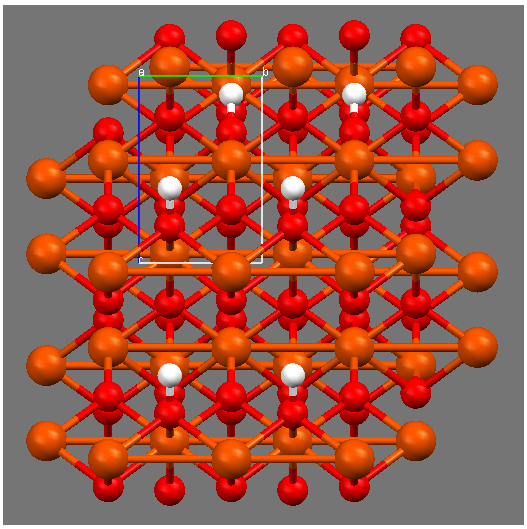

(a) a-axis

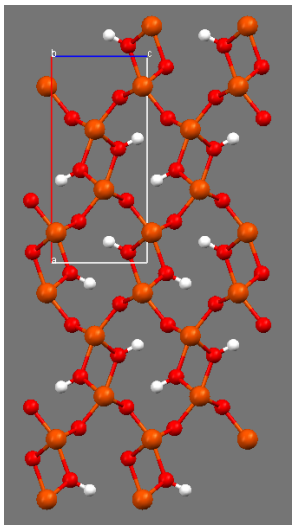

(b) b-axis

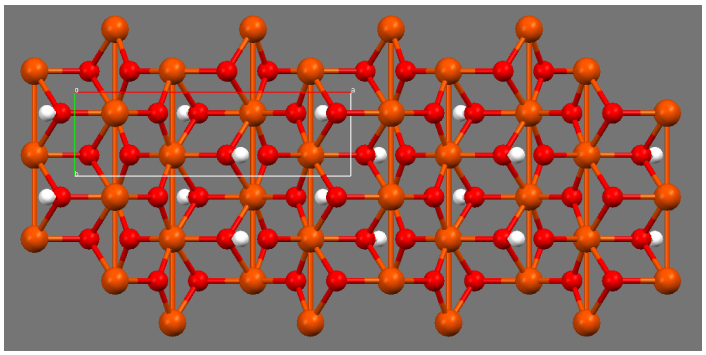

(c) c-axis

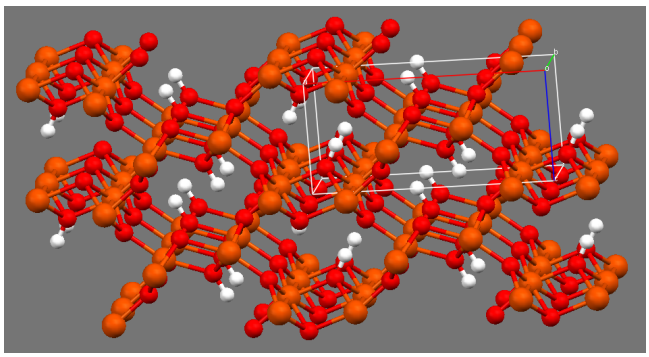

(d) Isometric

Figure 4.1: Structure of goethite. Eight unit cells plotted down the principle crystallographic axes and isometrically, from data in [73]. Iron = brown, oxygen = red, hydrogen = white.

Mn-sub Goethite	% Mn substitution[a]	BET surface area ($m^2 \cdot g^{-1}$)	PZC
MG-1.0	1.0 ± 0.2	19.7	6.46 ± 0.09
MG-0.5	0.5 ± 0.1	13.9	6.78 ± 0.05
pure Goethite	0.051 ± 0.007	32.8	7.46 ± 0.02

a. % Mn substitution expressed as $\frac{\text{Mn}}{\text{Mn+Fe}} \cdot 100$

Table 4.1: Characterization data for synthesized pure goethite and two synthesized Mn-substituted goethite minerals. Error bars are presented at the 1σ confidence level.

4.2 Goethite

4.2.1 Synthesis

Goethite (table 4.1) was synthesized by adapting the procedure of Schwertmann and Cornell [75]. Slight changes were made to the synthesis procedure from Schwertmann and Cornell to ensure that nitrates were not present in the final mineral because nitrate complexation with plutonium may influence its redox chemistry. For the synthesis, NaOH (Sigma Aldrich, Reagent Grade) and $FeCl_3 \cdot 6\,H_2O$ (Sigma Aldrich, Reagent Grade) were used instead of KOH and $Fe(NO_3)_3 \cdot 9\,H_2O$. To minimize silica contamination, all synthesis steps were conducted using plastic labware. The laboratory synthesis of goethite requires relatively large amounts of strong base. The removal of this base after synthesis is therefore necessary to ensure a clean material for proper characterization and plutonium sorption experiments (see chapter 7). The precipitate was washed with 18.2 MΩ (Milli-Q) water and then suspended in dialysis tubing (SnakeSkin Pleated Dialysis Tubing 3500 MCWO) in Milli-Q water exchange solution until the conductivity of the exchange solution was < 2.0 μS. The sieved 63-212 μm fraction goethite was then characterized by XRD, BET, and SEM before use.

4.2.2 Sample Characterization

BET Surface Area Determination

The goethite surface area (table 4.1) was determined using a 5-point BET N_2 adsorption on an ASAP 2010 Micromeritics Instrument (Norcross, GA). A NIST standard was included with these samples: NIST SRN 1900 Si_3N_4 with a surface area of 2.84 ± 0.09 m^2/g. This standard was measured to be 2.83 m^2/g, which is within the error bar of the NIST standard.

XRD and SEM

Powder X-ray diffraction (XRD) spectra of commercial goethite (Alfa Aesar) versus our synthesized goethite were recorded using a Panalytical X'Pert Pro powder X-ray diffractometer using Cu-K_α radiation and a Ni filter on dried and finely ground mineral samples. The mineral powder was placed on a zero background plate with a thin layer of immersion oil. Data were collected over a two theta angle (2θ) from 10.0° to 70.0°. Data processing

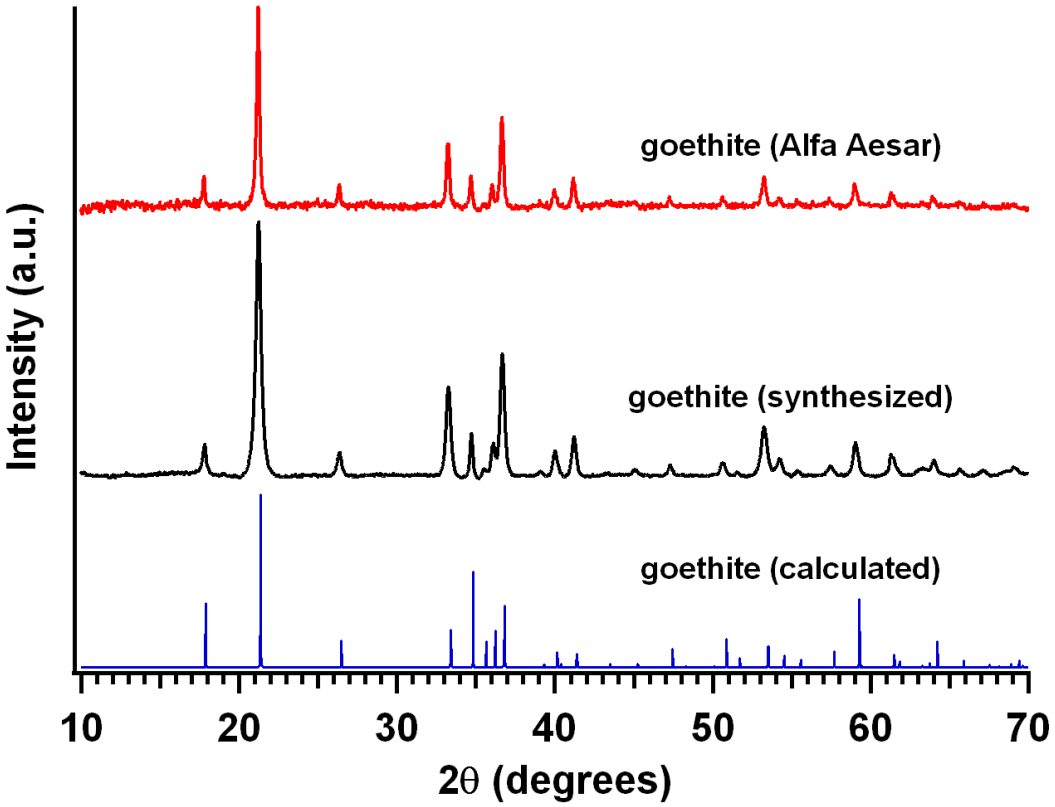

Figure 4.2: Powder XRD spectra of commercial goethite, synthesized goethite, and the calculated goethite powder XRD spectra.

involved fitting and subtracting a smooth polynomial background from each scan to facilitate comparisons between scans. Scanning electron microscopy (SEM) was conducted on the goethite using a LEO Model 440 (Peabody, MA).

Powder XRD of the synthesized mineral compared to commercial goethite and the calculated goethite powder XRD spectra (figure 4.2) showed Bragg peaks indicative of the goethite structure with no significant shifts, indicating that the goethite synthesis was successful.

SEM measurements (figures 4.3 and 4.6(a)) show that the mineral is crystalline and that sieving is isolating the proper mineral size fraction. Close inspection of the micrograph (in the 1 μm range) shows round rod-like structure morphologies [71].

Point of Zero Charge Determination

Point of zero charge (PZC) measurements (see section 3.2) were conducted on the goethite using the potentiometric titration method [53], mass titration method [57], and the powder addition method [74, 60].

Potentiometric titrations of goethite were performed under CO_2-free argon atmosphere using an automatic titrator (751 GPD Titrino, Metrohm). The minerals were added to 15 mL of $NaClO_4$ at concentrations of 0.001, 0.01, and 0.1 M. The solid/liquid ratio was fixed at 6 g/L. The suspension was equilibrated for 20 min under argon blanketing and the pH was

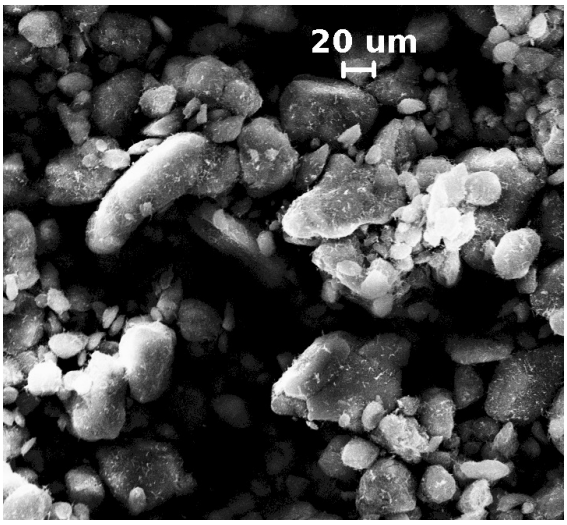

Figure 4.3: Scanning electron micrograph image of the 63-212 μm size fraction of synthesized goethite. Upon inspection of the micrograph (in the 1 μm range) round rod-like morphologies are seen for goethite.

recorded. Before the analysis, a predetermined amount of NaOH was added to increase the pH to 11. The titrations were carried out from high to low pH by adding 0.0773 M $HClO_4$ at 25 $\pm$ 1 °C. The titration parameters were: 1 μL as the minimum volume increment at the beginning and at the equivalence point; outside these ranges the increment was constrained between 5 μL and 50 μL. Each small volume of titrant was added as soon as a 1 mV/min signal drift criterion was met. Blank titrations were performed under the same conditions.

The powder addition method was performed using a procedure described by Mustafa *et al.* [60]. A set of 0.01 M $NaClO_4$ solutions were adjusted to pH 4, 5, 6, 7, 8, 9, and 10 using CO_2-free NaOH and $HClO_4$. The initial pH (pH_i) was recorded and a given amount of solid (5 g/L) was added to each solution. The tubes, back-filled with argon, were placed on a shaker and the final (pH_f) was measured after 24 h at 25 $\pm$ 1 °C. The ΔpH ($pH_f - pH_i$) was plotted versus pH_i and the value on the curve where ΔpH was equal to zero was taken to be the PZC. The final pH values were regularly checked for 50 days and the PZC values were constant during the whole period.

Mass titration measurements on goethite was performed under argon following the method proposed by Noh and Schwarz [57]. Mineral suspensions with a solid to water ratio of 1%, 5%, 10%, 15%, and 20% by weight were placed on a shaker in O-ring sealed tubes. These tubes were back-filled with argon and shaken until equilibrium was reached. The sample pH was checked after 24 h and then every week for several months using a glass pH electrode (Orion, 8103BNUWP, filling solution 3 M NaCl) at 25 $\pm$ 1 °C. The suspension pH at 20% was taken as the PZC.

4.3 Manganese-Substituted Goethite

4.3.1 Synthesis

Manganese substituted (Mn-substituted) goethite ($Fe_{1-x}Mn_xOOH$) (table 4.1) was synthesized by adapting a procedure from Schwertmann and Cornell [75, 76, 77]. Reagent grade $FeCl_3 \cdot 6\,H_2O$ and $MnCl_2 \cdot 4\,H_2O$ were used instead of $Fe(NO_3)_3 \cdot 9\,H_2O$ and $Mn(NO_3)_2 \cdot 4\,H_2O$, and NaOH was used instead of KOH. The precipitate was washed repeatedly with 18.2 MΩ (Milli-Q) water and then suspended in dialysis tubing (SnakeSkin Pleated Dialysis Tubing 3500 MWCO) in Milli-Q water exchange solution until the conductivity of the exchange solution was < 2.0 μS. The sieved 63-212 μm fraction of the Mn-substituted goethite was used in later experiments.

The same changes in the goethite synthesis procedure (see section 4.2) were made for the Mn-substituted goethite minerals to ensure a clean product.

4.3.2 Sample Characterization

XANES

Manganese K-edge X-ray absorption near-edge structure (XANES) spectra were collected at the Stanford Synchrotron Radiation Lightsource (SSRL) on beamline 10-2 using a fully tuned Si(220) $\phi - 90°$ double-crystal monochromator with a harmonic rejection mirror set to an 8 keV cut-off. Data were collected in fluorescence mode using a 13-element germanium detector. Count rates were sufficiently low that a dead time correction was unnecessary. Energy calibration was performed in transmission mode by simultaneously measuring the manganese K-edge of a manganese metal foil.

Raw data were pre-edge subtracted and normalized using the Real-Space X-ray Analysis Package (RSXAP) [78, 79], a software package for XAS data analysis. Manganese XANES spectra were energy calibrated by setting the first inflection point of the K-edge of a manganese metal reference sample to be 6540.0 eV [80].

XANES measurements for the Mn-substituted minerals (figure 4.4) show that the position of the characteristic white line coincides with that of the Mn(III) reference compound $LaMn^{III}O_3$, suggesting that manganese is substituted into the goethite structure in the trivalent state. Schwertmann and Cornell [75] propose that, although added as Mn(II), the manganese is oxidized and incorporated into the mineral as Mn(III) during the synthesis. Our direct spectroscopic measurement is in agreement with previous work by Alvarez *et al.* [81]. It is important to note, however, the slight shoulder on the Mn-substituted goethite XANES spectra at approximately 6550 eV. This shoulder is also present in the spectra taken by Alvarez *et al.* [81], and does not rule out the possibility of small amounts of Mn(II) present in the mineral. The shoulder could also be caused by the presence of pre-edge features arising from a dipole-forbidden transition to an unoccupied energy state.

Inductively Coupled Plasma - Mass Spectrometry

The 63-212 μm size fraction of the two Mn-substituted minerals that were synthesized for this study, MG-1.0 and MG-0.5, were analyzed using inductively coupled plasma - mass

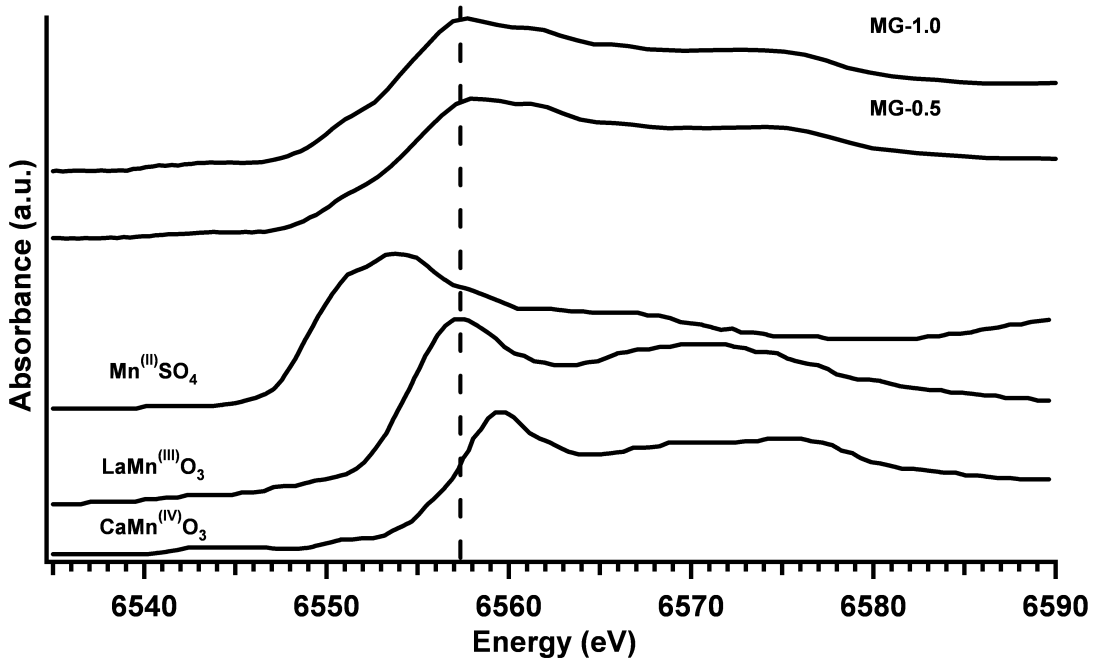

Figure 4.4: Manganese K-edge XANES spectra for Mn-substituted goethite (MG-1.0 and MG-0.5) and reference compounds. Reference scan for $Mn^{II}SO_4$, $LaMn^{III}O_3$, and $CaMn^{IV}O_3$ taken from Alvarez *et al.* [81]. A dashed line is drawn at the peak position of the $LaMn^{III}O_3$ reference compound and shows that manganese in the Mn-substituted goethite is incorporated into the mineral structure as Mn(III).

spectrometry (ICP-MS) to quantify the exact manganese substitution (table 4.1). Measured values were in agreement with initial target synthesis values. Synthesized goethite samples were fully dissolved in a solution of 1 M oxalic acid and 0.01 M L-ascorbic acid at room temperature. These solutions were then filtered, properly diluted, and the elemental composition of Mn and Fe measured using a Perkin-Elmer Elan DRC II ICP-MS with a Sc or Ga internal standard.

BET Surface Area Determination

The Mn-substituted goethite surface area (table 4.1) was determined using the same method as was used above to determine the goethite surface area. Measurements showed the Mn-substituted goethite surface area to be less than that of pure goethite.

Point of Zero Charge Determination

PZC measurements were conducted on the Mn-substituted goethite using the powder addition method [74, 60]. This method was chosen because of two distinct advantages: the process is fast, and it requires a small amount of mineral compared to other methods, such as potentiometric titration [53] and mass titration [57]. The PZC of the minerals were measured for comparison to pure goethite and as a guide in planning plutonium sorption measurements. The results are presented in table 4.1 and indicate that the greater the Mn substitution, the lower the PZC. The implication of this is that at paraneutral pH levels, we would expect greater plutonium electrostatic attraction to the 1% than the 0% or 0.5% substituted goethite samples.

XRD and SEM/EDX

Powder XRD spectra of Mn-substituted goethite were collected under the same conditions used above to collect XRD spectra of synthesized and commercially available goethite. Spectra (figure 4.5) showed Bragg peaks indicative of the goethite structure with no significant shifts. Such shifts in the Bragg reflections are present in Mn-substituted goethite with larger manganese percent substitutions, and have previously been shown to be caused by the shrinking of the a- and c-crystallographic parameters and the expansion of the b-parameter resulting from increased manganese substitution into the goethite crystal lattice [82].

SEM measurements (figure 4.6) indicated that the mineral is crystalline and that sieving is isolating the proper mineral size fraction. Close inspection of the micrographs (in the 1 μm range) shows the following morphologies: round rod-like structures for pure goethite and an increase in the length-to-width ratio in crystal growth for Mn-substituted goethite as compared to pure goethite. This result is in agreement with previous studies [82, 81, 71]. Importantly, EDX measurements on the synthesized minerals showed the presence of manganese homogeneity in the substitution for iron at the mineral surface to within the resolution of the method, and that the manganese did not exist as discrete phases within the goethite minerals.

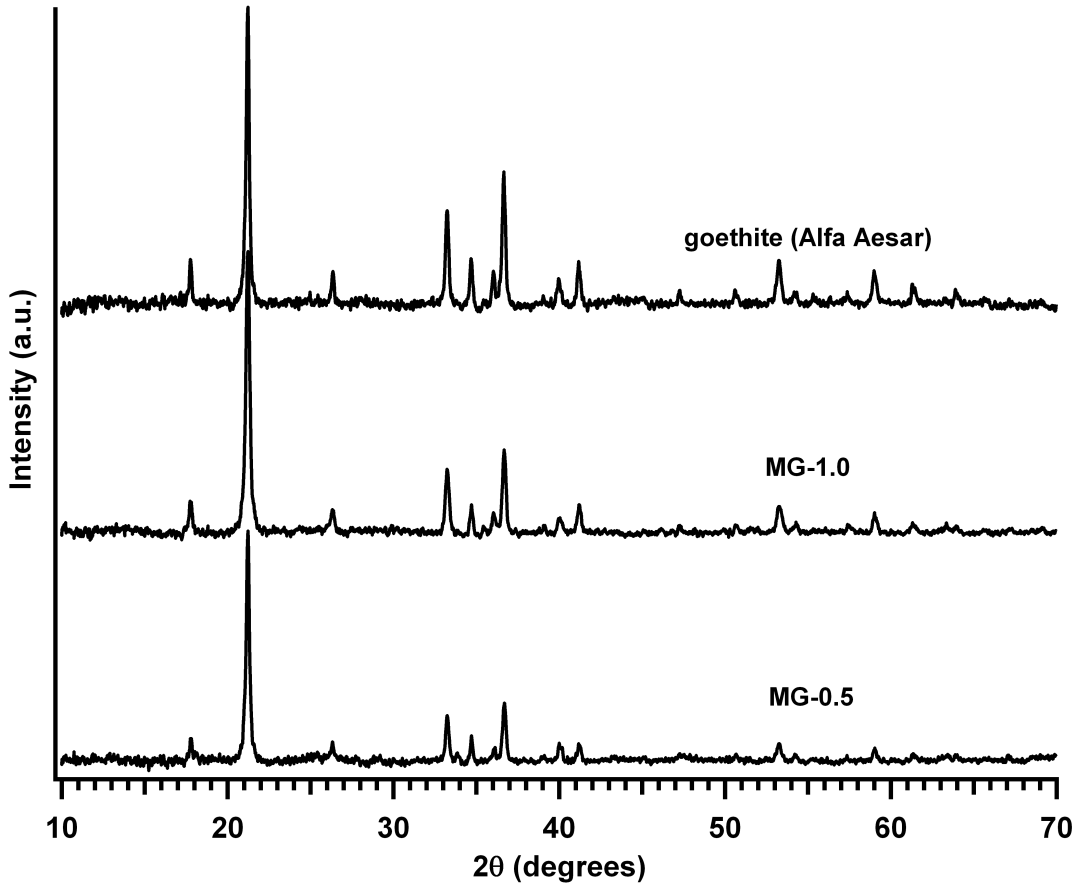

Figure 4.5: Powder XRD spectra of commercial goethite and Mn-substituted goethite.

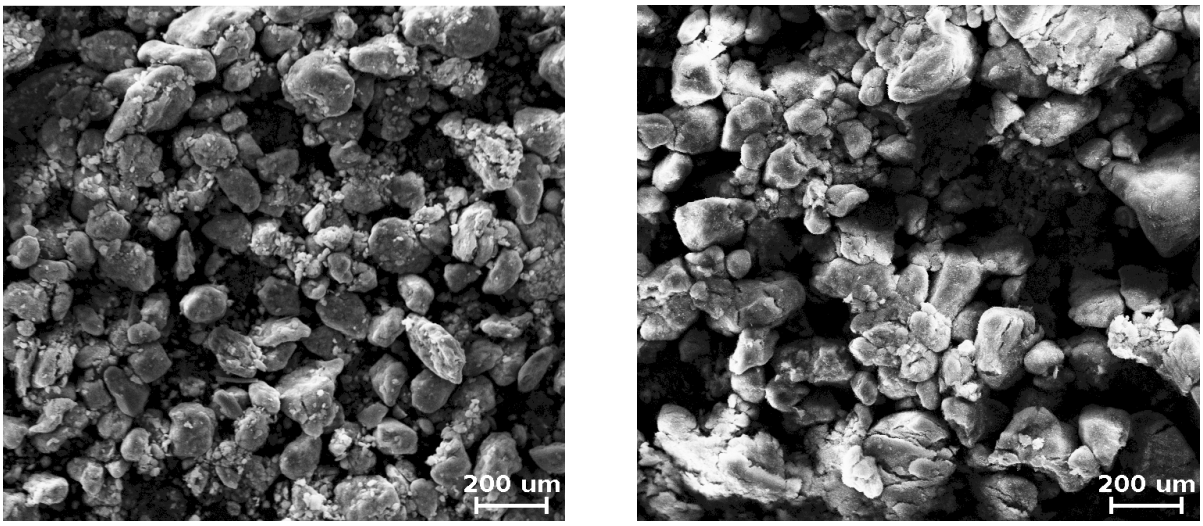

(a) Goethite (b) MG-1.0

Figure 4.6: Scanning electron micrograph images of the 63-212 μm size fraction of (a) goethite and (b) MG-1.0. Upon inspection of the micrographs (in the 1 μm range) the following morphologies are seen: round rod-like structures for pure goethite and an increase in the length-to-width ratio in crystal growth for Mn-substituted goethite as compared to pure goethite.

Mössbauer Spectroscopy

Mössbauer spectra were collected for the Mn-substituted goethite using a 50 mCi (initial strength) ^{57}Co/Rh source. The velocity transducer MVT-1000 (WissEL) was operated in a constant acceleration mode (23 Hz, $\pm$12 mm/s). An Ar-Kr proportional counter was used to detect the radiation transmitted through the holder, and the counts were stored in a multichannel scalar (MCS) as a function of energy (transducer velocity) using a 1024-channel analyzer. Data were folded to 512 channels to give a flat background and a zero-velocity position corresponding to the center shift (CS) of a metal Fe foil at room temperature. Calibration spectra were obtained with a 25 μm thick Fe metal foil (Amersham, England) placed in the same position as the samples to minimize any errors due to changes in geometry. The Mössbauer data were modeled with Recoil software (University of Ottawa, Canada) using a Voigt-based structural fitting routine [83]. The coefficient of variation of the spectral areas of the individual sites generally ranged between 1% and 2% of the fitted values. A closed cycle cryostat (Janis) was used for measurements below room temperature.

^{57}Fe-specific Mössbauer spectroscopy was employed to characterize the Mn-substituted goethite for purity and confirm manganese incorporation. Mössbauer spectra of both MG-0.5 and MG-1.0 were collected at room temperature and 77 K. At both the temperatures, the spectral sextet features of the samples are similar to each other; the similarity is apparent from a comparison of their room temperature spectra (figure 4.7a). The similarity of the samples is also evident from the modeled hyperfine field distribution (figure 4.7b). The derived hyperfine field parameters of the samples are slightly lower than that of pure goethite,

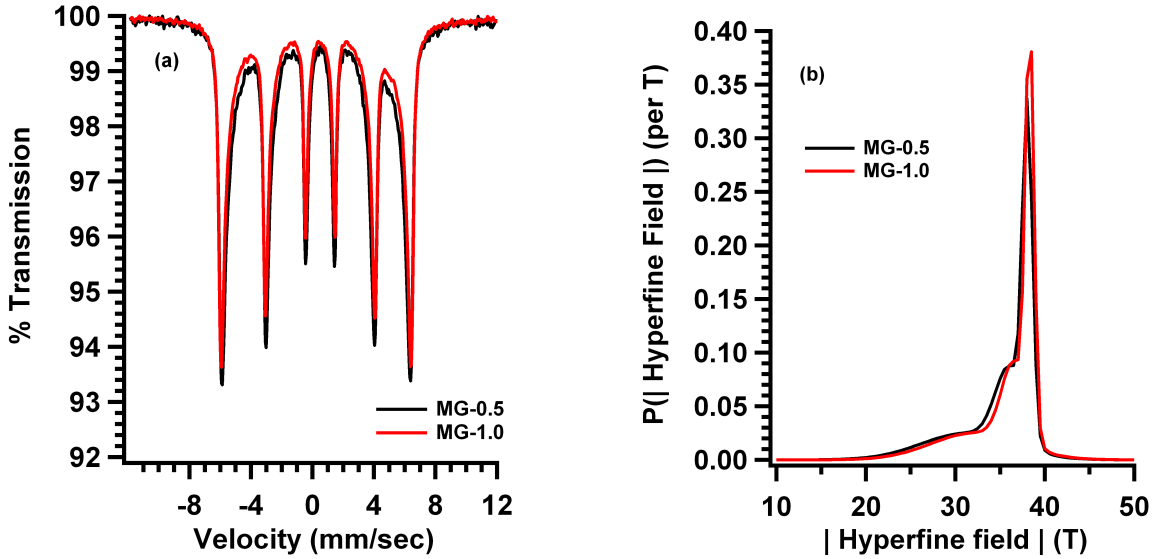

(a) (b)

Figure 4.7: Room temperature Mössbauer spectra (a) and the modeled hyperfine field distribution (b) for Mn-substituted goethite samples.

implying substitution of Mn. Absence of doublet peaks in both room temperature and 77 K (not shown) spectra is in agreement with the absence of relatively small goethite particles (< 8 nm), and the absence of poorly-crystalline Fe-oxides. Furthermore, the spectra show that the iron in the synthesized mineral is in the form Fe(III), with no Fe(II) present.

Chapter 5

The Chemistry of Plutonium

> We almost made a mistake, a terrible mistake, because we thought we'd reached the very top of the periodic table, that nobody would ever go higher than atomic number 94. So we thought we should name it "extremium" or "ultimium," you know, the ultimate.
>
> *Glenn T. Seaborg*

5.1 Introduction

Element number 94, plutonium, holds a special position both in the periodic table and in human history. As the second man-made transuranic element, $^{239}_{94}$Pu is an essential isotope in nuclear weapons fabrication and energy production in nuclear reactors. Along with the discovery of nuclear fission in 1939 [84], plutonium was essential in ushering in the Atomic Era, the period in history between the end of World War II and the fall of the Soviet Union. This era marked the first large-scale practical use of nuclear technology in the form of military ordnances and electric power generation.

Chemically, plutonium is positioned at the boundary between the heavy actinides (Am-Lr) and the light actinides (Th-Pu). The heavy actinides, due to an increased number of 5f-electrons and the relativistic effects, which cause the well-known actinide contraction, are chemically similar to the lanthanide elements. They exhibit fewer oxidation states (mostly 3+ and 2+) and consequentially have relatively simpler chemistries. The lower actinides tend to share more characteristics with the transition metals. Plutonium specifically has seven accessible oxidation states including the pure metal, with four of these oxidation states accessible under environmental conditions (see subsection 5.3.3 and section 5.4). The electronic ground state of plutonium, $[Rn]7s^25f^6$, suggests that under highly oxidizing conditions the Pu(VIII) species should be accessible. However, no experimental evidence of this species has ever reported.

5.2 Nuclear Reactions

The synthesis of plutonium occurred in December 1940 at the 60-inch cyclotron at the University of California, Berkeley. Professor Glenn T. Seaborg, Professor Joseph W. Kennedy, and graduate student Arthur C. Wahl conducted an experiment where deuterium was used to bombard a target made of ^{238}U, causing the following nuclear reactions to occur:

$$\begin{aligned} {}^{238}_{92}\mathrm{U} + {}^{2}_{1}\mathrm{H} &\longrightarrow {}^{238}_{93}\mathrm{Np} + 2\,{}^{1}_{0}\mathrm{n} \\ {}^{238}_{93}\mathrm{Np} &\longrightarrow {}^{238}_{94}\mathrm{Pu} + \beta^{-} \end{aligned}$$

The resulting $^{238}_{94}$Pu isotope has a half-life of 87.7 years and is the second man-made transuranic element [85]. Further chemical separations added more proof that a new element had in fact been produced [86]. Many publications concerning the properties of plutonium, were submitted to journals in 1941 but withheld from publication until after the Second World War at the request of the U.S. Government. Hoffman *et al.* [87] later discovered the presence of natural plutonium in the environment.

The more well-known isotope of plutonium, $^{239}_{94}$Pu, was first produced at the 60-inch cyclotron in the spring of 1941 by neutron capture and subsequent decay, as shown in the following reactions:

$$\begin{aligned} {}^{238}_{92}\mathrm{U} + {}^{1}_{0}\mathrm{n} &\longrightarrow {}^{239}_{92}\mathrm{U} \\ {}^{239}_{92}\mathrm{U} &\longrightarrow {}^{239}_{93}\mathrm{Np} + \beta^{-} \\ {}^{239}_{93}\mathrm{Np} &\longrightarrow {}^{239}_{94}\mathrm{Pu} + \beta^{-} \end{aligned}$$

The central importance of $^{239}_{94}$Pu ($t_{1/2} = 24110$ y) as a fuel in nuclear ordnance was measured in an experiment by Kennedy *et al.* [89] that measured a thermal-neutron (0.025 eV) induced fission cross section for $^{239}_{94}$Pu approximately 50% larger than $^{235}_{92}$U. Figure 5.1 shows a log-log plot of the neutron capture cross section for $^{239}_{94}$Pu as a function of neutron energy with an abrupt increase in fission cross section for neutrons with energy of approximately 0.025 eV. Figure 5.2 shows a log plot of the percent fission yield as a function of fission product atomic number for $^{239}_{94}$Pu spontaneous fission. The bi-modal distribution shows that the fission process for $^{239}_{94}$Pu is asymmetric. The main radioactive fission products usually decay by beta emission and have significantly shorter half-lifes than $^{239}_{94}$Pu itself. The peak at ∼100 A corresponds to the elements Mo, Tc, and Ru while the peak at ∼140 A corresponds to Cs, Ba, or the lanthanide elements. In addition to the fission fragments, on average about 2 neutrons [90] are also released during the fission of an atom of $^{239}_{94}$Pu. Under certain conditions these fission neutrons can be used to sustain or accelerate a chain reaction with other atoms of $^{239}_{94}$Pu or other fissile isotopes. Such a process is used both in nuclear power generation and nuclear weapons. Since World War II a quantity of $^{239}_{94}$Pu on the order of 1000 metric tons has been manufactured [91]. The half-lifes, α decay energies, and decay intensities of other notable plutonium isotopes are shown in table 5.1.

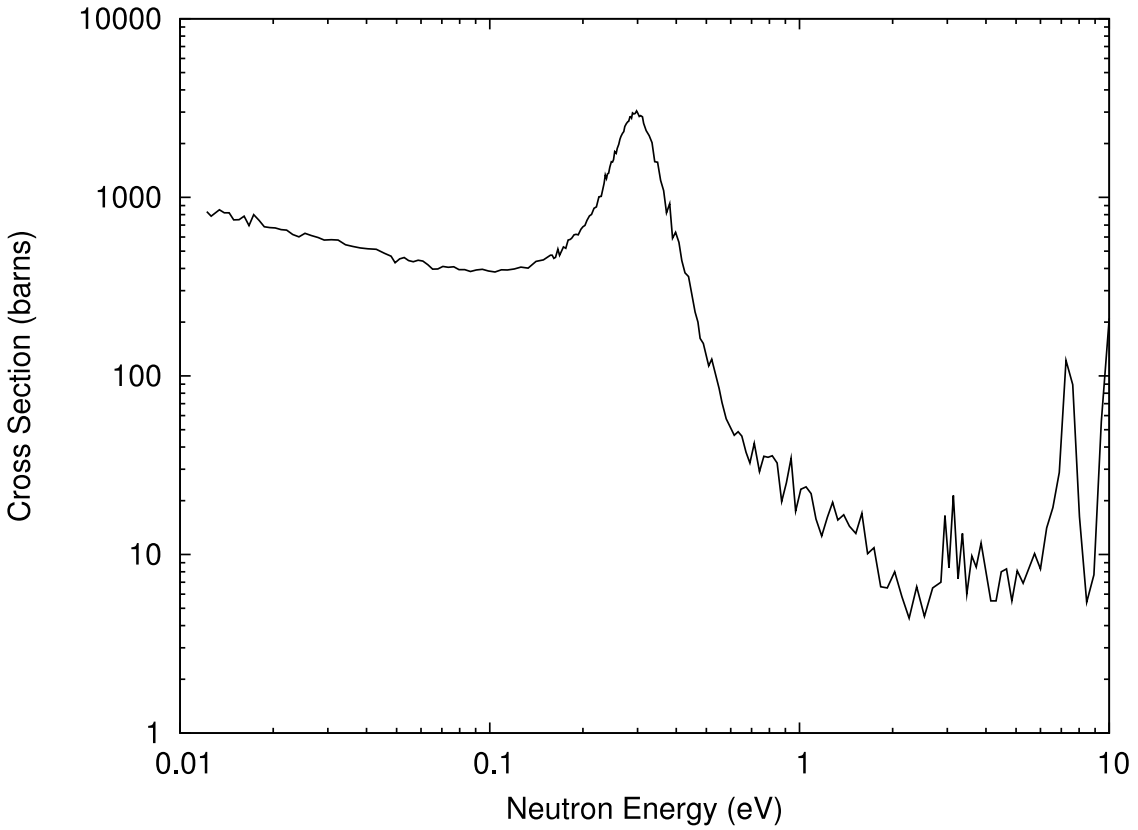

Figure 5.1: Log-log plot of neutron on $^{239}_{94}$Pu fission cross section. Adapted from the OECD Nuclear Energy Agency [88].

Isotope	Half-life	α Energy (MeV) and Intensity (%)
^{236}Pu	2.858 y	5.721(30.6), 5.768(69.3)
^{237}Pu	45.2 d	5.334(43.5), 5.356(17.2)
^{238}Pu	87.7 y	5.456(30.0), 5.499(70.9)
^{239}Pu	2.411×10^4 y	5.144(15.1), 5.157(73.3)
^{240}Pu	6563 y	5.123(27.1), 5.168(72.8)
^{241}Pu	14.35 y	4.853(12.2), 4.896(83.2)
^{242}Pu	3.733×10^5 y	4.856(22.4), 4.901(77.5)
^{243}Pu	4.956 h	
^{244}Pu	8.08×10^7 y	4.546(19.4), 4.589(80.6)

Table 5.1: Half-lifes, α decay energies, and α decay intensities for selected isotopes of plutonium [92].

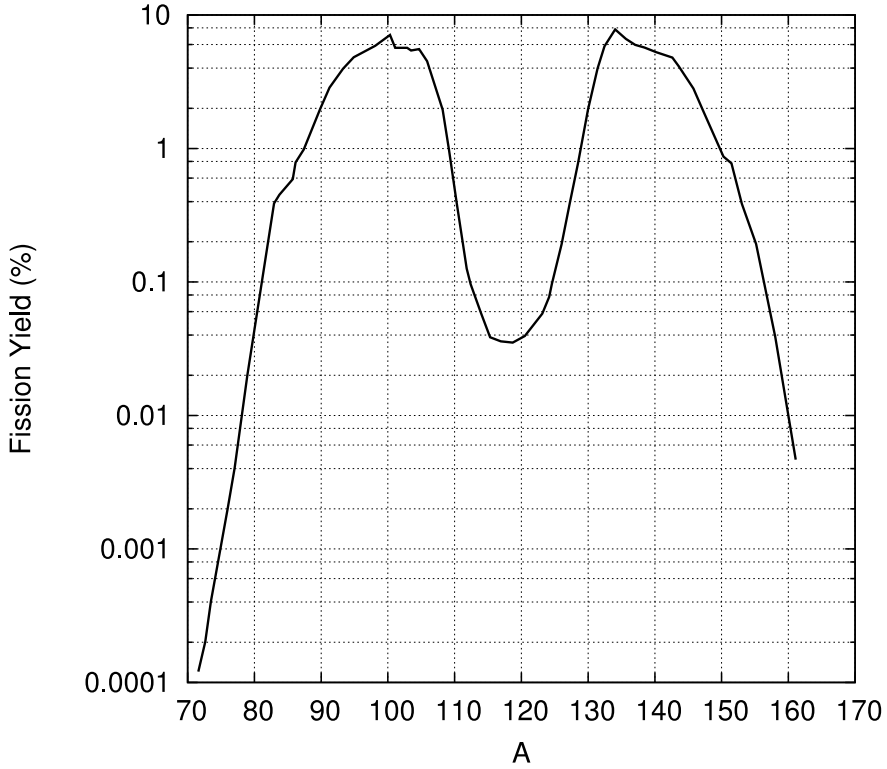

Figure 5.2: Log plot of the distribution of fission product nuclei of atomic number (A) versus percent fission yield for the neutron-induced fission of $^{239}_{94}$Pu. Adapted from Friedlander [93].

Reaction	$\log_{10}\beta^\circ$	Reference
Hydrolysis Complexes		
$PuO_2^{2+} + H_2O \rightleftharpoons PuO_2OH^+ + H^+$	-5.5 ± 0.5	[41]
$PuO_2^{2+} + 2\,H_2O \rightleftharpoons PuO_2(OH)_2 + 2\,H^+$	-13.2 ± 1.5	[41]
$2\,PuO_2^{2+} + H_2O \rightleftharpoons (PuO_2)_2(OH)_2^{2+} + 2\,H^+$	-7.5 ± 1.0	[41]
Carbonate Complexes		
$PuO_2^{2+} + CO_3^{2-} \rightleftharpoons PuO_2CO_3$	9.5 ± 0.5	[41]
$PuO_2^{2+} + 2\,CO_3^{2-} \rightleftharpoons PuO_2(CO_3)_2^{2-}$	14.7 ± 0.5	[41]
$PuO_2^{2+} + 3\,CO_3^{2-} \rightleftharpoons PuO_2(CO_3)_3^{4-}$	18.0 ± 0.5	[41]

Table 5.2: Thermodynamic data for the hydrolysis and formation of carbonate species in aqueous solution for Pu(VI). Error bars are representative of the 95% confidence interval.

5.3 Aqueous Plutonium Chemistry

5.3.1 Hydrolysis and Carbonate Complexes of Plutonium(VI)

Understanding the speciation of plutonium in aqueous environmental conditions is essential to understanding the way plutonium interacts with a soil/solution mixture. This is because it is the aqueous solution species that are available for interactions with the surface, be they inner-sphere, or outer-sphere interactions (see section 3.3). Section 2.3 already covered general complex formation in solution and the process by which speciation diagrams are generated. Table 5.2 lists all of the available aqueous species formation constants for Pu(VI) hydrolysis and carbonate complexes. Metal hydrolysis occurs according to the general chemical equation

$$M^{x+} + nH_2O \rightleftharpoons M(OH)_n^{(x-n)+} + nH^+ \tag{5.1}$$

and is dependent on pH.

The formation of metal carbonate complexes occurs according to the following general chemical equation:

$$M^{x+} + nCO_3^{2-} \rightleftharpoons M(CO_3)_n^{(x-2n)+} \tag{5.2}$$

Metal carbonate complex formation is also indirectly dependent on pH since the carbonate anion (CO_3^{2-}) is only present under certain pH conditions (see section 2.5).

A plutonium(VI) solution speciation diagram was calculated using the in-house code SPECIATE (see sections 2.3.2 and F.4) from the thermodynamic data in table 5.2, and is shown in figure 5.3. Knowledge of the presence or absence of plutonium species in solution as a function of pH is an important factor in understanding the kinds of plutonium complexes available for sorption onto the mineral surface. For elements that have precisely measured thermodynamic formation constants, it is sufficient to simply use the average measured values to calculate a speciation diagram since propagated errors in these speciation diagrams will be small. However, in the case of many plutonium solution species, where measured formation

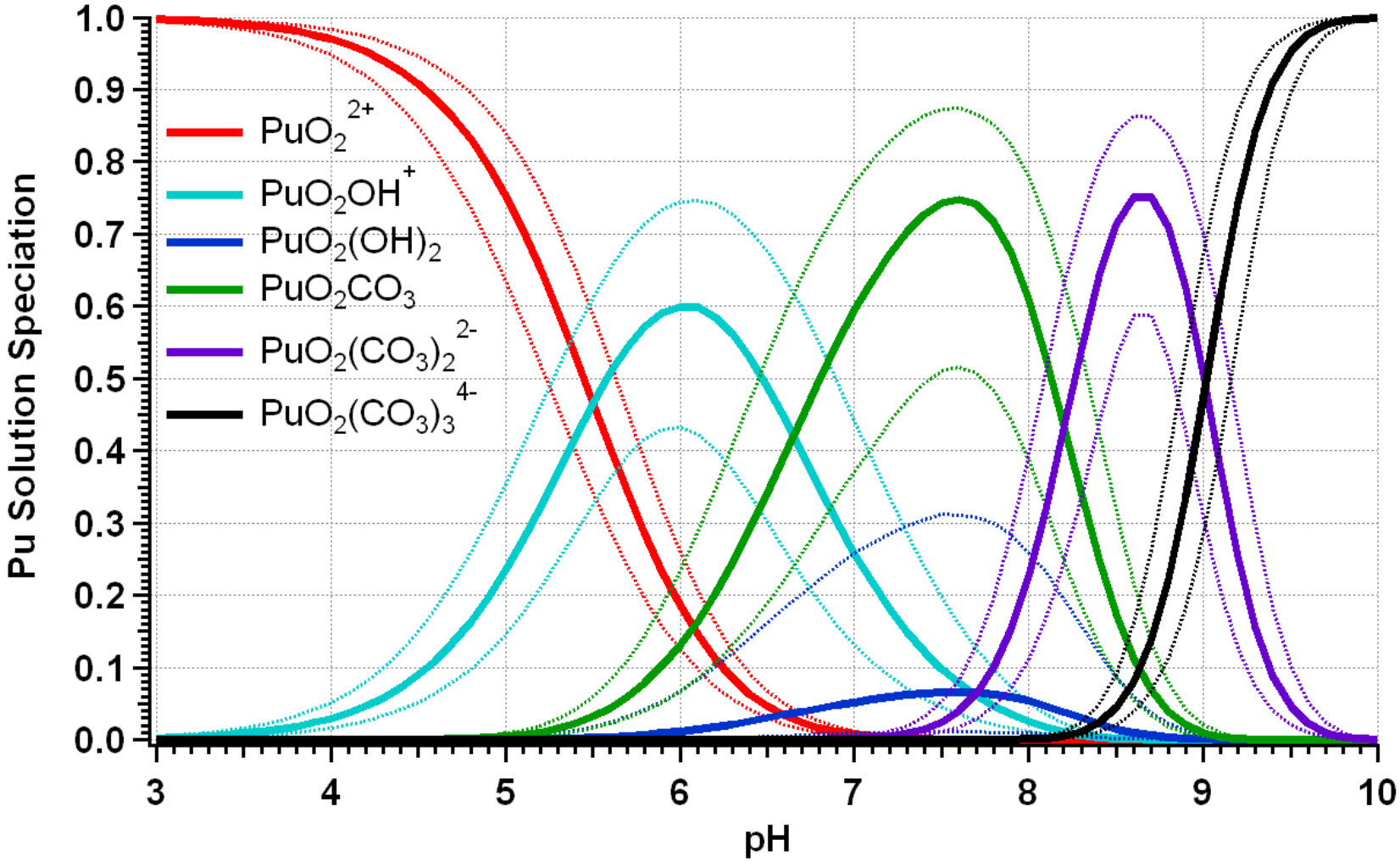

Figure 5.3: Pu(VI) speciation diagram calculated using the in-house code SPECIATE. Solid middle bands represent the average species. Upper and lower dashed bands represent error propagated into the speciation diagram at the 1σ level. Thermodynamic data used to calculate this diagram is shown in table 5.2 and taken from Guillaumont *et al.* [41]. The plutonium species $(PuO_2)_2(OH)_2$ did not exceeded 1% of the total solution species and was not plotted for the sake of clarity.

Reaction	$\log_{10}K^{\circ}_{sp}$	Reference
Pu(III) species		
$Pu^{III}(OH)_{3\,(s)} + 3\,H^{+} \rightleftharpoons Pu^{3+} + 3\,H_2O$	15.8 ± 0.8	[8, 41]
$Pu^{III}(OH)_{3\,(s)} \rightleftharpoons Pu^{3+} + 3\,OH^{-}$	-26.2 ± 0.8	[8, 41]
Pu(IV) species		
$Pu^{IV}O_{2\,(am,hyd)} + 4\,H^{+} \rightleftharpoons Pu^{4+} + 2\,H_2O$	-2.33 ± 0.52	[8, 41]
$Pu^{IV}O_{2\,(am,hyd)} + 2\,H_2O \rightleftharpoons Pu^{4+} + 4\,OH^{-}$	-58.33 ± 0.52	[8, 41]
Pu(V) species		
$Pu^{V}O_2(OH)_{(am)} + H^{+} \rightleftharpoons Pu^{V}O_2^{+} + H_2O$	5.0 ± 0.5	[8, 41]
$Pu^{V}O_2(OH)_{(am)} \rightleftharpoons Pu^{V}O_2^{+} + OH^{-}$	-9.0 ± 0.5	[8, 41]
Pu(VI) species		
$Pu^{VI}O_2(OH)_2 \cdot H_2O_{(s)} + 2\,H^{+} \rightleftharpoons Pu^{VI}O_2^{2+} + 3\,H_2O$	5.5 ± 1.0	[8, 41]
$Pu^{VI}O_2(OH)_2 \cdot H_2O_{(s)} \rightleftharpoons Pu^{VI}O_2^{2+} + 2\,OH^{-} + H_2O$	-22.5 ± 1.0	[8, 41]
$Pu^{VI}O_2CO_{3\,(s)} \rightleftharpoons Pu^{VI}O_2^{2+} + CO_3^{2-}$	-14.65 ± 0.47	[8, 41]

Table 5.3: Available experimentally determined standard solubility products, $\log_{10}(K^{\circ}_{sp})$, for plutonium oxides, hydroxides, and carbonate complexes in aqueous solution. Error bars are representative of the 95% confidence interval.

constants have large associated measurement errors, it is essential to take into account these measured errors when calculating speciation diagrams. Examination of table 5.2 shows that associated errors are as high as ± 1.5 for some plutonium complexes. Note that the values listed are the base-10 logarithm of the formation constant so an error of ± 1.0 represents an error in the measurement of the formation constant by one order of magnitude on either side. Such large errors in the formation constant manifest themselves in the large error bands in the calculated speciation diagram shown in figure 5.3. We use the results from the speciation diagram calculation later to assist us in the modeling of mineral surface structures in the EXAFS fits (see chapter 7).

5.3.2 Plutonium Solubility

Table 5.3 lists all of the available experimentally determined standard stability products, $\log_{10}(K^{\circ}_{sp})$, for plutonium oxide, hydroxide, and carbonate species for Pu(III), Pu(IV), Pu(V), and Pu(VI). The plutonium oxide and hydroxide solubility products have been listed for both reactions that take place in acidic and basic solutions. These two solubility products are fairly easy to derive from one another with the help of the auto-dissociation constant of water (see equation 2.5). The calculation for the insoluble $Pu^{III}(OH)_{3\,(s)}$ species is as follows. The

dissociation reaction in the presence of acid is:

$$Pu^{III}(OH)_{3\,(s)} + 3\,H^{+} \rightleftharpoons Pu^{3+} + 3\,H_2O \tag{5.3}$$

with the solubility product

$$K_{sp}(5.3) = \frac{[Pu^{3+}]}{[H^{+}]^3} \tag{5.4}$$

The same dissociation reaction in basic solution is:

$$Pu^{III}(OH)_{3\,(s)} \rightleftharpoons Pu^{3+} + 3\,OH^{-} \tag{5.5}$$

with the solubility product

$$K_{sp}(5.5) = [Pu^{3+}][OH^{-}]^3 \tag{5.6}$$

The relationship between $K_{sp}(5.3)$ and $K_{sp}(5.5)$ can be shown to be:

$$K_{sp}(5.5) = [Pu^{3+}][OH^{-}]^3 = \frac{[Pu^{3+}]}{[H^{+}]^3} \cdot [H^{+}]^3[OH^{-}]^3 = K_{sp}(5.3) \cdot (K_w)^3$$

Taking the base-10 logarithm of both sides of the above equation gives:

$$\log_{10}(K_{sp}(5.5)) = \log_{10}(K_{sp}(5.3)) + 3\log_{10}(K_w)$$

Therefore, the solubility in acidic, or basic solution, can be calculated if one of the two solubility products and the auto-dissociation constant of water is known. Similar calculations can be carried out for the insoluble oxide and hydroxide species of the other plutonium oxidation states. For a full treatment of the solubility of plutonium hydroxides and hydrous oxides refer to the equations and derivations found in Neck *et al.* [8]. For the insoluble Pu(VI) carbonate species, $Pu^{VI}O_2CO_{3\,(s)}$, the solubility product favors the insoluble species. However, this species will not be a major component until CO_3^{2-} is present in appreciable amounts in solution at higher pH values (see section 2.5).

It can easily be seen from the information listed in table 5.3 that the solubility of plutonium in solution is highly dependent on both pH and the oxidation state of the plutonium. For example, tetravalent plutonium is much less soluble than the formally divalent PuO_2^{2+} moiety. It can also be seen that the solubility of plutonium hydroxide species, other than Pu(IV), are relatively high, particularly in acidic solutions. This is very important when attempting to understand the many processes by which plutonium can be made available for transport through the environment. In addition to soluble and insoluble species formation, plutonium can also undergo redox reactions (see subsection 5.3.3). Such reactions could easily shift the proportion of soluble and insoluble species.

5.3.3 Redox Chemistry of Plutonium

General solution redox chemistry has already been covered in section 2.4. Here we give an overview of the possible redox reactions that plutonium can undergo. Figure 5.4 shows a Latimer diagram of the redox couples of the environmentally available plutonium species and plutonium metal in acidic conditions. Notice that the redox couples between Pu^{3+}, Pu^{4+},

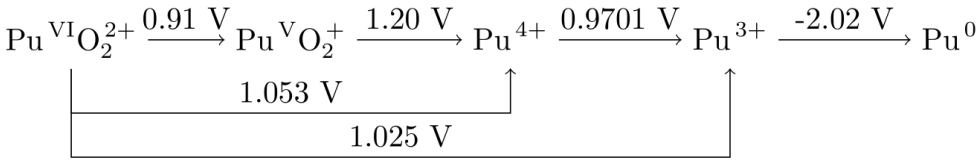

Figure 5.4: Formal reduction potentials presented in a Latimer diagram for the four environmentally available plutonium species and plutonium metal. Potentials were measured in 1 M $HClO_4$ at 25 C° [94].

$Pu^{V}O_2^+$, and $Pu^{VI}O_2^{2+}$ all have similar standard reduction potentials of approximately one volt. These very similar redox couples are what allows plutonium to exist in as many as four different oxidation states under certain conditions, and greatly complicates the understanding of plutonium solution chemistry.

Determination of whether a species will undergo disproportionation by inspecting Latimer diagrams is fairly straightforward. For any particular species in the Latimer diagram, if the potential to the right of the species is higher than the potential to the left of the species, the species will disproportionate. Examination of the Latimer diagram shows that the species $Pu^{V}O_2^+$ is capable of disproportionation under the conditions at which the Latimer diagram potentials were measured. However, Latimer diagram inspection does not work when multi-step disproportionation reactions occur, such as equation 5.7 and equation 5.8 below.

$$3\,Pu^{4+} + 2\,H_2O \rightleftharpoons 2\,Pu^{3+} + Pu^{VI}O_2^{2+} + 4\,H^+ \tag{5.7}$$

The disproportionation of reaction of Pu(IV) appears to be tri-molecular as it is written in equation 5.7. However, the overall reaction actually proceeds through two separate reactions:

$$2\,Pu^{4+} + 2\,H_2O \rightleftharpoons Pu^{3+} + Pu^{V}O_2^+ + 4\,H^+$$

$$Pu^{4+} + Pu^{V}O_2^+ \rightleftharpoons Pu^{3+} + Pu^{VI}O_2^{2+}$$

The first reaction above is the slow reaction, because it involves the making of the plutonium-oxygen bonds in the plutonyl moiety $Pu^{V}O_2^+$. The second reaction proceeds quickly because it only involves a simple electron transfer. Generally it is the case that simple electron transfer reactions proceed faster than reactions which involve the making or breaking of chemical bonds.

The disproportionation of Pu(V) can occur in two ways and is dependent on the presence of Pu(III) in solution [95]. If Pu(III) is present then the disproportionation reaction will proceed according to the following overall reaction:

$$3\,Pu^{V}O_2^+ + 4\,H^+ \rightleftharpoons Pu^{3+} + 2\,Pu^{VI}O_2^{2+} + 2\,H_2O \tag{5.8}$$

This apparent tri-molecular reaction actually proceeds through the two separate reactions:

$$Pu^{V}O_2^+ + Pu^{3+} + 4\,H^+ \rightleftharpoons 2\,Pu^{4+} + 2\,H_2O$$

$$Pu^{V}O_2^+ + Pu^{4+} \rightleftharpoons Pu^{3+} + Pu^{VI}O_2^{2+}$$

where two Pu^{4+} atoms are generated in the (slow) first reaction, and these atoms are consumed by running the second (fast) reaction twice to give the overall reaction shown in equation 5.8.

If only Pu(V) species are available then the disproportionation of Pu(V) is as follows:

$$2\,Pu^{V}O_2^+ + 4\,H^+ \rightleftharpoons Pu^{4+} + Pu^{VI}O_2^{2+} + 2\,H_2O \tag{5.9}$$

This reaction is initiated by the formation of cation-cation complexes that undergo protonation, followed by disproportionation. Theoretical calculations have also been conducted on this system and support this mechanism [96]. This reaction is slower than the ones above because it involves the breaking of the plutonium-oxygen bonds in the plutonyl moiety of one of the $Pu^{V}O_2^+$ species.

Other types of redox reactions may also occur in solution. One important reaction is the reduction of Pu(VI) by H_2O_2, which follows the net reaction:

$$2\,Pu^{VI}O_2^{2+} + H_2O_2 \rightleftharpoons 2\,Pu^{V}O_2^+ + 2\,H^+ + O_2 \tag{5.10}$$

Experiments in both acidic and basic solutions have been conducted [97, 98], but the exact set of individual reactions that add up to the net reaction shown in equation 5.10 has not been conclusively determined. We shall return to these equations in chapter 7 section 7.3 when modeling the possible mechanisms for X-ray beam-induced reduction of our experimental samples.

5.4 Detection and Measurement of Plutonium Oxidation States

5.4.1 UV-Vis Spectroscopy

UV-Vis spectroscopy measures the absorption of light as it passes through a sample of fixed length. The Beer-Lambert Law (Beer's Law) quantitatively defines the photon absorption (as a function of energy) that occurs as light travels through the sample. For one photon wavelength, Beer's Law has the functional form:

$$A = -\log_{10}\left(\frac{I}{I_o}\right) = \epsilon c l \tag{5.11}$$

where A is the absorption, I is the transmitted photon intensity, I_o is the incident photon intensity, ϵ is the so-called molar absorptivity or molar extinction coefficient, c is the molar concentration of the solution, and l is the path length that the light travels as it traverses the sample. UV-Vis spectroscopy cells often have a standard path length of 1 cm. However, 10 cm and even 1.0 m long cells [99] have been used for measuring low concentration actinide samples. For UV-Vis absorption measurements, the convention is to measure the solution concentration in molarity and the sample cell path length in centimeters. Therefore, the extinction coefficient must have units of $M^{-1}cm^{-1}$ since absorption is a unitless value.

UV-Vis spectra will change as the solution species changes. These changes in peak intensity and position are a result of the changing electronic structure for different species in solution. Because UV-Vis measurements are macroscopic in scale, the final measured absorption spectrum will be the linear combination of all the species found in solution with peak intensities proportional to the percent composition of the species in solution. For i solution species, each with its own absorption spectrum, the total absorption as a function of wavelength, $A_{tot}(\lambda)$, is given by the equation:

$$A_{tot}(\lambda) = l \sum_i \epsilon(\lambda)_i c_i \tag{5.12}$$

It is therefore important to make the proper choice of background electrolyte to ensure that other types of solution complex formation is not occurring with our metal of interest. The perchlorate anion (ClO_4^-) is chosen as a background electrolyte for UV-Vis measurements, as well as in other experiments, because perchloric acid has been shown to not form solution complexes with the uranyl cation (UO_2^{2+}) below 11.5 M [100]. The similar molecular structure of the plutonyl cation (PuO_2^{2+}) suggests that complex formation does not occur for plutonium either.

Figure 5.5 shows the UV-Vis spectra of all four environmentally accessible plutonium aquo-cations in a solution of 1 M $HClO_4$. All four spectra are significantly different despite the fact that Pu(III) and Pu(IV) are radially symmetric, and Pu(V) and Pu(VI) share a similar plutonyl moiety structure. This shows the functionality of using UV-Vis spectroscopy to measure the oxidation states of acidic aqueous plutonium solutions. The sharpness of the peak transitions and the relatively low molar extinction coefficients result from these transitions arising from dipole forbidden f-f electronic transitions.

The UV-Vis spectra for Pu(III) (figure 5.6), Pu(IV) (figure 5.7), Pu(V) (figure 5.8), and Pu(VI) (figure 5.9) have been plotted separately for easier reference. The Pu(IV) spectra exhibits what appears to be a large background absorption at low photon wavelength. This has historically been attributed to light scattering in the solution due to possible formation of the Pu(IV) polymer species. Pu(V) exhibits the smallest extinction coefficients of the four oxidation states, making it the species with the highest limit of detection. The very large resonance for Pu(VI) near 830 nm has an extinction coefficient of approximately 550 $M^{-1}cm^{-1}$ and is an excellent indicator of the presence of $Pu^{VI}O_2^{2+}$ in the sample solution. Unfortunately, most spectrometers do not have the resolution to properly resolve the sharp peak, resulting in a spectra with a truncated peak height. The use of this improperly measured peak height for quantitative solution concentration measurement of Pu(VI) is therefore suspect. Other methods to sidestep this problem would be to fit the entire absorption spectrum, fit the peak integral, or simply use another method to measure the concentration of the solution, such as radioactive counting.

5.4.2 X-ray Absorption Near Edge Structure Spectroscopy

The fundamentals of X-ray absorption near edge structure (XANES) spectroscopy, the theoretical origins of the XANES spectra, and spectral data analysis are covered in detail in section 6.3. Here, we cover the use of XANES spectroscopy as a probe to measure the oxidation state of plutonium in mineral solution samples [102, 103, 104, 105]. Despite the vast

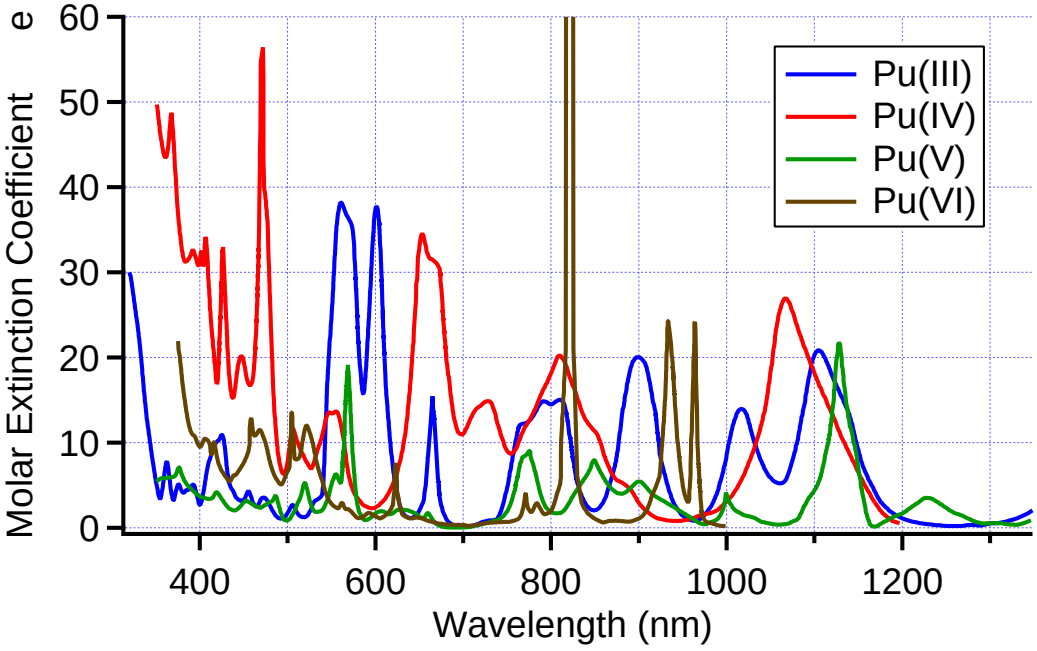

Figure 5.5: Overlay of UV-Vis spectra of Pu(III), Pu(IV), Pu(V), and Pu(VI) in 1 M $HClO_4$. Notice the large differences in the absorption spectra and sharp absorption features caused by the dipole forbidden f-f electronic transitions. Adapted from Cohen [101].

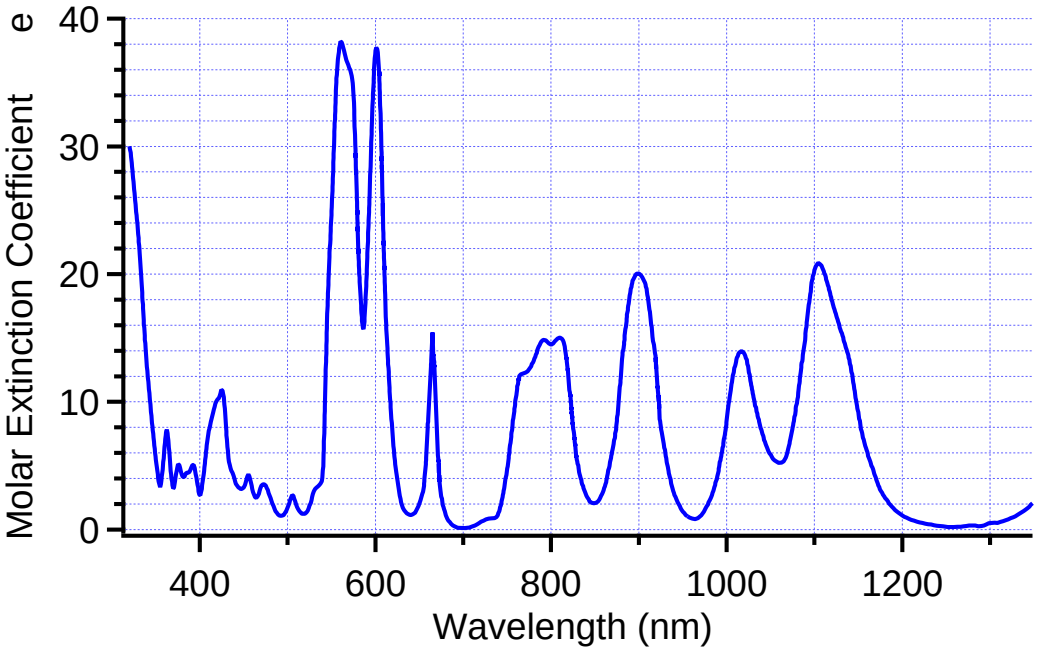

Figure 5.6: UV-Vis spectra of Pu(III) in 1 M $HClO_4$. Adapted from Cohen [101].

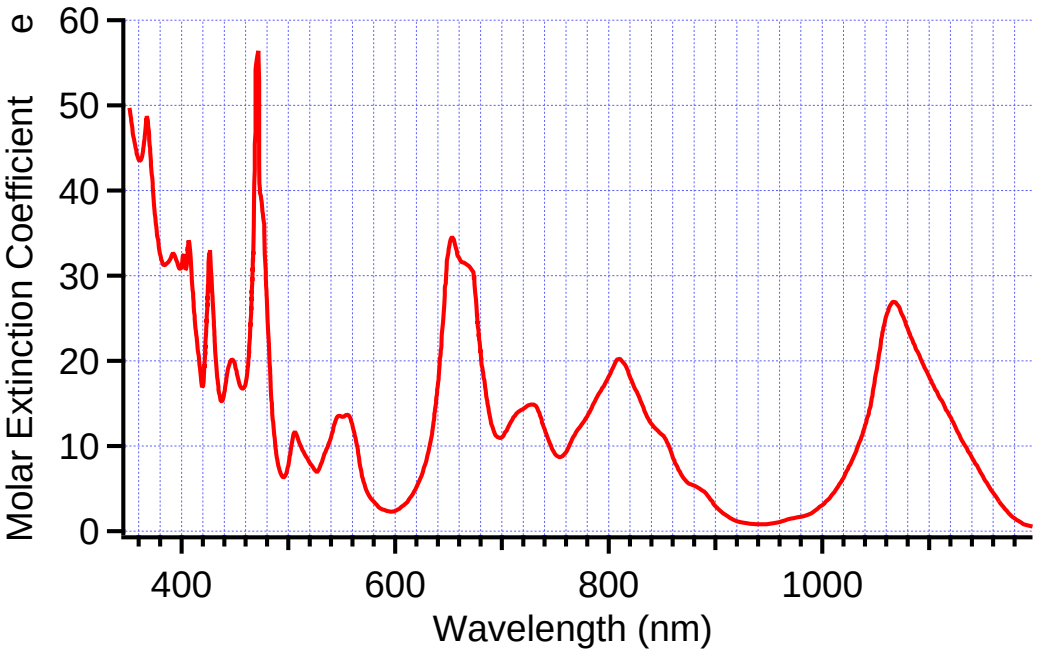

Figure 5.7: UV-Vis spectra of Pu(IV) in 1 M $HClO_4$. The steady increase in absorption beginning at 600 nm, and increasing as the photon wavelength gets smaller, has been historically attributed to light scattering in the solution. Adapted from Cohen [101].

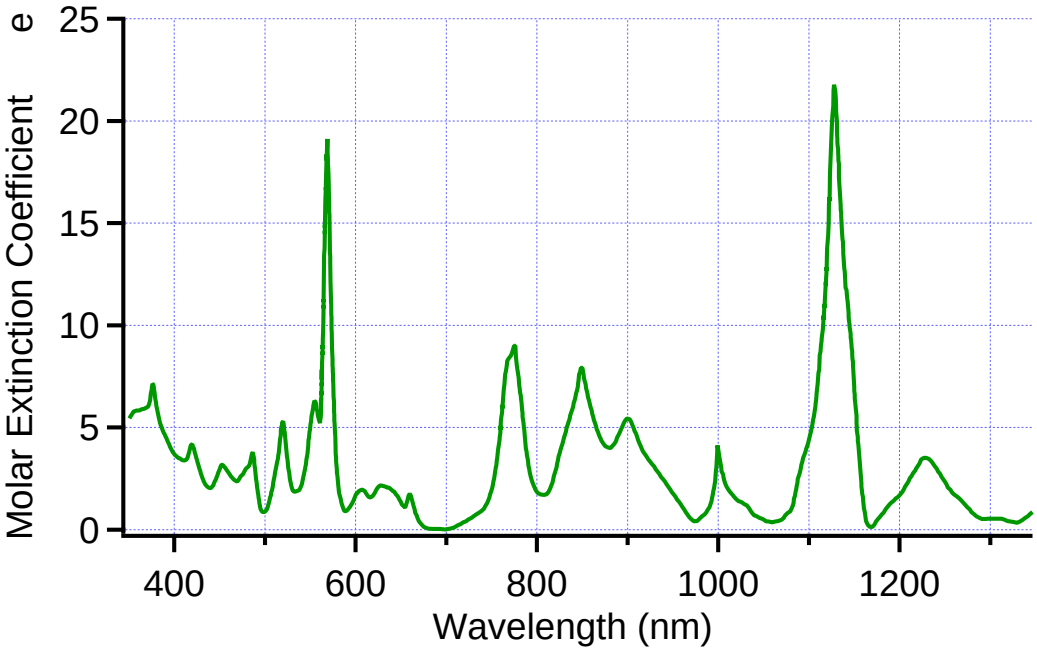

Figure 5.8: UV-Vis spectra of Pu(V) in 1 M $HClO_4$. Note that Pu(V) has the smallest molar extinction coefficients of any of the plutonium ions shown. Adapted from Cohen [101].

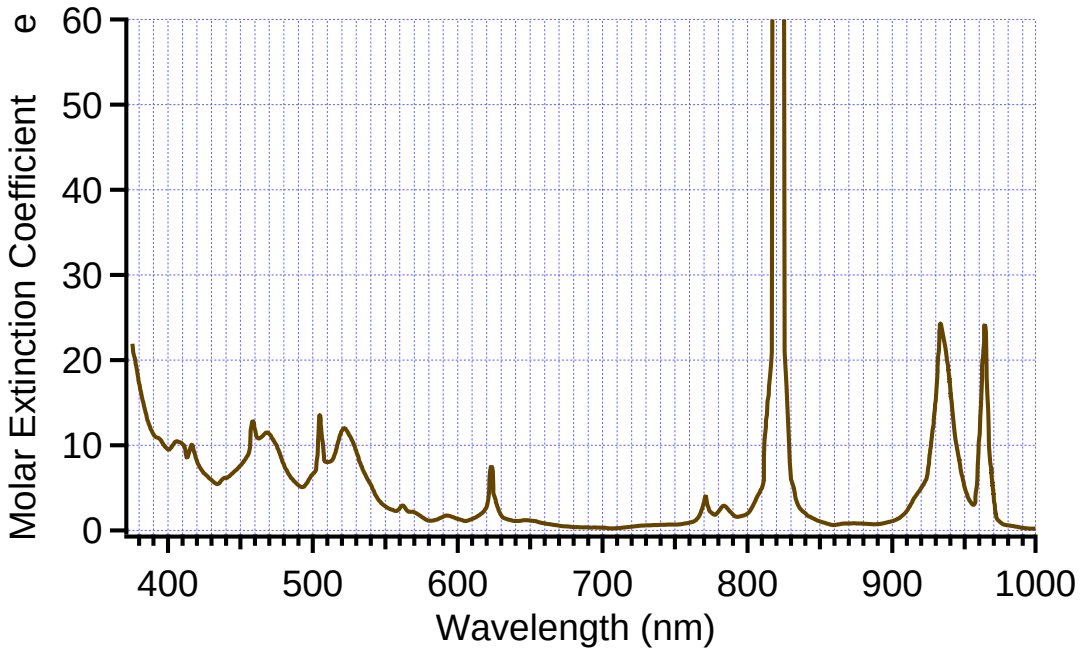

Figure 5.9: UV-Vis spectra of Pu(VI) in 1 M $HClO_4$. The very large peak at approximately 830 nm has an extinction coefficient of ∼550 $M^{-1}cm^{-1}$. Adapted from Cohen [101].

difference in photon energy used, the basic physical process for XANES (see subsection 6.3.2) is the same as for UV-Vis absorption spectroscopy (see subsection 5.4.1). The advantage of using X-rays is that it allows the experimenter to probe deep into the sample. If visible light were to be used, all of the incident photons would be absorbed and the absorption spectrum would hold very little information. The penetrating properties of X-rays allow us to probe both the plutonium present in solution, as well as the plutonium sorbed onto the mineral surface.

Using X-rays, we excite an electron in a specific core-level electronic state. For the Pu L_{III}-edge, this state is the $2p_{3/2}$ state. The exact photon energy required to excite this state depends on the electronic structure of the whole system, including the oxidation state of the plutonium atom. The electronic configuration of plutonium is $[Rn]7s^25f^6$. Changes in oxidation state correlate with changes in the electron occupancy for the 7s and/or 5f orbitals. Since electrons in these orbitals have a non-zero probability of being closer to the nucleus than the electron in the $2p_{3/2}$ orbital, the electrons in the 7s and 5f orbitals spend some of their time partially shielding the nuclear charge from the electron in the $2p_{3/2}$ orbital. A shielded $2p_{3/2}$ electron feels a smaller effective nuclear charge that results in a smaller Coulombic attractive force between the nucleus and the $2p_{3/2}$ electron. This smaller attractive force means a lower energy photon is required to eject the $2p_{3/2}$ electron and the XANES absorption edge (white-line) is shifted to lower energies (left). As electrons are removed from the valance orbitals (as the oxidation state increases) these valance electrons are no longer available to shield the $2p_{3/2}$ electron from the nucleus, increasing the Coulombic force between the $2p_{3/2}$ electron and the nucleus. This larger attractive force means a higher energy photon is required to eject the $2p_{3/2}$ electron and the XANES absorption edge is

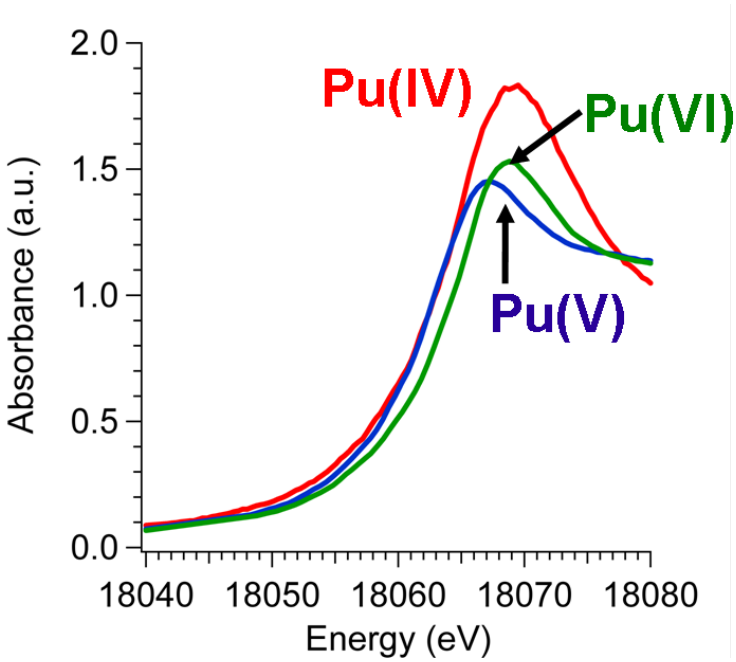

Figure 5.10: Plot of normalized XANES spectra as a function of energy for Pu(IV), Pu(V), and Pu(VI) in aqueous acidic solution. Note the reduced intensity in the white-line and associated high-energy shoulder for the plutonyl ($Pu^{V}O_2^+$ and $Pu^{VI}O_2^{2+}$) species.

shifted to higher energies (right). Therefore, as the oxidation state of plutonium (or any other element) increases the position of the XANES absorption edge should increase in energy as well.

Figure 5.10 shows a plot of Pu(IV), Pu(V), and Pu(VI) XANES plots overlaid for comparison. The plot shows that as the oxidation state of plutonium increases from Pu(V) to Pu(VI) we do in fact see an increase in the photon energy needed to eject the core-level electron. However, Pu(IV) does not follow this trend. The reason for this phenomenon lies in the molecular moieties that the higher oxidation states of plutonium form in aqueous solution. Figure 5.11 shows ball and stick models for the radially symmetric Pu^{4+} cation, and the two plutonyl moieties $Pu^{V}O_2^+$ and $Pu^{VI}O_2^{2+}$ with plutonium-oxygen bond lengths of 1.81 Å and 1.74 Å, respectively [33]. The presence of these plutonyl oxygens at such short bond lengths increases the electron density around the plutonium atom in a similar fashion as decreasing the oxidation state of the plutonium would. This causes the Pu(V) and Pu(VI) XANES spectra to shift to lower energies, resulting in overlap with the Pu(IV) spectrum as seen in figure 5.10. The shoulder to the right of the white line for the Pu(V) and Pu(VI) spectra are caused by photoelectron backscattering (see subsection 6.4.2) from the plutonyl oxygens [106] and are very helpful when attempting to fit sample EXAFS spectra to oxidation state pure EXAFS standards.

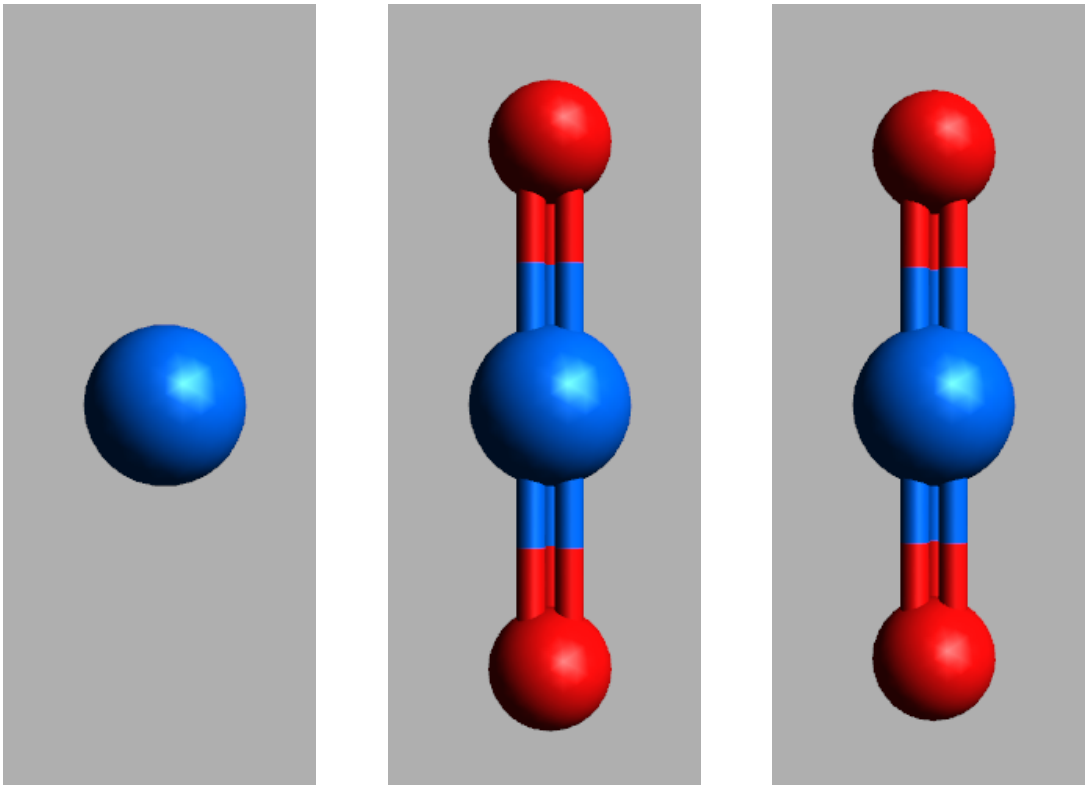

(a) Pu^{4+} (b) $Pu^{V}O_2^{+}$ (c) $Pu^{VI}O_2^{2+}$

Figure 5.11: Ball and stick models of (a) Pu^{4+}, (b) $Pu^{V}O_2^{+}$, and (c) $Pu^{VI}O_2^{2+}$. Plutonium = blue and oxygen = red. Relative bond distances are drawn accurately, but atomic radii are not. Notice the slightly shorter plutonyl bond distance for $Pu^{VI}O_2^{2+}$ due to the higher cationic charge on the plutonium atom.

Chapter 6

X-ray Absorption Spectroscopy

6.1 Introduction

X-ray absorption spectroscopy (XAS) has been used for many years to elucidate the local structure of environmental contaminants at low contaminant concentrations (< 1 %) [107, 108, 102]. For many studied systems this type of experiment is the only way to acquire direct information about binding interactions at the mineral/solution interface.

Below is an introduction to XAS and various related techniques. This type of spectroscopy can be conducted in regular laboratories using conventional X-ray sources or, as is more common, at large synchrotron user facilities. The use of synchrotron radiation is critical in collecting high-quality XAS data in a timely fashion; therefore, we will start off with a short discussion on the characteristics of such radiation sources. Next we will discuss the theory and experimental considerations necessary to conduct XAS spectroscopy. The two main types of XAS spectroscopy are X-ray absorption near-edge structure (XANES) spectroscopy and extended X-ray absorption fine structure (EXAFS) spectroscopy. When the XANES technique is applied to lighter elements it is sometimes referred to as near-edge X-ray absorption fine structure (NEXAFS) spectroscopy. However the two spectroscopies (XANES and NEXAFS) are a result of the same physical phenomenon and these two terms are often used interchangeably. Following the overview about conventional XAS techniques, we introduce and discuss the benefits of using two relatively new techniques: micro synchrotron X-ray fluorescence (μ-SXRF) spectroscopy and micro X-ray absorption near-edge structure (μ-XANES) spectroscopy.

6.2 Synchrotron Radiation

6.2.1 Introduction

Electromagnetic radiation is emitted when a charged particle, such as an electron, undergoes acceleration. In radiochemistry, this effect is best exemplified by the physical process known as Bremsstrahlung (breaking radiation) emission. A common example is that of a beta particle interacting with a high-Z material such as lead. As the beta particle interacts with the nucleus of a high-Z material it is deflected through a curved trajectory, and

consequentially accelerated. This acceleration causes the beta particle to emit a continuous spectrum of radiation. This effect increases as the Z-value of the material increases since the force of the electrostatic attraction between the beta particle and the nucleus is defined by Coulomb's law:

$$F \propto \frac{Z \cdot e^2}{r^2} \tag{6.1}$$

For sufficiently high-Z material the emitted radiation is in the X-ray region of the electromagnetic spectrum. This is the reason why beta particle radiation is best shielded using low-Z material such as polycarbonate.

The ability to study the structure of a particular material requires access to photon wavelengths of the same order of magnitude, or smaller. In the case of probing molecular structure, we need access to photon wavelengths in the range from 10 to 10^{-2} Å. These wavelengths encompass the "soft" and "hard" X-ray region of the electromagnetic spectrum. While "soft" X-ray sources are difficult to work with, "hard" X-ray sources are commonly available. The advantage of utilizing synchrotron radiation, as opposed to X-ray tubes, lies in the significantly higher X-ray flux and broad spectral range available at such user facilities.

In a way synchrotron radiation can be considered to be a type of Bremsstrahlung emission. However, the exact definition of synchrotron radiation is electromagnetic radiation emitted by electrons as they move at relativistic speeds along a macroscopic curved trajectory. Such radiation extends from the microwave region up through the X-ray region of the electromagnetic spectrum, offering high photon flux over many orders of magnitude in photon energy. Originally, in the early 1940's, this type of radiation was considered to be a hindrance in the building of circular electron accelerators [109] It was not until 1947 that experiments attempting to characterize and use synchrotron radiation where first conducted. The following paragraph, from Elder *et al.* [110], describing the initial observations of synchrotron light shows the progress that has been made in both the field of synchrotron radiation and health physics:

> The radiation is seen as a small spot of brilliant white light by an observer looking into the vacuum tube tangent to the orbit and towards the approaching electrons. The light is quite bright when the X-ray output of the machine at 70 MeV is 50 roentgens per minute at one meter from the target and can still be observed in daylight at outputs as low as 0.1 roentgen.

6.2.2 Theory

XAS measurements benefit from a lightsource that emits radiation evenly as a function of energy. This is true for X-rays emitted from bending magnets, or wiggler type insertion devices, but not for undulator type insertion devices. Therefore, when conducting XAS measurements, it is best to choose bending magnet (SSRL BL 2-3) or wiggler (SSRL BL 10-2 or 11-2) beamlines.

Figure 6.1 shows a schematic of a bending magnet X-ray source. As the electron beam passes through the magnet, the beam trajectory is changed, causing the electrons to accelerate and consequentially emit electromagnetic radiation. Synchrotron radiation intensity is fairly flat as a function of energy below the critical energy of the beamline (E_c) and begins

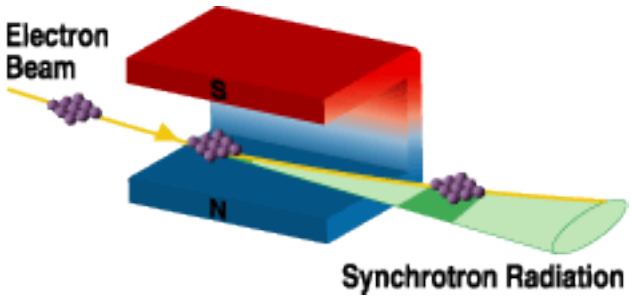

Figure 6.1: Schematic of a bending magnet [111].

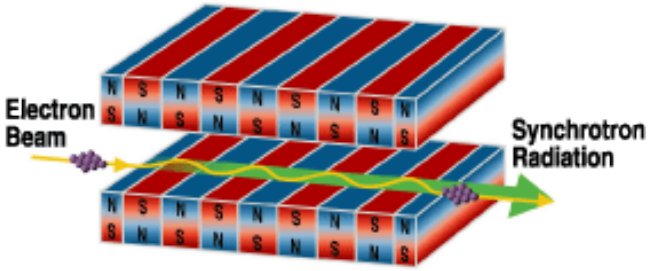

Figure 6.2: Schematic of a wiggler/undulator [111].

to drop above the critical energy. Here the critical energy is defined as the energy at which half the total power is radiated. For a bending magnet, the critical energy can be calculated using the following equation.

$$E_c[eV] = 665.0 \cdot E_e^2[GeV]B[T] \tag{6.2}$$

where E_c is the critical energy in units of electron volts, E_e is the energy of the electrons in the storage ring in units of giga-electron volts, and B is the strength of the magnet in units of tesla. We may also calculate the critical wavelength of the bending magnet using the following equation.

$$\lambda_c[nm] = \frac{1.864}{E_e^2[GeV] \cdot B[T]} \tag{6.3}$$

The Stanford positron-electron accelerating ring (SPEAR) stores synchrotron radiation producing electrons at 3.0 GeV. Beamline 2-3 has a 1.3 T bending magnet, resulting in a critical energy of 7780.5 eV. Often the useful energy range of a bending magnet extends up to $4E_c$. In the case of beamline 2-3, we are able to access the K-edge of most of the transition metals, and the L-edges for all of the elements up to the end of the periodic table.

Figure 6.2 shows a schematic of both a wiggler and an undulator source. As the electron beam passes through the periodic set of magnetic poles, the beam trajectory oscillates back and forth, again causing acceleration of the electrons and the emission of electromagnetic radiation. Such insertion devices can be operated in both wiggler mode, producing a white light similar to that of bending magnet radiation; or in undulator mode, useful when experiments call for a high photon flux at a particular energy. The operation mode depends on the separation of the magnetic poles in the insertion device.

hkl	d (Å)
111	3.136
220	1.920
440	0.960

Table 6.1: Silicon crystal d-spacings between adjacent crystal planes for different crystal cuts.

The equations for calculating the critical energy and wavelength for wigglers are more mathematically involved and beyond the scope of this overview. However, the advantage of using wiggler X-ray sources lies in the $2N$ photon flux amplification compared to bending magnets of the same magnetic strength, where N is the number of wiggler magnetic poles. Interested parties should reference the introductory text to X-ray radiation by David Attwood [112] for a complete treatment of this subject.

6.2.3 Radiation Characteristics

Electromagnetic radiation generated at synchrotron facilities has a set of very important characteristics including: high photon flux, broad spectral range, high polarization, pulsed time structure, and natural collimation [110]. Such characteristics in electromagnetic radiation sources, particularly X-ray sources, are very difficult, if not impossible, to produce through conventional laboratory-based equipment. For the purposes of the XAS measurements presented in chapter 7, we are mainly concerned with the availability of high photon flux in what is known as the "hard" X-ray region of the electromagnetic spectrum.

Since our experiments probe the local structure of samples that have no long-range order and on time-scales of tens of minutes, some characteristics of synchrotron radiation, such as high polarization and pulsed time structure, are not utilized. The three characteristics of synchrotron X-ray radiation that we must understand are the high flux, broad spectral range, and monochromaticity. As it turns out, these characteristics are interrelated.

White light, or radiation containing photons of many different energies, is generated when electrons in the storage ring travel through a bending magnet or insertion device. For XAS measurements, much of this light needs to be filtered away, resulting in near monochromatic light. The most common way of doing this is through the use of a silicon double-crystal monochromator. Figure 6.6 shows a schematic of a typical experimental beamline setup with the double-crystal monochromator labeled. A double-crystal monochromator set-up allows the experimenter to continuously rock the monochromator crystals through various energies without changing the direction of the reflected X-ray beam. X-ray photon energy is selected according to the well-known Bragg equation:

$$2d[\text{Å}]sin(\theta) = \frac{12.4}{E[keV]} \tag{6.4}$$

where d is the spacing between crystal planes for the monochromator crystal. Table 6.1 lists the d-spacing for some commonly used silicon crystal cuts. Figure 6.3 shows the reflected

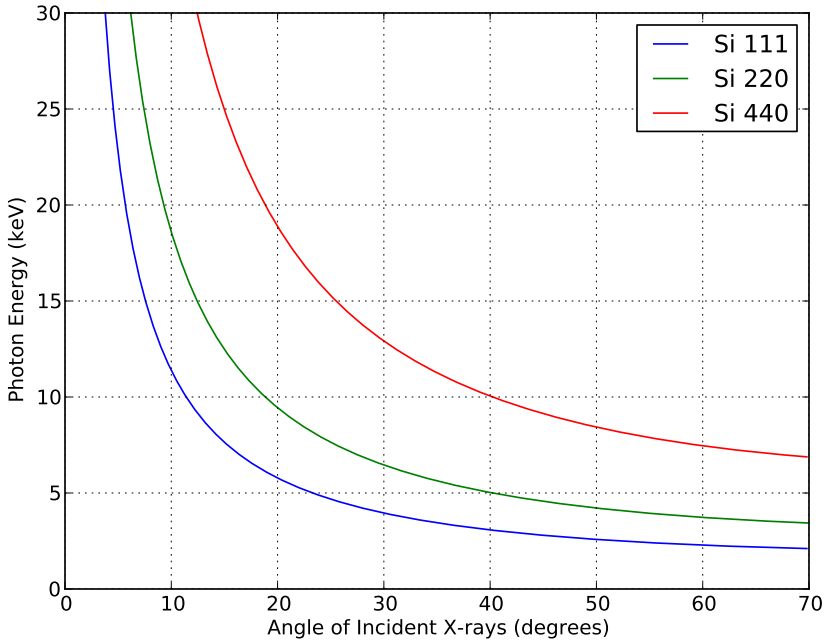

Figure 6.3: Reflected photon energy as a function of incident X-ray angle for various silicon monochromator crystal cuts.

photon energy as a function of the incident X-rays impinging on the monochromator crystal. As the crystal is rocked, different photon energies can be accessed. Notice that low (more glancing) crystal angles reflect higher energy X-ray photons.

An important property of any monochromator crystal is the achievable energy resolution as a function of selected photon energy. This property can be calculated using the derivative of the Bragg equation (equation 6.4):

$$\frac{\Delta E}{E} = cot(\theta)\Delta\theta \tag{6.5}$$

where θ is the Bragg angle and $\Delta\theta$ is the angular spread of the X-ray beam. The term $\Delta E/E$ is also referred to as the energy bandwith of the beamline and is a measure of the level of monochromaticity in the beam. The term $\Delta\theta$ consists of the angular spread of the incident X-ray beam and the intrinsic reflection width of the monochromator. To first order, this term can be estimated by the geometry of the beamline set-up using the equation:

$$\Delta\theta \approx \frac{\Delta a}{L}[rad] \tag{6.6}$$

where Δa is the height of beam-defining slits and L is the distance from the X-ray source to the slits. Figure 6.4 shows the energy resolution as a function of selected photon energy for a set of commonly used silicon monochromator crystals using equation 6.6. The plot shows better energy resolution for monochromator cuts that have smaller crystal plane separations. It is important to note that the trade-off for higher energy resolution is lower photon flux. Furthermore, higher energy resolution can be achieved through the proper setting of the

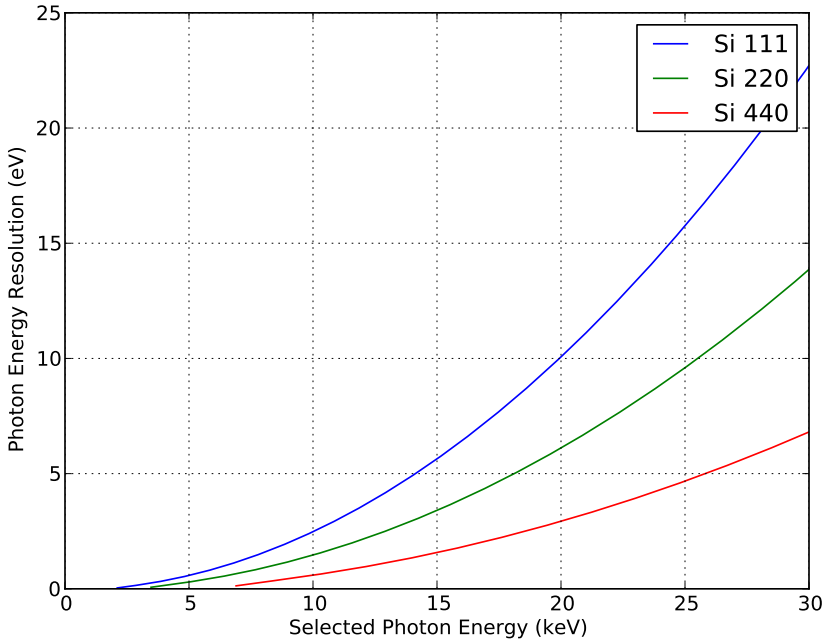

Figure 6.4: Photon energy resolution as a function of selected photon energy for various silicon monochromator crystal cuts.

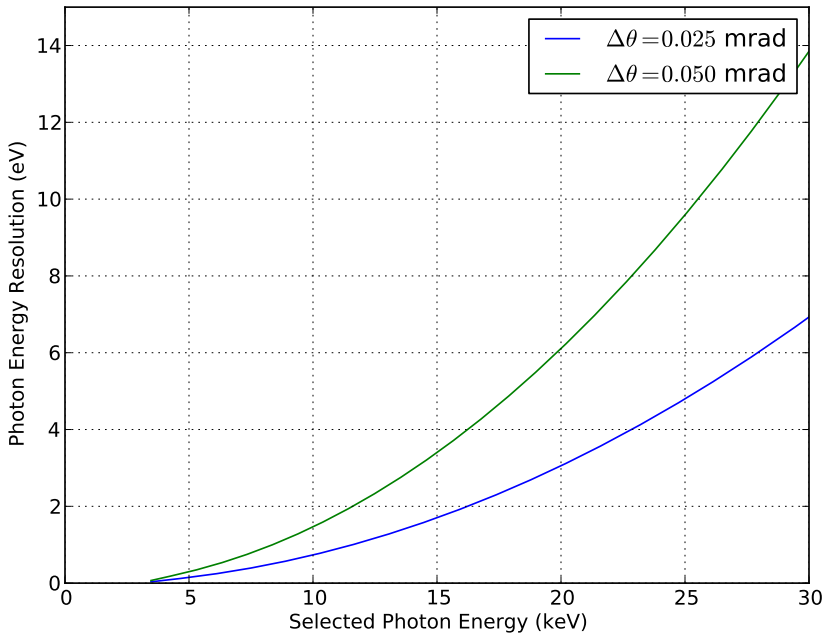

Figure 6.5: Photon energy resolution as a function of selected photon energy for for a Si 220 monochromator with 0.025 mrad and 0.050 mrad slit size.

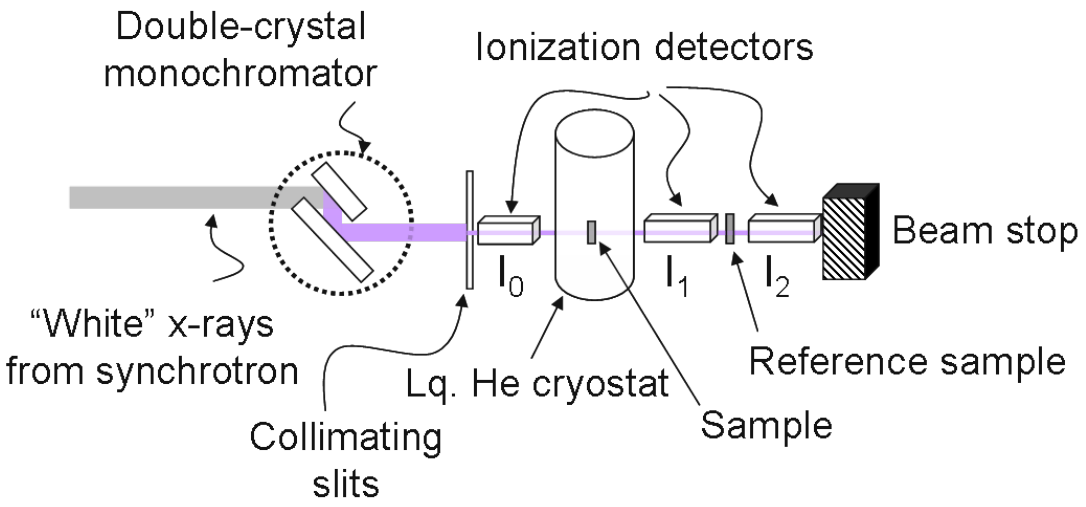

Figure 6.6: Schematic of a typical experimental beamline set-up for XAS collection in transmission mode.

beam-defining slits, again at the cost of photon flux. Assuming the distance from the X-ray source to the beam-defining slits is 20 m, and our two choices for the slit-height, Δa, are 0.5 mm and 1.0 mm, then our geometric estimate for $\Delta\theta$ is 0.025 mrad and 0.05 mrad, respectively. Figure 6.5 shows a plot of the photon energy resolution as a function of selected photon energy for these two slit-heights for a Si 220 monochromator crystal. Notice that a fair increase in resolution can be achieved simply through a reduction in the vertical slit-height.

6.2.4 XAS Beamline Setup

Figure 6.6 shows a schematic for a typical beamline setup to collect XAS data in transmission mode. White light synchrotron radiation impinges on the monochromator and a certain photon energy is selected by rotating the monochromator crystals to the correct angle (see equation 6.4 and figure 6.3). This relatively monochromatic light is then re-defined by x-y collimating slits. The X-rays pass through the first ionization chamber (see subsection 6.2.5), conventionally called I_0. The photon flux measured at I_0 is considered to be the initial photon flux before any X-ray absorption with the sample has occurred. The X-rays then interact with the sample. Any photons that are not absorbed or scattered then pass through the second ionization chamber, conventionally called I_1. The X-ray absorption spectrum is defined as the natural logarithm of the ratio between I_0 and I_1:

$$\mu x = ln\left(\frac{I_0}{I_1}\right) \tag{6.7}$$

where μ is the linear absorption coefficient of the material, x is the thickness of the material, and I_0 and I_1 are as previously defined. When collecting data in transmission mode the sample is usually rotated so that it is normal to the X-ray beam. This geometry exposes the maximum amount of sample to the X-ray beam. Notice the similarity between equation 6.7

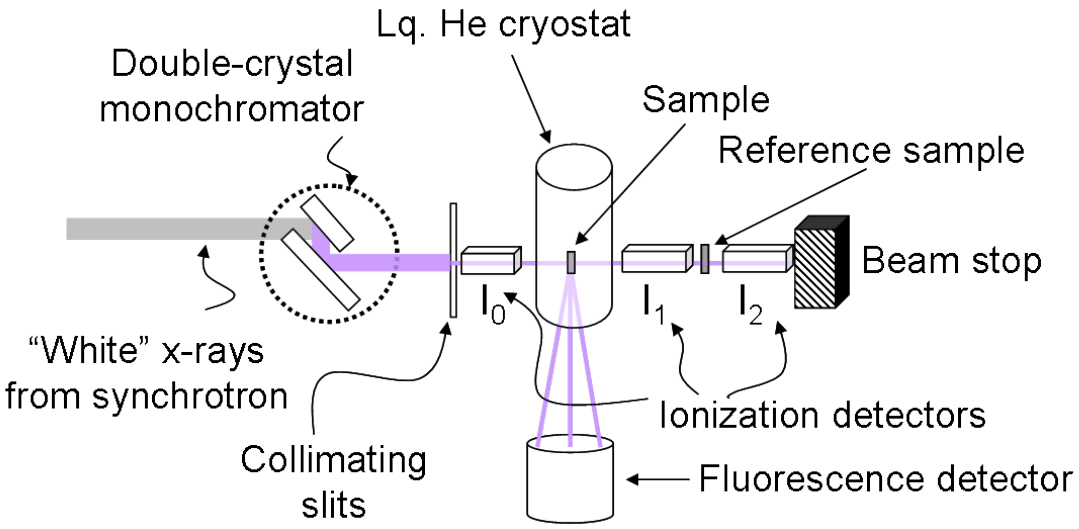

Figure 6.7: Schematic of a typical experimental beamline set-up for XAS collection in fluorescence mode.

and Beer's law for UV-Vis absorption (equation 5.11). Here, μ plays a similar role to the molar extinction coefficient, ϵ, in Beer's law. However, here the absorption is defined using the natural logarithm instead of the base-10 logarithm. The use of the base-10 logarithm in Beer's law is simply a matter of convention.

Often times a reference sample is collected at the same time for energy calibration purposes. In this case the reference sample is placed between the second and third ionization chambers (conventionally called I_1 and I_2). The absorption spectrum for the standard is defined similarly to equation 6.7:

$$\mu_{std} x_{std} = ln\left(\frac{I_1}{I_2}\right) \tag{6.8}$$

As figure 6.6 shows, using this setup it would theoretically be possible to collect two sample XAS spectra in transmission mode at the same time. This is normally not done because the beam attenuation that occurs as the beam traverses the sample in the first position greatly reduces the photon flux. Furthermore, inhomogeneities or artifacts in the sample in the first position could affect the data collected for the sample in the second position. There is much less concern of this occurring if a standard is placed in the second position because often the standard is simply used as a form of energy calibration, something that does not require high quality data.

Figure 6.7 shows schematics for a typical beamline setup to collect XAS data in fluorescence mode. The setup is similar to that for transmission data collection except for the addition of a fluorescence detector that is placed 90° with respect to the beam path, directed at the sample. When collecting data in fluorescence mode the sample is usually rotated so that it is 45° with respect to both the beam and the fluorescence detector so that fluorescence photons leaving the sample are not blocked by the sides of the sample holder. Fluorescence detectors are available as either energy insensitive detectors, such as Lytle detectors (not

discussed), or energy resolving detectors (see subsection 6.2.5), such as silicon or germanium detectors. The benefit of energy resolving detectors is the ability to separate the fluorescence photons by energy, and only count fluorescence photons of a certain energy. Energy discrimination also allows us to separate out fluorescence photons from other elements in the sample, and elastic scatter of the incident X-ray beam by the sample. This results in better atom specificity and a reduced background, which ultimately lowers the detection limit for trace elements in the measured sample. Such solid-state detectors are essential when working with environmental samples.

6.2.5 Detector Systems

Introduction

X-ray radiation is not perceivable by the human eye. Therefore other means of detection must be devised to quantify both the number and the energy of the X-ray photons that are produced in XAS experiments. It is essential to understand how these types of X-ray detectors work in so much as how certain parameters may or may not affect the end result of the experiment. Many excellent introductory textbooks on the subject of X-ray detection and detector properties have been written [47, 113, 114]. Below is a short discussion of the detector properties for the types of detectors pertinent to the measurement of XAS data.

Detector Deadtime

All detector systems require a certain amount of time to process an event after it arrives at the detector. During this time period, if another event occurs at the detector, the detector will not register this count. This time period, known as the detector deadtime, is effectively the time during which the detector is inactive, or dead.

There are two models for detector deadtime, the nonparalyzable and the paralyzable model. Let us define the true event rate to be r, the count rate in the detector to be c, and the detector deadtime to be τ. For the nonparalyzable detector the true event rate is related to the count rate by the equation

$$r(c)_{\text{nonpara}} = \frac{c}{1 - c\tau}$$

When a nonparalyzable detector experiences very high event rates the count rate will asymptotically approach $1/\tau$. This can be seen by solving for c in the above equation and taking the limit as r approaches infinity

$$c(r)_{\text{nonpara}} = \frac{r}{1 + r\tau}$$

$$\lim_{r \to \infty} c(r)_{\text{nonpara}} = \frac{1}{\tau}$$

For a paralyzable detector the count rate is related to the true event rate by the equation

$$c(r)_{\text{para}} = re^{-r\tau}$$

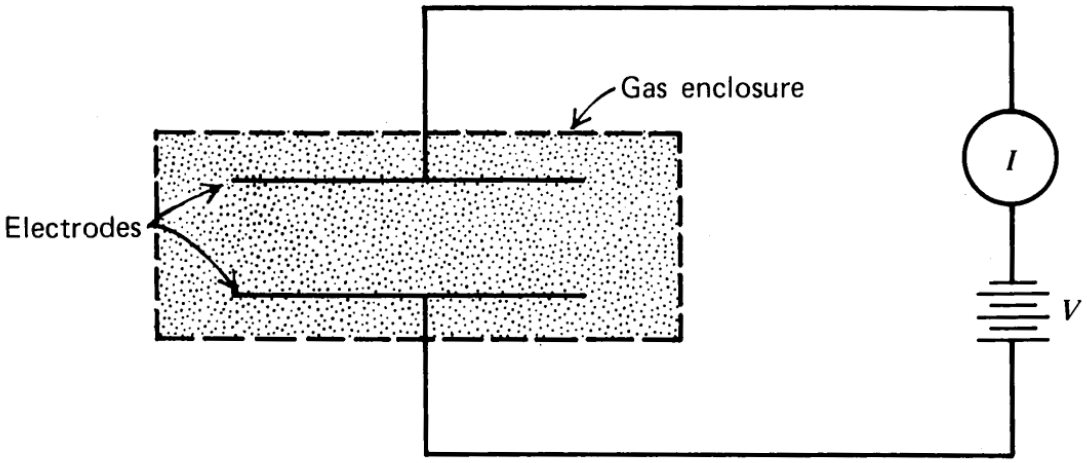

Figure 6.8: Schematic of an ion chamber. From Knoll [114].

This equation is more difficult to work with because there is no analytical solution for r as a function of c. Such solutions can only be calculated through iterative techniques.

When a paralyzable detector experiences very high event rates the count rate will asymptotically approach 0. This can be seen by taking the limit as r approaches infinity for the above equation, yielding

$$\lim_{r\to\infty} c(r)_{\text{para}} = 0$$

Notice that for a paralyzable detector the count rate will first go up, reach a maximum, and at sufficiently high event rates, the detector count rate will approach zero, becoming completely paralyzed.

A major component of XAS signal attenuation is due to detector deadtime. This effect is easily accounted for by measuring deadtime curves and applying a deadtime correction to the collected data. Deadtime correction is most pronounced in fluorescence scans with high event rates because of the high temporal cost of event pulse shaping and reading in energy resolved detectors. For this reason, deadtime corrections for fluorescence data amounts to most of the systematic error introduced by detector deadtime, and corrections to ion chamber readings are rarely done.

Ion Chambers

Ion chamber style detectors are based on the interaction of ionizing radiation, such as X-rays, with the fill gas present in the chamber. A schematic of an ion chamber is shown in figure 6.8. X-ray interaction with the fill gas causes the gas to ionize, and under an applied electric field these ionized gas particles will charge separate and migrate towards the electric field inducing plates. As these charged particles accelerate towards their respective electrode plates, secondary ionization occurs due to the ions colliding with other gas molecules in the chamber. As long as the gas in the ion chamber continues to be ionized, a steady-state current will be setup. This current can either be measured directly using a galvanometer, or (as more often is the case) it can be measured indirectly as the voltage drop across a known

resister using Ohm's law:

$$V = IR$$

If the current is constant, the voltage should also be constant and directly related to the photon flux traversing the ion chamber. However, to calculate the exact photon flux we will need to do a little more work. Conservation of photon flux through the detector tells us that the beam flux leaving the ion chamber must be equal to the initial beam flux minus the amount that was absorbed by the fill gas in the ion chamber. In functional form

$$I = I_o - I_{gas} \tag{6.9}$$

where I_o is the incident photon flux on the ion chamber, I_{gas} is the photon flux absorbed by the ion chamber gas, and I is the photon flux exiting the back end of the chamber.

We also know from equation 6.7 that absorption of photons across a sample (even a sample of gas) has the functional form

$$I = I_o e^{-\mu L} \tag{6.10}$$

where μ is the absorption cross-section of the gas and L is the length of the ionization chamber.

Substituting equation 6.10 into equation 6.9 and pulling a factor of I_o out in front gives

$$I_o = I + I_{gas} = I_o e^{-\mu L} + I_{gas} = I_o \left(e^{-\mu L} + \frac{I_{gas}}{I_o} \right)$$

which can be rearranged to

$$\frac{I_o}{I_o} = e^{-\mu L} + \frac{I_{gas}}{I_o}$$
$$\frac{I_{gas}}{I_o} = 1 - e^{-\mu L}$$

Solving this equation for I_o gives

$$I_o = \frac{I_{gas}}{1 - e^{-\mu L}} \tag{6.11}$$

an equation for the incident photon flux on the front of the ion chamber as a function of I_{gas}, L, and μ. Equation 6.10 can also be solved for I_o and substituted into equation 6.9 to give

$$I = \frac{I}{e^{-\mu L}} - I_{gas} = \frac{I - I_{gas} \cdot e^{-\mu L}}{e^{-\mu L}}$$

Rearranging this equation to solve for I gives

$$I e^{-\mu L} = I - I_{gas} \cdot e^{-\mu L}$$

$$I_{gas} \cdot e^{-\mu L} = I - I e^{-\mu L}$$

$$I = \frac{I_{gas} \cdot e^{-\mu L}}{1 - e^{-\mu L}} \cdot \frac{e^{\mu L}}{e^{\mu L}}$$

Gas	W_{gas} (eV)
He	42.3
Ne	36.6
Ar	**26.4**
Kr	24.2
Xe	22.0
H_2	36.3
Air	**34.0**
N_2	**35.0**
O_2	30.9
CO_2	32.9
C_2H_4	26.2
C_2H_6	24.8
CH_4	27.3
C_2H_2	25.9

Table 6.2: W_{gas} values for common gases used in ion chambers [115]. Values listed in bold are commonly used for ion chambers in XAS experiments.

$$I = \frac{I_{gas}}{e^{\mu L} - 1} \tag{6.12}$$

an equation for the photon flux leaving the rear of the ion chamber as a function of I_{gas}, L, and μ. The equation for I_{gas} is:

$$I_{gas} = \frac{IC_{\text{current}} \cdot W_{gas}}{1.602 \times 10^{-19} \cdot E_{ph}} \tag{6.13}$$

where E_{ph} is the photon energy in electron volts, IC_{current} is the ion chamber current in amps, and W_{gas} is the energy loss per ion pair, an empirically determined constant specific to the gas being used. Table 6.2 lists W_{gas} values for most common gases used in ion chambers.

Checking units for sanity we see that:

$$(\text{photons/sec}) = \frac{(\text{coulombs/sec}) \cdot (\text{eV/ion pair})}{(\text{coulombs/ion pair})(\text{eV/photon})}$$

This calculation assumes that the ion chamber high voltage is sufficient to collect the charge before any recombination takes place. It is always wise to test this assumption by increasing the high voltage on the ion chamber and verifying that the current being measured does not increase. On a high flux beamline it will be necessary to use He as the absorption medium in order to achieve this.

At low to moderate photon energies air is usually a suitable fill gas for the ion chamber. However, as photon energies increase the photon absorption cross section with air will go down. At sufficiently high energies, ion chambers may need to be purged and refilled with

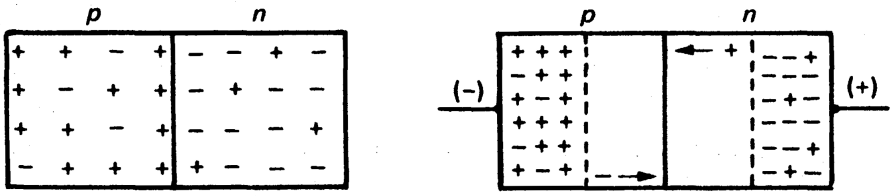

Figure 6.9: p-n junction without applied voltage (left) and with applied voltage (right) [47].

a fill gas that has more electrons to give sufficient photon absorption. Argon is an excellent fill gas at higher photon energies (> 18 keV).

The noise that is introduced through the use of an ion chamber comes from counting statistics. Therefore, signal fluctuation has a standard deviation of $\sqrt{N}$, where N is the number of counts measured. Notice that this is different from the number of ion pairs collected in the detector. Since each photon that is absorbed will result in many ion pairs produced and collected, the error in the counting statistics is most pronounced in photon counting error, not ion-pair counting error.

Solid State Detectors

Solid state detectors have the benefit of both measuring individual photon events and the associated photon energy. This allows us to collect X-ray energy spectra and discriminate for only a range of photons that are produced by the phenomenon of interest. This type of detector is usually made out of two types of materials: silicon or germanium.

Just as with the ion chamber fill gas, it is important to select the correct detector material for the photon energy range that is being detected. Higher energy photons are more easily detected using a solid state detector with germanium detector crystals. A Ge detector is a type of semiconductor detector. Semiconductor detectors work on the basis of p-n junctions. In p-type semiconductors there are sites that are positively charged (holes) that can move around the crystal lattice of the detector material. In n-type semiconductors there are sites that are negatively charged (electrons) that can move around the crystal lattice. A p-n junction occurs when a p-type semiconductor is placed next to an n-type semiconductor. By itself a small electric field is formed between the p-end and the n-end of the detector. If high voltage is applied across the detector then this electric field increases and a depletion zone is formed at the p-n junction (see figure 6.9).

When radiation interacts with the detector it creates electron/hole pairs in this depletion area where the electric field exists. Holes are attracted to the negative side and electrons are attracted to the positive side (see figure 6.10). These charges are then collected and processed by electronics to yield a spectrum.

The band gap for Ge detectors is approximately 0.75 eV. This is the amount of energy required to produce an electron/hole pair and is comparable to the W_{gas} values listed in table 6.2 for gases. The very small band gap means more ionizations per photon interaction, which results in better energy resolution. The band gap is so small that the detector must be cooled with liquid nitrogen, otherwise thermal fluctuations could cause ionizations that

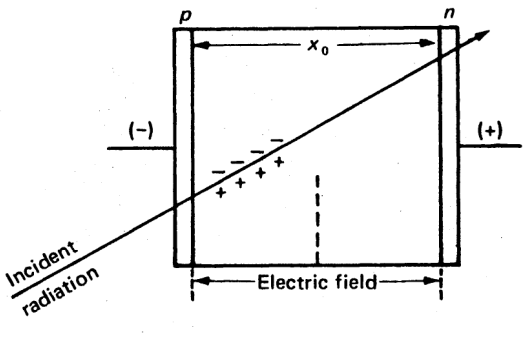

Figure 6.10: p-n junction acting as a detector. Here x_o defines the active detector area where charge separation occurs as the measured photon interacts with the detector material [47].

would manifest as detector noise.

Once the signal has been measured, a deadtime correction is conducted on the data. For our deadtime corrections we assume that the incoming count rate (ICR) has a sufficiently fast shaping time to approximate the true event rate. This is then plotted against the single channel analyzer (SCA) to form our approximate deadtime curve. Deadtime corrections using this approximation are usually of excellent quality. For multi-element detectors, such as the 13-element or 32-element germanium detectors at SSRL, each element must be deadtime corrected individually, since each element will have a different set of electronics and differ in intrinsic efficiencies.

The collected deadtime curves are fit to a paralyzable detector model of the functional form

$$c(r) = Are^{-r\tau} + B$$

where A is a proportionality constant and B is an offset term. Here c is the SCA data and r is the ICR data. A least squares fitting algorithm is used to fit the variables A, B, and τ.

It is important to note that at sufficiently high event rates the ICR will also start experiencing deadtime counting losses and our deadtime correction will no longer fully compensate for the total detection system deadtime loss. It is best not to collect data at such high event rates.

6.3 XANES

6.3.1 Introduction

XANES spectroscopy refers to the measurement of the X-ray photoabsorption cross-section as a function of incident photon energy. The equation defining the quantitative relationship between a photon energy, the ionization energy of a bound electron, and the kinetic energy of the ejected electron was first formulated by Einstein in his well-known 1905 paper on the photoelectric effect [116]. The equation for the photoelectric effect, given in

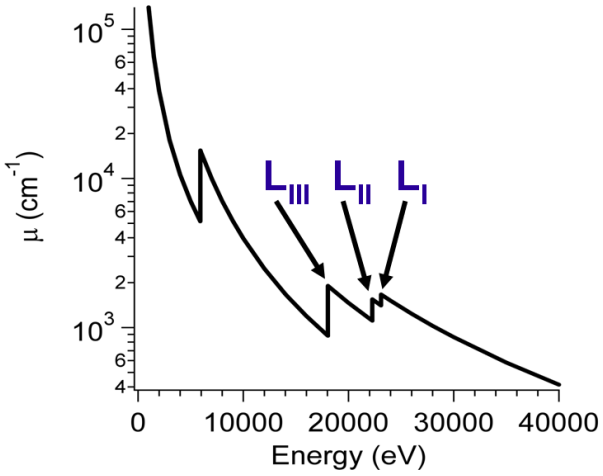

Figure 6.11: Log plot of absorption cross-section as a function of photon energy for elemental plutonium . The L_I-edge, L_{II}-edge, and L_{III}-edge positions are labeled for clarity. Data from McMaster X-ray cross-section tables [80].

contemporary notation, is:

$$h\nu = IE + \frac{1}{2}m_e v^2 \tag{6.14}$$

where $h\nu$ is the energy of the incoming photon, IE is the specific ionization energy of an electron in a particular atomic/molecular orbital, m_e is the mass of an electron, and v is the velocity of the ejected electron. When an electron is ionized as a result of photon impingement, the process is called photoionization, and the ejected electron is called a photoelectron.

The observed fine structure at the photoabsorption edge/peak was first described by Kossel in 1920, in a pair of papers [117, 118], and at the time was referred to as the "Kossel structure." The strongest peak in the absorption edge is now commonly referred to as the "white-line." Since XANES spectra arise from transitions to bound states in the system under study, XANES spectroscopy is a direct probe of the electronic structure and density of states at and around the absorption edge. For the actinide elements, XANES spectra are used to probe atom specific *in-situ* information about the oxidation state of the sample.

6.3.2 Theory

As shown in equation 6.7, X-ray absorption for a sample occurs with the functional form

$$I = I_o e^{-\mu x}$$

where I is the transmitted photon intensity, I_o is the incident photon energy, μ is the absorption cross-section of the material, and x is the thickness of the material. As the incident photon energy is increased, the absorption cross-section for a particular material will change. Figure 6.11 shows a plot of the absorption cross-section for elemental plutonium [119, 80]. The sharp discontinuities in the plot coincide with the photoelectric effect for core-level electrons (see equation 6.14). In the case of the L-edges, shown in figure 6.11, these core level electrons are the 2s and 2p electrons for plutonium.

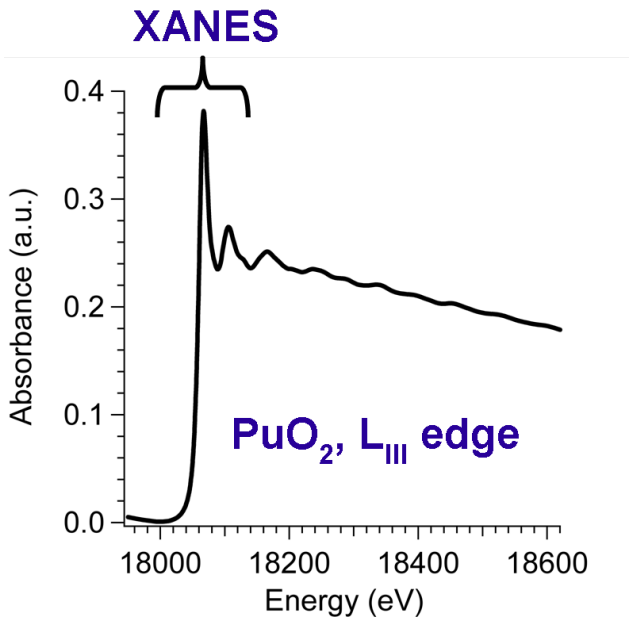

Figure 6.12: XAS spectra of the PuO_2 L_{III}-edge with the XANES region labeled.

For real spectra of actual samples, these photoexcited discontinuities are not infinitely sharp. Near and above the edge there are various fine structures present. The structures near the edge were first explained by Kossel [117, 118] and are a result of changes in the absorption cross-section as a function of energy. The absorption cross-section, μ, as a function of incident photon energy can be calculated from first principles using Fermi's so-called Golden Rule:

$$P_{if} = \frac{2\pi}{\hbar}|\langle f|V(t)|i\rangle|^2 \cdot \rho_f(E) \tag{6.15}$$

where P_{if} is the probability per unit time of a transition occurring from the initial state, $|i\rangle$, to the final state, $|f\rangle$, given a perturbation, $V(t)$, and the final state density of states, $\rho_f(E)$. Note that for XANES spectra $|f\rangle$ describes an unoccupied bound state of the system. Furthermore, the exact calculation of XANES spectra involve accurate knowledge of the initial state, the final state, and density of states for a particular model, making it very difficult to solve numerically. Despite these challenges, a few groups have made advances in *ab initio* calculations of XANES spectra [120, 121] and these calculations are quickly approaching quantitative agreement with collected experimental spectra. For a complete treatment of XANES theory please refer to the excellent text by Stöhr [122].

For low Z materials, the long core-hole lifetime of the photoelectron allows us to resolve fine transition structure that is important for comparing to theoretical calculations. High Z materials, such as plutonium, have very short core-hole lifetimes, causing the XANES spectra to be broadened out in accordance with the uncertainty principle, and sharp structure is lost. This effect benefits actinide chemists who usually use the location and shape of the L_{III}-edge as a measure of of the actinide oxidation state, independent of the local molecular structure [102]. This can only be achieved because of the core-hole broadening found in these elements.

6.3.3 Data Analysis

XANES data analysis requires that the collected data first be energy calibrated to a pre-determined value. The point in the spectrum at which energy calibration occurs varies from experimenter to experimenter, and the exact energy calibration methodology is often explicitly explained in the published literature. For the studies presented here, the first inflection point of the reference XANES spectra is either arbitrarily set to 0.0 eV, or to an agreed upon energy. For the PuO_2 L_{III}-edge the chosen value is 18062.3 eV [123], and for the Mn K-edge the chosen value is 6540.0 eV [80]. After energy calibration is conducted, a pre-edge background is subtracted from the spectrum, and the edge step of the absorption edge is normalized to a value of one. This allows for the comparison of the different white line heights of spectra with different oxidation states.

Once all spectra are energy calibrated and normalized, it is possible to use edge positions as a way of measuring oxidation states in XANES spectra (see subsection 5.4.2). The problem with only using the edge position as defined by the peak, or the inflection point of the white-line, is that all of the collected XANES data (commonly many hundreds of data points) are being reduced to one data point with an obvious loss of information. Furthermore, this point is very sensitive to the arbitrary nature in which many XAS practitioners decide to "properly" background subtract their data. Better fits can therefore be achieved by fitting the whole XANES spectra at once using a least-squares fitting routine [103] and a set of pure oxidation state standards. Figure 5.10 shows a plot of the Pu(IV), Pu(V), and Pu(VI) oxidation states in aqueous solution. Extending the XANES fit to include the region where plutonyl oxygen multiple scattering occurs [106] also helps fits to converge with a smaller fit error. FITES, part of the XAS data analysis package RSXAP [78], is used to fit XANES data. In an effort to expedite XANES fitting, a graphics user interface was programmed for FITES named GFITES. The code listing for GFITES can be found in section F.4.

6.4 EXAFS

6.4.1 Introduction

The observed fine structure that extends from a few 100 eV above the photoabsorption edge, now known as EXAFS, was first described by Kronig in 1931 [124, 125] and at the time was referred to as the "Kronig structure." Figure 6.13 shows the region in the XAS spectrum commonly defined as EXAFS. There is no specific point that separates the XANES and the EXAFS regions of an X-ray absorption spectrum. In fact, the EXAFS region blends into the XANES region all the way up to the absorption edge. It is also of interest to note that the same structural information is contained in both the XANES and the EXAFS portions of the spectrum. Given the ability to accurately calculate the XANES spectrum from first principles, it should theoretically be possible to probe the full three-dimensional environment surrounding the atom of interest (see subsection 6.3.2). Developing *ab initio* computational programs to be able to do so is currently a very active topic of research.

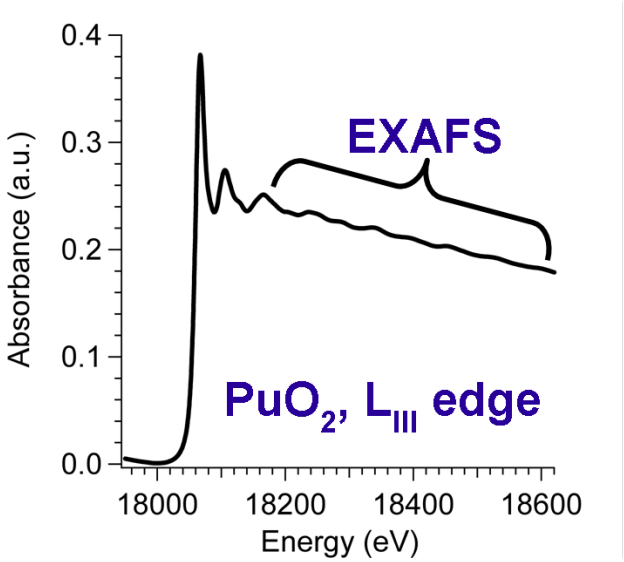

Figure 6.13: XAS spectra of the PuO_2 L_{III}-edge with the EXAFS region labeled.

6.4.2 Theory

The oscillatory structure in the region shown in figure 6.13 is caused by a change in the X-ray absorption cross-section, μ, and can again be described from first principles using Fermi's Golden Rule (equation 6.15). In the case of EXAFS, the final state, $|f\rangle$, describes the continuum state where a photoelectron exists in the field of the probed atom with one positive charge.

Figure 6.14 shows a schematic of the photoexcitation of a 2p core-electron into the continuum. The transition probability is proportional to μ, which in turn is related to the final state, $|f\rangle$, in the Golden Rule. Since the final state changes according to the molecular environment around the probed atom, EXAFS spectroscopy allows us to measure information about the environment surrounding the element of interest.

Figure 6.15 shows a schematic of the fluorescence process that occurs following the photoexcitation of a 2p core-level electron. During the fluorescence process a higher energy electron will decay into the core hole left by the initially photoexcited electron and emit a fluorescence photon ($h\nu'$ in figure 6.15). Since this fluorescence photon is characteristic of the atom being probed, an energy discriminating detector (see subsection 6.2.5) can be used to select photons resulting from this fluorescence process. Furthermore, since the fluorescence transition is directly related to the presence of a core-hole, measuring these fluorescence photons is another way of measuring the EXAFS spectra. The experimental setup for this type of experiment is shown in figure 6.7. Measuring EXAFS spectra in fluorescence mode is often essential when working with samples that contain the atom of interest as a small component (< 1 %). The discrimination of fluorescence photons allows us to greatly increase the signal to noise ratio by removing signal due to background processes that would normally have to be removed as a post-processing step.

The derivation of the EXAFS equation has been shown in various textbooks [126, 127, 128] and in the literature [120, 129, 130, 121]. Here we simply quote the result and introduce

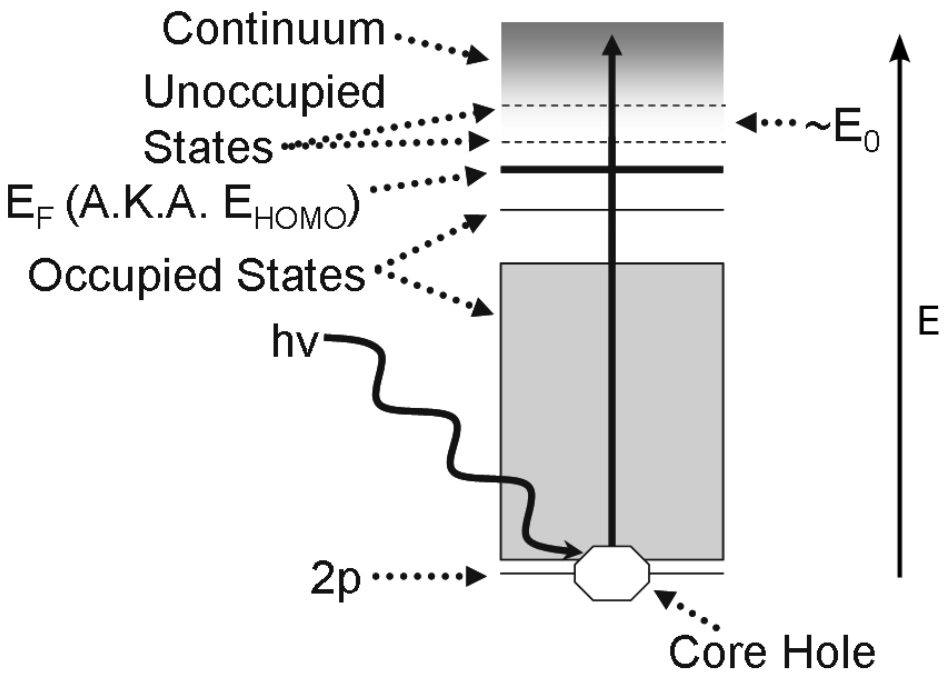

Figure 6.14: Schematic of the photoexcitation of the 2p core-electron into the continuum by an incident photon of energy $h\nu$.

each part of the equation individually. The full EXAFS equation is

$$\chi(k) = \sum_j N_j S_i(k) F_j(k) e^{-2\sigma_j^2 k^2} e^{-2r_j/\lambda_j(k)} \frac{sin(2kr_j + \phi_{ij}(k))}{kr_j^2} \tag{6.16}$$

The first step in fitting EXAFS data is to produce a reasonable model of the coordination environment around our atom of interest. When probing disorder in crystalline material, the model may be constructed from X-ray diffraction data. When measuring samples that have no long-range order, a model must be built by hand using different known pieces of information, such as hydration number/bond length, atomic structure of the surface where sorption is occurring, and chemical intuition. Once a model is built it must be deconstructed into its constituent parts and standards must be measured, or calculated for each part.

The phenomenon of EXAFS involves the interference between the photoejection of a core-level electron and its backscattering off of neighboring atoms. All of these processes are summed together, as seen in the summation term in equation 6.16, to produce the EXAFS oscillation spectrum, $\chi(k)$. To a first approximation, $\chi(k)$ should be reproducible by taking account of all photoejections that are backscattered by one neighboring atom back towards the central atom. This type of scattering event is referred to as a two-legged path, or single-scattering path, and tend to constitute > 90 % of the full EXAFS spectrum. Paths involving the photoelectron scattering off of more than one neighboring atom require some special considerations, which will be discussed below in subsection 6.4.3.

Experimentally measuring a library of standards to be able to build a model is both time consuming and difficult if the appropriate model compounds are not available for the atom

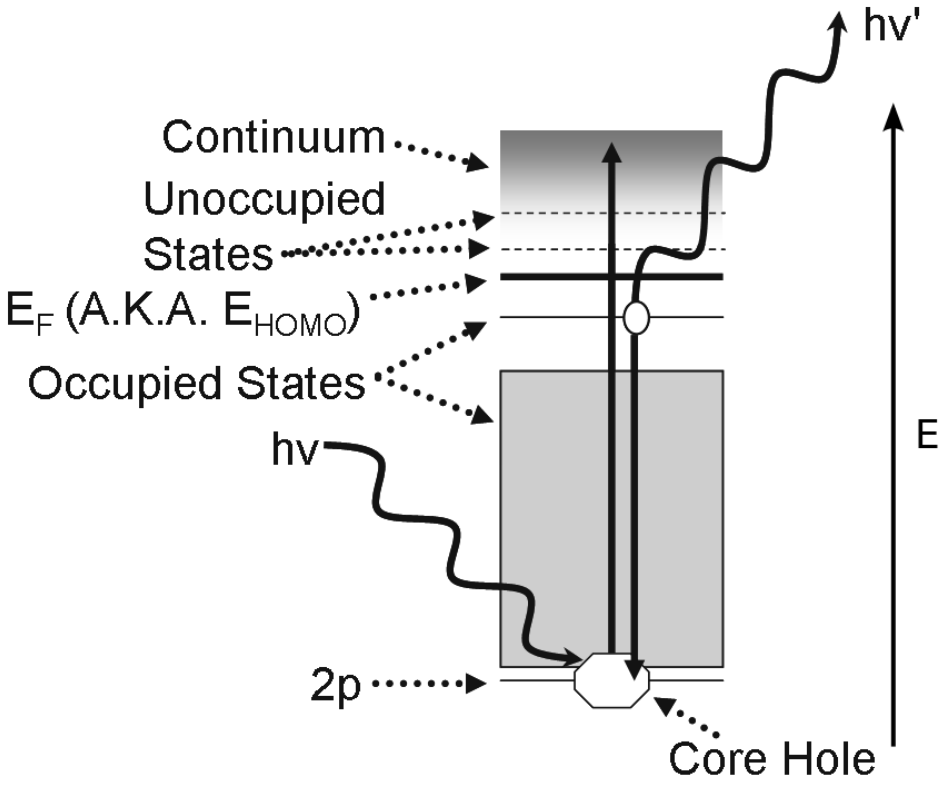

Figure 6.15: Schematic of the photoexcitation of the 2p core-electron into the continuum by an incident photon of energy $h\nu$ and the subsequent decay of a higher energy electron into the core-hole with emission of fluorescence photon $h\nu'$.

of interest. This tends to be a problem for the actinide elements. Thankfully, it is possible to accurately calculate these scattering paths individually using *ab initio* computational programs, the most widely used being FEFF [131, 132]. Using FEFF, the bolded terms in the equation below can be calculated from first principles.

$$\chi(k) = \sum_j N_j \mathbf{S_i}(\mathbf{k}) \mathbf{F_j}(\mathbf{k}) e^{-2\sigma_j^2 k^2} e^{-2r_j/\boldsymbol{\lambda_j}(\mathbf{k})} \frac{sin(2kr_j + \boldsymbol{\phi_{ij}}(\mathbf{k}))}{kr_j^2} \tag{6.17}$$

The term $S_i(k)$ is the amplitude reduction factor due to many-body effects about the atom that is being probed. Despite the fact that it is shown here to be a function of k, it is often constrained to a constant value in EXAFS fits. $F_j(k)$ is the backscattering amplitude for each atom, where the subscript j designates the identity of a particular neighboring atom. $\lambda_j(k)$ is the mean free path of the electron and $\phi_{ij}(k)$ is the total phase shift experienced by the photoelectron as it leaves the central atom, interacts with the neighboring atom(s), and returns to the central atom again. The remaining terms, shown in bold in equation 6.18, are free parameters that need to be fit to acquire information about the system under study.

$$\boldsymbol{\chi}(\mathbf{k}) = \sum_j \mathbf{N_j} S_i(k) F_j(k) e^{-2\boldsymbol{\sigma_j}^2 k^2} e^{-2\mathbf{r_j}/\lambda_j(k)} \frac{sin(2k\mathbf{r_j} + \phi_{ij}(k))}{k\mathbf{r_j}^2} \tag{6.18}$$

Here, $\chi(k)$ is the modeled EXAFS spectrum that must be compared to the collected experimental spectra for goodness-of-fit. N_j is the number of neighboring atoms of type j. Each atom-type has an individual Debye-Waller factor, σ_j, which takes into account both thermal vibrational disorder and static disorder for that particular atom. Each atom-type also has an individual bond length, r_j. Therefore, each type of atom in our model has 3 variable parameters, N_j, σ_j, and r_j. One final parameter, known as E_o, is also variable and is involved in the conversion from energy-space to k-space. It is conventional to fit one global E_o variable for all the EXAFS scattering paths in a model. Further discussion of E_o is found below in subsection 6.4.3.

Depending on the software used to fit EXAFS spectra, standards may need to be in k-space or r-space. k-space standards are simply the function $\chi(k)$ as calculated from the EXAFS equation (equation 6.16). r-space standards are the Fourier transform of the k-space standards. Some experimenters prefer one type of plot to the other. However, since k-space spectra and r-space spectra are Fourier transform pairs of each other, both spectra have the same amount of information. The information is simply reordered. Figure 6.17 shows a collected EXAFS spectrum of PuO_2 and the accompanying Fourier transform.

When fitting EXAFS spectra it is important to be mindful of the number of independent variables that are being fit. If this number exceeds the number of independent data points of the EXAFS spectra, then the fit will not be unique, and statistical analysis of the fitted variables can not be conducted. Further discussion of this topic is found below in subsection 6.4.3.

6.4.3 Data Analysis

Background Subtraction and Estimate of E_o

XAS data is measured as the natural logarithm of the ratio of signals between two ion chambers (see equation 6.7) as a function of the energy of the incident X-ray beam (in units of eV). During the process of EXAFS data analysis a smooth pre-edge and post-edge are subtracted from the spectrum to yield only the EXAFS oscillations.

$$\chi(E) = \frac{\mu(E) - \mu_o(E)}{\mu_o(E)} \tag{6.19}$$

where χ is the EXAFS oscillations as defined in equation 6.16, μ is the measured XAS absorption and μ_o is the background. The background consists of absorption processes that occur for the isolated atom with no neighbors (i.e. "in the gas phase").

When analyzing EXAFS data it is necessary to make an approximation of the pre-edge and post-edge region for purposes of background subtraction. Background subtraction is used to isolate only the EXAFS oscillation signal.

One method would be to subtract out the calculated bare atom absorption cross-section as a function of incident X-ray energy for the particular element(s) under investigation. An empirical formula for calculating the absorption cross-sections for much of the periodic table is given by Victoreen [119]. However, in practice this method often introduces a large amount of error because it is unable to take into account shifting of the absorption maximum due to the chemical environment of the probed element, non-ideal measurement conditions, or measurement of EXAFS using different methods such as measuring in fluorescence mode. Furthermore, we are often not interested in the pre-edge background or the photopeak (XANES) portion of the spectra when we are analyzing EXAFS oscillations, so accurate background subtraction in this region is unnecessary.

The most often utilized method begins with subtracting a pre-edge background from the spectrum, and normalizing the edge step of the absorption edge to a value of one. This is similar to the data processing that is done for XANES in section 6.3. The initial estimated value for E_o is taken to be the energy value at which half of the edge step occurs. This is simply an initial guess, and further refinement of E_o can be done later in the data analysis process. Finally, a cubic spline is fit above the absorption edge and subtracted out to remove background effects and isolate the EXAFS oscillations.

Conversion from Energy-space to k-space and Fourier Transformation

Once EXAFS oscillations are properly isolated, the units of the abscissa need to be converted from energy-space (eV) to k-space (Å^{-1}). It is important here to recall the physical process that is occurring that warrants this conversion. In an EXAFS experiment a core-level electron is being ejected from an absorbing atom. Assuming that the incident X-ray energy matches the energy of the core-level electron state, an electronic transition occurs from the core-level state out to infinity, but with zero kinetic energy. As the incident X-ray energy is increased, the amount of kinetic energy that is imparted to the photoelectron is also increased, which allows the photoelectron to move out (as both a wave and a particle) and interact with the neighboring atoms. Conversion from energy-space to k-space merely

unit	SI
$\hbar$	$1.054571 \times 10^{-34}\text{J} \cdot \text{s}$
m_e	$9.109 \times 10^{-31}\text{kg}$
1 eV	$1.60217653 \times 10^{-19}\text{J}$

Table 6.3: Constants and conversion factors for converting from units of eV to SI units.

changes the abscissa from incident photon energy to the photoelectron wavevector ($k = 2\pi/\lambda$). It is important to realize that the excited photoelectron wavevector does not exist until the photoelectron is excited, which means that a new zero value must be set for the x-axis for the plot at the point where the ionization occurs (E_o). For simplicity E_o is set at the half-height of the edge step because the true value of E_o is a function of various parameters, including oxidation state, coordination geometry, and nearest neighbor identity, making it difficult to measure. Later, when fitting the EXAFS spectrum with model scattering paths a variable ΔE_o will be defined that accounts for errors that may be introduced in arbitrarily selecting E_o.

The equation to calculate the wavevector (k) of the ejected photoelectron is:

$$k = \sqrt{\frac{2m_e}{\hbar^2}(E - E_o)} \tag{6.20}$$

where m_e is the rest mass of the electron, $\hbar$ is Planck's constant divided by 2π, and E_o is the "ionization energy" of the electron being ejected by the incident X-ray beam [126]. Intrinsic to the equation is the subtraction of the ionization energy for the core hole state, effectively setting a new zero value in the abscissa. Unit analysis using SI units for equation 6.20 shows that k is in units of inverse length.

$$\text{m}^{-1} = \sqrt{\frac{\text{kg}}{\left(\frac{\text{kg}\cdot\text{m}^2}{\text{s}^2}\cdot\text{s}\right)^2}\left(\frac{\text{kg}\cdot\text{m}^2}{\text{s}^2}\right)}$$

For EXAFS measurements it is worth understanding the theoretical limit for how far one can measure in k-space. Measurements are restricted by a variety of physical reasons. For example, continued measurement of any edge except for the K edge will result in eventually hitting another absorption edge at higher energies. Let us assume that we are interested in measuring the L_{III} EXAFS of Pu, with an edge position of 18057.0 eV. If there is data in the higher k-range, then it is surely worth the time to collect an EXAFS spectrum out as far as possible in k-space, but we are limited by the L_{II} edge of Pu, at 22266.0 eV. Therefore, only 4209.0 eV of L_{III} EXAFS data can be collected before the spectra starts becoming contaminated with the L_{II} edge.

Using these values and the constants given in table 6.4 the calculation works out to be:

$$\text{k} = \sqrt{\frac{2(9.109 \times 10^{-31})}{(1.054571 \times 10^{-34})^2}(4209.0 \cdot 1.60217653 \times 10^{-19})}$$

unit	atomic unit
$\hbar$	1
m_e	1
27.2 eV	1 hartree
1 eV	$\frac{1}{27.2} = 0.0368$ hartree
0.529 Å	1 a_o

Table 6.4: Constants and conversion factors for converting from units of eV to atomic units.

which gives a k value of 3.3237×10^{10} m^{-1} or 33.237 Å^{-1}. However, as seen above, working in SI units requires dealing with very unwieldy numbers. A better set of units to use would be atomic units.

Atomic units (table 6.4) are convenient to use in this type of calculation because many atomic level universal constants are set to one, vastly simplifying calculations. Using atomic units, the calculation works out to be:

$$k = \sqrt{\frac{2(1)}{(1)^2}\left(\frac{4209.0}{27.2}\right)}$$

where k is expressed in inverse Bohr radii (the unit of length in atomic units). Dividing by 0.529 converts k in inverse Bohr radii back to k in Å^{-1}, giving the same answer as before (to within round-off error), but this time with a much simpler calculation. Bringing the conversion factor for Bohr radii to Ångströms inside the square root and collecting constant terms gives us the equation:

$$k = \sqrt{0.2628(E - E_o)} \tag{6.21}$$

Figure 6.16 shows a plot of the equation as a function of energy above the ionization energy.

According to this calculation, one can theoretically measure Pu L_{III} EXAFS out to a k value of 33.237 Å^{-1}. However, in practice, EXAFS oscillations tend to attenuate due to the mean-free path term ($\lambda_j(k)$) or cancel out due to the radial term (r_j) in the EXAFS equation (6.16) long before a k value of 33 Å^{-1} is ever reached. Further measurements beyond a k-range where data is present only serves to introduce more stochastic noise to the measured EXAFS spectra and does not produce spectra that fit better to model standards (see section 7.2).

This interference effect when collecting EXAFS spectra may be more pronounced when there is a possibility of other elements of similar Z value being present in the sample. For example, the Am L_{III} edge at 18510.0 eV, given high enough sample concentration, could interfere with the measurement of Pu L_{III} EXAFS at approximately 10.91 Å^{-1}. Such interference may have been inappropriately attributed to multi-electron excitations in the past [133], and underscores the importance of proper sample preparation, especially plutonium ion-exchange separations (see appendix E).

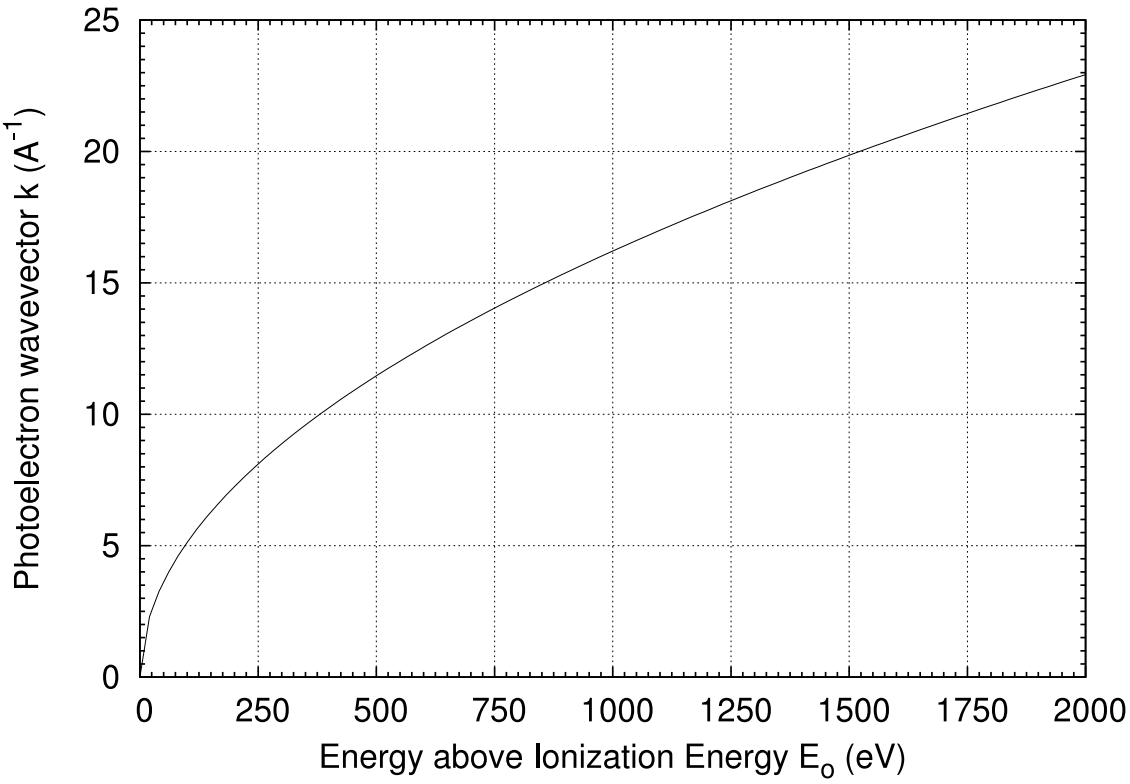

Figure 6.16: Plot of the photoelectron wavevector, k, as a function of energy above the photoionization energy, E_o, as defined in equation 6.21.

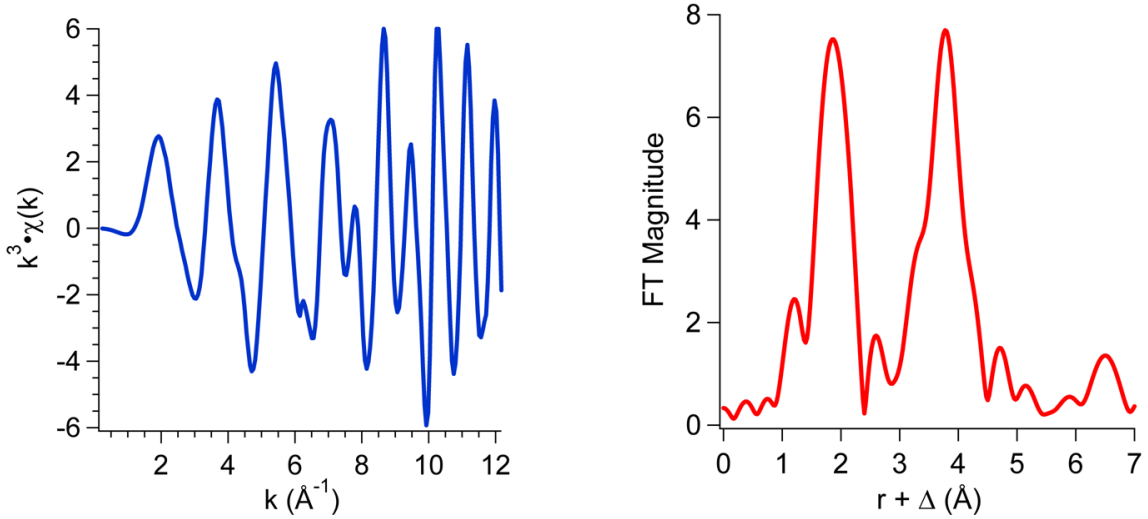

(a) k-space (b) r-space

Figure 6.17: Plot of the extracted EXAFS oscillations for PuO_2 in (a) k-space and Fourier transformed into (b) r-space.

Once background subtraction and conversion to k-space has been achieved, the EXAFS spectrum, $\chi(k)$, can be Fourier transformed from k-space to r-space. By convention the EXAFS spectrum is first weighted by k^3. Figure 6.17 shows an example of such a transformation. The process of Fourier transformation is well documented and only the results will be reproduced here. Note that it is easier for humans to visually process the r-space plot to see that there are two shells of atoms around each Pu central atom in PuO_2. The first shell at $\sim$1.8 r + Δ(Å) is a shell of oxygen atoms and the second shell at $\sim$3.8 r + Δ(Å) is a shell of plutonium atoms. However, the two plots in figure 6.17 contain the same information.

It is also important to point out that peaks in the r-space plot do not correlate exactly with the bond distances of neighboring atom shells. That is to say, the Fourier transform of $k^3 \cdot \chi(k)$ is not a radial pair distribution function (rPDF). This discrepancy between FT[$k^3 \cdot \chi(k)$] and the rPDF of the sample is a result of the phase shift ($\phi_{ij}(k)$ in equation 6.16) that the photoelectron undergoes. Recently, Roßberg and Funke [134] have developed a method for directly inverting the XANES spectrum, $\chi(k)$, to give the rPDF. However, the method currently only works for spectra that are dominated by single-scattering (two-legged) paths.

Number of Independent Data Points in an EXAFS Spectrum

Prior to data fitting, it is necessary to evaluate the number of independent data points in the collected EXAFS spectra. It is important to note the difference between collected data points and independent data points. The experimenter is free to collect as many data points as is allowed by time and patience, but a collected spectrum only holds a finite amount of information, which is represented by the number of independent data points. This topic derives from the field of Information Theory. The number of independent data points can be considered the upper limit to the number of EXAFS fitting parameters used to try and reproduce the collected spectrum from a set of standards. Interested parties are referred to introductory texts on the topic [135] and the seminal paper by Edward A. Stern [136]. A full derivation of Stern's rule is presented below.

The final result of this derivation will be a numerical value for the number of independent data points, N_{ind}, in an EXAFS spectrum. In general this value is the fundamental limit to the number of independent parameters that can be fit to a particular EXAFS spectrum. Examples of fitting parameters are bond distances, Debye-Waller factors, and nearest-neighbor coordination numbers. Fitting more parameters to an EXAFS spectrum than is allowed by N_{ind} results in a fit that is not mathematically unique and is statistically meaningless.

The idealized EXAFS spectrum, $\chi(k)$, actually consists of various discrete measurements at points k_j. Ideally, for statistical reasons, one would want to measure each k_j more than once. This results in both an error in the measurement of k_j and the value of $\chi(k)$ at k_j. The latter is defined as $k_j \pm \sigma(k_j)$. For simplicity we assume that $\sigma(k_j)$ is independent of k_j (i.e. the reproducibility of k_j is the same for all values of k_j) and simply write it as a constant, σ_k. It is also assumed that all the values of k_j are already uniformly spaced on a grid, or the data has been interpolated on a uniformly spaced grid with spacing constant Δk_o. This results in the following equation for k_j

$$k_j = k_{min} + n_j \Delta k_o$$

where $0 \leq n_j \leq N_{max}$. It follows that the maximum value for k is

$$k_{max} = k_{min} + N_{max}\Delta k_o$$

The function that we will be fitting in real space is the Fourier transform of $\chi(k)$

$$f(r_x) = \sum_x \chi(k_j) e^{i2k_j r_x}$$

where $f(r_x)$ is the pseudo-radial distribution plot commonly sought after in EXAFS spectroscopy.

Although we only have information about $\chi(k_j)$ over the range $\delta k = k_{max} - k_{min}$ the transform is usually extended over a longer range $K > \delta k$. The function is therefore said to be periodic over a period K. This is done so that the density of points in real space is greater (i.e. the spacing between points is smaller) since the grid in real space is given by the equation

$$r_x = \frac{\pi n_x}{K}$$

where n_x are integers.

When we measure the EXAFS spectrum, $\chi(k_j)$, we undoubtedly also measure random noise in $\chi(k_j)$. Because of this noise there is also error in $f(r_x)$, which is calculated from $\chi(k_j)$. This can be found to be

$$\langle |\Delta f(r_x)|^2 \rangle \equiv \sigma_x^2 \tag{6.22}$$

Here we are defining the mean-squared uncertainty in real space to be the average of all the measured uncertainties squared for each data point in real space, where averaging is denoted by angled brackets. Substituting in the equation

$$f(r_x) = \sum_x \chi(k_j) e^{i2k_j r_x}$$

for $f((r_x)$ we get

$$\sigma_x^2 = \langle \sum_{jl} \Delta\chi(k_j) e^{ik_j r_x} \Delta\chi(k_l) e^{-ik_l r_x} \rangle$$

Notice that there are two indices that we are summing over since we are making two (independent) measurements of the same value. Also notice that since we were taking the absolute value squared of $\Delta f(r_x)$ the second exponent is raised to a negative value (complex conjugate). After reorganizing the above equation we get

$$\sigma_x^2 = \langle \sum_{jl} \Delta\chi(k_j) \Delta\chi(k_l) e^{i(k_j - k_l) r_x} \rangle \tag{6.23}$$

Given that

$$\sigma_k = \frac{|\Delta\chi(k_j)|^2}{\text{sample \#}}$$

we know that all σ_k values are the same, but can say nothing about the sign of $\Delta\chi(k_j)$ except for the case where $\chi(k_j) = \chi(k_l)$, in which case we are sure to get out a positive number.

When all other combinations of $\chi(k_j) \neq \chi(k_l)$ are averaged, the average value should be 0. This is succinctly written in as the relation

$$\langle \Delta\chi(k_j)\Delta\chi(k_l)\rangle = \sigma_{k_j}^2 \delta_{jl}$$

Note that the variance is conventionally defined as $\sigma^2 = \frac{1}{N-1}\sum_i (x_i - \bar{x})^2$, but since the process of data analysis demands that $\langle \chi(k_j)\rangle = 0$, we know that $\sigma^2 = \frac{1}{N-1}\sum_i (x_i)^2$, which can also be written as $\sigma^2 = \langle x_i^2\rangle$. In the case where $\chi(k_j) = \chi(k_l)$, the term $e^{i(k_j - k_l)r_x}$ becomes unity and the summation across both indices, due to the delta function, also becomes unity for each data point in k-space. This means that the result $\langle \Delta\chi(k_j)\Delta\chi(k_l)\rangle = \sigma_{k_j}^2 \delta_{jl}$ will be multiplied by the number of data points in k-space, which is $N_{max} + 1$ since $n_j = \{0, 1, 2, ..., N_{max}\}$. Therefore

$$\sigma_r^2 = (N_{max} + 1)\sigma_k^2 \tag{6.24}$$

Equation 6.24 defines the functional relationship between the noise of a specific point in real-space as the noise from all the different points in k-space. Notice that each point in real-space should have the same error since we're summing over all of the same errors in k-space. This measurement of correlation is known as autocorrelation.

There is also generally a correlation between successive points r_x and $r_x + \Delta r$ (termed the crosscorrelation) that can be calculated similarly to equation 6.22 above

$$\langle \Delta f(r_x)\Delta f(r_x + \Delta r)\rangle = \sigma_k^2 \sum_j e^{i2k_j\Delta r} \tag{6.25}$$

Remembering that $k_j = k_{min} + n_j\Delta k_o$ and assuming that Δk_o is small compared to the variation in the EXAFS, we can approximate the above equation as an integral. The above statement essentially means that we are oversampling our EXAFS spectrum, which should be true for any well-measured EXAFS spectrum.

$$\sigma_k^2 \sum_j e^{i2k_j\Delta r} = \sigma_k^2 \sum_j e^{i2(k_{min} + n_j\Delta k_o)\Delta r}$$

Ignoring the σ_k^2 for now (we will put it back at the end) we have

$$\sum_j e^{i2(k_{min} + n_j\Delta k_o)\Delta r} = e^{i2k_{min}\Delta r} \sum_j e^{i2n_j\Delta k_o\Delta r} \approx e^{i2k_{min}\Delta r} \int_0^{N_{max}} e^{i2n_j\Delta k_o\Delta r}\, dn_j$$

Taking the integral of the exponential term we get

$$e^{i2k_{min}\Delta r} \int_0^{N_{max}} e^{i2n_j\Delta k_o\Delta r}\, dn_j = e^{i2k_{min}\Delta r} \cdot \frac{1}{i2\Delta k_o\Delta r}(e^{i2n_j\Delta k_o\Delta r})|_0^{N_{max}}$$

$$e^{i2k_{min}\Delta r} \cdot \frac{1}{i2\Delta k_o\Delta r}(e^{i2n_j\Delta k_o\Delta r})|_0^{N_{max}} = \frac{e^{i2k_{min}\Delta r}}{i2\Delta k_o\Delta r}(e^{i2N_{max}\Delta k_o\Delta r} - 1)$$

$$\frac{e^{i2k_{min}\Delta r}e^{i2N_{max}\Delta k_o\Delta r} - e^{i2k_{min}\Delta r}}{i2\Delta k_o\Delta r}$$

$$\frac{e^{i2(k_{min}+N_{max}\Delta k_o)\Delta r} - e^{i2k_{min}\Delta r}}{i2\Delta k_o \Delta r}$$

$$\frac{e^{i2k_{max}\Delta r} - e^{i2k_{min}\Delta r}}{i2\Delta k_o \Delta r} \tag{6.26}$$

Recall that we already defined $\delta k = k_{max} - k_{min}$, the range of k values over which the Fourier transform was made. Now let us define another term $\bar{k} = \frac{k_{max}+k_{min}}{2}$, which is the average k value over which we are Fourier transforming. Notice that with this clever change of variables we have

$$\bar{k} - \frac{\delta k}{2} = \frac{k_{max} + k_{min}}{2} - (\frac{k_{max} - k_{min}}{2}) = k_{min}$$
$$\bar{k} + \frac{\delta k}{2} = \frac{k_{max} + k_{min}}{2} + (\frac{k_{max} - k_{min}}{2}) = k_{max}$$

Now going back to equation 6.26 and inserting the above change of variables we get

$$\frac{e^{i2(\bar{k}+\frac{\delta k}{2})\Delta r} - e^{i2(\bar{k}-\frac{\delta k}{2})\Delta r}}{i2\Delta k_o \Delta r}$$

Collecting constants out in front, the equation becomes

$$\frac{e^{i2\bar{k}\Delta r}}{\Delta r \Delta k_o}(\frac{e^{i\delta k\Delta r} - e^{-i2\delta k\Delta r}}{i2}) \tag{6.27}$$

Recalling from calculus, the identity

$$sin(x) = \frac{e^{ix} - e^{-ix}}{2i} \tag{6.28}$$

we can substitute

$$\frac{e^{i\delta k\Delta r} - e^{-i2\delta k\Delta r}}{i2} = sin(\delta k \Delta r)$$

for the second half of equation 6.27 to give

$$\frac{e^{i2\bar{k}\Delta r}}{\Delta r \Delta k_o} sin(\delta k \Delta r)$$

Remembering to put the σ_k^2 term back we have the equation for the cross correlation between a data point in r-space and the point Δr in front of it.

$$\sigma_k^2 \frac{e^{i2\bar{k}\Delta r}}{\Delta r \Delta k_o} sin(\delta k \Delta r) \tag{6.29}$$

The equation for the cross correlation between a data point in r-space and the point Δr behind it can also be derived. The calculation is similar to the one above.

$$\sigma_k^2 \sum_j e^{-i2k_j\Delta r} = \sigma_k^2 \sum_j e^{-i2(k_{min}+n_j\Delta k_o)\Delta r}$$

Ignoring the σ_k^2 again gives

$$\sum_j e^{-i2(k_{min}+n_j\Delta k_o)\Delta r} = e^{-i2k_{min}\Delta r}\sum_j e^{-i2n_j\Delta k_o\Delta r} \approx e^{-i2k_{min}\Delta r}\int_0^{N_{max}} e^{-i2n_j\Delta k_o\Delta r}\,dn_j$$

Taking the integral of the exponential term we get

$$e^{-i2k_{min}\Delta r}\int_0^{N_{max}} e^{-i2n_j\Delta k_o\Delta r}\,dn_j = e^{-i2k_{min}\Delta r}\cdot\frac{1}{-i2\Delta k_o\Delta r}(e^{-i2n_j\Delta k_o\Delta r})|_0^{N_{max}}$$

$$e^{-i2k_{min}\Delta r}\cdot\frac{1}{-i2\Delta k_o\Delta r}(e^{-i2n_j\Delta k_o\Delta r})|_0^{N_{max}} = \frac{e^{-i2k_{min}\Delta r}}{-i2\Delta k_o\Delta r}(e^{-i2N_{max}\Delta k_o\Delta r}-1)$$

$$\frac{e^{-i2k_{min}\Delta r}e^{-i2N_{max}\Delta k_o\Delta r}-e^{-i2k_{min}\Delta r}}{-i2\Delta k_o\Delta r}$$

$$\frac{e^{-i2(k_{min}+N_{max}\Delta k_o)\Delta r}-e^{-i2k_{min}\Delta r}}{-i2\Delta k_o\Delta r}$$

$$\frac{e^{-i2k_{max}\Delta r}-e^{-i2k_{min}\Delta r}}{-i2\Delta k_o\Delta r}$$

Again, with the clever change of variables we have

$$\frac{e^{-i2(\bar{k}+\frac{\delta k}{2})\Delta r}-e^{-i2(\bar{k}-\frac{\delta k}{2})\Delta r}}{-i2\Delta k_o\Delta r}$$

After collecting constants in front, the equation becomes

$$\frac{e^{-i2\bar{k}\Delta r}}{\Delta r\Delta k_o}(\frac{e^{-i\delta k\Delta r}-e^{i2\delta k\Delta r}}{-i2})\frac{-1}{-1}$$

Above, we multiply the top and bottom of the equation by -1. Using the identity found in equation 6.28, the second half of the above equation becomes

$$\frac{e^{i\delta k\Delta r}-e^{-i2\delta k\Delta r}}{i2} = sin(\delta k\Delta r)$$

and the whole equation becomes

$$\frac{e^{-i2\bar{k}\Delta r}}{\Delta r\Delta k_o}sin(\delta k\Delta r)$$

Finally, we return the σ_k^2 term, giving the equation for the cross correlation between a data point in r-space and the point Δr behind it.

$$\sigma_k^2\frac{e^{-i2\bar{k}\Delta r}}{\Delta r\Delta k_o}sin(\delta k\Delta r) \tag{6.30}$$

Notice that all of the k values are independent and uncorrelated since they were measured that way. However, when transforming to r-space the r values may be correlated unless they are separated by the special value Δr_o. Δr_o is defined as the spacing between data points in r-space that is far enough apart so that the cross correlation between data points goes to zero. This is exactly what we would expect if those two points were independent and uncorrelated. To find the numeric value of Δr_o we check where equations 6.29 and 6.30 goes to zero. This will occur for both equations when

$$sin(\delta k \Delta r) = 0$$

and under these conditions

$$\Delta r = \Delta r_o$$

Therefore,

$$\Delta r_o = \frac{\pi}{\delta k} \tag{6.31}$$

Assuming that we begin fitting at an r-space value of r_{min} and fit to r_{max}, where both values coincide with an independent data point, then the fit range is defined as

$$\delta r = r_{max} - r_{min}$$

and the number of independent data points in the fit range is

$$n_{ind} = \frac{\delta r}{\Delta r_o} + 1 \tag{6.32}$$

since there is one more data point than there are intervals between data points. Substituting equation 6.31 into equation 6.32 and multiplying the whole equation by two, to account for the fact that each data point in r-space has both a real and imaginary component, gives Stern's Rule.

$$N_{ind} = \frac{2\delta r \delta k}{\pi} + 2 \tag{6.33}$$

EXAFS Data Fitting

Many computer programs are available to assist XAS practitioners in fitting EXAFS spectra. The most widely used programs are EXAFSPAK [137], WINXAS [138], FEFFIT [139], and IFEFFIT [140]. IFEFFIT is also used as the processing back-end to ATHENA [141] and SIXPACK [142], two excellent graphical user interface programs that simplify fitting of EXAFS spectra. EXAFS spectra shown in this study have been analyzed using the program suite RSXAP [78]. The procedure and exact mathematical algorithms used for EXAFS spectrum fitting are addressed in the documentation accompanying each computer program and will not be discussed here.

There are two distinct methods of EXAFS spectrum fitting. The model EXAFS spectrum can be fit to the collected experimental data in either r-space or k-space. Since these two representations of the collected EXAFS spectrum are Fourier transform pairs of each other, both contain the exact same amount of information. Therefore, either method of data fitting is valid. However, fitting a spectrum in k-space using the Fourier filtering method requires

conversion to r-space, filtering, and then reconverting to k-space before a goodness-of-fit parameter can be calculated. If such filtering methods are going to be applied, then fitting directly in r-space requires one less Fourier transformation. Each time a computer is used to calculate a Fourier transformation, small systematic errors can be introduced due to the round-off error and finite storage of computer memory. Therefore, in this case, fitting in r-space will reduce unneeded introduction of such systematic errors [136].

When fitting EXAFS spectra, certain sets of parameters tend to be correlated in the fits. This is a direct result of the functional form of the EXAFS equation (equation 6.16). r_j is correlated to E_o through the conversion of energy-space to k-space and the sine term in equation 6.16. N_j, σ_j, and $S_i(k)$ are also correlated to each other.

Until now we have only discussed EXAFS scattering paths that consists of single-scatter (two-legged) paths. However, for some systems, higher order paths play a significant role in the total EXAFS spectrum. For example, in the plutonyl moieties ($Pu^{V}O_2^{+}$ and $Pu^{VI}O_2^{2+}$) the three-legged scattering paths that involve the photoelectron leaving a plutonium atom, scattering off of an axial oxygen, scattering of of the other axial oxygen, and returning to the plutonium atom (Pu-O_{ax1}-O_{ax2}-Pu) play an important role because of the lensing effect caused by the central plutonium atom. FEFF is able to calculate these multiple-scattering paths given the correct input parameters. However, one must be careful when fitting parameters to such paths. Usually these multiple-scattering path parameters can easily be constrained to the single-scattering path parameters that make up the total scattering path. Furthermore, the term σ_j for the multiple-scattering path may be complicated depending on if atomic vibrations are symmetric or asymmetric. This problem has been addressed for the uranyl moiety ($U^{VI}O_2^{2+}$) and should be qualitatively similar for the plutonyl system [106].

The RSXAP program suite is able to estimate asymmetric errors for each of the fit parameters by inspecting the goodness-of-fit for the whole spectrum. The full error analysis procedure can be found in the publication by Booth and Hu [143], and the citations therein. Large error bars for the fitted parameters results from a goodness-of-fit surface that is fairly flat with respect to the fitted minimum and may indicate that a particular model is not properly representing the collected EXAFS spectra.

6.5 Micro-SXRF

6.5.1 Introduction

A major limiting constraint in the bulk XAS techniques described in sections 6.3 and 6.4 is the inability to spatially resolve heterogeneous samples that are smaller than the average XAS beam spot size (approximately 0.5 mm x 1.0 mm). This makes it difficult to explore environmental samples that may have heterogeneity in the sample at the micrometer range. To acquire a better understanding of processes occurring on the surface of such samples it becomes necessary to utilize smaller beam sizes while continuing to attain sufficient signal to noise in sample measurements.

Micro-synchrotron X-ray fluorescence (μ-SXRF) is primarily used to measure the spatial distribution of elements in a sample by rastering the sample in the plane that is perpendicular to the incoming micro-focused X-ray beam while collecting X-ray fluorescence spectra

for each rastered position. Because at sufficiently high incident photon energy all elements will begin to produce characteristic fluorescence lines, it is possible to make a complete two-dimensional elemental map of the sample through a combination of sample rastering and fluorescence measurements using a detector capable of energy discrimination (see subsection 6.2.5). The ultimate resolution of the elemental map is defined by the spot size of the X-ray microprobe beam. An excellent overview of the μ-SXRF technique is available from Sparks [144].

6.5.2 Theory

Micro-synchrotron X-ray fluorescence works on the principle that above a certain photon excitation energy, elements will emit fluorescence lines at discrete energies that are characteristic of the element. Figure 6.11 shows a log plot of the plutonium X-ray absorption cross-section as a function of photon energy. As long as the incident photon has sufficient energy to eject an electron from a bound state into the continuum and the transition is allowed, then the transition probability is defined by Fermi's Golden Rule (equation 6.15). The empty state that is left by the photoejected electron then has a probability of being filled by an electron from a higher energy level state, resulting in the emission of a characteristic fluorescence photon. Again, this probability is defined by the Golden Rule. The schematic for this process is similar to that shown in figure 6.15 for a fluorescence photon being emitted when a core hole is filled with an electron from a higher energy state.

μ-SXRF can be collected using either white light [145] or monochromatic light [146] from a synchrotron X-ray source. The benefit of using white light arises from the higher photon flux. However, μ-SXRF measurements using white light cause a large elastic scattering and Compton scattering background to be superimposed on top of the characteristic elemental fluorescence lines, resulting in poor signal to noise. Using monochromatic light allows the experimenter to restrict the elastic scattering peak and Compton peak to within a narrow range of energies. Proper selection of the incident photon energy can also tune these background peaks away from important fluorescence features [144, 146].

The X-ray absorption cross-section greatly decreases for lower Z elements as the photon energy increases, resulting in a decrease in characteristic fluorescence emission for lighter elements as the incident photon energy increases. It is fortuitous that trace environmental contaminants tend to consist of higher Z elements. Therefore, using a high-energy monochromatic beam also allows the experimenter to preferentially increase the detection sensitivity of the trace-level higher Z elements present in the sample.

6.5.3 Micro-SXRF Beamline Setup

The dedicated hard X-ray imaging station at SSRL beamline 2-3 is specifically set up to perform a wide range of experiments, including μ-SXRF and micro-XANES (μ-XANES). The setup is similar to that of bulk XAS beamlines (see subsection 6.2.4), with the addition of a Kirkpatrick-Baez (K-B) X-ray mirror focusing system [144] in place down stream of the monochromator. The result is a micro-focused X-ray beam spot size of approximately 2×2 μm^2 and photon flux densities that are comparable to the unfocused X-ray beams from the undulator source on beamline 11-2 at SSRL. The energy range of the beam line

optics at beamline 2-3 goes from 5-23 keV, allowing access to the Pu L_{III}-edge. Sample sizes are limited to approximately 2 cm^2 due to the limited range of the high-resolution sample positioner. Both a 4-element VORTEX Si-drift X-ray fluorescence detector and a single element Ge X-ray fluorescence detector are available for measuring fluorescence photons from the sample.

6.5.4 Data Analysis

The process of measuring a fluorescence spectra on an energy discriminating solid state detector, binning the appropriate fluorescence photons, and plotting the results is relatively mathematically simple. However, the process is quite computationally intensive, especially for large high-resolution sample scans. This procedure is an excellent example of data analysis that benefits from computer automated analysis and plotting. Elemental maps shown in this study have been analyzed using Sam's Microprobe Analysis Kit (SMAK) [147]. The procedure and exact mathematical algorithms used for elemental mapping are addressed in the documentation accompanying SMAK and will not be discussed here.

6.6 Micro-XANES

6.6.1 Introduction

μ-SXRF (section 6.5) allows the experimenter to map two-dimensional elemental associations of a sample, but does not offer any insight into the valance states of these elements. As has been previously stated (see chapter 5), plutonium chemistry is strongly dependent on the oxidation state of the plutonium atom in solution and on the mineral surface. The μ-XANES technique allows us to probe element-specific oxidation states in a similar way as bulk XANES measurements do (see section 6.3). However, μ-XANES gives the added benefit of viewing specific element speciation on samples that are heterogeneous on the micrometer scale. Bertsch *et al.* [148] first showed the feasibility of using such microprobe techniques on the actinides over 15 years ago, but only recently has there been a critical level of support at user-facility beamlines to make this type of measurement routine.

6.6.2 Theory

The fundamental processes that are responsible for the XANES phenomenon (see section 6.3) are the same as those in μ-XANES. In fact, the only instrumental difference between bulk XANES measurements and micro-XANES measurements is the spot size of the incident X-ray probe.

6.6.3 Micro-XANES Beamline Setup

The μ-XANES beamline setup is the same as that for μ-SXRF (section 6.5), except a short ion chamber is placed before the sample to measure I_o, for normalization purposes, and the incident photon energy is changed by rocking the double-crystal monochromator across

the absorption edge of the element of interest. During this process, fluorescence spectra are collected for each incident photon energy and the characteristic fluorescence photons from the element of interest are summed up to give the final X-ray absorption spectra. In this way, the method is the same as bulk XANES (see section 6.3), except with a very small beam size. The collected data can then be fit to standard spectra to yield the oxidation state identity of the element of interest in our sample. This process is repeated for each sample position as the sample is rastered in the plane normal to the incident X-ray beam. Obviously, doing such measurements for large samples can result in extended data collection times if too many XANES data points are collected. Therefore, less than ten energy data points are measured for each rastered sample position and measured energy values are selected to have the maximum absorption difference between different oxidation states.

6.6.4 Data Analysis

Just as the fundamental theory of μ-XANES is the same as for bulk XANES measurements, so is the data analysis procedure (see subsection 6.3.3). For data analysis, SMAK [147] is used to conduct the linear least-squares fitting of pure plutonium oxidation state standards onto the collected μ-XANES sample maps. Again, the procedure and exact mathematical algorithms used for μ-XANES fitting are addressed in the documentation accompanying SMAK and will not be discussed here.

Chapter 7

Experiments

7.1 Introduction

This section presents different aspects of the over-arching project to understand plutonium interactions on mineral surfaces and relates these aspects to each other to synthesize a larger picture. Separate sections have been or will be submitted for publication in peer-reviewed journals in a similar format as is presented here. Future work for the overall project is addressed in chapter 8.

7.2 Predetermining Acceptable EXAFS Spectral Noise in the Limit of Stochastic Noise

7.2.1 Overview

The effect of stochastic noise on extended X-ray absorption fine structure (EXAFS) data measurement, analysis, and fitting is discussed. Various aspects of this section have been published in the peer-reviewed journal "Journal of Physics: Conference Series" [149].

EXAFS measurements are used to probe a variety of experimental systems, but excel at elucidating local structure in samples that have slight disorder or no long-range crystalline order. Of special interest to us is the use of EXAFS in understanding the molecular-level binding structure and characteristics of actinides on the surface of environmental minerals and model mineral analogs [102]. In environmental systems the element of interest can be on the order of 10^{-7}% by weight of the total sample. Such samples would be impossible to measure using EXAFS techniques. It is therefore essential to increase the concentration of the element of interest while still preserving a sample's ability to represent environmental conditions. Under such low concentration limits it is expected that the collected data is count-rate, or stochastically, limited. This condition occurs as we approach the signal-to-noise (S/N) limit of the technique where the random noise of the measurement process dominates over possible systematic errors [150, 151]. When stochastic error is expected to dominate systematic error, it is possible to predict, with the use of computer simulations, the ability of model fits to tolerate a certain level of stochastic noise. In the case when

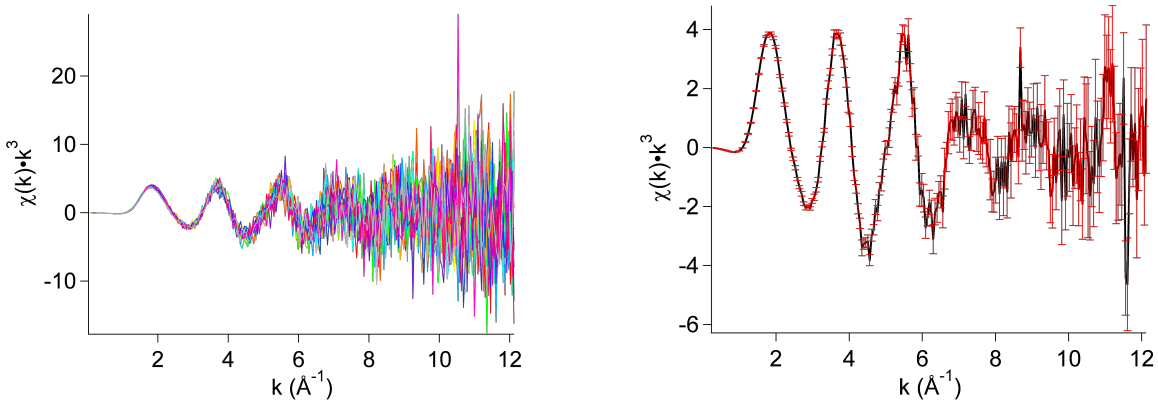

(a) Raw data (b) Average and standard deviation

Figure 7.1: $k^3\chi(k)$ verses k plots of (a) 15 experimental scans of plutonium sorbed on pyrolusite. (b) The average and standard deviation of the mean for the 15 scans. Red error bars show the error at 1σ.

systematic errors dominate, other methods of error analysis and confidence-level estimation are available [143].

Stochastic noise reduces the ability to uniquely fit a calculated model to measured EXAFS data. Such noise can be reduced by common methods that increase the signal-to-noise ratio. Figure 7.1 (a) is a plot of 15 scans of k-space EXAFS data measured out to a k value of 12 Å^{-1}. Note the high noise level at higher k value. Figure 7.1 (b) is a plot of the average of the 15 files (black) with error bars (red) representing the standard deviation of the mean and shows the increase in signal-to-noise ratio by repeating scans. Other methods of increasing the signal-to-noise ratio include increasing the concentration of the element of interest in the sample, and increasing the sample and X-ray beam size; however, these methods are not always practical. Therefore, predetermined, quantitative knowledge of the level of acceptable stochastic noise when fitting for a particular model system is essential in maximizing the chances of a successful EXAFS experiment and minimizing wasted beamtime. This section outlines a method to estimate, through computer simulation, the acceptable level of stochastic noise in EXAFS spectra that still allows a successful test of a proposed model compound.

7.2.2 Simulation Method

Here, we outline a technique for determining the number of EXAFS scans necessary to test the relevance of a given structural model. Appropriate stochastic noise levels are determined for each point in k-space by collecting data on a real system. These noise levels are then applied to EXAFS simulations using a test model. In this way, all significant systematic error sources are eliminated in the simulated data. The structural model is then fit to the simulated data, decreasing the noise and increasing the k-range of the fit until the veracity of the model passes an F-test [152, 153].

The simulations begin with a theoretical calculation [129] of an EXAFS spectrum from a

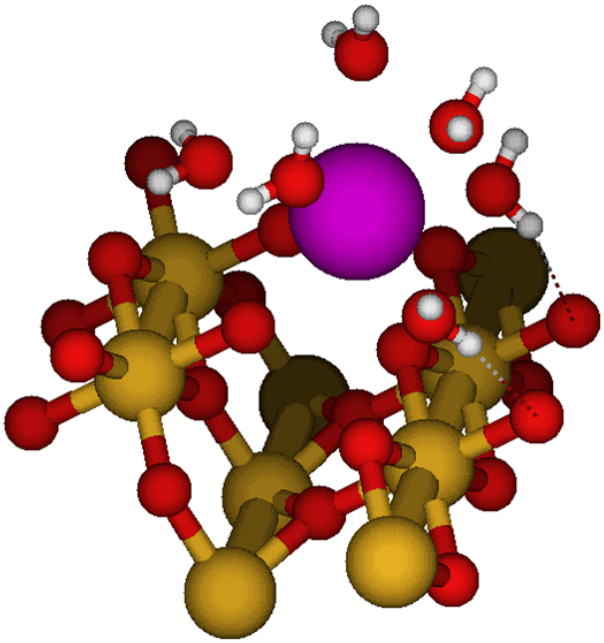

Figure 7.2: Molecular model of plutonium (magenta) sorbed on the surface of pyrolusite with associated first hydration shell of waters. Manganese = brown, oxygen = red, hydrogen = gray. Metrics used for the simulation are found in table 7.1.

path	N	R(Å)	σ^2(Å^2)
Pu−O_1	9	2.3800	0.0049
Pu−O_2	2	3.6912	0.0081
Pu−Mn	4	3.8086	0.0081
Pu−O_3	2	3.9943	0.0081

Table 7.1: Proposed EXAFS model for plutonium sorbed at the mineral-water interface of pyrolusite in solution. Note the subscripts next to O in the paths column are indices for different plutonium-oxygen paths.

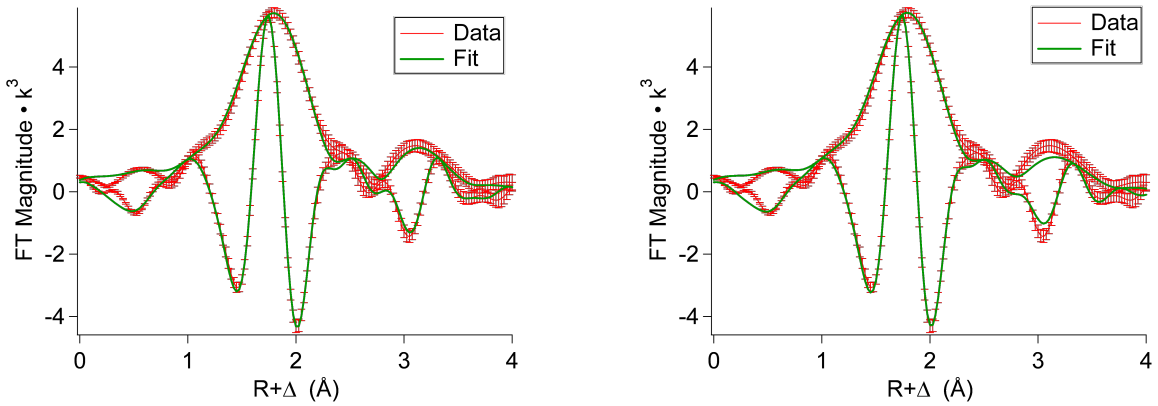

(a) Pu-Mn + Pu-O paths (b) Pu-O paths

Figure 7.3: r-space fits to simulated data using (a) both Pu-Mn and Pu-O paths and (b) only Pu-O paths.

proposed structural model (figure 7.2 and table 7.1). Randomly generated (Gaussian) noise with a standard deviation characteristic of the noise previously extracted from the experimental data is applied point-by-point in k-space using pseudo-random numbers generated by the Mersenne Twister algorithm [154]. This simulation is implemented in the Python programming language [155] and the code listing is available in section F.4. The stochastic noise in each simulated spectrum then corresponds to that expected for a single experimental scan within the original experimental conditions on the beamline. Note that here we have created a method of simulating a 15 minute experimental scan in a fraction of a second. This allows us to explore both different fitting parameters and fit models on a large set of simulated data without resorting to collecting a large amount of real data on the beamline.

Following the generation of simulated data, two different chemically-feasible model systems are fit to the data using RSFIT (part of the RSXAP package [78]). In the example case given here one model with both manganese and oxygen scattering paths (figure 7.3 a), and one with only oxygen scattering paths (figure 7.3 b) are chosen to be tested against each other. Note that both fits appear reasonable by eye, although the fit shown in figure 7.3 (a) does appear to be better. The question then becomes, "Is the better fit justified by the increase in parameters being fit"? The F-Test is the quantitative method of answering this question. Obviously, the chemically feasible systems will change depending on the exact molecular system being studied. For this model, fits were conducted varying the maximum k of the data in the fit ($k_{\max} = 10 \rightarrow 18$ Å^{-1}) and the number of simulated EXAFS scans (20-2500 files). No fits were extended below a $k_{\max}$ of 10 Å^{-1} because the number of degrees of freedom would be less than the number of parameters being fit [136]. For each model system an R-factor is calculated by RSFIT. The R-factor for a fit is commonly defined as:

$$R = \sqrt{\frac{\sum_i (y_{i(obs)} - y_{i(model)})^2}{\sum_i y_{i(obs)}^2}} \cdot 100 \tag{7.1}$$

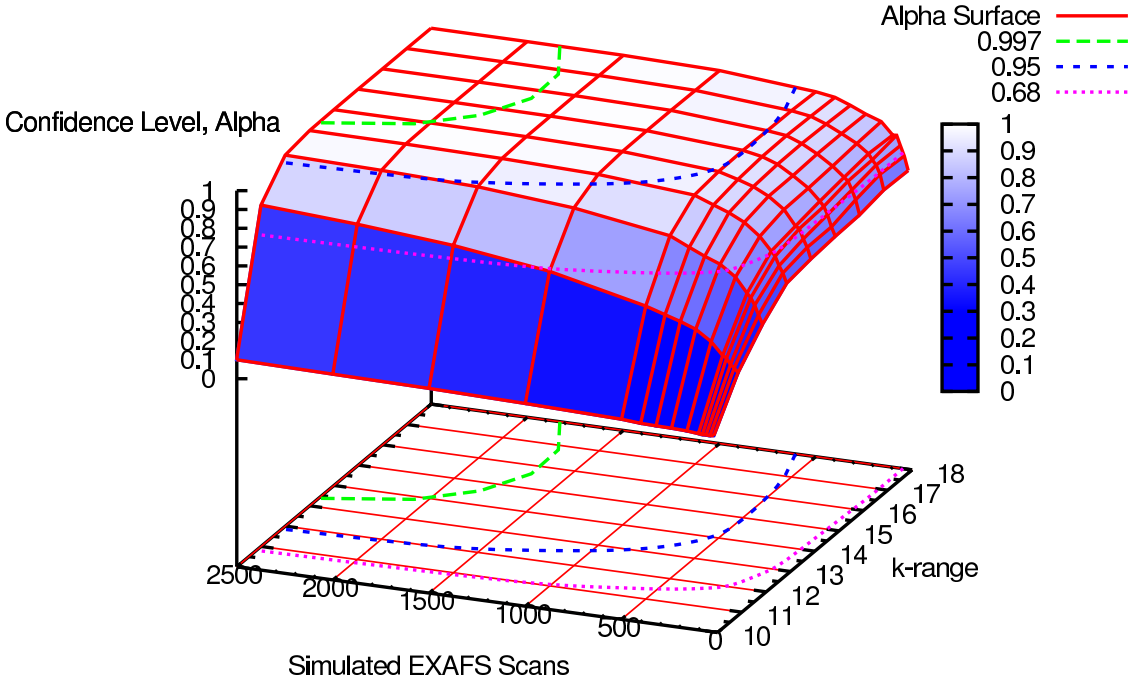

Figure 7.4: Surface plot of the α surface as a function of simulated EXAFS scans and fit k-range in Å^{-1}.

In RSFIT the R-factor is exactly defined as:

$$R = \sqrt{\frac{\sum_i (\Delta(k^n \chi^R(r_i)))^2 + \sum_i (\Delta(k^n \chi^I(r_i)))^2}{\sum_i (k^n \chi_D^R(r_i))^2 + \sum_i (k^n \chi_D^I(r_i))^2}} \tag{7.2}$$

where $\Delta(k^n\chi(r))$ is the difference between the data and the model that is being fit, the R and I superscripts refer to the real and imaginary parts of the Fourier transform, and the D subscript revers to the measured data. It is worth noting that the R-factor calculated by RSFIT compares the data and the fit in r-space. This is equivalent to comparing them in k-space as long as one compares both the real and imaginary parts independently.

Once R-factors are calculated for each fit, a confidence level, α, that the fit including the manganese scattering path is statistically better than the fit without it, is obtained using a modified F-Test. The α parameter of two fits is defined by the equation:

$$\alpha = P(\Re > \Re_{b,n-m,\alpha}) = P(\mathbf{F} > \mathbf{F}_{b,n-m,\alpha}) = I - I_x \left[\frac{n-m}{2}, \frac{b}{2}\right] \tag{7.3}$$

where b is the difference in the number of fitting parameters, $n-m$ is the number of degrees of freedom in the better fit, I_x is the incomplete beta function, and $x = (R_o/R_1)^2$ [152, 153, 156].

The α values are calculated 1000 times for each combination of simulated files and $k_{\max}$. The average is then plotted as a function of the two variables, forming a confidence-level surface.

Figure 7.4 shows a 3D plot of the average confidence level, α, as a function of both the measured k-range and number of simulated EXAFS scans. The plot represents the

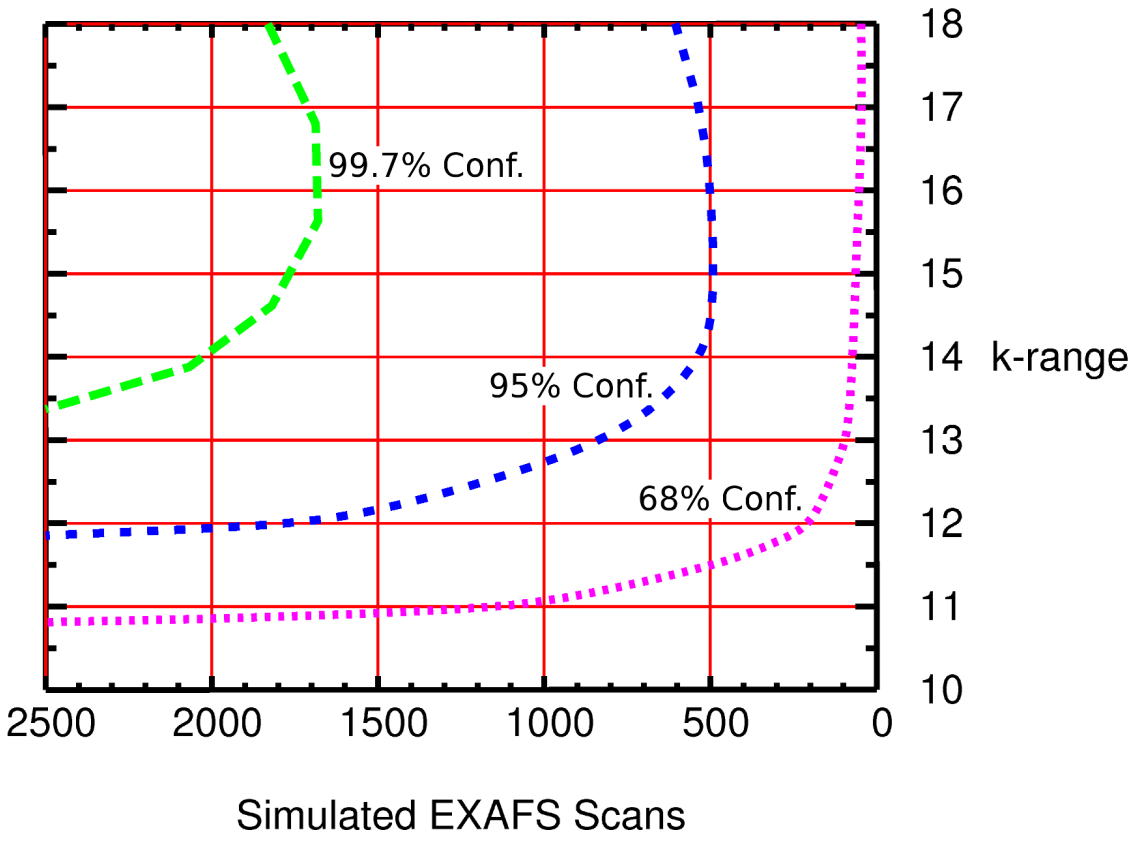

Figure 7.5: Contour plot of the α surface as a function of simulated EXAFS scans and fit k-range in Å^{-1}.

accumulation of F-Tests on $\sim$ 130000 individual simulations. Lines of constant confidence are drawn at the 68%, 95%, and 99.7% level by fitting a B-spline through the surface.

7.2.3 Discussion

Manual fitting of various parts of the α surface was conducted before automatic calculations were started to ensure that fits were likely to converge. Even in fits that had not completely converged the α metric had typically converged to better than 0.1%. Large numbers of calculations were conducted to ensure that our mean estimate for α was precise. In any case, since individual monitoring of each of the $\sim$ 130000 fits would have been exceedingly difficult, the large number of simulations serves to reduce the weight of the occasionally un-converged fit.

According to the contour plot shown in figure 7.5, under our initial experimental conditions, assuming only stochastic noise, we would have had to collect over 500 experimental scans (about 125 hours) out to a $k_{\max}$ of greater than 14.5 Å^{-1} before we would expect to be 95% confident that our fitting model containing the manganese scattering path represented our data statistically better than the fitting model with only oxygen scattering paths. Various other effects that could have limited our $k_{\max}$ would have resulted in the need to take even more experimental scans. However, within the limit of stochastic error, the effect of in-

creasing experimental scans is simply to increase the S/N ratio. Another option to increase the S/N ratio is to increase the concentration of the element of interest. For example, a two-order of magnitude increase in the element of interest will increase S/N by a factor of 10, assuming counting statistics. In other words, a 95% confidence level could be reached after 50 experimental scans, or about 13 hours.

The contour plot in figure 7.5 also shows an extrema in the contour lines at a point between $k_{\max} = 14.5$ Å^{-1} and 16.5 Å^{-1} depending on the confidence level. As the fit is increased to higher $k_{\max}$ values, α degrades slightly, showing that more simulated EXAFS scans are needed to keep the same confidence level at higher $k_{\max}$. This degradation is likely due to the lower S/N ratio at large $k_{\max}$ and is the reason why most EXAFS practitioners collect for longer times at high k values. However, as the contour plot shows for this particular model, a better use of beamtime would be to collect data using a shorter k-range than attempt to measure data out to a large $k_{\max}$. Furthermore, figure 7.5 shows that under a certain $k_{\max}$, in the example case about 10.75 Å^{-1}, no amount of signal-to-noise increase will allow us to differentiate the two test models above a confidence level of 68% on average.

All of the above discussed metrics are of utmost importance when planning to use limited synchrotron X-ray beamtime wisely. It is important to reiterate that the calculated α surface in figure 7.4 is only applicable to the particular model shown in figure 7.2 and table 7.1. Therefore, this simulation must be recalculated when the system being studied deviates greatly from the one shown here. Furthermore, this procedure only takes into account stochastic noise; consequently any confidence levels calculated should be viewed as upper limits to the confidence levels in systems that also contain a significant amount of systematic noise.

7.3 Synchrotron X-ray Beam-Induced Chemistry on Plutonium Sorbed on Various Substrates

7.3.1 Overview

The use of synchrotron-radiation based X-ray absorption spectroscopy as an *in-situ* method of elucidating the oxidation state and local structure of plutonium sorbed to the surface of various substrates is an established method and has proven to be indispensable in the field of environmental actinide chemistry and heterogeneous actinide separations and sensing [102]. Very often such molecular-level atom-specific spectroscopy yields the only kind of information that can be measured from such non-periodic low-concentration samples.

However, some experiments involving X-ray spectroscopy on samples of plutonium(VI) sorbed onto different substrates under conditions of varying pH, plutonium concentration, and temperature have shown that certain data collection parameters may result in synchrotron X-ray beam-induced chemistry to occur in plutonium. These types of X-ray beam-induced effects are most likely a result of radiolytic reactions occurring between the X-ray photon used to probe the sample and the water content in the sample itself. Such reactions have long been known to affect the day-to-day operation of water cooled nuclear reactors [157] and have more recently become a concern for protein crystallography [158, 159, 160]. Certain biological fields have even developed methods to directly measure native protein folding struc-

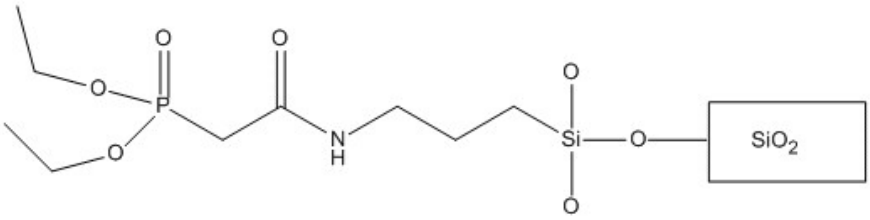

Figure 7.6: Chemical structure of acetamide phosphonate (Ac-Phos) silane grafted to the mesoporous silica substrate SBA-15, represented as a box labeled SiO_2.

ture in solution using such synchrotron X-ray generated radiolysis products [161, 162, 163]. For XAS measurements, beam-induced redox reactions are often unwanted and complicate data measurement when the focus of the work is to elucidate the exact oxidation state of plutonium in the measured sample. The work presented here is intended to call attention to the possibility of unwanted X-ray beam-induced chemistry when working with highly redox sensitive elements, especially plutonium, and suggests ways in which to minimize or otherwise mitigate unwanted chemistry from occurring during sample measurement.

7.3.2 Materials and Methods

Pure goethite (α-FeOOH) was acquired from Alfa Aesar and used as received. The synthesis and characterization of manganese-substituted goethite has been covered in section 4.3. Two-dimensional hexagonally ordered SBA-15 type mesoporous silica was synthesized by standard procedures [164] and characterized with low-angle powder X-ray diffraction (XRD), transmission electron microscopy (TEM), and N_2 adsorption isotherms. The unmodified SBA-15 has a Brunauer-Emmett-Teller (BET) surface area of 727 $\pm$ 1 m^2/g, a pore volume of 0.93 $\pm$ 0.05 cm^3/g, and an average pore size of 7.9 $\pm$ 0.2 nm. The acetamide phosphonate (Ac-Phos) silane, shown in figure 7.6, was synthesized by the amidation reaction inspired by [165] between (3-aminopropyl)triethoxysilane and diethylphosphonoacetic acid, activated beforehand by 1,1'-carbonyldiimidazole. Covalent grafting of silane molecules onto SBA-15 was achieved by a method adapted from Fryxell [166], which was optimized for the SBA-15 substrate. The SBA-15 was hydrated (0.24 mL/g) prior to the addition of the ligand mixture, then the grafting proceeded in refluxing toluene. After completion of the reaction, side products were removed by distillation and the product obtained after filtration was washed and air-dried to constant weight. The functionalized SBA-15 was characterized by attenuated total reflection (ATR) Fourier Transform Infrared (FTIR) spectroscopy, Raman spectroscopy, ^{13}C cross-polarization magic angle spinning nuclear magnetic resonance (CP-MAS-NMR), and ^{29}Si MAS-NMR, which confirmed that the ligand was covalently grafted to the SBA-15. The ^{13}C spectrum also revealed the possibility of the presence of a side product or impurity. Work on the Ac-Phos system is currently being conducted in our group by Tashi Parsons-Moss. More information about this system will be included in her thesis.

The preparation of Pu(VI) stock solution is covered in appendix C.5. XAS sample preparation for goethite has been previously described [37]. XAS sample preparation for manganese-substituted goethite is described below in subsection 7.4.2. XAS sample prepa-

ration for Ac-Phos functionalized SBA-15 is as follows. 0.0963 ± 0.0001 g of Ac-Phos functionalized SBA-15 was mixed with 10.0 ± 0.1 mL of approximately 0.1 M $NaClO_4$ solution in a polypropylene tube. The pH was then adjusted to 4.4. Two 105 μL aliquots of ^{239}Pu stock solution in 10 M $HClO_4$ were added, giving a total addition of 45 ± 3 μCi (approximately 0.7 mg of ^{239}Pu). After each aliquot was added, the pH of the solution was equilibrated with small amounts of NaOH and $HClO_4$. The solution was placed on a rocker and allowed to equilibrate at a pH environment between 4.3 and 4.6 for the four days. A 250 μL aliquot of the solution was then removed and filtered through a 30,000 MWCO regenerated cellulose centrifuge filter before triplicate assay via liquid scintillation counting (LSC). The LSC analysis demonstrated that over 99% of the Pu sorbed to the solid phase. The solid was loaded as a wet paste into a Kapton tube (11 mm × 1.8 mm diameter), and packed by centrifugation. The tube was sealed with epoxy and triply contained for transport to the Stanford Synchrotron Radiation Lightsource (SSRL) for XAS analysis.

Plutonium XAS sample spectra were collected at either 20, 30, 50, or 300 K, using a specially-engineered liquid helium cryostat (Janis). The vertical aperture of the beam in all cases was held at 0.5 mm. Plutonium L_{III}-edge XANES spectra were collected at SSRL on beamline 11-2 or at the APS on beamline 12M at BESSRC-CAT using a 30% detuned Si(220) ϕ-0° double-crystal monochromator. Data were collected in fluorescence mode using a 32-element germanium detector. A dead time correction was applied to the spectra. Energy calibration was performed in transmission mode by measuring the plutonium L_{III}-edge of a $^{242}PuO_2$ powder reference or the K-edge of a zirconium metal foil reference between scans.

Plutonium XANES spectra were energy calibrated by setting the first inflection point of the L_{III}-edge of a PuO_2 reference sample to be 18062.3 eV [123] or the first inflection point of the Zr K-edge reference sample to be 17998.0 eV [80]. Plutonium oxidation state percentages were acquired through least-squares fitting of normalized Pu(IV), Pu(V), and Pu(VI) standard XANES spectra [103]. Fit errors are estimated through inversion of the covariance matrix.

7.3.3 Evidence of X-ray Beam-Induced Chemistry on Pu(VI)

Normalized XANES plots of Pu(VI) sorbed on the mineral surface goethite in a mineral solution of pH 8.0 at 300 K are shown in figure 7.7. The sample is exposed to the X-ray beam during the duration of all the sample scans. Therefore, as the scan number increases the sample is exposed to the X-ray beam for a longer period of time. The overlaid set of spectra clearly show the loss of the characteristic XANES plutonyl shoulder at approximately 18090 eV, and an increase in the white-line peak of the plutonium edge at approximately 18065 eV, both indicative of reduction from a higher plutonium oxidation state to Pu(IV) (see subsection 5.4.2).

Figure 7.8 shows a plot of the least-squares fit of the 12 XANES spectra (shown in figure 7.7) as a function of time. For these types of plots the beginning of the initial scan is arbitrarily set to a beam exposure time of zero and the beam exposure time for the remaining scans are defined as the beginning of each particular scan. The relatively large error bars are a result of estimating the error bars through inversion of the covariance matrix and the similar spectral shape of Pu(V) and Pu(VI). The plot shows the monotonic increase of Pu(IV) in the sample. Furthermore, it appears that the initial effect of the X-ray beam on

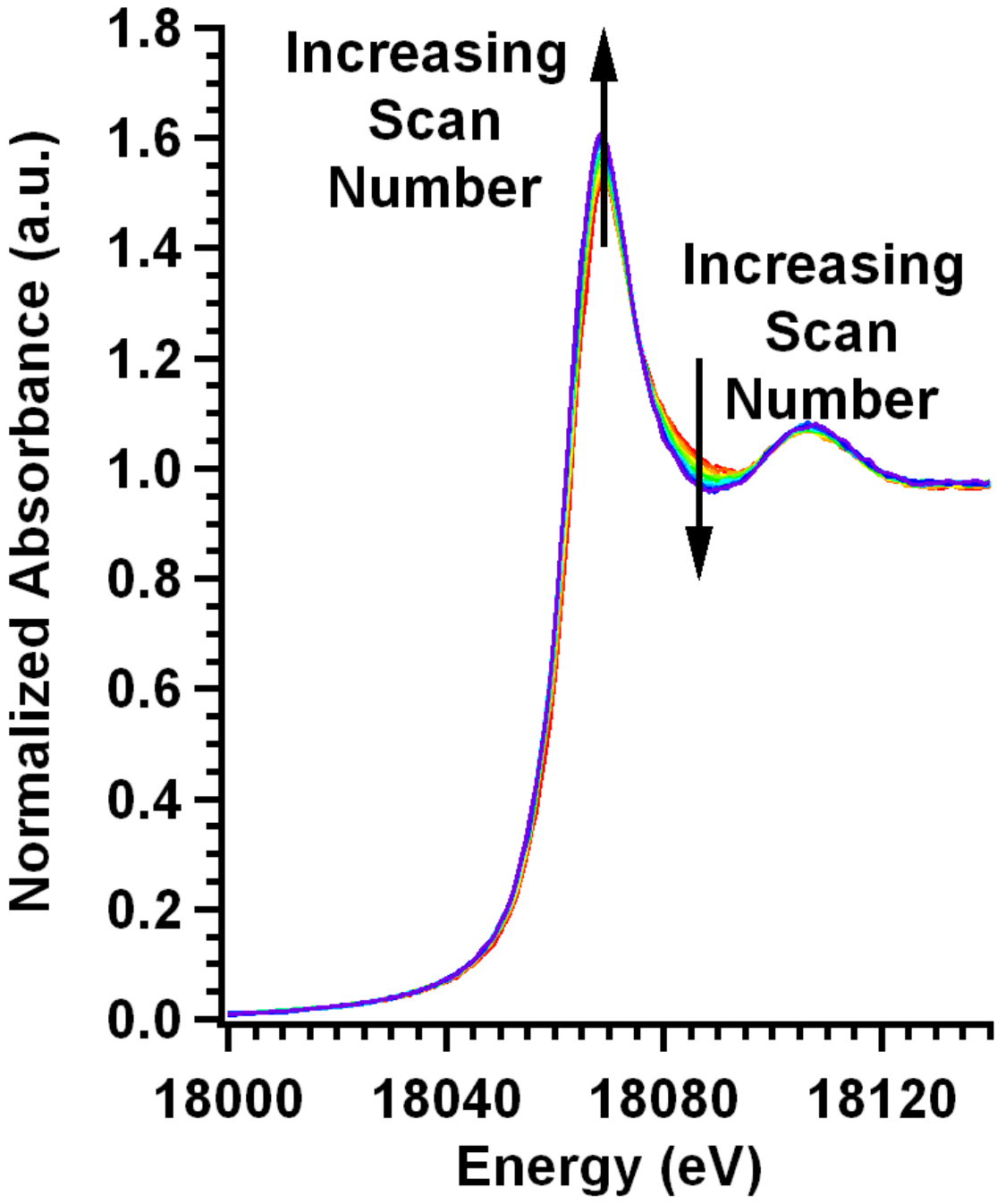

Figure 7.7: L_{III}-edge XANES spectra of plutonium on goethite in a pH 8.0 mineral solution at 300 K. 12 scans at approximately 40 minutes per scan are overlaid and show the effect of beam-induced reduction on the XANES spectra of plutonium [37].

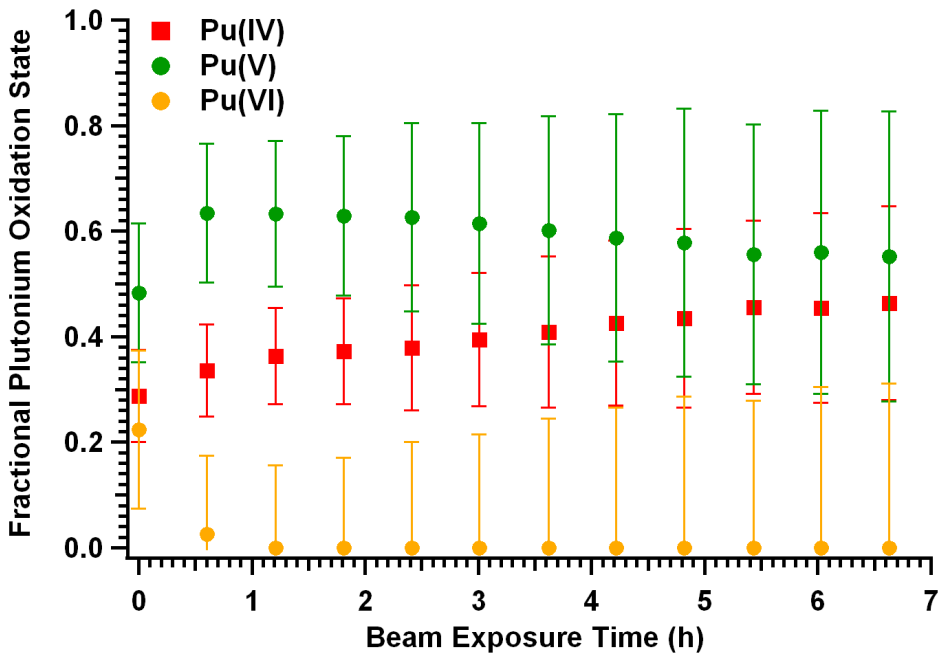

Figure 7.8: Least-squares fit of L_{III}-edge XANES spectra of plutonium on goethite in a pH 8.0 mineral solution at 300 K (shown in figure 7.7) plotted against the time exposed to the X-ray beam.

the sample at 300 K results in the slight reduction of Pu(VI) to Pu(V). This quantitative information is much more difficult to discern from simply inspecting a plot of the overlaid spectra, as in figure 7.7.

Figure 7.9 shows the normalized XANES plot of Pu(VI) sorbed on the surface of goethite in a mineral solution of pH 7.5 at 20 K. The set of spectra clearly show the characteristic XANES plutonyl shoulder with little change in the spectra for each successive scan (see subsection 5.4.2). Upon closer inspection there does appear to be a slight shift in the position of the white-line. Again, this effect is more clearly shown in the least-squares fits of the individual spectra (figure 7.10). Here the initial reduction of Pu(VI) to Pu(V) appears to proceed slower than in the sample measured at 300 K. More importantly, the temperature reduction has suppressed the X-ray beam-induced reduction of plutonium in the sample to Pu(IV). Figure 7.10 shows that the component of Pu(IV) in the sample appears to be less than 2 % over a measurement period of 9 hours.

Figure 7.12 is a plot of the least-squares fit of 16 XANES spectra (shown in figure 7.11) of plutonium sorbed on the surface of 0.5 % manganese-substituted goethite (see section 4.3) as a function of time. The smaller error bars are a result of an increase in data quality for these measurements. Manganese-substituted goethite has been shown to induce the reduction of Pu(VI) to Pu(IV), possibly due to the availability of Mn(III) or Mn(II) in the manganese-substituted goethite [68] (also see section 4.3 and 7.4). The plot shows very little fluctuation in the plutonium oxidation state as a function of beam exposure time, suggesting that no X-ray beam-induced chemistry is occurring in these types of samples at cryogenic temperatures.

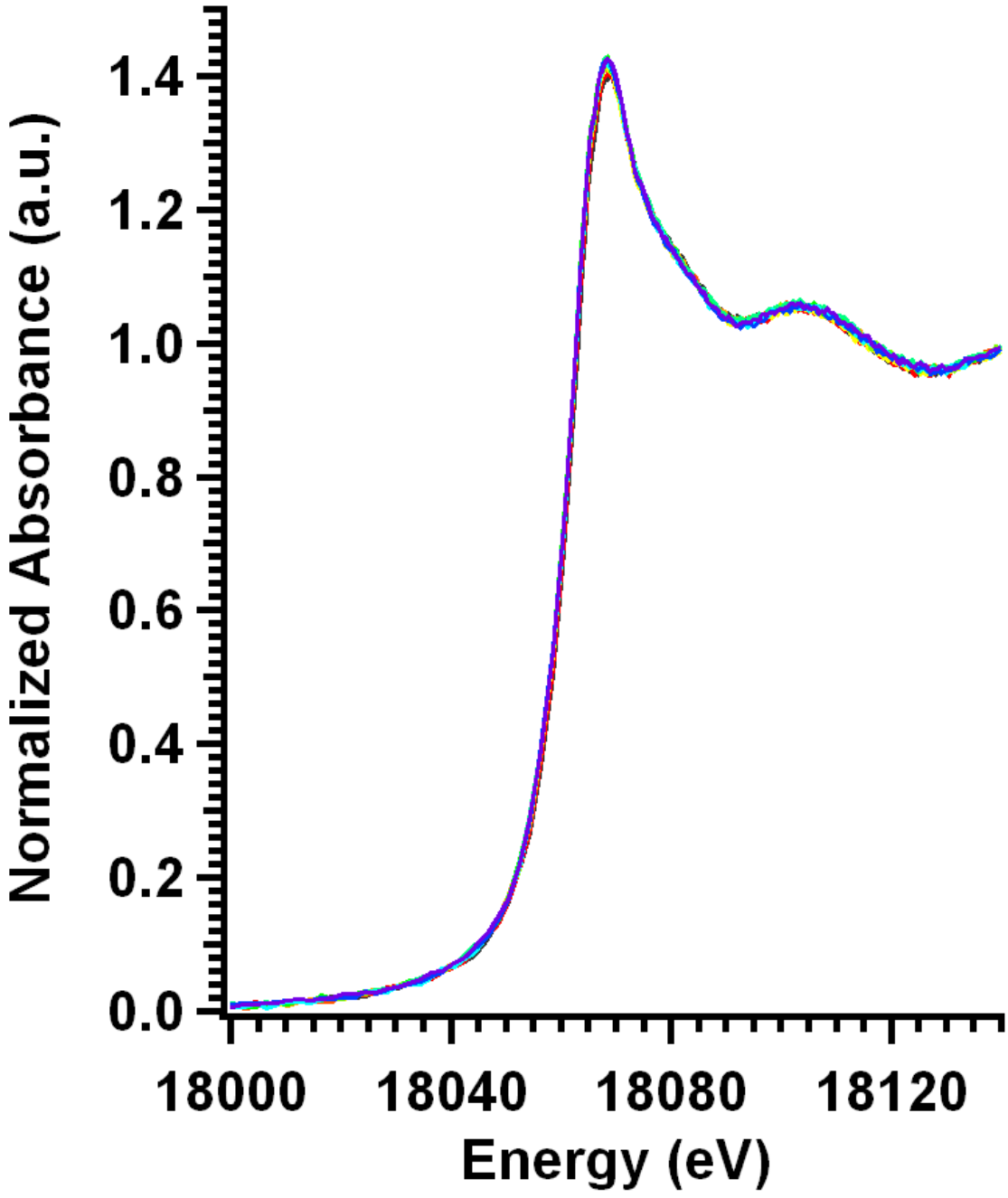

Figure 7.9: L_{III}-edge XANES spectra of plutonium on goethite in a pH 7.5 mineral solution at 20 K. 11 scans at approximately 40 minutes per scan show no beam-induced reduction occurring at low temperature [37].

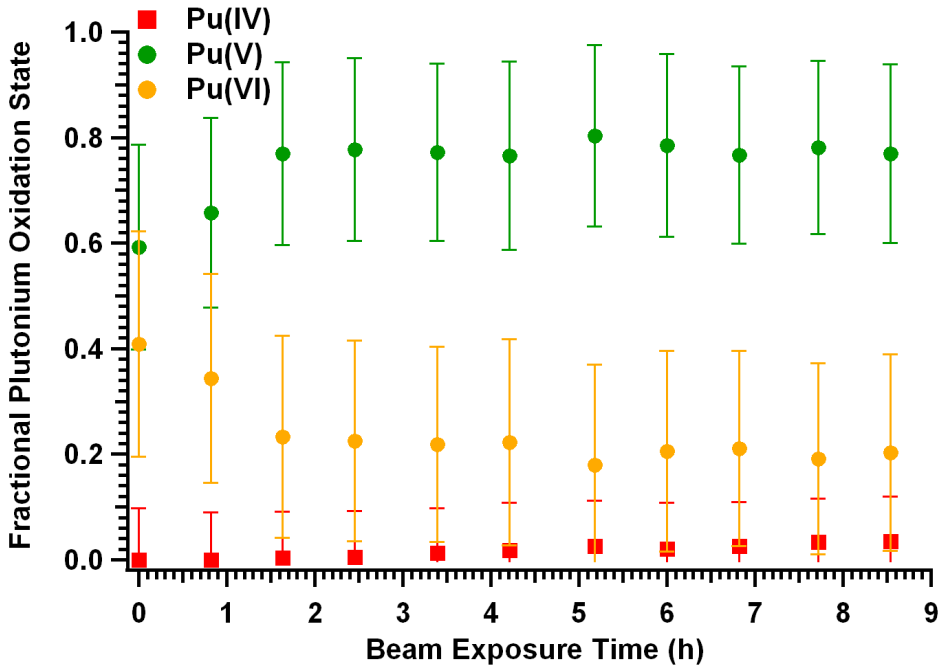

Figure 7.10: Least-squares fit of L_{III}-edge XANES spectra of plutonium on goethite in a pH 7.5 mineral solution at 20 K (shown in figure 7.9) plotted against the time exposed to the X-ray beam.

A normalized XANES plot of Pu(VI) sorbed on the surface of Ac-Phos bound to a mesoporous silica substrate (SBA-15) in a pH 4.4 solution is shown in figure 7.13. The set of spectra show a shift in the absorption edge position towards lower energy with each successive scan. There is also an accompanying reduction in the height of the white-line as exposure to the X-ray beam increases. These two effects indicate reduction of the plutonium in the sample from Pu(VI) to Pu(V). The sharp peak at the plutonyl shoulder of the XANES spectrum is an artifact from the monochromator crystal set used in this experiment and does not affect the fits.

Figure 7.14 shows the successive least-squares fits of the individual XANES spectra plotted in figure 7.13. Despite the measurements taking place under cryogenic conditions X-ray beam-induced reduction is still occurring for this sample. The reduction of Pu(VI) is accompanied by the expected fractional increase of Pu(V) and a slight but significant increase in Pu(IV) in the sample as it continues to be exposed to the X-ray beam.

After collection of the final data point in figure 7.14 the sample was warmed to 300 K and allowed to rest for approximately 42 hours. The sample was then exposed to the beam again and 5 additional XANES spectra were collected at 300 K (spectra not shown). Figure 7.15 shows the least-squares fits of these spectra as a function of the time this sample was exposed to the X-ray beam a second time. The plot shows a decrease in Pu(VI), an increase in Pu(V), and most importantly, a steady increase in Pu(IV) as a function of time.

A composite plot of figures 7.14 and 7.15 is shown in figure 7.16. It is important to note the split in the x-axis during which time the sample was held at 300 K with no exposure to the X-ray beam. The left side of the plot shows data collected at 30 K, while the right

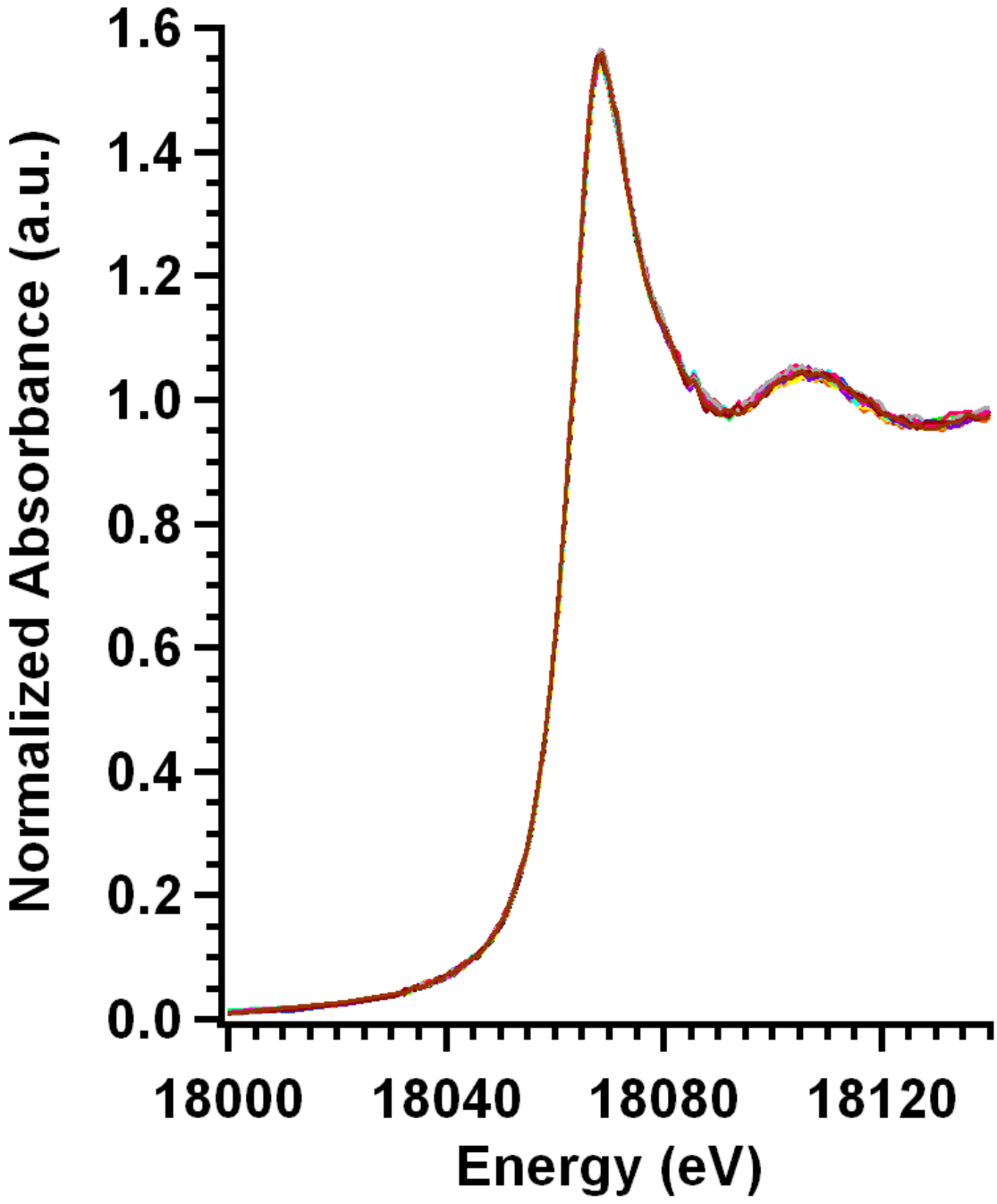

Figure 7.11: L_{III}-edge XANES spectra of plutonium on 0.5 % manganese-substituted goethite in a pH 7.63 mineral solution at 50 K. 16 scans at approximately 25 minutes per scan are overlaid and show no beam-induced reduction occurring at low temperature.

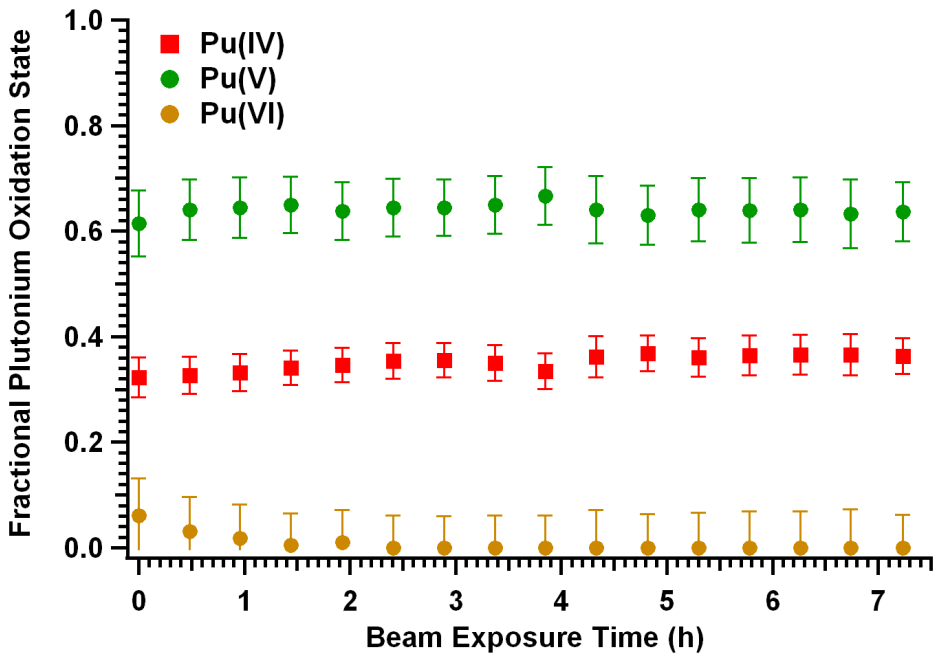

Figure 7.12: Least-squares fit of XANES spectra of plutonium on 0.5 % manganese-substituted goethite in a pH 7.63 mineral solution at 50 K (shown in figure 7.11) plotted against the time exposed to the X-ray beam.

side of the plot shows data collected at 300 K. The sample was removed from the beam after the scan taken at approximately 8 hours of X-ray beam exposure and the sample was warmed to 300 K. Approximately 50 hours after the initial exposure to the X-ray beam and approximately 42 hours after warming the sample to 300 K, 5 additional XANES scans were measured over the period of approximately half an hour.

7.3.4 Discussion and Conclusions

The field of radiation chemistry and the topic of ionizing radiation interaction with aqueous solution is very mature and has been the focus of various books [167, 168] in addition to hundreds of research papers [169, 170, 171, 172, 173]. However, experiments in this field have historically been concentrated on pure aqueous solutions as opposed to interfacial systems, such as the interface between aqueous solution and an organic/inorganic substrate, as is found in the measured XAS samples outlined in subsection 7.3.2.

Radiation chemistry processes occurring at a solid/liquid interface are expected to be different from what is seen in bulk liquids and should be considered explicitly. Specifically, diffusion properties and the reactivity of radiolytically produced species may be very different in the presence of a solid/liquid interface [174]. However, the field of interfacial radiation chemistry is still fairly young. Therefore, we will need to leverage knowledge from bulk aqueous radiolysis experiments in an effort to understand the specific beam-induced chemistry occurring in our samples.

When a water molecule is ionized by some form of ionizing radiation, such as gamma-rays,

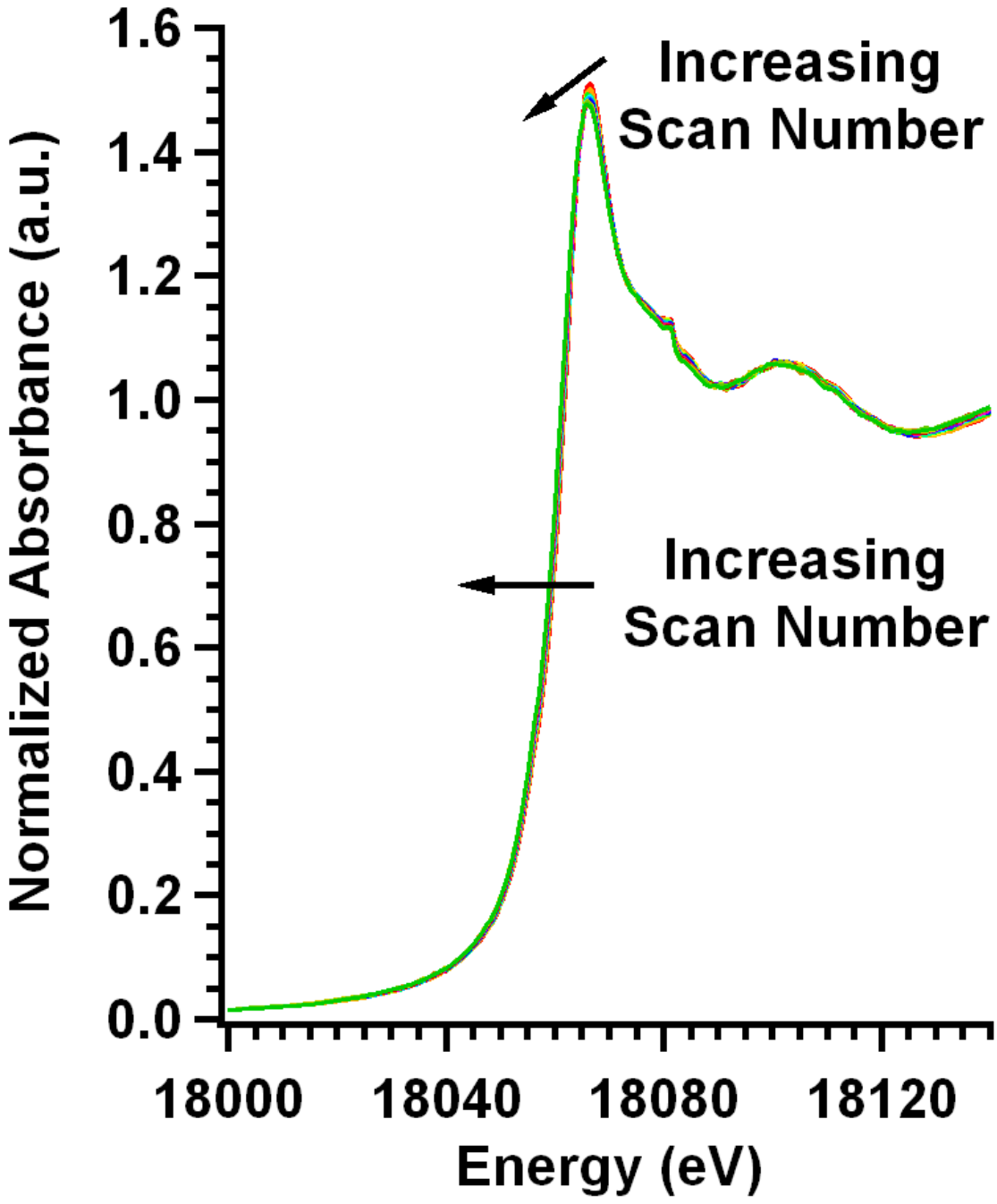

Figure 7.13: XANES spectra of plutonium on Ac-Phos (see figure 7.6) bound to a mesoporous silica substrate in a pH 4.4 solution at 30 K. 20 scans at approximately 25 minutes per scan are overlaid and show the effect of beam-induced reduction on the L_{III}-edge XANES spectra of plutonium.

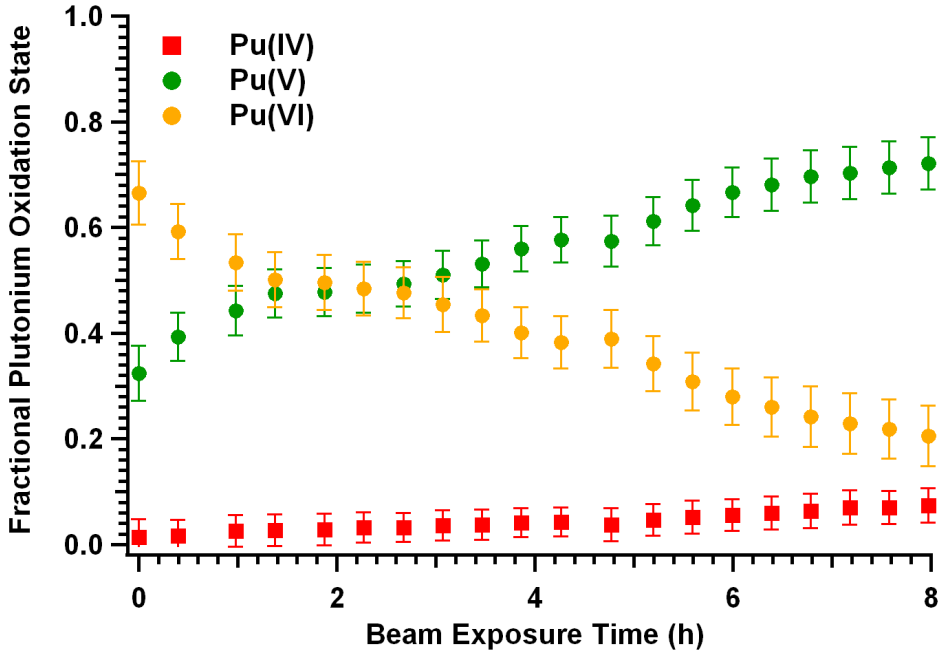

Figure 7.14: Least-squares fit of XANES spectra of plutonium on Ac-Phos bound to a mesoporous silica substrate in a pH 4.4 solution at 30 K (shown in figure 7.13) plotted against the time exposed to the X-ray beam.

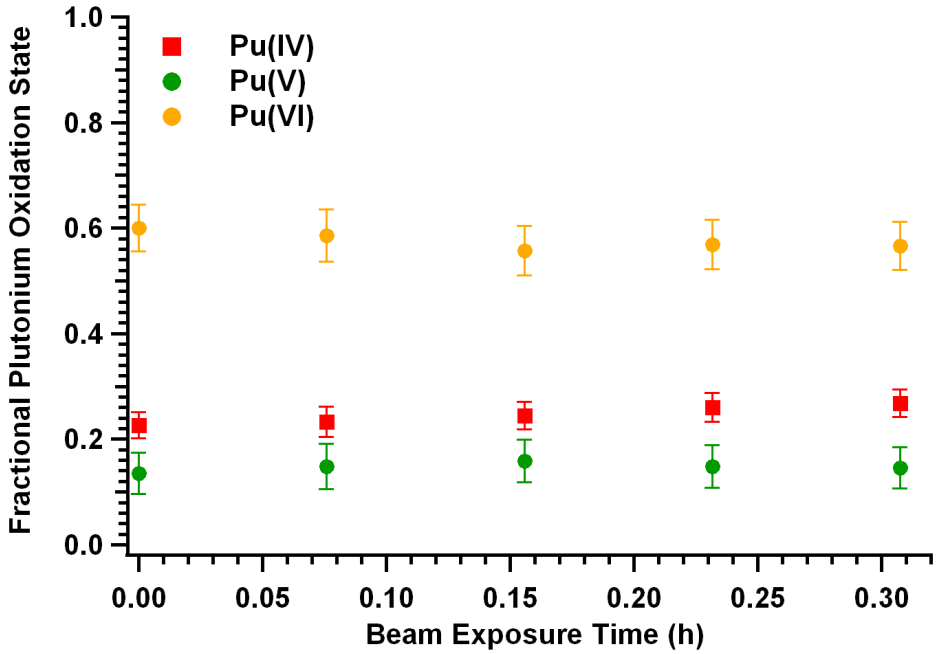

Figure 7.15: Least-squares fit of 5 XANES spectra of plutonium on Ac-Phos bound to a mesoporous silica substrate in a pH 4.4 solution at 300 K (XANES spectra not shown) plotted against the time exposed to the X-ray beam. Each scan took approximately 5 minutes.

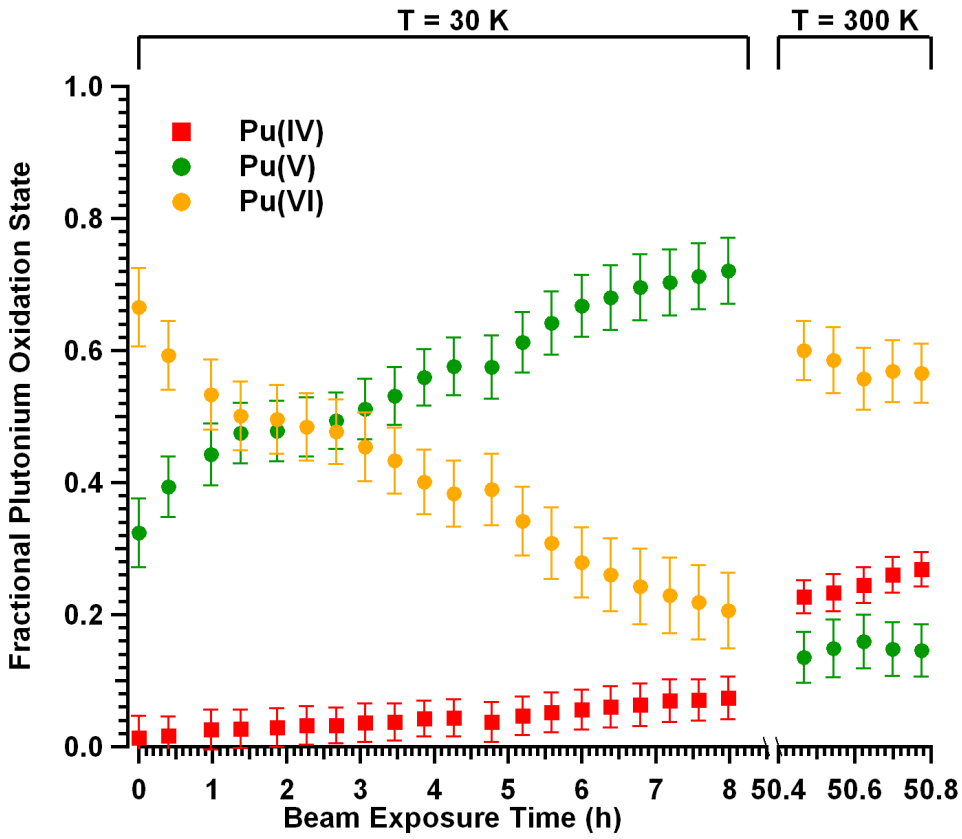

Figure 7.16: Composite plot of figures 7.14 and 7.15 above, showing the full beam exposure time for the sample of plutonium on Ac-Phos bound to a mesoporous silica substrate in a pH 4.4 solution. After 8 hours of X-ray beam exposure at 30 K the sample was warmed to and left at 300 K for approximately 42 hours before being exposed to the X-ray beam again while 5 additional XANES spectra were collected at 300 K. Notice the split x-axis and different x-axis scaling on this plot.

X-rays, or alpha particles, the electron that is liberated in the ionization process generally has sufficient energy to further ionize surrounding water molecules. This process causes the formation of clusters of ions around the path that the ionizing radiation takes through the solution. These clusters are known as spurs. The quantity and type of ions formed in the spurs, and the spatial distribution of these ions, are dependent on the energy and the type of ionizing particle. The linear energy transfer (LET) is a measure of the energy that is transfered from the ionizing particle to the surrounding medium as it travels through the medium [167, 168]. Gamma-rays and X-rays are low-LET types of ionizing radiation, while alpha particle radiation has a high-LET value.

In aqueous solutions with pH values between 3 and 11 pH units, for low-LET ionizing radiation, the accepted values of the primary yields of radiolysis are pH independent and approximately follow the reaction:

$$4.0\ H_2O + h\nu \longrightarrow 2.6\ e^-_{aq} + 2.6\ HO\cdot + 0.6\ H\cdot + 0.4\ H_2 + 0.7\ H_2O_2 \tag{7.4}$$

for each 100 eV of ionizing energy absorbed by the water [175, 167, 157]. The species generated in equation 7.4 are commonly referred to as the primary radiolytic species, and the individual yield of each species is referred to as the primary yield of the radiolytic species.

The process that produces the species shown in equation 7.4 occurs on the order of 10^{-7} seconds. During this time various other radiolytic species form in the spurs, react with each other, and diffuse out into the surrounding solution to form a homogeneous distribution. Understanding the exact reactions that occur during this time is an active field of research [174]. Because our concern is with the chemistry that occurs on time scales longer than 10^{-6} seconds, we consider the homogeneous distribution of primary species to effectively occur instantaneously. Of the radiolysis products shown in equation 7.4, the hydrated electron (e^-_{aq}), the hydroxyl radical ($HO\cdot$), the hydrogen radical or hydrogen atom ($H\cdot$), and hydrogen peroxide (H_2O_2) could react with plutonium(VI) in various oxidation and reduction reactions.

It has been shown that plutonium has the ability to auto-reduce in aqueous solution due to alpha decay self-irradiation effects [94, 176, 177]. However, it is unlikely that this process plays a major role in our samples because the activity of the plutonium in our sample is relatively low and the data presented in subsection 7.3.3 clearly show the onset of plutonium redox chemistry is correlated with exposure to the X-ray beam. Furthermore, direct absorption of ionizing radiation by plutonium atoms can be ruled out as well because of the low concentration present in our samples [175]. Table 7.2 shows selected standard reduction potentials for the possible reactions discussed below.

The spectra in figure 7.7 and oxidation state fits in figure 7.8 show an initial reduction of Pu(VI) in the sample to Pu(V). Reaction with hydrogen peroxide (H_2O_2), one of the primary radiolytic species generated in the radiolysis of water (see equation 7.4), has been shown to reduce Pu(VI) to Pu(V) [94, 97, 98, 180, 181, 182] according to the chemical reaction:

$$2\,PuO_2^{2+} + H_2O_2 \rightleftharpoons 2\,PuO_2^{+} + 2\,H^+ + O_2 \tag{7.5}$$

Furthermore, the hydrated electron (e^-_{aq}), another primary radiolytically generated species, has also been shown to reduce Pu(VI) [183].

Reaction	Standard Reduction Potential, E^o(V)	Reference
$H^+ + e^-_{aq} \rightleftharpoons \frac{1}{2} H_2$	2.67	[178, 179]
$HO\cdot + e^- \rightleftharpoons OH^-$	2.02	[39]
$2\,H_2O + 2\,e^- \rightleftharpoons H_2 + 2\,OH^-$	-0.8277	[39]
$H_2O_2 + 2\,H^+ + 2\,e^- \rightleftharpoons 2\,H_2O$	1.776	[39]
$PuO_2^{2+} + \frac{1}{2} H_2 \rightleftharpoons PuO_2^+ + H^+$	0.91	[94]
$PuO_2^{2+} + 2\,H^+ + H_2 \rightleftharpoons Pu^{4+} + 2\,H_2O$	1.053	[94]

Table 7.2: Selected standard reduction potentials relative to the S.H.E. related to reactions involving plutonium and radiolytically generated species.

Further reduction of Pu(V) to Pu(IV) at longer time scales is also noticeable in both figures 7.7 and 7.8. Previous work has shown the capacity of H_2O_2 to reduce Pu(V) [184]. Inspection of the half reactions in table 7.2 shows that this reduction is thermodynamically favorable. It is also possible that the accumulation of Pu(V), in close proximity at the solution mineral interface, increases the Pu(V) disproportionation reaction rate (equation 5.9). The Pu(VI) formed during the disproportionation reaction could then be rapidly reduced to Pu(V) again, while the Pu(IV) accumulates slowly in the sample. Neither reaction pathway can be discounted through inspection of the measured data.

To minimize the effect of beam-induced reduction, samples were measured at cryogenic temperatures in a liquid helium cryostat. Figures 7.9 and 7.10 show samples measured at 20 K. Under these conditions, a small amount of beam-induced reduction of Pu(VI) to Pu(V) still appears to occur. Despite cooling the sample, the radiolytic reaction shown in equation 7.4 is still expected to occur, resulting in the formation of primary radiolytic species in the sample matrix. Under cryogenic temperatures, most of these species will take a much longer time diffusing from their point of formation to a point of potential reaction with plutonium, resulting in a slower rate of beam-induced reduction. However, it is possible for the hydrated electron or a partially hydrated electron (referred to as a trapped electron, e_t^-) to continue to react with surrounding redox active species by quantum mechanical tunneling [167, 185]. Tunneling has been observed to occur over a range of 15-35 Å and is suggested to enlarge the reaction radii of reactions with hydrated electrons [186].

More importantly, the formation of Pu(IV) within the sample due to beam-induced effects has been significantly retarded at cryogenic temperatures. This effect may be due to fewer reducing agents approaching plutonium, the lower temperature causing a kinetic hindrance of the Pu(V) disproportionation reaction, or both processes occurring simultaneously. It is clear to see that without proper temperature control, it is possible to mistake X-ray beam-induced chemistry for novel plutonium chemistry occurring at the water/mineral interface.

Figure 7.12 shows an example of Pu(VI) sorbed on a manganese-substituted iron oxide mineral. This mineral has been shown to cause Pu(VI) to be reduced to Pu(IV) at the mineral surface [68]. Measurements of this sample taken at 50 K show that the oxidation state of

plutonium in the sample is stable throughout the sample measurement period, suggesting that no beam-induced chemistry is occurring.

Other graduate students in the Nitsche group work with organically-functionalized mesoporous silica in an effort to sequester radionuclides with possible applications to sensing technology. In the process of measuring the local binding structure of Pu(VI) on these substrates it was discovered that Pu(VI) was not stable with respect to beam-induced chemistry, even at cryogenic temperatures. These types of samples are a marked change from the metal oxide mineral samples previously discussed. The spectra in figure 7.13 and oxidation state fits in figure 7.14 show XANES data of Pu(VI) sorbed on the surface of an organically-functionalized mesoporous silica. Here the samples are measured at 30 K, but still show a significant reduction of Pu(VI) to Pu(V) over the period of 8 hours. There is a steady increase in the Pu(IV) content of the sample during this time period as well. A linear fit to the Pu(IV) component in figure 7.14 shows that reduction to Pu(IV) in the sample is occurring at approximately 0.71 ± 0.03 % per hour of X-ray beam exposure.

It is possible that the organic ligands decorating the silica surface are reacting with the primary radiolytic species to generate secondary radicals that are more reactive with plutonium [167]. The silica surface itself may also be playing a role in the noticeable X-ray beam-induced plutonium reduction. Previous work has shown an enhanced generation of H_2 at the surface of silica glasses, mesoporous molecular sieves [187], silica gel [188], and type Y-zeolites [189]. Le Caër *et al.* [190] have shown that radiolytic hydrogen peroxide yields are much greater on nanoporous glasses than in bulk water and cite an efficient energy transfer from the glass to the confined water in the mesoporous sample as the cause. Hydrogen proxide yields increase with increased surface area of the mesoporous silica. The hypothesized radiolytic reaction mechanism is presented below:

$$\mathrm{SiO_2} \xrightarrow{h\nu} \mathrm{e^-} + \mathrm{h^+} \tag{7.6}$$

$$\mathrm{e^-} + \mathrm{h^+} \longrightarrow \text{ exciton} \tag{7.7}$$

$$\text{exciton} \ + \ \equiv\mathrm{SiOH} \longrightarrow \ \equiv\mathrm{SiO\cdot} + \mathrm{H\cdot} \tag{7.8}$$

Equation 7.6 shows the absorption of a high-energy photon in the bulk silica and formation of an electron-hole pair, $\mathrm{e^-}$ and $\mathrm{h^+}$, respectively. This pair recombines to form an exciton (equation 7.7), which then proceeds to migrate to the silica/water interface where it reacts with the surface hydroxyl groups, represented as $\equiv\mathrm{SiOH}$ and $\equiv\mathrm{SiO\cdot}$ in equation 7.8. The atomic hydrogen can form molecular hydrogen through the reaction:

$$\mathrm{H\cdot} + \mathrm{H\cdot} \longrightarrow \mathrm{H_2} \tag{7.9}$$

while the surface silicon oxide radical, $\equiv\mathrm{SiO\cdot}$, can react with water according to the equation:

$$\equiv\mathrm{SiO\cdot} + \mathrm{H_2O} \rightleftharpoons \ \equiv\mathrm{SiOH} + \mathrm{HO\cdot} \tag{7.10}$$

to form hydroxyl radicals. These radicals are then available to recombine and form hydrogen peroxide:

$$\mathrm{HO\cdot} + \mathrm{HO\cdot} \longrightarrow \mathrm{H_2O_2} \tag{7.11}$$

Increased radiolytic formation of hydroxyl radicals have also been seen in controlled pore glasses with a pore size ranging from 8 to 300 nm [191].

Whether the potential increase in radiolytic primary species is affecting the rate of beam-induced reduction on the Ac-Phos sample is unknown. However, considering the cryogenic temperatures at which this sample was collected, it seems that reduction of Pu(VI) to Pu(V) and Pu(IV) most likely results from reaction with some form of hydrated or trapped electron.

Upon completion of the data collection shown in figure 7.14, the Ac-Phos sample was allowed to warm to room temperature and rest for approximately 42 hours in the absence of X-ray beam irradiation. Five XANES scans of the sample were then measured again at 300 K over the period of approximately half an hour. The least-squares fits to these 5 scans are shown in figure 7.15 (XANES spectra not shown). Comparison of the data from the first scan of these 5 scans at 300 K and the last scan at 30 K shows that during the time when the sample was at room temperature with no exposure to the X-ray beam the predominantly Pu(V) sample oxidized to become a predominantly Pu(VI) sample. This change is most easily seen in the split-axis plot shown in figure 7.16.

The likely cause of the significant oxidation of Pu(V) to Pu(VI) is through reaction with hydroxyl radicals that are radiolytically generated and trapped at cryogenic temperatures, but become a more chemically viable reaction species as the sample temperature increases. Such hydroxyl radicals could react with Pu(VI) through inner-sphere substitution:

$$(H_2O)_5Pu^{V}O_2^{+} + HO\cdot \longrightarrow (H_2O)_4(OH)Pu^{VI}O_2^{2+} + H_2O \tag{7.12}$$

or outer-sphere electron transfer [175]:

$$(H_2O)_5Pu^{V}O_2^{+} + HO\cdot \longrightarrow (H_2O)_5Pu^{VI}O_2^{2+} + OH^{-} \tag{7.13}$$

although other metal-hydroxyl radical reaction mechanisms have also been suggested [192]. A portion of this oxidation could also be caused by the disproportionation reaction of Pu(V) (see equation 5.9) or formation of secondary radicals from the organic ligands on the surface of the mesoporous material.

During this time the Pu(IV) fraction of the sample also continues to increase, although at a slower rate than during the X-ray beam irradiation at 30 K. However, once the sample is exposed to the X-ray beam again at 300 K the rate of sample reduction to Pu(IV) rapidly increases. A linear fit to the Pu(IV) component in figure 7.15 shows that reduction to Pu(IV) in the sample at 300 K is occurring at approximately 14.2 ± 1.2 % per hour of X-ray beam exposure. This shows that cryogenically cooling the sample does in fact retard the rate of Pu(IV) formation in the sample by a factor of approximately 20.

It appears from our experiments that primary radiolytic species reaction with plutonium is retarded at cryogenic temperatures for metal oxide substrates. However, reduction of Pu(VI) continues to occur at the surface of organically-functionalized silica in the presence of a synchrotron X-ray beam at a measurable rate. Therefore, XAS work involving silica surfaces and plutonium may need careful handling and special data collection methods to keep beam-induced chemical reduction from occurring. Furthermore, it may be prudent to monitor oxidation state stability as a function of X-ray beam exposure time for XAS samples that contain redox reactive species such as plutonium. Methods of reducing the effects of X-ray beam-induced chemical reactions include faster collection of spectra, reducing X-ray

beam flux, rastering over fresh spots in the sample, or the introduction of chemicals that act as free-radical scavengers.

Although exact reaction mechanism assignment and accurate determination of rate laws and constants would be of great use to the plutonium chemist, such a study is beyond the scope or interest of the present investigation. Whatever the exact equations of such beam-induced chemistry end up being, the effect of synchrotron X-ray beam-induced chemistry for certain types of aqueous and wet-paste plutonium sorption samples is clear and unmistakable. It is therefore essential for the actinide XAS practitioner to minimize such unwanted chemistry through the judicious use of temperature control, and/or mitigation of peroxide and free-radical formation in the sample.

7.4 Plutonium(VI) Sorption on Manganese-Substituted Goethite

7.4.1 Overview

The molecular-level binding metrics and structure of plutonium sorbed to the surface of manganese-substituted goethite are discussed in the following section. Various aspects of this section have been published in the peer-reviewed journal "Radiochimica Acta" [68].

Plutonium can exist simultaneously in the environment as Pu(III), Pu(IV), Pu(V), and Pu(VI) [94], but mainly exists as the three higher oxidation states [Pu(IV), Pu(V), and Pu(VI)] in oxic waters [193]. Pu(V) and Pu(VI) exist in solution as the plutonyl moiety (PuO_2^{n+}) with effective aqueous solution charge, n, of +2.3 and +3.3, respectively [194]. This reduced effective charge, as compared to Pu(IV), results in the oxidized forms of plutonium being more soluble and, by extension, more mobile in the environment. This result has been experimentally measured in the past, showing that Pu(IV) is many orders of magnitude more insoluble than the oxidized Pu(V) and Pu(VI) forms [94]. Previous work by Kaplan *et al.* [69] using laboratory and lysimeter studies showed that $> 95\%$ of plutonium migrating from a purposefully placed solid $Pu^{IV}(NO_3)_4$ source remained within 1.25 cm of the source over an 11 year period under natural environmental conditions at the Department of Energy (DOE) Savannah River Site (SRS). Such work on large-scale environmental systems is an important part in uncovering essential components of the soil and mineral composition that control plutonium redox chemistry. However, individual sorption and redox processes must also be tested on well-characterized model mineral phases that properly represent individual environmental components. Shaughnessy *et al.* [20] have shown the capacity of the pure manganese minerals manganite (γ-$Mn^{III}OOH$) and hausmannite ($Mn^{II}Mn_2^{III}O_4$) to reduce plutonium from the hexavalent to the tetravalent form using X-ray absorption spectroscopy (XAS). Similar sorption studies of Pu(V) on magnetite ($Fe^{II}Fe_2^{III}O_4$) [21, 22] using solvent extraction also showed reduction to Pu(IV). However, previous XAS measurements involving goethite, $Fe^{III}O(OH)$ [37], a mineral devoid of Fe(II), showed reduction of Pu(VI) to Pu(V) at micromolar to millimolar concentrations, but no evidence of further reduction to Pu(IV). Powell *et al.* [70] and Keeney-Kennicutt and Morse [24] observed Pu(V) reduction by goethite to Pu(IV); neither identified the source of the reductant. Duff *et al.* [19, 18] observed oxidation of Pu(V) to Pu(VI) on the surface of Yucca Mountain Tuff in the vicinity of

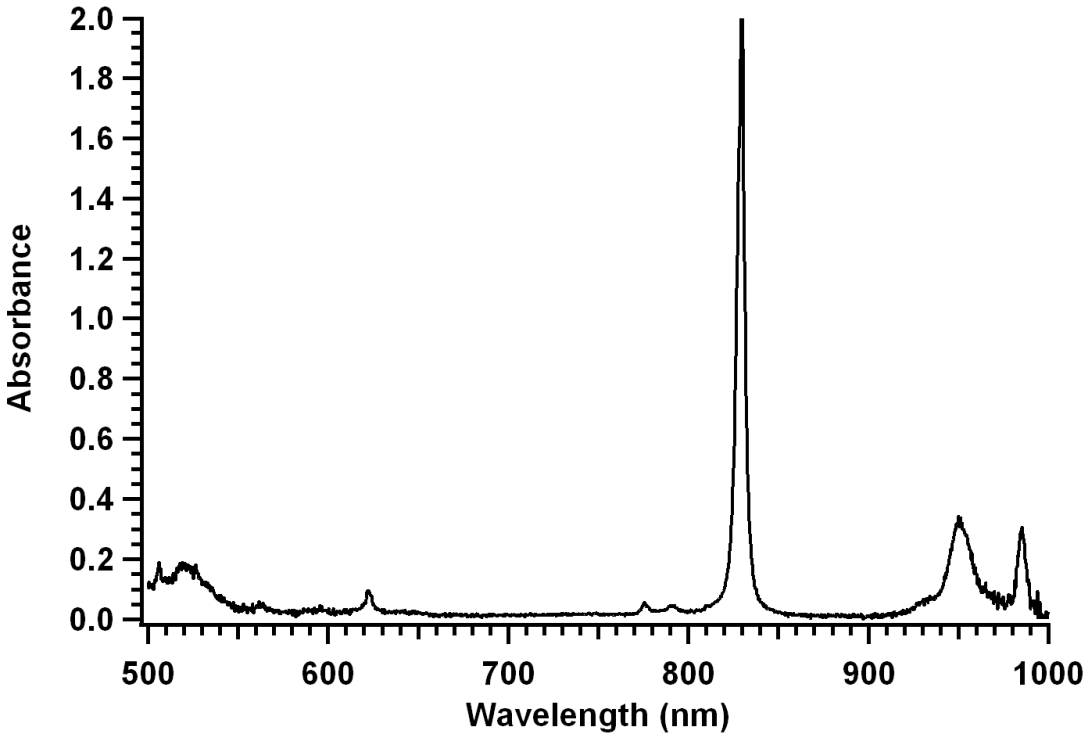

Figure 7.17: OceanOptics fiber-optic UV-Vis spectrum of Pu(VI). Note that the sharp peak at approximately 830 nm is partially truncated due to the resolution of the spectrometer.

manganese-containing minerals using the μ-XAS technique. Measurements on the same sample 2 years later, by Powell *et al.* [22], however, show that the majority of the plutonium eventually reduced to Pu(IV).

The purpose of this study was to acquire a molecular-level understanding of the sorption processes and redox reactions that are occurring between Pu(VI) and the surface of synthesized manganese-substituted goethite minerals (see section 4.3). Understanding such fundamental properties is essential in the proper modeling and risk-analysis of plutonium storage in underground geological repositories.

7.4.2 Materials and Methods

The synthesis and characterization of manganese-substituted goethite has already been covered in section 4.3. The preparation of Pu(VI) stock solution is covered in appendix C.5. The prepared stock solution was then diluted to about 1 M $HClO_4$. Plutonium oxidation state in the stock solution was confirmed by UV-Vis spectroscopy using an OceanOptics S2000 fiber-optic spectrometer as covered in subsection 5.4.1. Figure 7.17 shows that the prepared stock solution is Pu(VI) [101].

Approximately 100 mg of each mineral was placed in separate vials with approximately 8 mL of pH 5.5 solution held at a constant ionic strength of 0.1 M with $NaClO_4$ and open to air. Sufficient PuO_2^{2+} was loaded into each vial to bring the total Pu solution concentration to 250 μM and the pH was quickly adjusted using small amounts of $HClO_4$ and NaOH.

The relatively high concentrations of plutonium are required to acquire high-quality XAS data [149] (also see section 7.2). Samples were placed on a rocker and allowed to equilibrate for 48 hours. Following equilibration, samples were loaded as wet pastes into Kapton tubes and triply contained before transporting to the synchrotron for measurement. A separate aliquot of the solution in contact with the mineral was taken, filtered through a Microcon Ultracel YM-30 centrifugal filter (regenerated cellulose 30,000 MWCO) and counted using a Wallac 1414 liquid scintillation counter running in α/β discrimination mode to measure the percent plutonium sorbed on the mineral.

Plutonium XAS sample spectra were collected at 50 K, using a specially-engineered liquid helium cryostat (Janis), to mitigate beam-induced reduction of the sample. The effect of beam-induced reduction of Pu(VI) and Pu(V) to Pu(IV) on pure goethite at room temperature has been observed in the past and is hypothesized to be caused by radiolytic reactions within the system [37] (also, see section 7.3). The vertical aperture of the beam in all cases was held at 0.5 mm. Plutonium L_{III}-edge XANES and EXAFS spectra were collected at SSRL on beamline 11-2 using a 30% detuned Si(220) ϕ-0° double-crystal monochromator. Data were collected in fluorescence mode using a 32-element germanium detector. A dead time correction was applied to the spectra. Energy calibration was performed in transmission mode by measuring the plutonium L_{III}-edge of a $^{242}PuO_2$ powder reference between sample scans.

Plutonium XANES spectra were energy calibrated by setting the first inflection point of the L_{III}-edge of a PuO_2 reference sample to be 18062.3 eV [123]. Plutonium oxidation state percentages were acquired through least-squares fitting of normalized Pu(IV), Pu(V), and Pu(VI) standard XANES spectra [103]. Plutonium extended X-ray absorption fine structure (EXAFS) spectra were isolated using standard procedures [79] and fit to *ab-initio* calculated scattering paths from the FEFF7 [129] code out to a k-range of 12 $Å^{-1}$. The number of varied parameters in the fits was limited to be less than the number of independent data points in the spectrum (N_i). N_i is calculated using the adjusted Nyquist limit equation:

$$N_i = \frac{2\Delta k \Delta R}{\pi} + 2$$

where Δk is the k-range over which the fit is conducted and ΔR is the r-range over which the fit is being conducted [136]. For the full derivation of this equation please see subsection 6.4.3. S_o^2 for the fits was constrained to 1. Asymmetric error bars were calculated for the fits using the method outlined by Booth and Hu [143].

7.4.3 Evidence of Plutonium Reduction at the Surface of Manganese-Substituted Goethite

Plutonium XANES Spectral Fits

Plutonium XANES measurements provide a direct, *in-situ*, method for measuring the valence state of the plutonium atom present in the mineral solution in a non-destructive way. Figure 7.18 shows a representative fit of the Pu L_{III}-edge to pure oxidation state standards. The slight shoulder to the high energy side of the white-line is a result of multiple-scattering effects of the photoelectron off of the two axial oxygens present in the higher plutonium

Sample	PZC	Solution pH	% Pu Sorbed	%Pu(IV)	%Pu(V)
MG-1.0	6.46 ± 0.09	8.05 ± 0.05	35.6 ± 0.3	71 ± 8	29 ± 9
MG-0.5	6.78 ± 0.05	7.63 ± 0.05	46.8 ± 0.3	74 ± 6	26 ± 7
MG-0.5	6.78 ± 0.05	6.05 ± 0.05	43.5 ± 0.3	35 ± 3	65 ± 3

Table 7.3: Least-squares fits of Pu L_{III}-edge XANES data to Pu(IV), Pu(V), and Pu(VI) standard spectra. Fits consistently returned zero fit contribution from the Pu(VI) standard spectra. Error bars are presented at the 1σ confidence level.

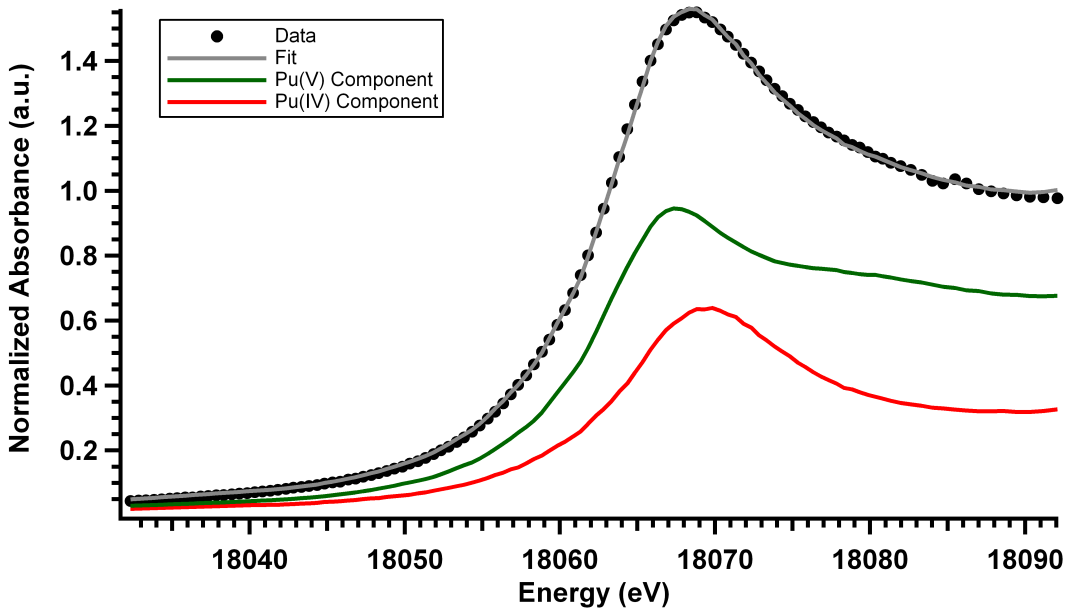

Figure 7.18: Representative plutonium L_{III}-edge XANES spectra for Pu(VI) sorbed on Mn-substituted goethite. The energy was calibrated by setting the first inflection point of the Pu L_{III}-edge of a PuO_2 reference sample to be 18062.3 eV [123]. Approximately 35% of the plutonium was Pu(IV) and 65% was Pu(V). Error in the fit at 1σ confidence is 3%.

oxidation states. This feature can be seen in the scaled Pu(V) component but is absent in the scaled Pu(IV) component. Results from the plutonium XANES measurements are shown in table 7.3. The percent of plutonium sorbed onto the mineral surface is lower than in previous experiments involving sorption of Pu(VI) to pure goethite [37]. However, this is expected because we are working at higher plutonium concentrations. The results from XANES measurements show reduction of plutonium from the more soluble Pu(VI) to the more insoluble Pu(IV) upon introduction to the mineral solution. Particularly important is the pH dependence for reduction. Table 7.3 shows that despite the small increase in Pu sorption upon increasing the solution pH from 6.05 to 7.63 for the MG-0.5 mineral, we see a significant ($40 \pm 7\%$) increase in the ability of the mineral to reduce Pu(VI) to Pu(IV). This increase in pH coincides with the transition of the mineral solution pH across the PZC of the mineral (see table 4.1). The point-of-zero-charge, as measured by the powder addition method, is more appropriately called the point-of-net-zero-proton-charge. This value represents the pH at which the surface of the mineral in the mineral solution has a net zero charge. At pH values below the point-of-zero-charge the mineral surface carries a net positive charge, while at pH values above the point-of-zero-charge the mineral surface carries a net negative charge. Positively charged or neutral species are therefore at an electrostatic disadvantage for sorption onto the surface of the mineral at lower pH values (figure 5.3). As the mineral solution pH increases above the PZC, the electrostatic interaction between the mineral surface and metal ions favors electrostatic sorption onto the surface as either an inner-sphere complex (directly bound to the mineral surface) or as an outer-sphere complex (see section 3.3). The significant increase in plutonium reduction upon increasing the solution pH suggests that the plutonium is being reduced to Pu(IV) through a surface-mediated mechanism. Such mechanisms have been proposed in the past for Pu(VI) on hausmanite ($Mn^{II}Mn_2^{III}O_4$) and manganite (γ-$Mn^{III}OOH$) [20] through the use of XAS measurements, and for Pu(V) on magnetite ($Fe^{II}Fe_2^{III}O_4$) [21, 22] using solvent extraction methods. The work by Shaughnessy *et al.* [20] showed no pH dependence on the amount of plutonium reduced from Pu(VI) to Pu(IV). Furthermore, these data suggest that it is unlikely that surface accumulation of Pu(V) followed by disproportionation to Pu(IV) and Pu(VI) is the major mechanism of reduction occurring at the solution-mineral surface. If such a mechanism controlled the redox chemistry at the solution-mineral surface the plutonium reduction would be expected to change as a function of the total amount of plutonium sorbed onto the mineral surface.

Plutonium EXAFS Spectral Fits

Figure 7.19 shows EXAFS spectra fits in both k-space and r-space with the accompanying fit parameters given in table 7.4. In the following discussion of the EXAFS spectra, Fourier transform (FT) peak positions are reported in units of Å with no correction for phase shift ($r+\Delta$). In contrast, when referring to bond lengths, we report actual distances in units of Å.

MG-0.5 pH 6.05 distinctly shows the well known "split-oxygen" shell associated with the actinyl moiety [11]. This spectral feature arises from interference between the EXAFS oscillations of the axial and equatorial oxygens. EXAFS fits for this split-oxygen shell show an expansion of the axial Pu-O bond length to approximately 1.85 Å, suggesting that the plutonium is in the pentavalent form as our XANES fits above indicate. Models for the

Sample	Solution pH	Scattering Path	R(Å)	N	σ(Å)	ΔE_o^a
MG-1.0	8.05 ± 0.05	Pu-O_{ax1}	1.89 ± 0.02	0.58[b]	0.03[c]	$-5.2^{+3.2}_{-2.4}$
		Pu-O_{ax1}-Pu-O_{ax2}	3.78[d]	0.58[d]	0.06[d]	
		Pu-O_a	2.23 ± 0.02	$9.7^{+1.0}_{-1.2}$	0.11 ± 0.01	
		Pu-O_b	$2.4^{+0.3}_{-1.4}$	$2.2^{+1.0}_{-1.4}$	0.11[e]	
		Pu-Fe	$3.36^{+0.02}_{-0.03}$	$2.17^{+2.5}_{-0.7}$	0.08 ± 0.03	
R(%) = 11.22						
F-Test for Pu-Fe Path Significance = 94.31%						
MG-0.5	7.63 ± 0.05	Pu-O_{ax1}	$1.91^{+0.04}_{-0.02}$	0.52[b]	0.03[c]	-5.1 ± 1.3
		Pu-O_{ax1}-Pu-O_{ax2}	3.83[d]	0.52[d]	0.06[d]	
		Pu-O_a	2.21 ± 0.02	$5.6^{+0.9}_{-0.8}$	$0.07^{+0.01}_{-0.03}$	
		Pu-O_b	2.37 ± 0.02	4.1 ± 0.3	0.07[e]	
		Pu-Fe	3.35 ± 0.02	$5.4^{+6.1}_{-3.0}$	0.15 ± 0.03	
R(%) = 10.07						
F-Test for Pu-Fe Path Significance = 91.67%						
MG-0.5	6.05 ± 0.05	Pu-O_{ax1}	1.85 ± 0.02	1.3[b]	0.07 ± 0.02	-2.3 ± 2.1
		Pu-O_{ax1}-Pu-O_{ax2}	3.71[d]	1.3[d]	0.14[d]	
		Pu-O_a	2.19 ± 0.02	$4.7^{+1.4}_{-0.7}$	0.08 ± 0.01	
		Pu-O_b	2.40 ± 0.02	$6.5^{+1.6}_{-1.2}$	0.08[e]	
		Pu-Fe	$3.33^{+0.03}_{-0.02}$	$5.4^{+6.1}_{-3.0}$	$0.14^{+0.04}_{-0.14}$	
R(%) = 13.08						
F-Test for Pu-Fe Path Significance = 69.26%						

[a] ΔE_o was set to be the same for all paths.
[b] SS plutonyl oxygen coordination number constrained to data acquired from XANES.
[c] SS plutonyl oxygen Debye-Waller factor constrained to 0.03 Å.
[d] MS plutonyl oxygen bond lengths, coordination number and Debye-Waller factors constrained to single scattering path [106].
[e] Pu-O_b Debye-Waller factor constrained to Pu-O_a.

Table 7.4: Fit parameter results from Pu L_{III}-edge EXAFS fits. Symmetric and asymmetric error bars are presented at the 1σ confidence level.

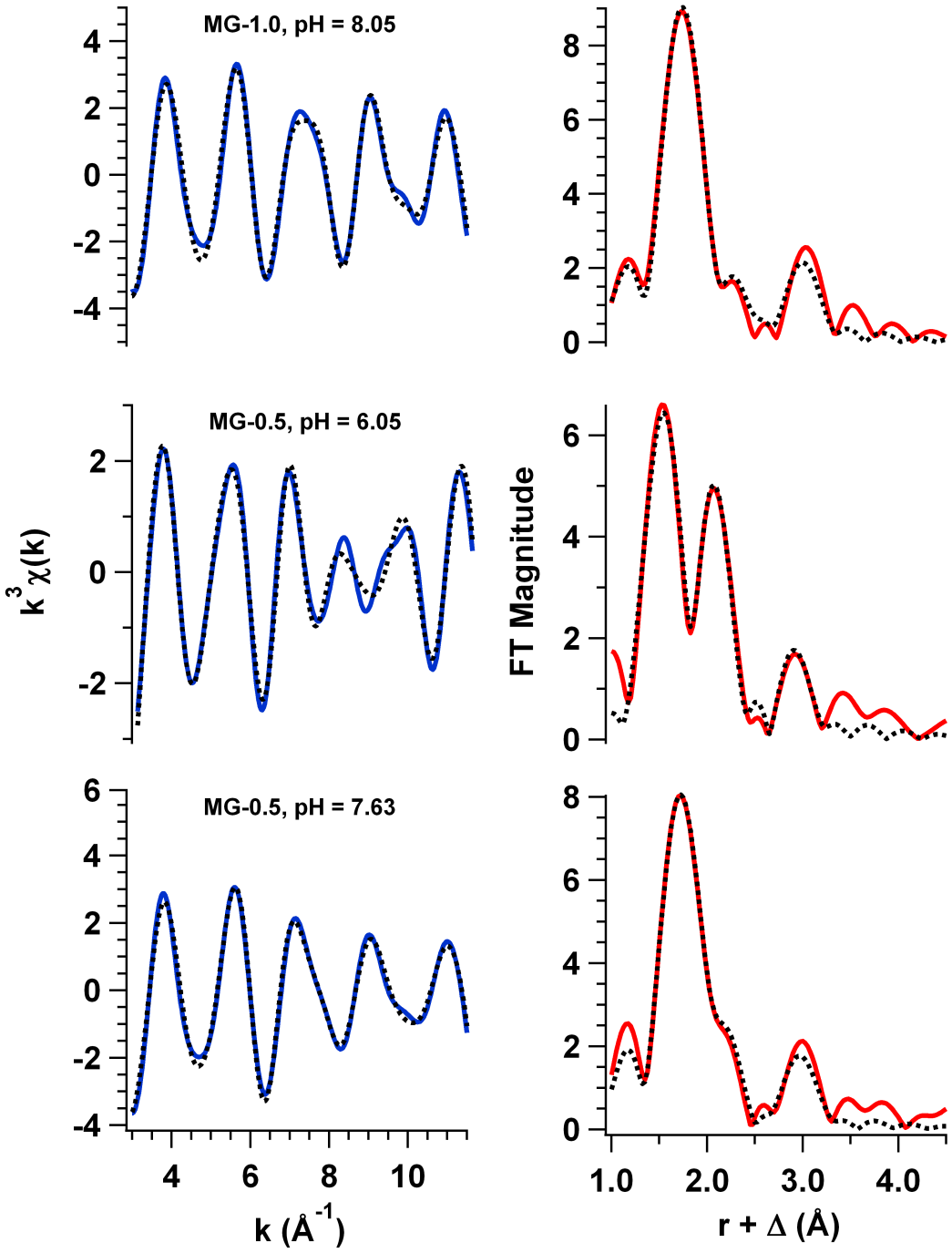

Figure 7.19: EXAFS spectra fits in k^3-weighted $\chi(k)$ vs. k, the photoelectron wave vector (left column, blue line) and the corresponding Fourier transform magnitude verses $r + \Delta$, the pseudo-radial distribution function (right column, red line). Dashed black lines are the associated fits. The position of the Pu-Fe scattering path is at roughly 3.0 $r + \Delta$.

other two samples also take into account the smaller percentage of Pu(V) present by fitting a Pu-O_{ax} single-scattering (SS) path and a Pu-O_{ax1}-Pu-O_{ax2} multiple-scattering (MS) path with coordination numbers, N_{SS} and N_{MS}, constrained to the percent Pu(V) determined in the XANES fits. Other parameters for the MS were highly constrained to the $Pu - O_{ax}$ SS paths. Only the Pu-O_{ax1}-Pu-O_{ax2} MS path is considered in our fits because other possible MS paths tend to cancel at a $k < 5$ Å^{-1}. At k values larger than 5 Å^{-1} MS amplitude contributions dampen out more quickly than SS amplitudes. This effect has been observed in the past for the uranyl moiety [106]. For the MS path, R_{MS} was set to $2R_{Oax}$, and the MS Debye-Waller (DW) factor was constrained to be twice the single-scattering (SS) DW factor ($\sigma^2_{MS} = 2\sigma^2_{SS}$) as was done in previous studies with uranyl [106].

The Pu-O_a path fits an unusually small plutonium-oxygen bond length of approximately 2.2 Å. Similar bond lengths have been reported in the literature [195] for uranyl and have been assigned as hydroxide complexation to the uranyl moiety, but to the best of our knowledge have not been reported for Pu-O bond lengths. Such bond length shortening could be the result of Pu(VI) bound to the mineral surface via a surface oxygen. At higher solution pH, more mineral surface sites are deprotonated and available for binding in such a fashion. The Pu-O_b path fits to a bond length of approximately 2.37-2.40 Å, suggesting the presence of coordinated water around the plutonium atom. The increase in coordination number for Pu-O_b and decrease in coordination number for Pu-O_a as sample pH decreases implies hydroxide complexation (or Fe-O-Pu complexation) decreases and water coordination increases as the sample pH decreases, suggesting that our assignment above is correct.

The FT peak at approximately 3.0 Å fits well with a Pu-Fe bond length of approximately 3.33-3.36 Å. A Pu-Fe path was chosen for the model instead of a possible Pu-Mn path because of statistical reasons; it is simply more probable that plutonium will encounter a surface binding site which contains a distal iron atom as opposed to a distal manganese, assuming that site reactivity is similar for the two metal sites. Furthermore, it is not possible to differentiate a Pu-Fe path from a Pu-Mn path using the bulk XAS technique because of the similar scattering strengths of the iron and manganese atoms. Previous calculations and measurements collected on uranyl model compounds have shown that actinyl MS paths can also contribute to the FT peak at about 3.0 Å [11, 106]. This effect should be relatively small for our samples at higher pH since the majority of the plutonium is in the tetravalent form. Furthermore, the constraints on the plutonyl MS path imposed by the plutonyl SS path and geometric arguments take this effect into account for all sample fits. However, the large errors in the coordination number for the Pu-Fe path fit, in conjunction with the large DW factors, suggest the possibility of contributions from other paths. Most notably, a Pu-C scattering path could partially account for the FT peak at 3.0 Å. However, a fit without the Pu-Fe scattering path present results in an unreasonable number of carbons in that shell or a poor fit if the number of carbons is constrained. The MS from bidentate carbonate ligation is difficult to resolve as well because the EXAFS oscillations from the potential Pu-O_{dis}-C and Pu-C-O_{dis}-C paths are exactly π radians out of phase and of similar magnitude; that is, the EXAFS signal from these two MS paths destructively interfere with each other. Inspection of the Pu(VI) speciation diagram in figure 5.3 shows the possibility of carbonate coordination for the two higher pH samples. To take this possibility into account we conducted a modified F-test [156, 153, 152] to check for the significance of the Pu-Fe scattering path in the presence of a Pu-C scattering path in our fits. The results of the

F-test are shown in table 7.4 and represent our confidence that the Pu-Fe scattering path in our model is necessary to reproduce the spectral features of our data. Attempts were also made to fit Pu-Pu scattering paths, which would indicate Pu(IV) precipitation. Such attempts resulted in poor fits due to phase mismatch.

The fits presented in table 7.4 have relatively large coordination numbers compared to the number of available coordination sites around the plutonium atom. This is particularly evident for sample MG-1.0, which fits 9.7 and 2.2 coordinated oxygens for scattering paths Pu-O_a and Pu-O_b, respectively. This is a result from coupling to a large DW factor. If σ is constrained to 0.08 Å approximately 6 and 2 oxygens are fit to the paths, respectively. Coordination numbers could also be inflated by roughly 10% due to errors in S_o^2, which has been artificially fixed at 1.0 for these fits. Furthermore the coordination numbers for the outer shells contain large associated error bars. Such large errors preclude any attempts to reconstruct the exact surface binding structure, but use of the F-test lends credence to our proposed Pu-Fe scattering path fit. This, in turn, allows us to confidently assign plutonium interaction with the surface as an inner-sphere complex.

7.4.4 Conclusions

In this section direct spectroscopic evidence is shown suggesting surface-mediated reduction of Pu(VI) to Pu(IV) on manganese-substituted goethite. The use of XAS allows for unambiguous, atom-specific determination of the oxidation state of plutonium *in-situ*. However, the identity of the backscattering atom is unclear because iron and manganese have very similar EXAFS backscattering amplitudes. Bulk XAS measurements therefore cannot be used to clarify the identity of the distal metal bound to the plutonium atom. It is assumed that sorption is occurring on sites nearest a distal iron since manganese concentrations are low. However, past work has shown the preferential sorption of plutonium near manganese sites, even in minerals with low manganese concentrations [18, 19].

These results show the capacity of Mn-substituted goethite to reduce plutonium from Pu(VI) to the more insoluble Pu(IV) oxidation state. Knowledge of such reduction processes is essential in understanding the migration of plutonium through the geosphere and plays an important role in the proper modeling and risk-analysis of plutonium storage in underground geological repositories.

7.5 Interactions of Plutonium(VI) with Samples Containing Mixed Goethite / Manganese-Substituted Goethite using Microprobe X-ray Analysis

7.5.1 Overview

The development of μ-SXRF (see section 6.5) and μ-XAS (see section 6.6) has been active for many years [145, 196]. However, only relatively recently has the advent and deployment of advanced X-ray focusing mirrors and third generation synchrotron light sources allowed experimenters to probe samples with heterogeneity on the order of 1 μm. Recent studies

using this technique applied to the actinide elements include the characterization of nuclear fuel sintering [197] and investigations into the migration of uranium in environmental soils at contaminated sites [148, 198, 199, 200]. However, few microprobe studies have been conducted on plutonium interactions with environmental systems [18, 19].

Here we present the results from bulk sorption studies of Pu(VI) on the surface of 1 % manganese-substituted goethite, compared to previous measurements of Pu(VI) on goethite [37]. Mixed mineral samples at select pH values are then prepared and analyzed using the μ-SXRF and μ-XANES spectroscopic techniques to measure the distribution of plutonium on the surface of a heterogeneous sample mixture of synthetic goethite and manganese-substituted goethite.

7.5.2 Materials and Methods

Bulk Sorption Sample Preparation

The synthesis and characterization of manganese-substituted goethite has been covered in previous papers [68, 74] (also see chapter 4). The preparation of solutions of ^{239}Pu(VI) in the form PuO_2^{2+} is covered in appendix C.5. Approximately 10 mg of the $63 - 212$ μm size fraction of 1 % manganese-substituted goethite was placed in a polypropylene vial with approximately 8 mL of solution held at a constant ionic strength of 0.1 M with $NaClO_4$ and open to air at various pH values. Sufficient PuO_2^{2+} was loaded into each vial to bring the total Pu solution concentration to 50 μM and the pH was quickly adjusted using small amounts of $HClO_4$ and NaOH. Samples were placed on a rocker and allowed to equilibrate for 48 hours.

A separate aliquot of the solution in contact with the mineral was taken, filtered through a Microcon Ultracel YM-30 centrifugal filter (regenerated cellulose 30,000 MWCO), and counted using a Wallac 1414 liquid scintillation counter running in α/β discrimination mode. The percent plutonium sorbed on the mineral surface was calculated to be the difference between the amount loaded and the amount left in solution.

Microprobe Sample Preparation

The synthesis and characterization of goethite has been covered in previous papers [74] (also see chapter 4). The 1 % manganese-substituted goethite is the same as that used in the bulk sorption measurements. Approximately 50 mg of goethite and 50 mg of 1 % manganese-substituted goethite dry-mixed and placed in a polypropylene vial with approximately 8 mL of solution held at a constant ionic strength of 0.1 M with $NaClO_4$ and open to air. The sieved mineral size fraction selected for this study was $63 - 212$ μm. Sufficient PuO_2^{2+} was loaded into each vial to bring the total Pu solution concentration to 250 μM and the pH was quickly adjusted using small amounts of $HClO_4$ and NaOH. Samples were prepared at pH values of 5.32, 6.78, and 8.56. These pH values represent solution conditions that are below, between, and above the point of zero charge for the two types of minerals (see section 3.2 and table 4.1). Samples were placed on a rocker and allowed to equilibrate for 48 hours. Following equilibration, mineral solutions were loaded in specially engineered microprobe sample holders (see subsection G.3.3 and section G.4) and triply contained before

transporting to the synchrotron beamline for measurement. Percent sorption in the samples were measured using the same technique as were used to measure sorption in the bulk experiments.

Microprobe Measurements

Microprobe-based synchrotron X-ray fluorescence (SXRF) imaging and plutonium L_{III}-edge μ-XANES spectra were collected at SSRL on beamline 2-3 using a fully tuned Si(220) ϕ-0° double-crystal monochromator. The monochromatic beam from the monochromator passes through a 100×100 μm^2 aperture, defining a virtual beam source. This beam is then focused using a Kirkpatrick-Baez (K-B) microfocus system down to a 2×2 μm^2 spot size at the beam focal point. Harmonic rejection is achieved through the use of the K-B focusing mirrors. The sample was rastered across the focal point of the microprobe X-ray beam using an xyz-sample stage while fluorescence data were collected using a 4-element silicon X-ray detector. Deadtime correction for the detector was unnecessary because fluorescence counts were sufficiently low. Microprobe elemental mapping was conducted using a 18100 eV incident X-ray beam. Fluorescence data were collected at 5 μm step sizes with a dwell time of 100 ms per step. Energy dependent mapping was conducted using incident photon energies of 18058, 18067, 18084, 18100, and 18130 eV. Full plutonium L_{III}-edge μ-XANES spectra were collected at points of interest on the sample. All sample spectra were collected at ambient temperatures. To minimize possible beam-induced reduction of the sample (see section 7.3) all elemental mapping occurred before any full μ-XANES spectra were collected.

Microprobe elemental maps and principle component analysis (PCA) plots were produced using Sam's Microprobe Analysis Kit (SMAK) [147]. Plutonium μ-XANES spectra were fit to normalized Pu(IV), Pu(V), and Pu(VI) standard XANES spectra [103] to determine the percent plutonium oxidation state at specific spatial positions in the sample.

7.5.3 Results and Discussion

Bulk Sorption

Figure 7.20 shows the bulk sorption data of Pu(VI) on the surface of goethite and 1 % manganese-substituted goethite as a function of pH. Error bars represent measurement error at 1σ. Goethite data (open circles and triangles) are taken from work done by Wilson [37]. The reduction in percent plutonium sorbed on the manganese-substituted goethite surface is expected from saturation of available sorption sites at the solution/mineral interface for manganese-substituted goethite. Conversion of the percent plutonium sorbed into units of milligrams of plutonium sorbed per square meter of mineral substrate surface area (see figure 7.21 and talbe 4.1) shows that the bulk sorption properties of goethite and 1 % manganese-substituted goethite are similar in both sorption capacity and pH dependence.

Figure 7.22 shows the sorption of Pu(VI) on manganese-substituted goethite as a function of pH with the calculated fractional component of the Pu(VI) solution species PuO_2^{2+}, PuO_2OH^+, and $PuO_2(CO_3)_3^{4-}$. Only the average solution species are plotted. However, a full speciation diagram with associated errors for each solution species has been calculated [68] (also see figure 5.3). Comparison of the sorption curve to the plotted species suggests that

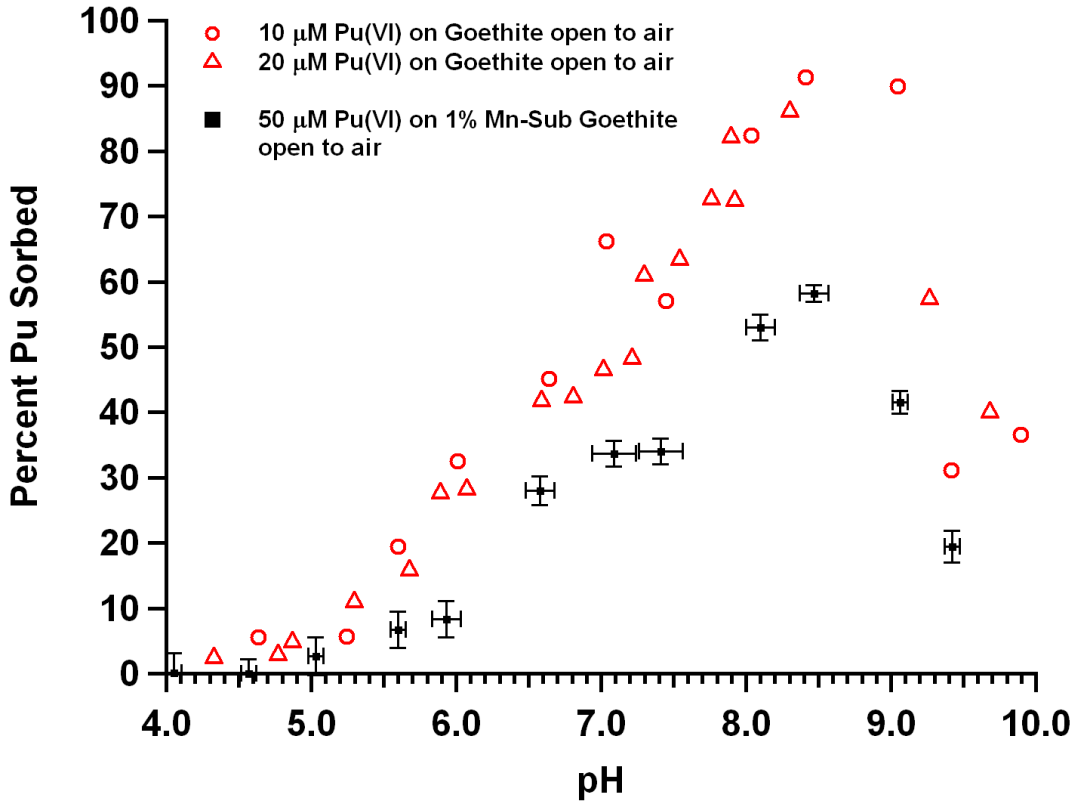

Figure 7.20: Percent sorption of Pu(VI) on the surface of goethite (red open circles and triangles) [37] and manganese-substituted goethite (black squares) as a function of solution pH at an ionic strength of 0.1 M and open to air.

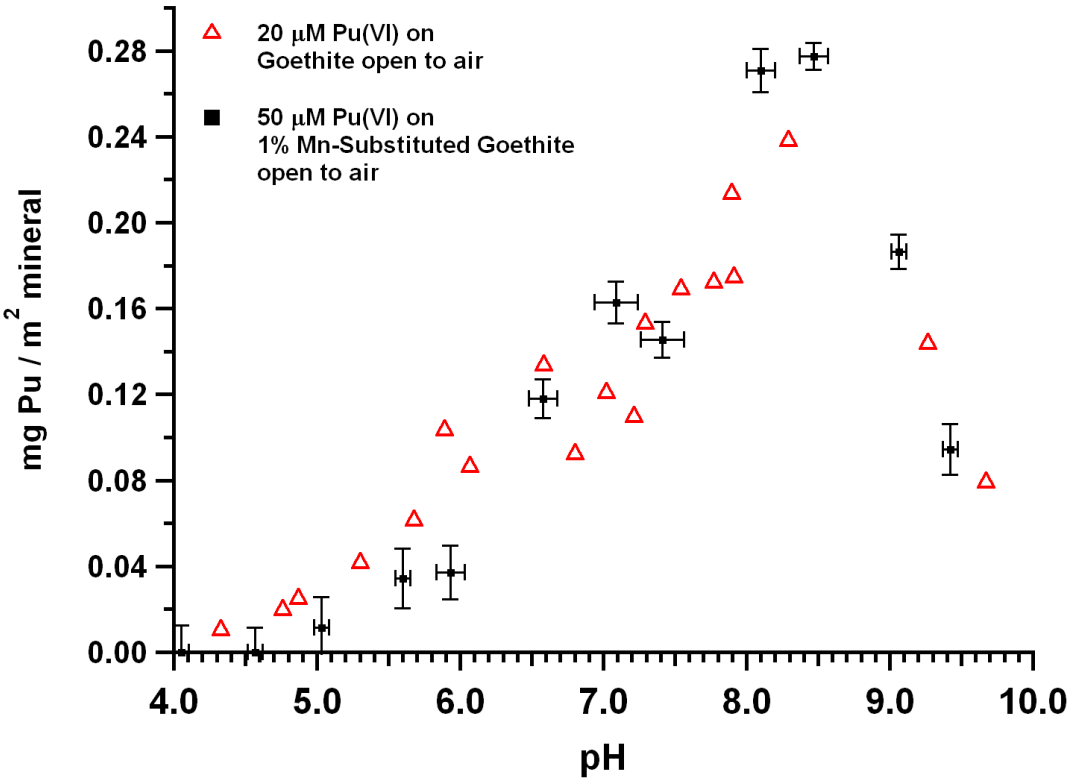

Figure 7.21: Sorption of Pu(VI) on the surface of goethite (red open triangles) [37] and manganese-substituted goethite (black squares) normalized to mineral surface area as a function of solution pH at an ionic strength of 0.1 M and open to air.

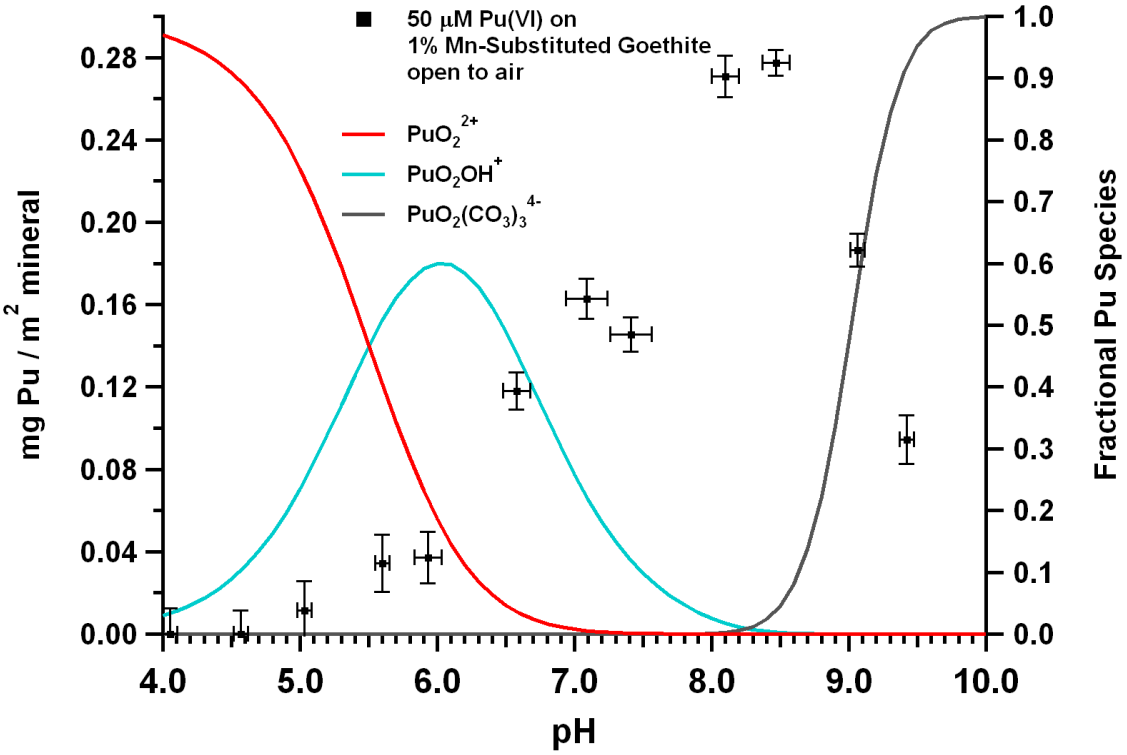

Figure 7.22: Sorption of Pu(VI) on the surface of 1 % manganese-substituted goethite in units of mg Pu per m^2 of mineral (left axis) open to air. Fractional Pu(VI) solution species (see figure 5.3) unlikely to sorb to the mineral surface are overlayed (right axis).

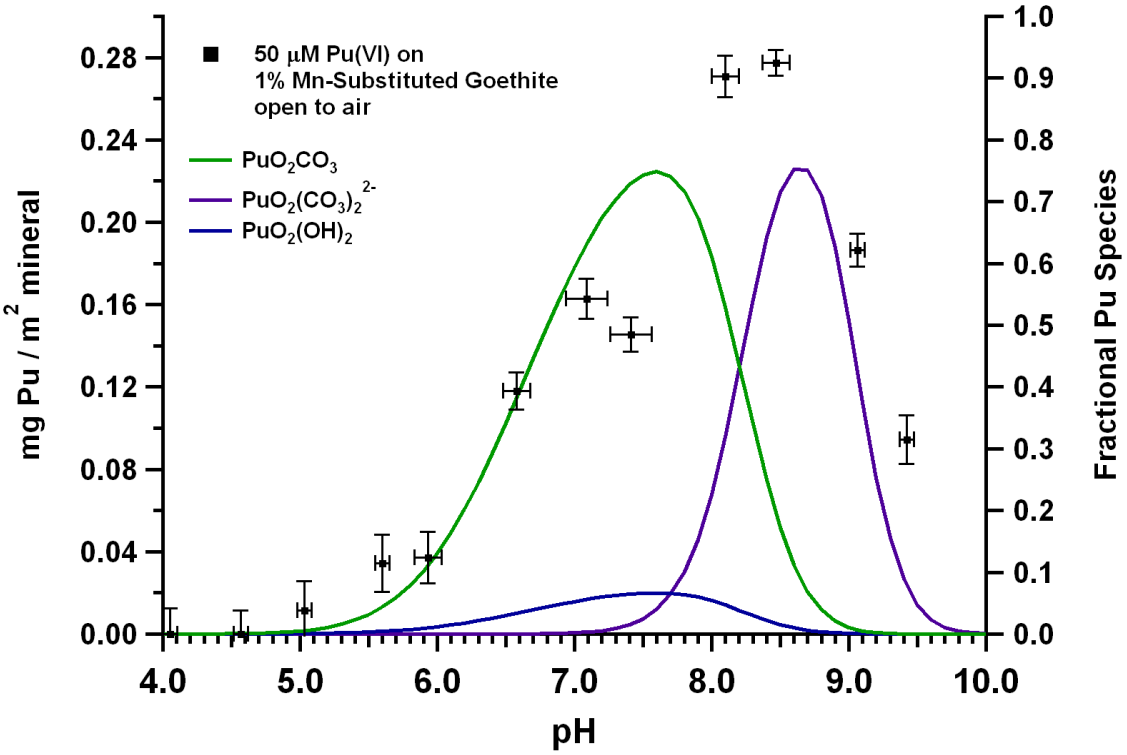

Figure 7.23: Sorption of Pu(VI) on the surface of 1 % manganese-substituted goethite in units of mg Pu per m^2 of mineral (left axis) open to air. Fractional Pu(VI) solution species (see figure 5.3) likely to sorb to the mineral surface are overlayed (right axis).

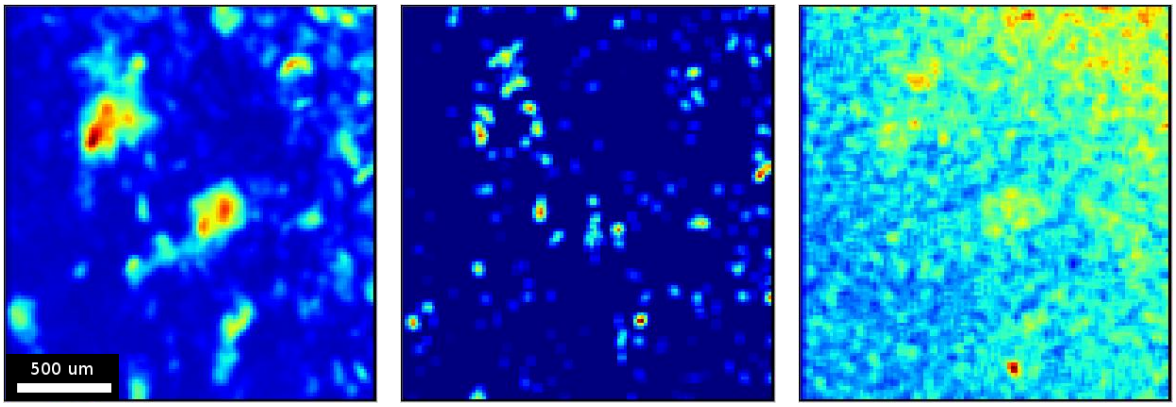

(a) Fe (b) Mn (c) Pu

Figure 7.24: Elemental heat maps for mixed goethite / 1 % manganese-substituted goethite sample in a mineral solution at pH 5.32.

these Pu(VI) solution species are unlikely to sorb onto the manganese-substituted goethite mineral surface. It is likely that the positive charges of the PuO_2^{2+} and PuO_2OH^+ solution species are electrostatically repelled from the net positive surface charge present at the mineral surface at pH values below the point of zero charge of the mineral (PZC = 6.78 ± 0.05; see section 3.2 and table 4.1). A similar argument can be made for electrostatic repulsion between the highly negatively charged species $PuO_2(CO_3)_3^{4-}$ and the net negative surface charge present at the mineral surface at pH values above the point of zero charge of manganese-substituted goethite.

Figure 7.23 shows the sorption of Pu(VI) on manganese-substituted goethite as a function of pH with the calculated fractional component of the other expected Pu(VI) solution species: PuO_2CO_3, $PuO_2(CO_3)_2^{2-}$, and $PuO_2(OH)_2$. Full error bars for these species are shown in figure 5.3. Comparison of the sorption curve with these solution species shows that they are likely candidates for sorption onto the mineral surface. These neutral and near neutral species are more likely to favorably interact with the mineral surface at and around the pH value where the net surface charge is near neutral as well (PZC = 6.46 ± 0.09; table 4.1). Previous bulk XAS measurements of Pu(VI) sorbed on manganese-substituted goethite have shown plutonium to sorb on the mineral surface as an inner-sphere complex. Reduction of Pu(VI) to Pu(IV) at the manganese-substituted goethite surface has also been shown to be pH dependent. Furthermore, detailed EXAFS fitting of the bulk XAS samples show the presence of surface plutonium hydroxide species and the possibility of surface carbonate species as well [68] (also see section 7.4).

Microprobe Analysis

The false color images shown in figure 7.24 are elemental heat maps for (a) iron, (b) manganese, and (c) plutonium in a mixed goethite / 1 % manganese-substituted goethite sample in a mineral solution at pH 5.32. The characteristic fluorescence lines from each element were binned on a solid-state energy dispersive X-ray detector. Low concentrations of a particular

Position	%Pu(IV)	%Pu(V)
1	72 ± 34	31 ± 36
2	55 ± 33	48 ± 36
3	46 ± 30	54 ± 32

Table 7.5: Least-squares fits of Pu L_{III}-edge μ-XANES data at the indicated spatial position (see figure 7.25). Error bars are presented at the 1σ confidence level.

element are shown in blue and high concentrations of a particular element are shown in red. The spatial differentiation of iron and manganese was achieved by using the scatter plot technique [201] since the fluorescence lines for iron and manganese are energetically close. Samples did not contain any elements that interfere with the plutonium L_α fluorescence line. In these images manganese will always be spatially associated with iron because half of the mineral sample consists of 1 % manganese-substituted goethite. However, the other half of the sample consists of only goethite, which will show up as hot spots in the iron elemental map, but not have associated spots in the manganese elemental map. In this way it is possible to spatially resolve grains of goethite verses grains of manganese-substituted goethite in the microprobe samples. A large grain of goethite is clearly visible in the middle of the iron elemental heat map and a small grain of manganese-substituted goethite is visible on the middle-right border of the manganese elemental heat map. Various other grains are also clearly discernible upon close inspection. The darker blue regions in both the iron and manganese elemental maps show the spatial position of the aqueous solution in contact with mixed minerals. The plutonium elemental heat map shows a few concentrated spots in the bottom-middle and top-right corner of the image. These spots indicate accumulation of plutonium at these positions, which correspond to the location of both goethite and manganese-substituted goethite. The fairly noisy background of the image (locations of cyan color in the heat map) indicates that relatively little plutonium is associated with the image as a whole. This property can also be discerned from the bulk sorption of plutonium on the surface of manganese-substituted goethite at pH 5.32 (see figure 7.21).

The elemental heat map images shown in figure 7.24 can also be plotted as a tri-color plot (see figure 7.25) [201] where each of three elements is plotted as one of the (red-green-blue) colors. The intensity of each color represents the relative concentration of the element at that particular position. Color mixtures represent spatial correlation between certain elements. For example the tri-color legend of figure 7.25 shows manganese displayed in red, iron displayed in blue, and plutonium displayed in green. In these types of plots grains of goethite will show up in a shade of blue. Manganese-substituted goethite will show up as a mixture of red and blue with an overemphasis in the color red, due to the way the fluorescence data is normalized. Plutonium will show up in shades of green. Any spatial correlation of plutonium with iron would show up as cyan in the plot, while correlation of plutonium with manganese would show up as yellow. Figure 7.25 shows that although plutonium does appear to aggregate on some mineral grains, the majority of the plutonium is not associated with any particular mineral species. Instead it seems that the plutonium

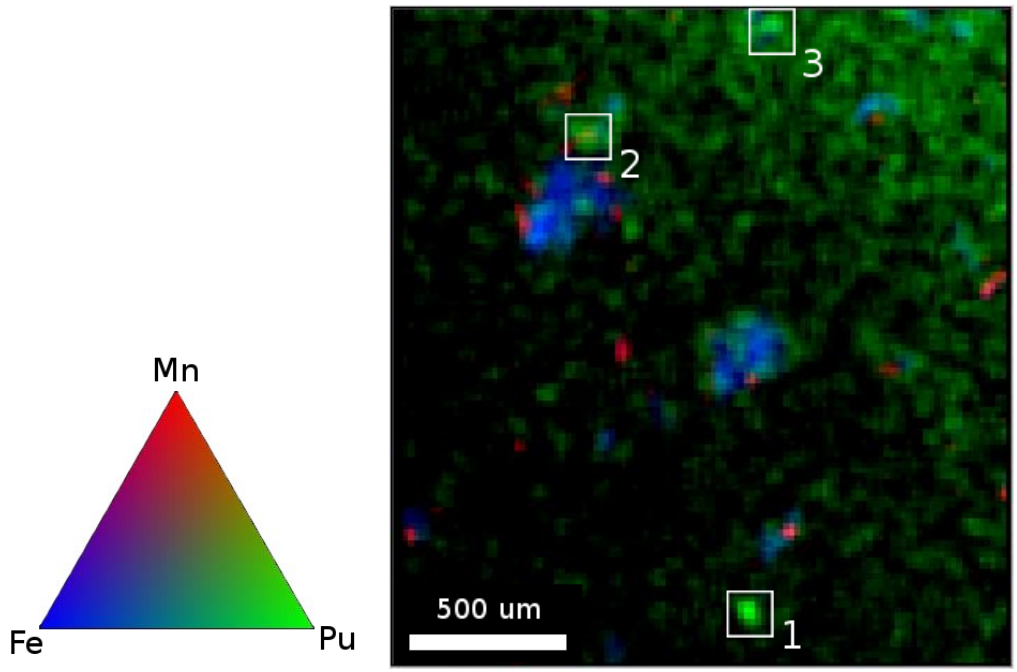

Figure 7.25: Tri-color plot of iron, manganese, and plutonium for mixed goethite / 1 % manganese-substituted goethite sample in a mineral solution at pH 5.32. White squares with accompanying numbers show positions where Pu-L_{III} edge μ-XANES spectra were collected. μ-XANES fit results are shown in table 7.5.

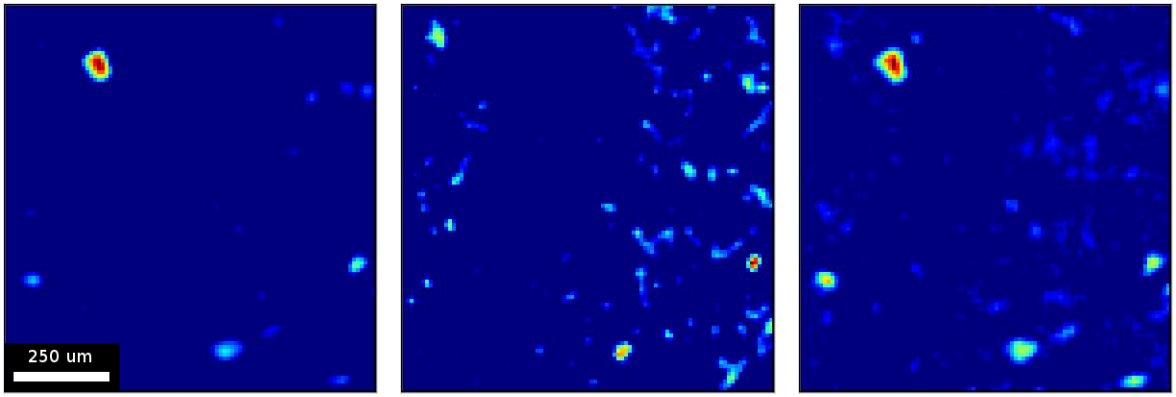

(a) Fe (b) Mn (c) Pu

Figure 7.26: Elemental heat maps for mixed goethite / 1 % manganese-substituted goethite sample in a mineral solution at pH 6.87.

is mostly distributed in the aqueous solution of the mineral solution (see figure 7.21).

The white numbered squares in figure 7.25 show the spatial positions where Pu L_{III}-edge μ-XANES data were collected on the microprobe sample. Table 7.5 shows the least-squares fit of the data to plutonium oxidation state standards. The large fit errors are due to signal-to-noise issues with the collected data. Such μ-XANES data could benefit from more scan repetition which would increase the signal-to-noise ratio. However, extended exposure to a synchrotron X-ray beam at room temperature could cause X-ray beam-induced chemistry to occur on the sample. The effect of beam-induced reduction of Pu(VI) and Pu(V) to Pu(IV) on pure goethite at room temperature has been observed in the past and is hypothesized to be caused by radiolytic reactions within the system (see section 7.3).

Cryogenic cooling of samples has been shown to mitigate this type of beam-induced chemistry in iron oxide minerals [37] (also see section 7.3). The difficulty with cryogenically cooling microprobe samples is due to the vibrational coupling of the cooling system to the sample. If the microprobe sample moves by significantly more than the spot size of the microprobe X-ray beam, then the spatial resolution of the technique is ruined. This is an even larger problem for spectroscopic methods such as μ-XANES or μ-EXAFS. The equipment necessary to cool microprobe samples without adding a significant amount of vibration to the sample itself is currently being developed by S. Webb at SSRL.

Given the possibility that a portion of the Pu(IV) present in the μ-XANES measurements may be due to beam-induced reduction and the large errors associated with the oxidation state fitting, it would be prudent to qualitatively assign the presence of Pu(IV) and Pu(V) at these microprobe sample positions as opposed to putting significant weight on the exact quantitative fit. The presence of Pu(IV) and Pu(V) was also detected on similar manganese-substituted minerals using the bulk XAS measurement technique at approximately pH 6, although in those measurements the majority of the plutonium was in the pentavalent state [68].

The false color images shown in figure 7.26 are elemental heat maps for (a) iron, (b) manganese, and (c) plutonium in a mixed goethite / 1 % manganese-substituted goethite sample

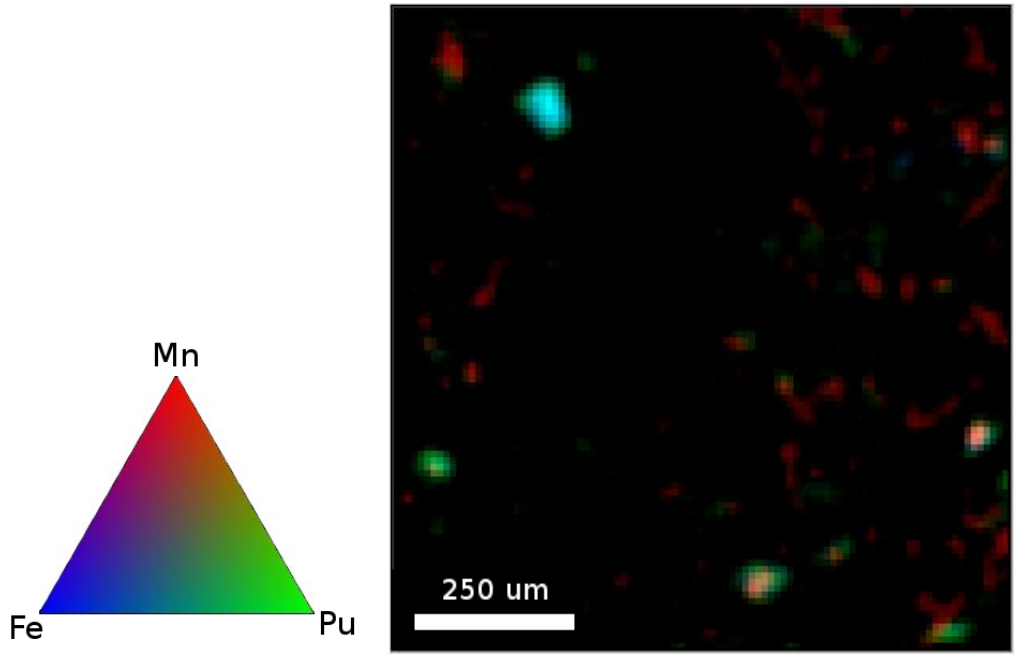

Figure 7.27: Tri-color plot of iron, manganese, and plutonium for mixed goethite / 1 % manganese-substituted goethite sample in a mineral solution at pH 6.87.

in a mineral solution at pH 6.87. A large grain of goethite is clearly visible in the top-left corner of the iron elemental heat map while three smaller grains of manganese-substituted goethite are visible on the bottom-right area of the manganese elemental heat map. The plutonium elemental heat map shows concentrated spots in the top-left and bottom-right regions of the image, indicating association with both goethite and manganese-substituted goethite. The less noisy plutonium heat map background indicates that more of the plutonium has concentrated on and around solid mineral grains as opposed to being in solution. This is also supported by the bulk sorption of plutonium on the surface of manganese-substituted goethite at pH 6.87 (see figure 7.21).

In the tri-color plot of the data from figure 7.26 (shown in figure 7.27) plutonium spatial correlation can be seen for both goethite (cyan color in the top-left corner) and manganese-substituted goethite (red-yellow color in the bottom-right corner) with no significant preference for either goethite or manganese-substituted goethite. Elemental maps for this sample were also measured at various incident X-ray energies covering the Pu L_{III}-edge. PCA conducted on these maps showed two distinct plutonium edge species that are being attributed to Pu(IV) and Pu(V). However, the analysis did not show significant preference of one component over another on either goethite or manganese-substituted goethite mineral grains.

The false color images shown in figure 7.28 are elemental heat maps for (a) iron, (b) manganese, and (c) plutonium in a mixed goethite / 1 % manganese-substituted goethite sample in a mineral solution at pH 8.56. The bulk sorption of plutonium on the surface of manganese-substituted goethite shows a maximum at approximately this pH value (see figure 7.21). A large grain of goethite is clearly visible in the lower-middle portion of the iron elemental heat map with a region of manganese-substituted goethite around the left side

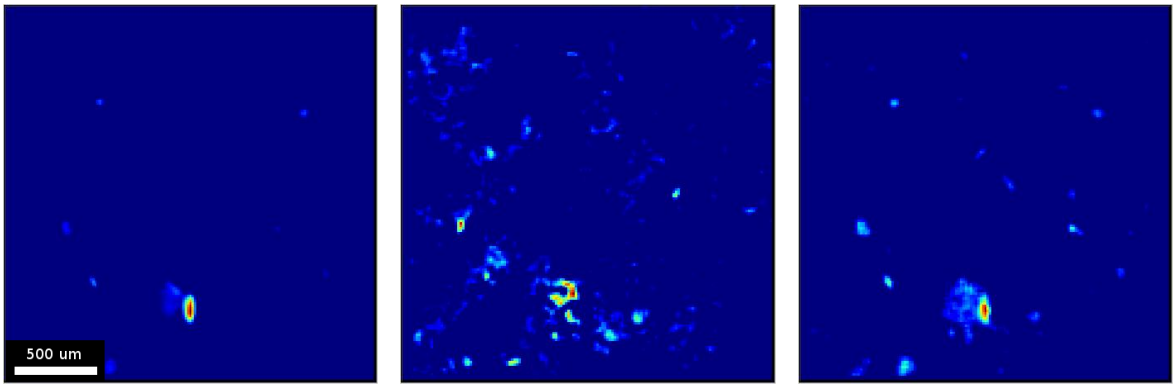

(a) Fe (b) Mn (c) Pu

Figure 7.28: Elemental heat maps for mixed goethite / 1 % manganese-substituted goethite sample in a mineral solution at pH 8.56.

of the goethite grain. The plutonium elemental heat map shows accumulation near both goethite and manganese-substituted goethite.

Position	%Pu(IV)	%Pu(V)
1	96 ± 53	26 ± 58
2	84 ± 56	33 ± 61

Table 7.6: Least-squares fits of Pu L_{III}-edge μ-XANES data at the indicated spatial position (see figure 7.29). Error bars are presented at the 1σ confidence level.

The tri-color plot for these data (figure 7.29) shows plutonium spatial correlation for both goethite (cyan color in the lower-middle region) and manganese-substituted goethite (red-yellow color to the left of the goethite region) with no significant preference for either goethite or manganese-substituted goethite. Pu L_{III}-edge μ-XANES data were collected on the microprobe sample at the indicated positions. Table 7.6 shows the least-squares fit of the data to plutonium oxidation state standards. Again, the presence of Pu(IV) and Pu(V) is suggested. The presence of Pu(IV) and Pu(V) was also detected on 1 % manganese-substituted goethite using the bulk XAS measurement technique at approximately pH 8 with the majority of the plutonium in the tetravalent state [68].

Data presented in this study suggest that Pu(VI) is not significantly preferentially sorbed on goethite or mangaese-substituted goethite. These results are in conflict with measurements from Duff *et al.* [18, 19] stating that plutonium preferentially associated with manganese-containing minerals on naturally occurring tuff from Yucca Mountain. The origin of this discrepancy is currently unclear. However, it is possible that a higher concentration of manganese is necessary to attain measurably high plutonium accumulation.

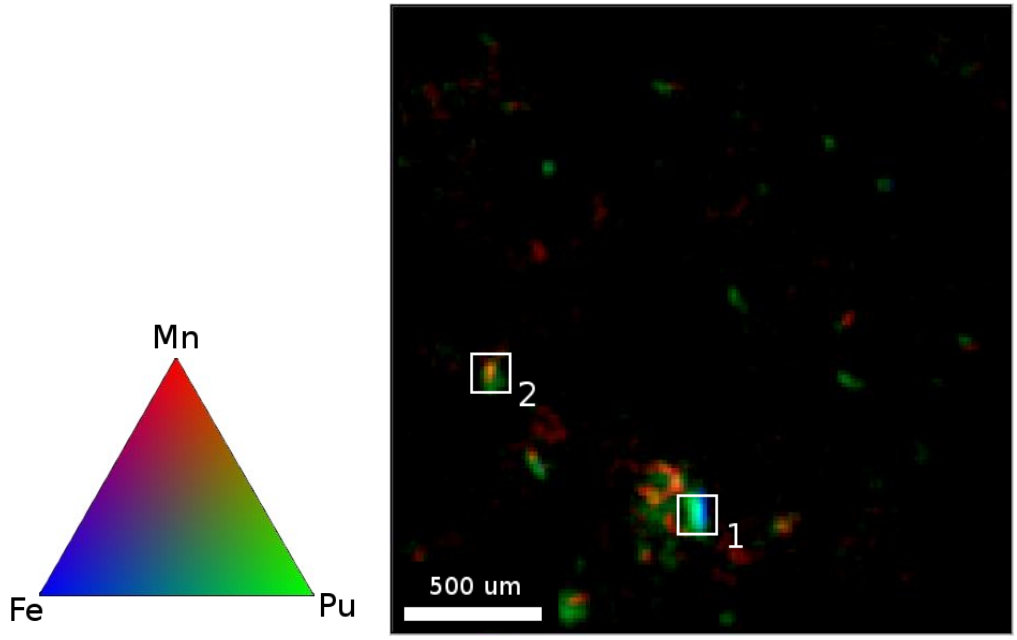

Figure 7.29: Tri-color plot of iron, manganese, and plutonium for mixed goethite / 1 % manganese-substituted goethite sample in a mineral solution at pH 8.56. White squares with accompanying numbers show positions where Pu L_{III} edge μ-XANES spectra were collected (see figure 7.25). μ-XANES fit results are shown in table 7.6.

7.5.4 Conclusions

Bulk sorption studies of Pu(VI) on the surface of 1 % manganese-substituted goethite and synchrotron X-ray microprobe analysis on mixed goethite / manganese-substituted goethite samples were conducted. Unlike previous work comparing plutonium sorption on manganese- and iron-rich environmental samples [18, 19] no significant sorption preference was shown for Pu(VI) on either goethite or manganese-substituted goethite. The presence of Pu(IV) is detected using PCA and μ-XANES techniques. However, due to the potential of beam-induced reduction of Pu(VI) and Pu(V) to Pu(IV), quantitative data concerning the plutonium oxidation state is currently unavailable. Work is currently being done to measure such samples under cyrogenic conditions, which should retard beam-induced reduction, allowing for higher quality μ-XANES and possibly μ-EXAFS data to be collected. Synchrotron based X-ray microprobe elemental fluorescence mapping and spectroscopy offers an excellent way to investigate increasingly complex model systems that better approximate real environmental samples.

Chapter 8

Conclusions and Future Work

> And a scientist — in the proper meaning of the term — is a man whose mind does not stand still.
>
> *Ayn Rand*

8.1 Conclusions

The focus of this work was a first step toward developing complex solution/mineral systems that better represent the natural environment. As a continuation of previous work by Wilson [37] of Pu(VI) sorption on the surface of the iron oxyhydroxide goethite (α-$Fe^{III}OOH$), manganese-substituted goethite, with the chemical formula $Fe^{III}_{1-x}Mn^{III}_{x}OOH$, was synthesized and characterized (see chapter 4). Bulk sorption studies of Pu(VI) on manganese-substituted goethite showed similar sorption properties as a function of pH to goethite when the mineral surface area is taken into account (see section 7.5).

Bulk XANES data of Pu(VI) sorbed onto manganese-substituted goethite showed reduction of the plutonium from Pu(VI) down to Pu(V) and Pu(IV), a marked difference from previous studies on goethite. This reduction appears to be pH dependent on the mineral solution, and is currently being attributed to the presence of manganese in the mineral system. EXAFS data confirms the proportion of Pu(V) and Pu(IV) in the wet paste sample. EXAFS data also confirms that the plutonium species is sorbed to the mineral surface as an inner-sphere species, with hydroxide complexation at higher pH values and possible carbonate complexation as well (see section 7.4). At the sample pH values all these species are available in solution for sorption onto the mineral surface (see figure 5.3).

Synchrotron hard X-ray microprobe fluorescence imaging and μ-XANES measurements were conducted on samples of Pu(VI) sorbed on a mineral solution containing a mixture of goethite and manganese-substituted goethite (see section 7.5). The images spatially resolved different grains of goethite and manganese-substituted goethite and showed sorption of plutonium on both types of minerals with no significant preference for either mineral. μ-XANES spectra showed the presence of Pu(IV) and Pu(V) associated with mineral grains,

while principle component analysis (PCA) suggested the presence of two different plutonium species in the microprobe sample.

The role of stochastic noise in the measurement of EXAFS spectra was examined through the use of Monte Carlo computer simulations (see section 7.2). Stochastic noise dominates EXAFS spectra of environmental samples where the element of interest is present in very low concentration. The simulation method developed here allows the experimenter to predetermine the quality of the measured data necessary to fit a proposed model with a certain level of statistical significance. Such knowledge can be acquired through simulation before taking physical samples to a synchrotron beamline source, allowing the experimenter to prioritize precious synchrotron beamtime and rule out intractable systems.

Scientific computing was used to propagate error from thermodynamic stability constants into calculated speciation diagrams through the use of Monte Carlo sampling (see section 5.3). Such calculations show the strong dependence of solution species on measured thermodynamic stability constant errors and help in modeling possible surface sorption species by defining available solution species as a function of solution pH.

X-ray beam-induced reduction of plutonium has previously been shown to occur at room temperature on samples of plutonium sorbed on iron oxide minerals [37]. Careful re-analysis of these data, in addition to data collected from plutonium sorbed on manganese-substituted goethite and plutonium sorbed on acetamide phosphonate functionalized mesoporous silica, suggests that beam-induced chemistry is occurring through radiolytic generation of hydrogen peroxide and free radicals produced by X-ray interaction with the water present in these samples. Cryogenically cooling samples mitigates the reaction of peroxide and some free radicals with the sample (see section 7.3).

8.2 Future Work

In an attempt to further develop and probe complex model systems that represent the natural environment, future work should focus on other possible minor mineral substitutions to major mineral phases. For example, both aluminum-substituted and chromium-substituted goethite minerals have been synthesized in the past and may prove to be interesting mineral substrates for plutonium sorption.

More emphasis should also be placed on ternary complexes containing actinides (Ac), organic ligands (Org), and mineral surfaces (M). Understanding the structure of such ternary systems (M-Ac-Org vs. M-Org-Ac) in aqueous solution will have major implications in elucidating actinide migration in the geosphere. Atom-specific spectroscopies such as XAS should be capable of probing such samples *in situ* and be able to resolve the bonding structure.

Other potential topics of study include understanding actinide incorporation into mineral structures. Synthesizing goethite in the presence of a small amount of plutonium may yield interesting mineral substitutions similar to the manganese substituted goethite prepared in this study. This includes the possibility of interesting coordination environments for plutonium. Such topics are important when trying to understand long-term incorporation of actinides in the geosphere.

More work also needs to be done in comparing XANES computational calculations with experimental measurements. The importance of using XANES to elucidate local structure

cannot be understated. Currently, XANES is mostly used as an oxidation state probe for the actinide elements, but being able to measure the full density of states at the absorption edge with techniques like partial fluorescence yield (PFY) spectroscopy and resonant inelastic X-ray scattering (RIXS) will allow experimenters to acquire complete geometric information on a particular sample. Measurement of the white line of the absorption edge is also more sensitive (greater signal-to-noise) than acquiring structural information through EXAFS measurements. Advanced, accurate *ab initio* calculations will allow experimenters to test theories and understand features present in XANES spectra that would be difficult or impossible to check through experiments alone.

Finally, further work must be done in developing and adapting new molecular-level measurement techniques, including adapting microprobe measurements for cyrogenically cooled samples. In recent years, the field of actinide chemistry has also seen a growth in the use of X-ray scattering techniques to measure amorphous and non-crystalline samples. Although X-ray scattering is not intrinsically an atom-specific probe, scattering does occur more intensely for elements with more electrons, such as the actinides. Furthermore, the high-energy photons necessary for high-resolution X-ray scattering are less likely to interact with the sample through processes such as radiolysis, thus possibly minimizing the beam-induced chemistry seen for some samples in this study.

Bibliography

[1] G. E. Brown, A. L. Foster, and J. D. Ostergren, Proceedings of the National Academy of Sciences **96**, 3388 (1999), 10.1073/pnas.96.7.3388.

[2] T. Fanghänel and V. Neck, Pure and Applied Chemistry **74**, 1895 (2002).

[3] B. Goodwin, Canadian Journal of Chemistry (1982).

[4] R. Knopp, V. Neck, and J. I. Kim, Radiochimica Acta **86**, 101 (1999).

[5] J. A. Leary, A. N. Morgan, and W. J. Maraman, Industrial and Engineering Chemistry **51**, 27 (1959).

[6] L. Soderholm, P. M. Almond, S. Skanthakumar, R. E. Wilson, and P. C. Burns, Angewandte Chemie International Edition **47**, 298 (2007).

[7] V. Neck and J. I. Kim, Radiochimica Acta **89**, 1 (2001).

[8] V. Neck, M. Altmaier, and T. Fanghänel, Comptes Rendus Chimie **10**, 959 (2007).

[9] M. A. Denecke, T. Reich, M. Bubner, S. Pompe, K. H. Heise, H. Nitsche, P. G. Allen, J. J. Bucher, N. M. Edelstein, and D. K. Shuh, Journals of Alloys and Compounds **271-273**, 123 (1998).

[10] D. Vulpius, G. Geipel, L. Baraniak, and G. Bernhard, Spectrochimica Acta Part A **63**, 603 (2006).

[11] P. G. Allen, J. J. Bucher, D. L. Clark, N. M. Edelstein, S. A. Ekberg, J. W. Gohdes, E. A. Hudson, N. Kaltsoyannis, and W. W. Lukens, Inorganic Chemistry **34**, 4797 (1995), doi: 10.1021/ic00123a013.

[12] P. G. Allen, D. K. Veirs, S. D. Conradson, C. A. Smith, and S. F. Marsh, Inorganic Chemistry **35**, 2841 (1996), 10.1021/ic9511231.

[13] H. Nitsche, E. M. Standifer, and R. J. Silva, Lanthanide and Actinide Research **3**, 203 (1990).

[14] C. Nguyen-Trung, G. M. Begun, and D. A. Palmer, Inorganic Chemistry **31**, 5280 (1992).

[15] D. L. Clark, D. E. Hobart, and M. P. Neu, Chemical Reviews **95**, 25 (1995).

[16] D. Xu, X. K. Wang, C. L. Chen, X. Zhou, and X. L. Tan, Radiochimica Acta **94**, 429 (2006).

[17] J. R. Bargar, R. Reitmeyer, J. J. Lenhart, and J. A. Davis, Geochimica et Cosmochimica Acta **64**, 2737 (2000).

[18] M. C. Duff, D. B. Hunter, I. R. Triay, P. M. Bertsch, D. T. Reed, S. R. Sutton, G. Shea-McCarthy, J. Kitten, P. Eng, S. J. Chipera, and D. T. Vaniman, Environ. Sci. Technol. **33**, 2163 (1999).

[19] M. C. Duff, M. Newville, D. B. Hunter, P. M. Bertsch, S. R. Sutton, I. R. Triay, D. T. Vaniman, P. Eng, and M. L. Rivers, J. Synchrotron Rad. **6**, 350 (1999).

[20] D. A. Shaughnessy, H. Nitsche, C. H. Booth, D. K. Shuh, G. A. Waychunas, R. E. Wilson, H. Gill, K. J. Cantrell, and R. J. Serne, Environ. Sci. Technol. **37**, 3367 (2003), 10.1021/es025989z.

[21] B. A. Powell, R. A. Fjeld, D. I. Kaplan, J. T. Coates, and S. M. Serkiz, Environmental Science and Technology **38**, 6016 (2004), doi: 10.1021/es049386u.

[22] B. A. Powell, M. C. Duff, D. I. Kaplan, R. A. Fjeld, M. Newville, D. B. Hunter, P. M. Bertsch, J. T. Coates, P. Eng, M. L. Rivers, S. M. Serkiz, S. R. Sutton, I. R. Triay, and D. T. Vaniman, Environmental Science and Technology **40**, 3508 (2006), doi: 10.1021/es052353+.

[23] A. L. Sanchez, J. W. Murray, and T. H. Sibley, Geochimica et Cosmochimica Acta **49**, 2297 (1985).

[24] W. L. Keeney-Kennicutt and J. W. Morse, Geochimica Et Cosmochimica Acta **49**, 2577 (1985).

[25] W. R. Penrose, D. N. Metta, J. M. Hylko, and L. A. Rinckel, Journal of Environmental Radioactivity **5**, 169 (1987).

[26] K. Nakata, S. Nagasaki, S. Tanaka, Y. Sakamoto, T. Tanaka, and H. Ogawa, Radiochimica Acta **90**, 665 (2002).

[27] S. Kihara, Z. Yoshida, H. Aoyagi, K. Maeda, O. Shirai, Y. Kitatsuji, and Y. Yoshida, Pure and Applied Chemistry **71**, 1771 (1999).

[28] G. R. Choppin, A. H. Bond, and P. M. Hromadka, Journal of Radioanalytical and Nuclear Chemistry **219**, 203 (1997).

[29] A. Morgenstern and G. R. Choppin, Radiochimica Acta **90**, 69 (2002).

[30] S. E. Horowitz and J. B. Marston, (2010), arXiv:1009.4343v1 [cond-mat.str-el].

[31] C. Hennig, P. J. Panak, T. Reich, A. Roßberg, J. Raff, S. Selenska-Pobell, W. Matz, J. J. Bucher, G. Bernhard, and H. Nitsche, Radiochim. Acta **89**, 625 (2001).

[32] P. J. Panak and H. Nitsche, Radiochimica Acta **89**, 499 (2001).

[33] P. J. Panak, C. H. Booth, D. L. Caulder, J. J. Bucher, D. K. Shuh, and H. Nitsche, Radiochimica Acta **90**, 315 (2002).

[34] P. J. Panak, R. Knopp, C. H. Booth, and H. Nitsche, Radiochimica Acta **90**, 779 (2002).

[35] W. Runde, Los Alamos Science 392 (2000).

[36] R. J. Silva and H. Nitsche, Radiochimica Acta **70-71**, 377 (1995).

[37] R. E. Wilson, Ph.D. thesis, University of California, Berkeley, 2005.

[38] P. Debye and E. Hückel, Physikalische Zeitschrift **24**, 185 (1923).

[39] *CRC Handbook of Chemistry and Physics*, 77 ed., edited by L. Gevantman (CRC Press, Boca Raton, FL, 1996).

[40] R. J. Lemire, J. Fuger, K. Spahiu, J. C. Sullivan, H. Nitsche, W. J. Ullman, P. Potter, P. Vitorge, M. H. Rand, H. Wanner, and J. Rydberg, *Chemical Thermodynamics of Neptunium and Plutonium*, Vol. 4 of *Chemical Thermodynamics*, oecd nuclear energy agency ed. (Elsevier, Amsterdamn, The Netherlands, 2001).

[41] R. Guillaumont, T. Fanghänel, V. Neck, J. Fuger, D. A. Palmer, I. Grenthe, and M. H. Rand, in *Update on the Chemical Thermodynamics of Uranium, Neptunium, Plutonium, Americium and Technetium*, Vol. 5 of *Chemical Thermodynamics*, oecd nuclear energy agency ed., edited by F. J. Mompean, M. Illemassene, C. Domenech-Orti, and K. Ben Said (Elsevier, Amsterdamn, The Netherlands, 2003).

[42] D. C. Harris, *Quantitiative Chemical Analysis*, 5th ed. (W. H. Freeman and Company, New York, 1999).

[43] D. L. Parkhurst and C. A. J. Appelo, Technical Report No. U.S. Geological Survey Water-Resources Investigations Report 99-4259, 1999 (unpublished).

[44] 2010, www.mineql.com.

[45] 2010, http://www.rockware.com.

[46] J. R. Taylor, *An Introduction to Error Analysis the Study of Uncertainties in Physical Measurements*, 2nd ed. (University Science Books, Sausalito, California, 1997).

[47] N. Tsoulfanidis, *Measurement and Detection of Radiation*, 2^{nd} ed. (Taylor & Francis, Washington, DC, 1995).

[48] M. Bulmer, *Principles of Statistics*, 2nd ed. (Dover Publications, New York, 1979).

[49] P. R. Bevington, *Data Reduction and Error Analysis for the Physical Sciences*, 1st ed. (McGraw-Hill Book Company, Columbus, Ohio, 1969).

[50] L. Lyons, *Statistics for nuclear and particle physicists* (Cambridge University Press, New York, 1986).

[51] C. Ekberg, A. Ödegaard Jensen, and G. Meinrath, Technical report, Swedish Nuclear Power Inspectorate, 2003 (unpublished).

[52] A. Ödegaard Jensen, C. Ekberg, and G. Meinrath, Talanta **63**, 907 (2004).

[53] W. Stumm, *Chemistry of the Solid-Water Interface*, 2nd ed. (J.Wiley and Sons, Inc., Indianapolis, IN, 1992).

[54] P. Tans, 2010, www.esrl.noaa.gov/gmd/ccgg/trends/.

[55] 2010, http://www.rxlist.com/kayexalate-drug.htm.

[56] G. A. Parks and P. L. De Bruyn, Journal of Physical Chemistry **66**, 967 (1962), 10.1021/j100812a002.

[57] J. S. Noh and J. A. Schwarz, Journal of Colloid and Interface Science **130**, 157 (1989), 10.1016/0021-9797(89)90086-6.

[58] K. Jiratova, Applied Catalysis **1**, 165 (1981).

[59] M. Mullet, P. Fievet, J. C. Reggiani, and J. Pagetti, Journal of Membrane Science **123**, 255 (1997).

[60] S. Mustafa, B. Dilara, K. Nargis, A. Naeem, and P. Shahida, Colloids and Surfaces a-Physicochemical and Engineering Aspects **205**, 273 (2002).

[61] M. Kosmulski, Journal of Colloid and Interface Science **253**, 77 (2002).

[62] F. A. Tourinho, A. F. C. Campos, R. Aquino, M. Lara, G. J. da Silva, and J. Depeyrot, Brazilian Journal of Physics **32**, 501 (2002).

[63] G. Sposito, *The Chemistry of Soils* (Oxford University Press, New York, 1989).

[64] B. J. Alloway, D. E. Baker, B. E. Davies, R. Edwards, K. C. Jones, L. Kiekens, N. W. Lepp, S. P. McGrath, R. H. Neal, P. O'Neill, J. E. Paterson, J. P. Senft, K. A. Smith, E. Steinnes, and A. M. Ure, in *Heavy Metals in Soils*, 2nd ed., edited by B. J. Alloway (Blackie Academic & Professional, London, UK, 1995).

[65] G. Sposito, *The Surface Chemistry of Soils* (Oxford University Press, New York, 1984).

[66] J. A. Coston, C. C. Fuller, and J. A. Davis, Geochimica Et Cosmochimica Acta **59**, 3535 (1995).

[67] C.-K. D. Hsi and D. Langmuir, Geochimica Et Cosmochimica Acta **49**, 1931 (1985), doi: DOI: 10.1016/0016-7037(85)90088-2.

[68] Y.-J. Hu, L. K. Schwaiger, C. H. Booth, R. K. Kukkadapu, E. Cristiano, D. I. Kaplan, and H. Nitsche, Radiochimica Acta **98**, (2010).

[69] D. I. Kaplan, B. A. Powell, D. I. Demirkanli, R. A. Fjeld, F. J. Molz, S. M. Serkiz, and J. T. Coates, Environmental Science and Technology **38**, 5053 (2004), doi: 10.1021/es049406s.

[70] B. A. Powell, R. A. Fjeld, D. I. Kaplan, J. T. Coates, and S. M. Serkiz, Environmental Science and Technology **39**, 2107 (2005), doi: 10.1021/es0487168.

[71] R. M. Cornell and U. Schwertmann, *The Iron Oxides* (John Wiley and Sons Ltd., New York, 1997).

[72] J. B. Dixon and S. B. Weed, *Minerals in Soil Environments*, *Soil Science Society of America Book Series*, 2nd ed. (Soil Science Society of America, Madison, 1989).

[73] A. Gualtieri and P. Venturelli, American Mineralogist **84**, 895 (1999).

[74] E. Cristiano, Y.-J. Hu, M. M. Siegfried, D. I. Kaplan, and H. Nitsche, "A Comparison of Point-of-Zero Charge Measurement Methodology" submitted to Clays and Clay Minerals (2011).

[75] U. Schwertmann and R. M. Cornell, *Iron Oxides in the Laboratory*, 2nd ed. (Wiley-VCH Publishers, Inc., Weinheim, 1991).

[76] R. M. Cornell and R. Giovanoli, Clays and Clay Minerals **35**, 11 (1987).

[77] W. Stiers and U. Schwertmann, Geochimica Et Cosmochimica Acta **49**, 1909 (1985).

[78] C. H. Booth, 2006, http://lise.lbl.gov/RSXAP/.

[79] G. G. Li, F. Bridges, and C. H. Booth, Phys. Rev. B **52**, 6332 (1995).

[80] W. H. McMaster, N. Kerr Del Grande, J. H. Mallett, and J. H. Hubbell, *Compilation of X-Ray Cross Sections* (National Institute of Standards and Technology, Gaithersburg, MD, 1995).

[81] M. Alvarez, E. H. Rueda, and E. E. Sileo, Geochimica Et Cosmochimica Acta **71**, 1009 (2007).

[82] E. E. Sileo, M. Alvarez, and E. H. Rueda, International Journal of Inorganic Materials **3**, 271 (2001).

[83] J. Y. Ping, D. G. Rancourt, and Z. M. Stadnik, Hyperfine Interactions **69**, 493 (1991).

[84] L. Meitner and O. R. Frisch, Nature **143**, 239 (1939).

[85] G. T. Seaborg, E. M. McMillan, J. W. Kennedy, and A. C. Wahl, Phys. Rev. **69**, 366 (1946).

[86] G. T. Seaborg, A. C. Wahl, and J. W. Kennedy, Phys. Rev. **69**, 367 (1946).

[87] D. C. Hoffman, F. O. Lawrence, J. L. Mewherter, and F. M. Rourke, Nature **234**, 132 (1971).

[88] Technical report, OECD Nuclear Energy Agency, 2010, (unpublished), http://www.nea.fr/dbdata/x4/.

[89] J. W. Kennedy, G. T. Seaborg, E. Segrè, and A. C. Wahl, Phys. Rev. **70**, 555 (1946).

[90] J. K. Shultis and R. E. Faw, *Fundamentals of Nuclear Science and Engineering*, 2nd ed. (CRC Press, Boca Raton, FL, 2007).

[91] L. Pauling, *General Chemistry*, 3rd ed. (Dover Publications, New York, 1970).

[92] D. C. Hoffman, in *Advances in Plutonium Chemistry 1967-2000*, edited by D. C. Hoffman (The American Nuclear Society, La Grange Park, Illinois, 2002), Chap. 1, pp. 1–5.

[93] G. Friedlander, J. Kennedy, E. Macias, and J. Miller, in *Nuclear and Radiochemistry*, 3rd ed. (John Wiley and Sons, New York, 1981), Chap. 4, p. 161.

[94] J. M. Cleveland, *The Chemistry of Plutonium*, 2nd ed. (American Nuclear Society, La Grange Park, IL, 1979).

[95] R. E. Connick, Journal of the American Chemical Society **71**, 1528 (1949).

[96] H. Steele and R. J. Taylor, Inorganic Chemistry **46**, 6311 (2007).

[97] B. Lesigne, Technical Report No. RFP-Trans-47, United States Atomic Energy Comission, 1967 (unpublished).

[98] K. Nash, M. E. Noon, S. Fried, and J. C. Sullivan, Inorganic and Nuclear Chemistry Letters **16**, 33 (1980).

[99] R. E. Wilson, Y.-J. Hu, and H. Nitsche, Radiochimica Acta **93**, 203 (2005).

[100] L. Sémon, C. Boehme, I. Billard, C. Hennig, K. Lützenkirchen, T. Reich, A. Roßberg, I. Rossini, and G. Wipff, ChemPhysChem **2**, 591 (2001).

[101] D. Cohen, Journal of Inorganic and Nuclear Chemistry **18**, 211 (1961).

[102] H. Nitsche, J. Alloys Compd. **223**, 274 (1995).

[103] S. D. Conradson, Applied Spectroscopy **52**, 252A (1998).

[104] S. D. Conradson, I. Al Mahamid, D. L. Clark, N. J. Hess, E. A. Hudson, M. P. Neu, P. D. Palmer, W. H. Runde, and C. D. Tait, Polyhedron **17**, 599 (1998).

[105] S. D. Conradson, D. L. Clark, M. P. Neu, W. Runde, and C. D. Tait, Los Alamos Science 364 (2000).

[106] E. A. Hudson, P. G. Allen, and L. J. Terminello, Phys. Rev. B **54**, 156 (1996).

[107] K. F. Hayes, A. L. Roe, G. E. J. Brown, K. O. Hodgson, J. O. Leckie, and G. A. Parks, Science **238**, 783 (1987).

[108] C. J. Chisholm-Brause, A. L. Roe, K. F. Hayes, G. E. J. Brown, G. A. Parks, and J. O. Leckie, Physica B: Condensed Matter **158**, 674 (1989).

[109] D. Iwanenko and I. Pomeranchuk, Phys. Rev. **65**, 343 (1944).

[110] F. R. Elder, A. M. Gurewitsch, R. V. Langmuir, and H. C. Pollock, Phys. Rev. **71**, 829 (1947).

[111] 2010, http://www.spring8.or.jp/en/about_us/whats_sr/generation_sr.

[112] D. Attwood, *Soft X-rays and Extreme Ultraviolet Radiation: Principles and Applications*, 1st ed. (Cambridge University Press, Cambridge, 1999).

[113] K. S. Krane, *Introductory Nuclear Physics* (Wiley, Hoboken, New Jersey, 1987).

[114] G. F. Knoll, *Radiation Detection and Measurement*, 3rd ed. (Wiley, San Francisco, 2000).

[115] S. C. Curran and H. W. Wilson, in *Alpha-, Beta- and Gamma-ray Spectroscopy*, edited by K. Siegbahn (North-Holland Publishing Company, Amsterdam, 1965), Vol. 1.

[116] A. Einstein, Annalen Der Physik **17**, 132 (1905).

[117] W. Kossel, Zeitschrift fr Physik A Hadrons and Nuclei **1**, 119 (1920), 10.1007/BF01881031.

[118] W. Kossel, Zeitschrift fr Physik A Hadrons and Nuclei **2**, 470 (1920), 10.1007/BF01329979.

[119] J. Victoreen, J.Appl.Phys. **19**, 855 (1948).

[120] J. J. Rehr, R. C. Albers, and S. I. Zabinsky, Physical Review Letters **69**, 3397 (1992).

[121] J. J. Rehr, A. L. Ankudinov, and S. I. Zabinsky, Catalysis Today **39**, 263 (1998).

[122] J. Stöhr, in *NEXAFS Spectroscopy*, Vol. 25 of *Springer Series in Surface Sciences*, edited by R. Gomer (Springer, Berlin, 1992).

[123] S. D. Conradson, K. D. Abney, B. D. Begg, E. D. Brady, D. L. Clark, C. den Auwer, M. Ding, P. K. Dorhout, F. J. Espinosa-Faller, P. L. Gordon, R. G. Haire, N. J. Hess, R. F. Hess, D. W. Keogh, G. H. Lander, A. J. Lupinetti, L. A. Morales, M. P. Neu, P. D. Palmer, P. Paviet-Hartmann, S. D. Reilly, W. H. Runde, C. D. Tait, D. K. Veirs, and F. Wastin, Inorganic Chemistry **43**, 116 (2003), doi: 10.1021/ic0346477.

[124] R. d. L. Kronig, Zeitschrift fr Physik A Hadrons and Nuclei **70**, 317 (1931), 10.1007/BF01339581.

[125] R. d. L. Kronig, Zeitschrift fr Physik A Hadrons and Nuclei **75**, 468 (1932), 10.1007/BF01342238.

[126] B. K. Teo, *EXAFS: Basic Principles and Data Analysis (Inorganic Chemistry Concepts)* (Springer, New York, 1986).

[127] E. A. Stern, in *X-Ray Absorption: Principles, Applications, Techniques of EXAFS, SEXAFS and XANES*, edited by D. C. Koningsberger and R. Prins (Wiley-Interscience, Hoboken, NJ, 1988).

[128] G. Bunker, *Introduction to XAFS: A practical Guide to X-ray Absorption Fine Structure Spectroscopy*, 1st ed. (Cambridge University Press, Cambridge, UK, 2010).

[129] S. I. Zabinsky, J. J. Rehr, A. Ankudinov, R. C. Albers, and M. J. Eller, Phys. Rev. B **52**, 2995 (1995).

[130] A. L. Ankudinov and J. J. Rehr, Physical Review B **56**, R1712 (1997).

[131] A. Ankudinov, Ph.D. thesis, University of Washington, 1996, this contains a review of x-ray absorption theory, a whole chapter of information about FEFF for expert users, example applications, and the full FEFF7 program tree.

[132] 2010, http://leonardo.phys.washington.edu/feff/.

[133] C. Hennig, Phys. Rev. B **75**, 035120 (2007).

[134] A. Roßberg and H. Funke, Journal of Synchrotron Radiation **17**, 280 (2010).

[135] J. R. Pierce, *An Introduction to Information Theory: Symbols, Signals and Noise*, 2nd ed. (Dover Publications, Inc., New York, NY, 1980).

[136] E. A. Stern, Phys. Rev. B **48**, 9825 (1993).

[137] 2010, http://www-ssrl.slac.stanford.edu/exafspak.html.

[138] 2010, http://www.winxas.de/.

[139] 2010, http://cars9.uchicago.edu/∼newville/feffit/.

[140] 2010, http://cars9.uchicago.edu/ifeffit/.

[141] 2010, http://cars9.uchicago.edu/∼ravel/software/aboutathena.html.

[142] 2010, http://sixpack.sams-xrays.com/.

[143] C. H. Booth and Y.-J. Hu, Journal of Physics: Conference Series **190**, (2009).

[144] C. J. J. Sparks, in *Synchrotron Radiation Research* (Plenum, New York, 1980), Chap. X-ray Fluorescence Microprobe for Chemical Analysis, pp. 459–512.

[145] A. L. Hanson, K. W. Jones, B. M. Gordon, J. G. Pounds, W. M. Kwiatek, G. J. Long, M. L. Rivers, and S. R. Sutton, Nuclear Instruments and Methods in Physics Research 400 (1987).

[146] M. A. Marcus, A. A. MacDowell, R. Celestre, A. Manceau, T. Miller, H. A. Padmore, and R. E. Sublett, Journal of Synchrotron Radiation **11**, 239 (2004).

[147] S. M. Webb, SMAK: Sam's Microprobe Analysis Kit, 2010, http://smak.sams-xrays.com/.

[148] P. M. Bertsch, D. B. Hunter, S. R. Sutton, S. Bajt, and M. L. Rivers, Environ. Sci. Technol. **28**, 980 (1994).

[149] Y.-J. Hu and C. H. Booth, Journal of Physics: Conference Series **190**, (2009).

[150] E. Curis, J. Osn, G. Falkenberg, S. Bnazeth, and S. Trk, Spectrochim. Acta, Part B **60**, 841 (2005).

[151] G. Li, F. Bridges, and X. Wang, Nucl. Instrum. Meth. A **340**, 420 (1994).

[152] W. C. Hamilton, Acta Cryst. **18**, 502 (1965).

[153] L. Downward, C. H. Booth, W. W. Lukens, and F. Bridges, AIP Conference Proceedings **882**, (2006).

[154] M. Matsumoto and T. Nishimura, ACM Trans. Model. Comput. Simul. **8**, 3 (1998).

[155] G. van Rossum, Proc 1991 EurOpen Spring Conf. (1991), Python, Available at http://www.python.org.

[156] A. Bacchi, V. S. Lamzin, and K. S. Wilson, Acta Cryst. D **52**, 641 (1996).

[157] R. G. Sowden, Journal of Nuclear Materials **8**, 81 (1963).

[158] M. Weik, R. Ravelli, G. Kryger, S. McSweeney, M. Raves, M. Harel, P. Gros, I. Silman, J. Kroon, and J. Sussman, Proceedings of the National Academy of Sciences of the United States of America **97**, 623 (2000).

[159] W. Burmeister, Acta Crystallographica Section D - Biological Crystallography **56**, 328 (2000).

[160] R. Ravelli and S. McSweeney, Structure **8**, 315 (2000).

[161] S. Maleknia, C. Ralston, M. Brenowitz, K. Downard, and M. Chance, Analytical Biochemistry **289**, 103 (2001).

[162] J. Guan, S. Vorobiev, S. Almo, and M. Chance, Biochemistry **41**, 5765 (2002).

[163] G. Xu and M. Chance, Analytical Chemistry **77**, 2437 (2005).

[164] D. Zhao, J. Feng, Q. Huo, N. Melosh, G. Fredrickson, B. Chmelka, and G. Stucky, Science **279**, 548 (1998).

[165] J. Birnbaum, B. Busche, Y. Lin, W. Shaw, and G. Fryxell, Chemical Communications 1374 (2002).

[166] G. E. Fryxell, Inorganic Chemistry Communications **9**, 1141 (2006).

[167] *Radiation Chemistry: Principles and Applications*, edited by Farhataziz and M. A. J. Rogers (VCH Publishers, Inc., New York, New York, 1987).

[168] A. Mozumder, *Fundamentals of Radiation Chemistry* (Academic Press, San Diego, California, 1999).

[169] C. J. Hochanadel, Journal of Physical Chemistry **56**, 587 (1952).

[170] A. O. Allen, C. J. Hochanadel, J. A. Ghormley, and T. W. Davis, Journal of Physical Chemistry **56**, 575 (1952).

[171] Z. D. Draganić and I. G. Draganić, Journal of Physical Chemistry **73**, 2571 (1969).

[172] Z. D. Draganić and I. G. Draganić, Journal of Physical Chemistry **75**, 3950 (1971).

[173] A. Hiroki, S. Pimblott, and J. LaVerne, Journal of Physical Chemistry A **106**, 9352 (2002).

[174] B. C. Garrett, D. A. Dixon, D. M. Camaioni, D. M. Chipman, M. A. Johnson, C. D. Jonah, G. A. Kimmel, J. H. Miller, T. N. Rescigno, P. J. Rossky, S. S. Xantheas, S. D. Colson, A. H. Laufer, D. Ray, P. F. Barbara, D. M. Bartels, K. H. Becker, H. Bowen, S. E. Bradforth, I. Carmichael, J. V. Coe, L. R. Corrales, J. P. Cowin, M. Dupuis, K. B. Eisenthal, J. A. Franz, M. S. Gutowski, K. D. Jordan, B. D. Kay, J. A. LaVerne, S. V. Lymar, T. E. Madey, C. W. McCurdy, D. Meisel, S. Mukamel, A. R. Nilsson, T. M. Orlando, N. G. Petrik, S. M. Pimblott, J. R. Rustad, G. K. Schenter, S. J. Singer, A. Tokmakoff, L. S. Wang, C. Wittig, and T. S. Zwier, Chemical Reviews **105**, 355 (2005).

[175] G. V. Buxton and R. M. Sellers, Coordination Chemistry Reviews **22**, 195 (1977).

[176] T. W. Newton, D. E. Hobart, and P. D. Palmer, Radiochimica Acta **39**, 139 (1986).

[177] K. Büppelmann, J. I. Kim, and C. Lierse, Radiochimica Acta **44-5**, 65 (1988).

[178] J. H. Baxendale, Radiation Research Supplement **S**, 139 (1964).

[179] G. P. J. Haight, Journal of Chemical Education **53**, 693 (1976).

[180] T. W. Newton, *The Kinetics of the Oxidation-Reduction Reactions of Uranium, Neptunium, Plutonium, and Americium in Aqueous Solutions* (U.S. Energy Research and Development Administration Technical Information Center, Oak Ridge, TN, 1975).

[181] C. Keller, in *The Chemistry of the Transuranium Elements*, Vol. 3 of *Kernchemie in Einzeldarstellungen*, edited by K. H. Lieser (Großdruckerei Erich Spandel, Nürnberg, Germany, 1971).

[182] C. W. Sill, D. R. Percival, and R. L. Williams, Analytical Chemistry **42**, 1273 (1970).

[183] A. K. Pikaev, M. P. Mefodeva, N. N. Krot, and V. I. Spitsyn, Bulletin of the Academy of Sciences of the USSR Division of Chemical Science **23**, 2751 (1974).

[184] A. Morgenstern and G. R. Choppin, Radiochimica Acta **86**, 109 (1999).

[185] G. V. Buxton, H. A. Gillis, and N. V. Klassen, Canadian Journal of Chemistry **55**, 2385 (1977).

[186] J. V. Beitz and J. R. Miller, Journal of Chemical Physics **71**, 4579 (1979).

[187] P. Rotureau, J. P. Renault, B. Lebeau, J. Patarin, and J. C. Mialocq, ChemPhysChem **6**, 1316 (2005).

[188] M. Nakashima and E. Tachikawa, Radiochimica Acta **33**, 217 (1983).

[189] M. Nakashima and N. M. Masaki, Radiation Physics and Chemistry **47**, 241 (1996).

[190] S. Le Caër, J. P. Renault, and J. C. Mialocq, Chemical Physics Letters **450**, 91 (2007).

[191] S. Foley, P. Rotureau, S. Pin, G. Baldacchino, J. P. Renault, and J. C. Mialocq, Angewandte Chemie - International Edition **44**, 110 (2005).

[192] D. Meyerstein, Accounts of Chemical Research **11**, 43 (1978).

[193] G. R. Choppin, Radiochimica Acta **91**, 645 (2003).

[194] G. R. Choppin and L. F. Rao, Radiochimica Acta **37**, 143 (1984).

[195] D. L. Clark, S. D. Conradson, R. J. Donohoe, D. W. Keogh, D. E. Morris, P. D. Palmer, R. D. Rogers, and C. D. Tait, Inorganic Chemistry **38**, 1456 (1999), doi: 10.1021/ic981137h.

[196] K. W. Jones, W. J. Berry, D. J. Borsay, H. T. Cline, W. C. Conner Jr., and C. S. Fullmer, X-Ray Spectrometry **26**, 350 (1997).

[197] J. Lechelle, P. Bleuet, P. Martin, E. Girard, F. Bruguier, M. A. Martinez, A. Somogyi, A. Simionovici, M. Ripert, F. Valdivieso, and P. Goeuriot, IEEE Transactions on Nuclear Science **51**, 1657 (2004).

[198] D. B. Hunter and P. M. Bertsch, Journal of Radioanalytical and Nuclear Chemistry **234**, 237 (1998).

[199] J. G. Catalano, J. P. McKinley, J. M. Zachara, S. M. Heald, S. C. Smith, and G. E. Brown, Environmental Science & Technology **40**, 2517 (2006).

[200] Y. Arai, M. A. Marcus, N. Tamura, J. A. Davis, and J. M. Zachara, Environ. Sci. Technol. **41**, 4633 (2007).

[201] A. Manceau, M. A. Marcus, and N. Tamura, Reviews in Mineralogy and Geochemistry **49**, 341 (2002).

[202] A. A. Schilt, in *Perchloric Acid and Perchlorates*, 2nd ed., edited by L. C. McBride and J. R. Long (GFS Chemicals, Inc., P.O. Box 245 Powell, Ohio 43065, 2003).

[203] B. Rodgers, Technical report, Research Solutions & Resoruces, 2003, (unpublished), http://www.consultrsr.com/resources/ref/agcl.htm.

[204] D. Cohen, Journal of Inorganic and Nuclear Chemistry **18**, 207 (1961).

[205] J. Kleinberg, Technical Report No. LA-1721, 5th Ed., Los Alamos National Laboratory, 1990 (unpublished).

[206] 2010, http://www.originlab.com/.

[207] 2010, http://www.wavemetrics.com/.

[208] F. P. Brooks, *The Mythical Man-Month: Essays on Software Engineering, Anniversary Edition*, 2nd ed. (Addison-Wesley Professional, Reading, Massachusetts, 1995).

[209] D. M. Etter, *Structured Fortran 77 for Engineers and Scientists*, 2nd ed. (The Mengamin/Cummings Publishing Company, Inc., Menlo Park, California, 1987).

[210] M. Kupferschmid, *Classical FORTRAN: Programming for Engineering and Scientific Applications* (Marcel Dekker, Inc., New York, 2002).

[211] M. Lutz and D. Ascher, *Learning Python*, 2nd ed. (O'Reilly Media, Sebastopol, California, 2003).

[212] M. Lutz, *Programming Python*, 3rd ed. (O'Reilly Media, Sebastopol, California, 2006).

[213] H. P. Langtangen, *Python Scripting for Computational Science*, 2nd ed. (Springer, New York, 2005).

[214] S. Tosi, *Matplotlib for Python Developers* (Packt Publishing, Birmingham, UK, 2009).

Appendix A

Perchloric Acid and Perchlorates

Working with plutonium doesn't bother me at all. What's scary is how you guys use perchloric acid.

Prof. Darleane C. Hoffman

It used to be that a chemist could do any chemistry he wanted, as long as he killed only himself.

Dr. David L. Clark

A.1 Introduction

Perchloric acid and perchlorate salts, usually sodium perchlorate, are used extensively in this work for pH adjustment or background electrolyte balancing because of many favorable characteristics, which have previously been discussed. However, the safe use of any chemical requires a thorough understanding of its properties. Because of the shock-sensitive and explosive nature of certain types of perchlorate compounds and their derivatives, it is of utmost concern to the chemist to understand the conditions under which these types of compounds could be formed, and to prevent such unwanted formation of explosive compounds. Much of the information from this appendix is taken from the excellent book by Schilt [202].

A.2 Aqueous Perchloric Acid

Aqueous perchloric acid boils at 203 °C, forming a 72.4% $HClO_4$ by weight azeotropic solution. Such solutions are stable indefinitely. Boiling or evaporation of an aqueous solution of perchloric acid at atmospheric pressure will not form the dangerously explosive anhydrous perchloric acid (A.3). However, shock sensitive and explosive species may still form if perchloric acid is allowed to evaporate to dryness in the presence of organic matter or certain

heavy metal ions. Perchloric acid has essentially no oxidizing power at ambient temperature, but at concentrated conditions and elevated temperatures it is strongly oxidizing. The perchlorate anion has a very weak affinity towards metal cations, making it an excellent non-interfering background electrolyte for complexation studies. In aqueous solution, perchloric acid can form as many as 5 different hydrates.

When handling compounds containing perchloric acid, it is wise to use an over-abundance of caution. The essential guidelines for safe handling of perchloric acid can be summarized in three important points: (1) control the temperature and concentration of the perchloric acid solution, (2) exclude chemicals that, when in contact with perchloric acid, will form unstable perchlorate compounds, and (3) minimize oxidizable matter that can come into contact with perchlorates. In an effort to minimize oxidizable material in hot perchloric acid solutions it is highly suggested that solutions be pretreated with nitric acid (HNO_3) before treatment with perchloric acid. If solutions are already in perchloric acid, nitric acid can be added to the mixture and boiled off (b.p. 120.5 °C), achieving the same result.

A cursory survey of the literature showed no previous work done on the possible explosive capabilities of plutonium perchlorate complexes. However, since most plutonium work occurs on the microgram to milligram level, accumulation of any explosive heavy metal perchlorate complexes are unlikely. Regardless of this fact, it is good practice to not let any solution of perchloric acid with heavy metal ions evaporate to dryness.

Boiling solutions of perchloric acid should never be done without the proper ventilation and/or vapor treatment equipment present. The reason is that unsequestered perchloric acid vapors can accumulate in conventional ventilation systems and form explosive compounds. In a negative pressure glovebox, the common practice is to send vapors from the boiling flask through two gas bubblers, the first filled with a solution of water, and the second filled with a solution of 8 M sodium hydroxide, thus neutralizing any perchloric acid vapors.

It is important to note that the suggestions and guidelines presented here are by no means exhaustive, should not be followed blindly, and are not a replacement for an in-depth discussion with an experimental chemist who is familiar with working with perchlorates.

A.3 Anhydrous Perchloric Acid

Anhydrous perchloric acid ($HClO_4$) can be prepared by fractional distillation of concentrated sulfuric acid with 65-70% perchloric acid. Magnesium perchlorate, phosphorus pentoxide, and sulfur trioxide can also be used in place of sulfuric acid. It can also be prepared by extraction into methylene chloride from a mixture of perchloric acid and fuming sulfuric acid.

Anhydrous perchloric acid is colorless, hydroscopic, volatile, extremely reactive, and explosively unstable. It freezes at -112 °C, boils at 16 °C and 0.02 atm without decomposition, and explodes at 90 °C. It can not be distilled at ordinary pressures without decomposition. The pure acid, left standing at ambient temperatures, will grow yellow and spontaneously explode within 10 to 30 days. Contact of anhydrous perchloric acid with wood, paper, or any other combustible material will result in explosions.

Anhydrous perchloric acid partially undergoes autodissociation above its melting point

(-112 °C) according to the equation below.

$$3\,HClO_4 \rightleftharpoons Cl_2O_7 + HClO_4{\cdot}H_2O \tag{A.1}$$

Anhydrous perchloric acid should only be prepared in very small amounts and stored at low temperatures under extraordinary needs. No work performed in this thesis required the production of anhydrous perchloric acid.

A.4 Perchloric Anhydrite

Perchloric anhydrite (Cl_2O_7), also known as chlorine heptoxide, is a colorless volatile oil. Upon standing for a few days it will decompose spontaneously, turning greenish-yellow in color. It can be made by adding anhydrous perchloric acid very slowly to phosphorus pentoxide at -10 °C, and distilling the product from the mixture at 82 °C. Perchloric anhydrite can also be made by heating anhydrous magnesium perchlorate and phosphorus pentoxide at 100-160 °C and 0.001-0.003 atm for 2-5 hours, and collecting the distillate in a receiver cooled to -77 °C.

Perchloric anhydrite reacts slowly with water to form perchloric acid. It is a shock-sensitive explosive and will also detonate upon contact with an ignition source. Perchloric anhydrite will also form shock-sensitive explosive alkyl perchlorates when reacted with olefins.

A.5 Perchlorate Toxicology

In addition to its explosive power, the perchlorate anion (ClO_4^-) is capable of competing with iodide for uptake in the human thyroid gland. This inhibition of iodide uptake is of concern since iodine is an essential nutrient, required by the thyroid to synthesize the thyroid hormone thyroxine. Maximum exposure limits have been set by the U.S. Environmental Protection Agency (EPA), despite the limited amount of current work done on studying human perchlorate toxicology as of 2003. When important information such as this is absent, it is best to err on the side of caution and use standard laboratory procedures to limit one's exposure to perchlorate.

Appendix B

Silver/Silver Chloride Electrodes

> You want to buy a silver chloride half-cell for how much? You know you can make these things out of 50 cents of silver wire, a battery, and a glass pipet right?
>
> *Prof. Heino Nitsche*

B.1 Making Ag/AgCl Electrodes

Silver/silver chloride (Ag/AgCl) reference electrodes can be easily constructed from silver wire, a glass pipet, a septum, a Vycor frit, and some heat shrink tubing. To make the electrode body a glass pipet is cut to length (∼5 cm) and the ends are fire polished. When fire polishing it is prudent to flair out the glass at the end of the electrode body that will have the glass frit attached to it. This gives the heat shrink tubing something to grab on to on the electrode body. A thirsty glass frit (Vycor(R), available from BAS-i: Part #:MF-1080) is cut (∼3-4 mm) and attached to the electrode body using heat shrink tubing. This frit allows for electrical contact between the inside and outside solution. Figure B.1 shows a schematic for assembling the reference electrode.

Different electrode filling solutions can be used depending on the system under study. The most common filling solution is saturated KCl (∼3.5 M). However, since we will be studying systems containing perchlorate, it is better to use a 3 M NaCl filling solution instead because $KClO_4$, an insoluble solid (MW: 138.55 g/mol; $K_{sp} = 1.05 \times 10^{-2}$ [39]), forms at the electrode junction and can block the glass frit after continued use.

Silver wire should be cut to the appropriate length, straightened, and slightly roughed up, either in a solution of dilute nitric acid or simply with sandpaper. This wire should then be attached as the working electrode in a 3-electrode potentiostat/galvanostat cell in a beaker of electrode filling solution. An Ag/AgCl electrode, as the reference electrode, and a platinum wire, as the counter electrode, completes the cell.

Rogers [203] suggests that for a 0.5 mm diameter silver wire a few centimeters long, the electrode should be plated at a current of 10 μA overnight. A quick calculation shows the

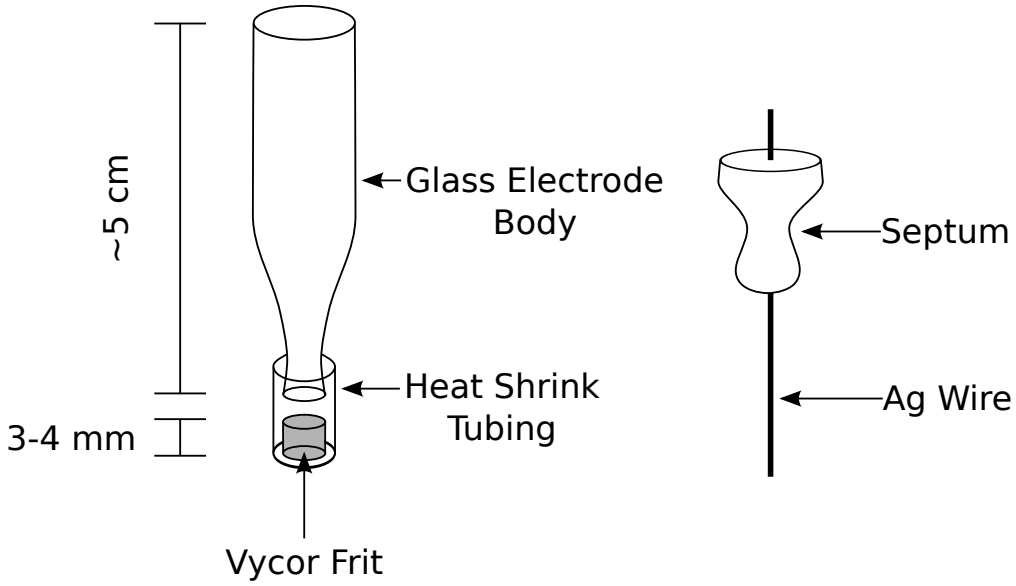

Figure B.1: Schematic of the Ag/AgCl electrode.

total amount of electrons needed to produce an Ag/AgCl electrode and the total amount of AgCl formed on the surface of the silver wire:

$$10\ \mu\text{A for 24 h} = 10\frac{\mu\text{C}}{\text{s}} \cdot 24\ \text{h} \cdot 60\ \tfrac{\text{min}}{\text{h}} \cdot 60\ \tfrac{\text{s}}{\text{min}} = 0.864\ \text{C}$$

$$\frac{0.864\ \text{C}}{9.649 \times 10^4 \frac{\text{C}}{\text{mol}}} = 8.954 \times 10^{-6}\ \text{mols of AgCl} = 0.00128\ \text{g of AgCl}$$

The appropriate wires are attached to a galvanostat and immersed in a solution of (∼3 M) NaCl. The galvanostat should be set to -5 μA and allowed to react for a few hours. The goal is to plate ∼ 900 mC of of AgCl onto the wire. A similar method for the impatient calls for immersion in a solution 0.1 M HCl for 10 minutes with a higher applied current. However, these electrodes tend to not be as good quality as the ones made slowly [203]. If done very slowly, a very thin layer of AgCl(s) will be coated on the surface of the silver wire. This wire is then threaded through a rubber septum, placed into the glass electrode body with filling solution, and allowed to equilibrate over night before being used.

B.2 Electrochemical Reactions

During the electrochemical reaction (see figure B.2) AgCl will be plated onto the surface of the silver wire through the use of coulometry. The oxidation half-reaction occurring on the surface of the working electrode is:

$$\text{Ag}^0(\text{s}) + \text{Cl}^- \rightleftharpoons \text{AgCl(s)} + \text{e}^-$$

As the silver wire becomes oxidized, Ag^+ will start to dissolve into solution. In the absence of Cl^- anions the Ag^+ would move towards the counter electrode to rejoin the electron that

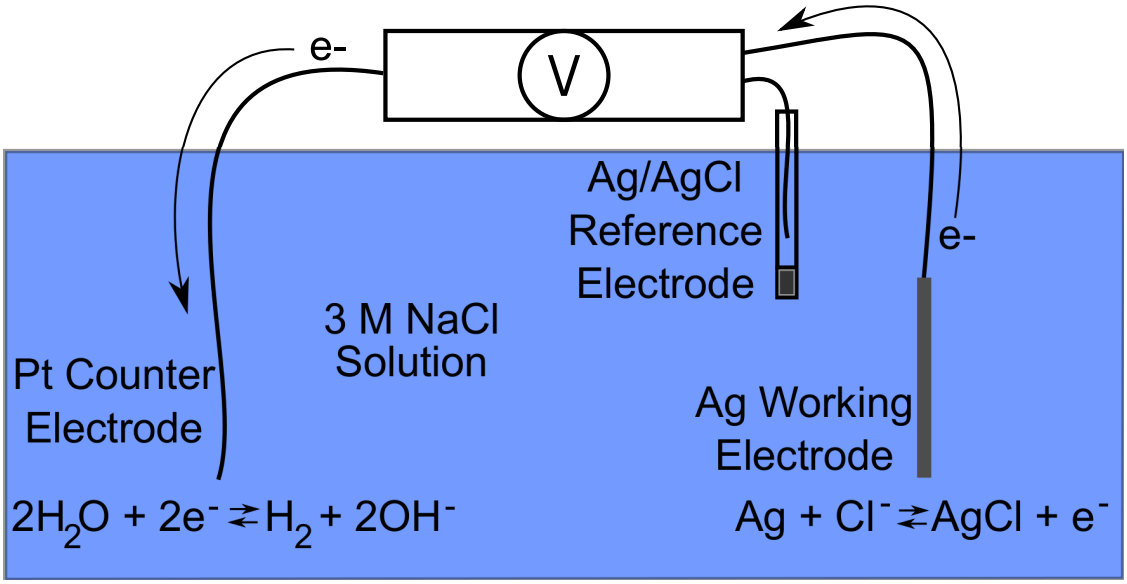

Figure B.2: Schematic of the galvanic Ag/AgCl plating cell.

Reaction	Standard Reduction Potential, E^o(V)
$AgCl(s) + e^- \rightleftharpoons Ag^0(s) + Cl^-$	0.22233
$2\,H_2O + 2\,e^- \rightleftharpoons H_2(g) + 2\,OH^-$	-0.8277
$O_2(g) + 4\,H^+ + 4\,e^- \rightleftharpoons 2\,H_2O$	1.229

Table B.1: Selected standard reduction potentials relative to the standard hydrogen electrode [39].

is lost, thus completing the circuit. In this case, silver would be plated onto the counter electrode. However, in the presence of a NaCl solution, silver cations react with chlorine anions to form insoluble AgCl(s) (MW: 143.421 g/mol; $K_{sp} = 1.77 \times 10^{-10}$ [39]). This occurs so quickly that the outside of the silver wire is coated with a very thin layer of insoluble sliver chloride. The electron that is lost by the silver then passes through to the counter electrode and reacts with water molecules to form H_2(g), which then bubbles away. The total reaction (shown in figure B.2) then becomes:

$$2\,Ag^0(s) + 2\,Cl^- + 2\,H_2O \rightleftharpoons 2\,AgCl(s) + H_2(g) + 2\,OH^- \tag{B.1}$$

Using the standard reduction potentials given in table B.1 and the Nernst equation (see equation 2.35) we can calculate the electrochemical potential required to generate a silver/silver chloride electrode. Let us assume that the electrochemical plating solution is neutral pH and 3 M NaCl, and the concentration of H_2(g) in a saturated aqueous solution is

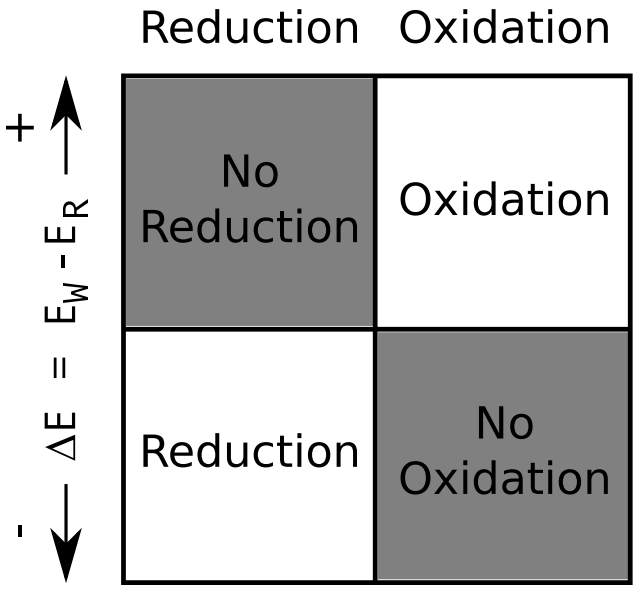

Figure B.3: E_R is the potential required for the reaction to occur and E_W is the potential the working electrode is set at, both with respect to the reference electrode. Figure adapted from [42].

0.00078 mol/L. The latter approximation is sufficient for solutions surrounding the counter electrode once the formation of $H_2(g)$ bubbles begins.

$$E = E^o - \frac{0.059\ \text{V}}{2} \cdot \log\left(\frac{[\text{Cl}^-]}{1}\right) = 0.194\ \text{V}$$

$$E = E^o - \frac{0.059\ \text{V}}{2} \cdot \log\left(\frac{[\text{H}_2(\text{g})][\text{OH}^-]^2}{1}\right) = -0.323\ \text{V}$$

The reduction potential for equation B.1 can then be calculated to be:

$$-0.194 - 0.323 = -0.517\ \text{V}$$

Note that the plating of AgCl(s) on the electrode surface is an oxidation reaction and so the AgCl reduction potential needs to be multiplied by -1 before being added to the water reduction potential.

Figure B.3 shows the coulometry reaction that occurs at the working electrode as a function of applied voltage. Reduction occurs at the working electrode when ΔE is negative. Oxidation occurs at the working electrode when ΔE is positive. Therefore, a potential of greater than -0.517 V must be applied for the oxidation reaction to occur in the three-electrode cell. Note that the nessary voltage applied may be much larger than -0.517 V depending on the resistance of the cell and the overpotential of the electrodes.

If the electroplating solution is replaced with 0.1 M HCl in an effort to expediate the electrode production process, then the reduction half-reaction

$$\text{O}_2(\text{g}) + 4\,\text{H}^+ + 4\,\text{e}^- \rightleftharpoons 2\,\text{H}_2\text{O}$$

may also play a part in the total reaction occuring in the three-electrode cell.

Appendix C

Chemical and Electrochemical Preparation of Plutonium Oxidation States in Aqueous Solution

C.1 Introduction

Below we discuss both simple chemical and electrochemical techniques to prepare pure oxidation state solutions of plutonium. Four plutonium oxidation states (III, IV, V, VI) are accessible in acidic aqueous solutions through the use of controlled-potential electrolysis with a three-electrode electrochemical cell. The procedure for producing Pu(V) electrochemically has been previously outlined [37, 94] and is not addressed here because it is not used in any of the above experiments.

Completion of any of the redox reactions presented below can be checked by taking an aliquot of the solution and measuring a UV-Vis spectrum (see subsection 5.4.1).

C.2 The Three-Electrode Cell

A schematic of the three-electrode cell used in these experiments is shown in figure C.1. It consists of a silver chloride reference electrode (see appendix B), a platinum wire counter electrode, and a platinum mesh working electrode. The working electrode is made of platinum mesh to increase the surface area of the electrode. This allows the electrochemical reaction to occur faster since there is a greater area for the plutonium to diffuse towards. It is essential that the working electrode and the counter electrode do not touch each other. If they touch then the circuit is completed and no electrochemical reaction will occur at either electrode. The counter electrode can be isolated from the rest of the solution by placing it in a glass electrode body (similar to the one shown on the left of figure B.1) filled with 3 M NaCl. However, when attempting to electrochemically adjust high concentrations of plutonium, a large amount of heat is given off, which tends to crack the Vycor frit in the electrode body. Under such conditions it is often better to simply remove the frit and filling solution and use the electrode body to physically separate the working and counter electrodes in the cell.

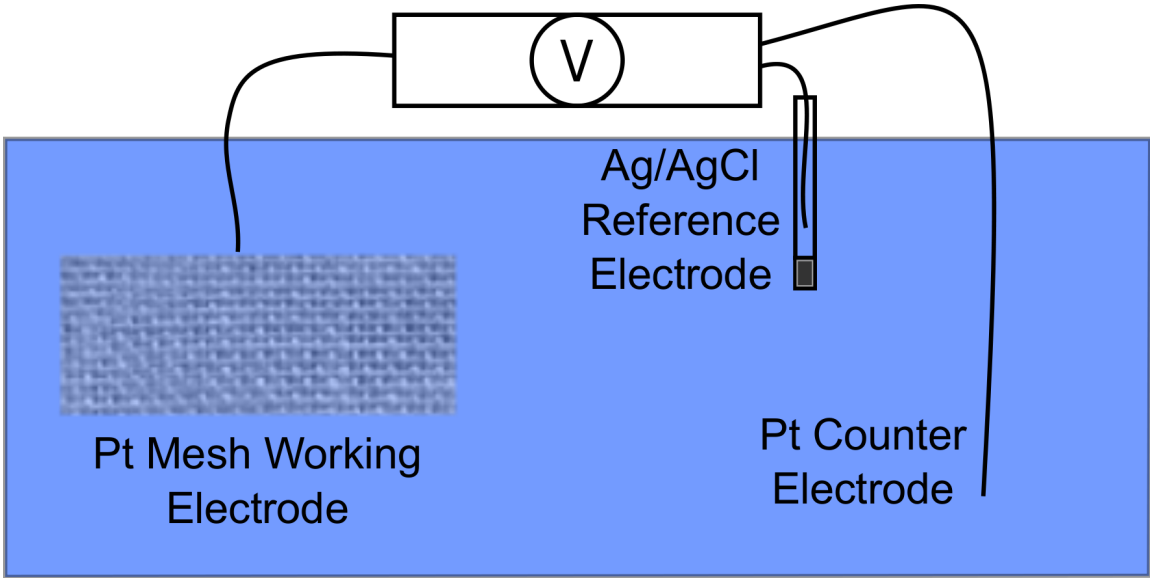

Figure C.1: A schematic of the three-electrode cell.

Reaction	Standard Reduction Potential, E^o(V)
$PuO_2^{2+} + e^- \rightleftharpoons PuO_2^+$	0.91
$PuO_2^+ + 4\,H^+ + e^- \rightleftharpoons Pu^{4+} + 2\,H_2O$	1.17
$Pu^{4+} + e^- \rightleftharpoons Pu^{3+}$	0.98

Table C.1: Selected standard reduction potentials for plutonium relative to the standard hydrogen electrode [204].

C.3 Preparation of Pu(III)

A solution of Pu(III) can be produced by reduction of Pu(IV) using Zn metal or I^- in a HI/HCl mixture. The latter is the preferred way to reduce Pu(IV) on anion exchange columns (see appendix E).

Pu(III) can also be electrochemically prepared. Figure C.2 shows the current-voltage diagram for plutonium in 1 M $HClO_4$ solution [204]. At an applied voltage between 0.9 and 0.0 V (relative to the SHE), a solution of plutonium (in any oxidation state) will be reduced to Pu(III). Note that the Pu(VI) $\rightarrow$ Pu(V) and Pu(IV) $\rightarrow$ Pu(III) reductions will occur fairly rapidly. However, the reduction of Pu(V) requires a high overpotential, characteristic of reactions that make or break bonds. In this case the cleavage of the plutonyl bonds in $Pu^{V}O_2^+$ is kinetically slow. The required overpotential in figure C.2 can be compared to the standard reduction potentials given in table C.1.

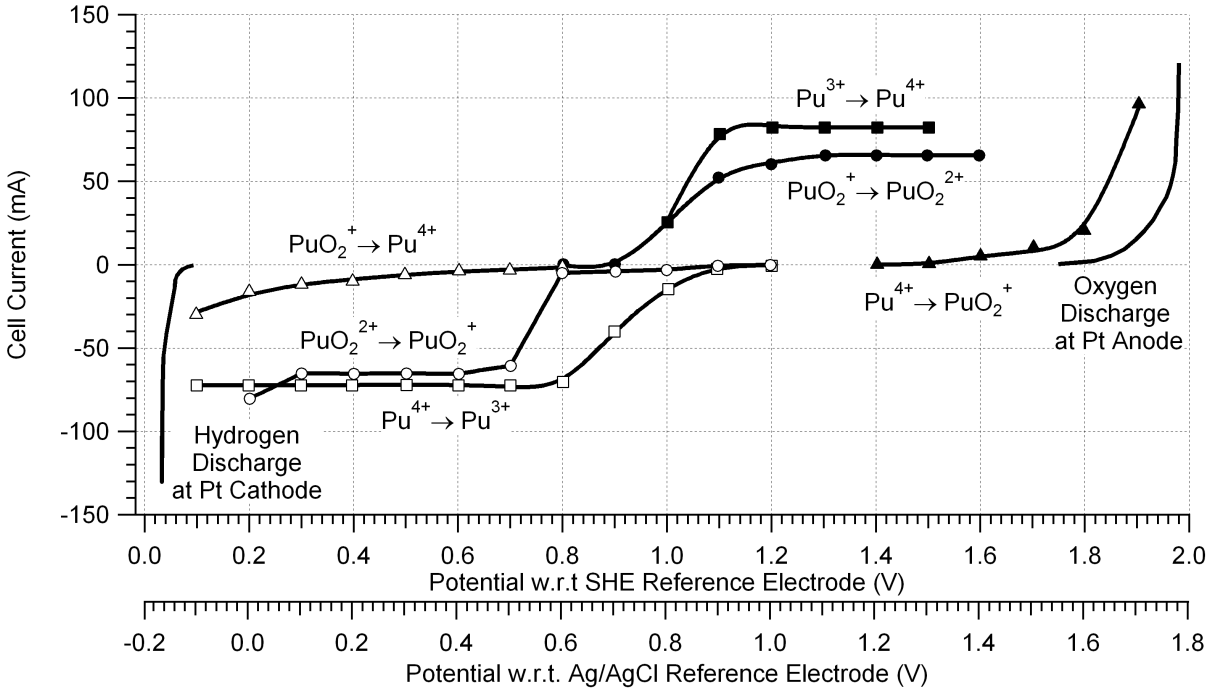

Figure C.2: Plutonium current-voltage diagram adapted from [94, 204]. Potentials referenced with respect to both the standard hydrogen and silver/silver chloride electrodes.

C.4 Preparation of Pu(IV)

Pu(IV) can be produced from any solution mixture by addition of sodium nitrite ($NaNO_2$). This reaction will cause the rapid reduction of Pu(VI) $\rightarrow$ Pu(V), and rapid oxidation of Pu(III) $\rightarrow$ Pu(IV). The slow reduction of Pu(V) $\rightarrow$ Pu(IV) is a kinetic effect of breaking the plutonyl bonds in $Pu^{V}O_2^{+}$. When adding $NaNO_2$ to the plutonium solution be aware that gas will be evolved from the reaction and add slowly.

A solution of Pu(IV) can be made cleanly from a starting solution of pure Pu(III) using electrochemistry. In this reaction, the high overpotential required to oxidize Pu(IV) $\rightarrow$ Pu(V) is used to our advantage. At an applied voltage between 1.0 and 1.4 V (relative to the SHE), the solution of Pu(III) will rapidly oxidize to Pu(IV).

C.5 Preparation of Pu(VI)

Pu(VI) is easily produced by boiling a solution of plutonium (in any previously prepared oxidation state) in perchloric acid ($HClO_4$). ***Before working with perchloric acid, be sure to review the information in appendix A and any other safety documentation needed to familiarize yourself with the dangers and safe handling of perchloric acid***. The solution should first be boiled to near-dryness several times with HNO_3 to ensure that all organics are destroyed. Once this is done, the solution is allowed to cool and then concentrated perchloric acid added to the reaction flask. The solution is then boiled until all the plutonium is oxidized to $Pu^{VI}O_2^{2+}$. One of the benefits of using

Chemical	Boiling Point (°C)	Notes
HF	19.54	Pure HF, not Hydrofluoric Acid
HCl	110.0	20.2% azeotrope in H_2O
HNO_3	120.5	68% azeotrope in H_2O
HI	127	57% azeotrope in H_2O
I_2	184.3	
$HClO_4$	203.0	72.5% azeotrope in H_2O

Table C.2: Boiling points of common chemicals used in plutonium oxidation state augmentation [39].

perchloric acid to oxidize the solution is its high boiling point (see table C.2). Therefore, in the process of oxidation, any left over HNO_3 will also be boiled off.

Pu(VI) can also be produced electrochemically. $Pu^{VI}O_2^{2+}$ can be formed by applying a positive voltage to the cell. However, the Pu(IV) $\rightarrow$ Pu(V) oxidation again requires a high overpotential, characteristic of reactions that make or break bonds. In this case the formation of the plutonyl bonds in $Pu^{V}O_2^{+}$ is kinetically slow.

C.6 Preparation and Removal of Pu(IV) Polymer

Invariably, in the course of conducting actinide chemistry the actinide chemist will produce some amount of plutonium polymer. This compound spontaneously forms in solutions of Pu(IV) at pH values higher than 1 and can be spectroscopically identified by an absorption peak at 613 nm in conjunction with light scattering or a significantly larger absorption peak at ~400 nm. If sufficient polymer is produced it can be visually identified by its bright green color [94]. Much work has been done in recent years to understand the structure and formation thermodynamics of Pu polymer through the use of various techniques, such as high energy X-ray scattering (HEXS) and laser-induced breakdown spectroscopy (LIBS) [6, 8]. However, a complete molecular description of Pu polymer formation still eludes the community.

Pu(IV) polymer formation will most likely occur when attempting to conduct a Pu solution volume reducing step by forming the plutonium hydroxide, $Pu(OH)_3$, in aqueous solution. The most efficient way to remove Pu(IV) polymer is to boil the polymer in a solution of 5 M HNO_3 with a fluoride concentration of 0.05 M [94]. Lower fluoride concentrations can be used, but will result in longer boiling times. After the polymer is de-polymerized, it is best to run the solution through an anion exchange column (see appendix E) to remove any unwanted ions. Because of the possibility of Pu(IV) polymer formation it is suggested that the lanthanum fluoride precipitation D be used for volume reduction of plutonium solutions.

Appendix D

Lanthanum Fluoride Precipitation

D.1 Introduction

The method of lanthanum fluoride co-precipitation is outlined by D. C. Hoffman on pages I-194 through I-196 in [205]. The method, along with anion exchange (see appendix E), is the preferred way to purify small (< 1 mg) amounts of plutonium that are already in acidic solution. It is also an excellent method for removing small amounts of plutonium from solutions with high salt content.

Hoffman uses hydroxylamine (NH_2OH) in her procedure to reduce plutonium in solution to lower valent states (Pu(III) and Pu(IV)) in preparation for co-precipitation with LaF_3. However, for small Pu concentrations this reduction can be done more efficiently and cleanly through the use of electrochemistry (see appendix C).

For solutions of plutonium that are more concentrated (> 1 mg) it should be possible to precipitate plutonium fluoride without the need for the lanthanum carrier.

D.2 Lanthanum Fluoride Co-Precipitation of Plutonium

The co-precipitation procedure requires a 20 mg/mL solution of La^{3+} made from the lanthanum salt $La(NO_3)_3 \cdot 6\,H_2O$, concentrated HF (∼29 M), a solution of 2 M HF/2 M HNO_3, a saturated solution of boric acid (H_3BO_3), and a strong acid to dissolve the precipitate. ***Before working with hydrofluoric acid, please review the proper procedures for safely handling this hazardous chemical. Concentrated HF causes severe burns which may not immediately be noticed and will cause bone damage. Always have calcium gluconate gel available when working with HF and wear proper personal protective equipment.***

The initial sample is diluted or concentrated to be ∼3 M in acid (HCl, HNO_3, or $HClO_4$). 3 drops of La_3^+ solution per mL of sample solution is added and thoroughly mixed. Then 3 drops of concentrated HF per mL of solution is added, thoroughly mixed and allowed to react for 5 minutes. During this time insoluble LaF_3 begins to precipitate out of solution and co-precipitate any Pu(III) or Pu(IV) in solution.

The sample is then centrifuged and the supernate discarded. The precipitate is washed with ∼10 drops of the 2 M HF/2 M HNO_3 solution, centrifuged, and the supernatant is

discarded again.

The pellet is solublized by adding 2 to 3 drops of saturated boric acid followed by ~ 0.5 mL of strong HCl or HNO_3. The chemical reaction proceeds according to the following equation:

$$LaF_3 + H_3BO_3 + 3\,H^+ \rightleftharpoons 3\,H_2O + La^{3+} + BF_3 \tag{D.1}$$

The strong acid is used to drive the reaction in equation D.1 to the right and is not anion dependent, so any acid is suitable. However, it is best to use either HNO_3 or HCl since this procedure is usually followed by anion exchange (See Appendix E) to separate the lanthanum carrier from the plutonium. Dissolution of the precipitate may take a few minutes and some agitation. If, after dissolution, the solution is slightly yellow the solution should be diluted to the correct acid concentration and re-precipitated without adding any more lanthanum carrier. Experiments have shown that conducting the precipitation on a solution with an acid concentration of > 3 M causes the redissolved solution to be slightly yellow in color. Any unreacted H_3BO_3 will stay in solution and be washed away. The remaining BF_3 can either be separated in a follow-up anion exchange step, or by boiling the solution. This method regularly produces recovery rates of $> 99.5\%$.

Appendix E

Anion Exchange of Plutonium

E.1 Column Preparation

Biorad AG1-X8, 100-200 mesh, chloride-form anion exchange resin is used to separate plutonium from fission products, lanthanides, and other actinides. First the exchange resin is prepared in nitrate-form by successive rinsing with 3 M HNO_3, 8 M HNO_3, and then repeated rinsing with Milli-Q H_2O until the pH of the rinse solution is approximately pH 4. This prepared resin is then stored a solution of HNO_3 at pH 4.

A column of suitable size is selected and thoroughly cleaned. The tip of the column is packed with a small amount of quartz wool. At this point the total column volume (TCV) is measured by filling the column with water and weighing the amount of water eluted after draining the column. The column is then packed with the exchange resin prepared above. Once the column is packed the full column volume (FCV) can be measured either through the AgCl method or through the use of a suitable pH indicator solution. The column is first rinsed with Milli-Q H_2O until the eluate from the column is of neutral pH. A solution of either $AgNO_3$ or water with pH indicator is prepared in a beaker and placed underneath the column. HCl is then added to the top of the column and the number of eluted drops is counted until either insoluble AgCl(s) begins to form in the beaker (MW: 143.421 g/mol; $K_{sp} = 1.77 \times 10^{-10}$ [39]), or the pH indicator changes color. The number of drops per FCV can then be converted to the volume of one FCV by weighing drops of Milli-Q H_2O eluted from the column. The prepared column can be stored in HNO_3 at pH 4 with the top and bottom sealed with Parafilm®.

E.2 HI Distillation

Solutions of HI available from chemical suppliers contain hypophosphorous acid (H_3PO_2), a reducing agent that preserves the HI by keeping it from oxidizing in solution. This preservative attacks and corrodes the platinum column tips and platinum α-spectroscopy plates. Therefore, fresh HI needs to be distilled each time it is required in a procedure. A simple distillation apparatus with a sample flask, condenser, and receiving flask is all that is necessary to distill HI. In aqueous solution, HI forms a 57% azeotrope with a boiling point of 127 °C. H_3PO_2 decomposes at temperatures above 130 °C. Distilled HI will undergo oxidation in a

few days according to the following reactions:

$$4\,HI + O_2 \longrightarrow 2\,H_2O + 2\,I_2$$

$$HI + I_2 \longrightarrow HI_3$$

HI_3 is dark brown, so aged HI solutions appear light to dark brown depending on the amount of aging. Dark brown solutions of HI should not be used when running an anion exchange column.

E.3 Pu Anion Exchange

The column is pre-conditioned with 3 FCV of 8 M HNO_3. The plutonium solution, as Pu(IV) in 8 M HNO_3, is then loaded in as small a volume as possible onto the column and allowed to bind to the resin as a green ($Pu^{IV}(NO_3)_6$) band at the top of the column. The vial containing the solution is then rinsed in 8 M HNO_3 and the washings are added to the column as well.

The column is then washed with 3 FCV of 10 M HCl. It is good practice to wash the sides of the column reservoir with the 10 M HCl to remove any trace of plutonium on the column walls. When the HCl reaches the green band it will become pink or clear (depending on the plutonium concentration) as the $Pu^{IV}(NO_3)_6$ species changes to the plutonium chloride species. The 10 M HCl removes any lanthanides and fission products, which do not stick to the column.

Plutonium is then eluted slowly with 4 FCV of a 1:9 ratio of concentrated HCl to freshly distilled HI solution. The plutonium is reduced from Pu(IV) to Pu(III) by the HI in the following reaction:

$$2\,Pu^{4+} + 2\,I^- \rightleftharpoons 2\,Pu^{3+} + I_2$$

After the reduction occurs, Pu(III) no longer binds to the column and is eluted off with the HCl/HI mixture. Finally any U(VI) and Np(IV) will be eluted off with 10 FCV of 1 M HCl. A flowchart of the procedure is shown in figure E.1. The plutonium eluted from the column will be in HCl with unwanted HI and I_2 contamination. HI and I_2 (boiling points 127 °C and 184.3 °C, respectively) can be removed by heating the eluted solution.

After all the activity is eluted from the column, it is essential that the column is rinsed with Milli-Q H_2O. Long term storage of ion exchange resin with high concentrations of HNO_3 may cause the formation of shock-sensitive, explosive organic material.

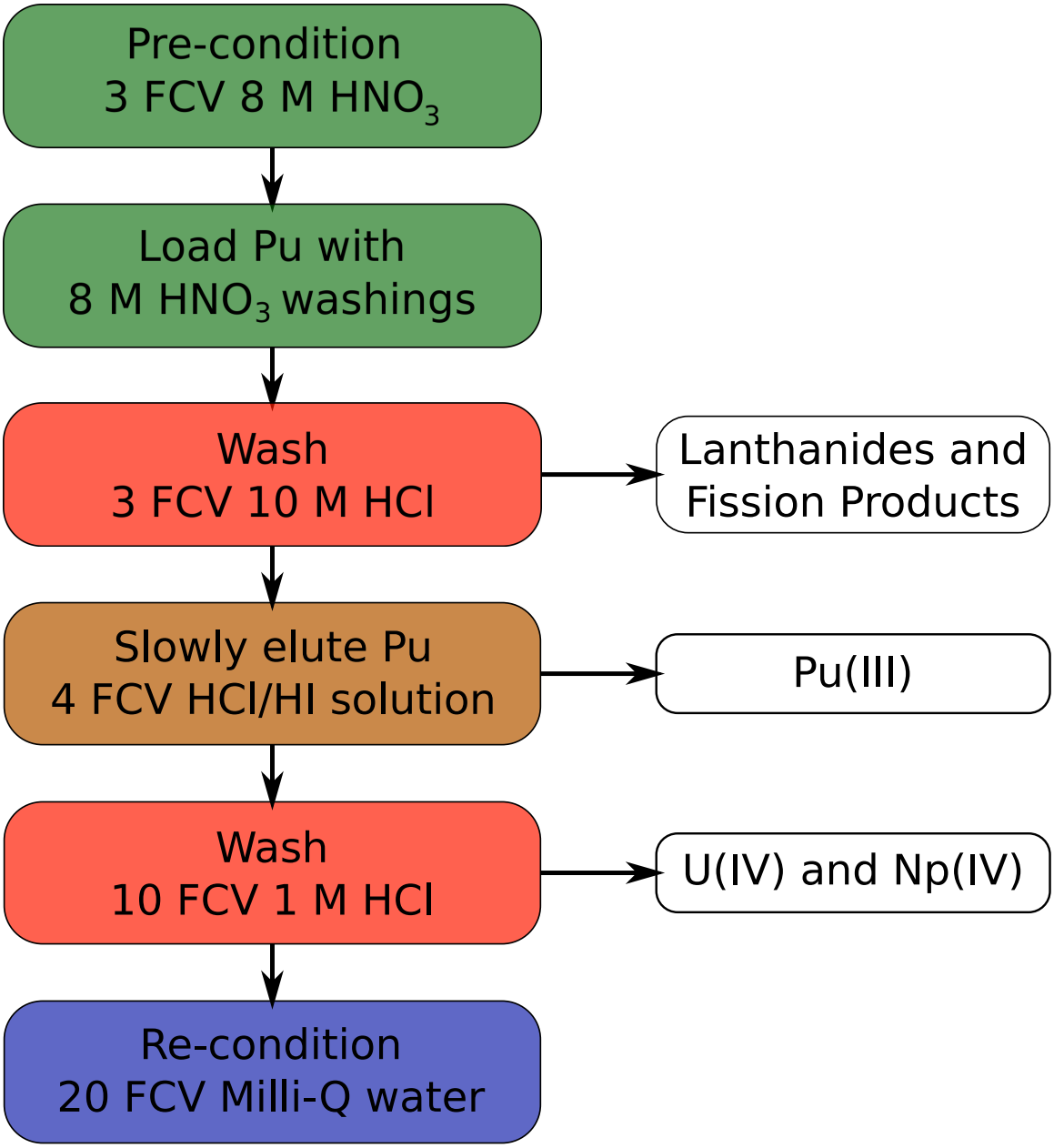

Figure E.1: Flow chart of plutonium separation in an anion exchange column.

Appendix F

Scientific Computing

And now for something completely different.

Monty Python

Computers are useless. They can only give you answers.

Pablo Picasso

F.1 Introduction

Modern scientific techniques produce relatively large volumes of data that must be thoroughly, accurately, and efficiently processed and analyzed so that conclusions, which are supported by the data, can be formed. The problem with data analysis purely by hand is that inevitably human error, be it from mis-transcription or miscalculation, will creep in. The likelihood of such an error occurring greatly increases as datasets become larger.

In a sense, very little science is done anymore without the aid of some type of scientific computing. Usually this presents itself in the form of a scientific analysis package such as Origin [206] or IGOR Pro [207]. Such packages are intended to be highly polished and developed to fulfill the user's every need. Both these programs also offer the option for the user to conduct more complicated analysis by using either the C or C++ programming language to extend the analysis package itself. The main issues with these programs are that of cost and their proprietary nature. Data that has been analyzed with a particular program is forever trapped within the confines of that particular piece of analysis software. Issues of backwards compatibility then arise when new versions of the software are released, or if companies stop supporting a particular piece of software entirely.

The alternative to using such commercial programs is to use open source scientific programs, or produce scientific programs "in-house" using an open source programming language. Open source software and languages are not limited by commercial restrictions in

terms of licensing agreements and other legal matters. Because open source languages and software are both free to use ("free as in beer"), and their underlying source code is freely available to be changed ("free as in speech"), using open source software mitigates the two main issues encountered when using commercial software.

The difficulty with using open source then is one of convenience. When extensive collaboration is required in order for work to be done quickly, it is often times more feasible to work with a commercial system that is easily accessible. An excellent example of this would be the Microsoft Office suite, which is both universally available, and has been adopted as a standard in most workplaces. Furthermore, the entry into open source software often times involves learning curves that are very steep. This is especially the case when computer programming is involved.

Furthermore, the ease of use of a particular program or data analysis routine should not be undervalued. One will find that software that computes numbers (calculates standard deviations, subtracts one vector from another, etc.) is relatively easy to produce. The problem arises from the interface between the computer and the person who is doing the computing (i.e. the software user). Well-designed software should have a shallow learning curve (easy for knowledgeable first-time users), but also have the ability to do more advanced analysis when necessary. The ability to produce such programs necessitates the use of graphics user interface (GUI) programming techniques and libraries.

Since the field of computing changes so rapidly, the best place to look for information and beginner tutorials would be on the Internet. However, in the sections below I suggest a few books that were of particular help to me. Books concerning the Python programming language will most likely be obsolete in the near future, however the Fortran texts have already stood the test of time and will likely continue to be pertinent. For those interested in the trials and tribulations of software programming and engineering in a general sense, "The Mythical Man-Month" by Brooks [208] is an excellent collection of essays, which are immensely readable and entertaining.

F.2 Fortran

Fortran, derived from a shortening of the name **For**mula **Tran**slating System, was originally developed by IBM in the 1950s as a general-purpose, procedural, imperative, compiled programming language for scientific and engineering applications. Now, more than 60 years after its inception, the Fortran programming language still holds a central position in scientific computing. The reason why scientists initially adopted, and still support the use of Fortran, is because it is a high-level language, and it is relatively easy to program in, compared to other similar high-level languages such as C or C++. Here the term high-level language is used to describe a programming language that is fairly abstract when compared to what a computer processor can natively understand (r.e. machine code). All of RSXAP is written in Fortran 77, the specification of the Fortran programing language that was approved in 1977. Since that time newer versions of the Fortran language have come out to extend its capabilities into a full programming language, adding support for things such as object-oriented programming. However, the scientific community has tended to stick with the more familiar Fortran 77 release. Since Fortran is a compiled language, the source code

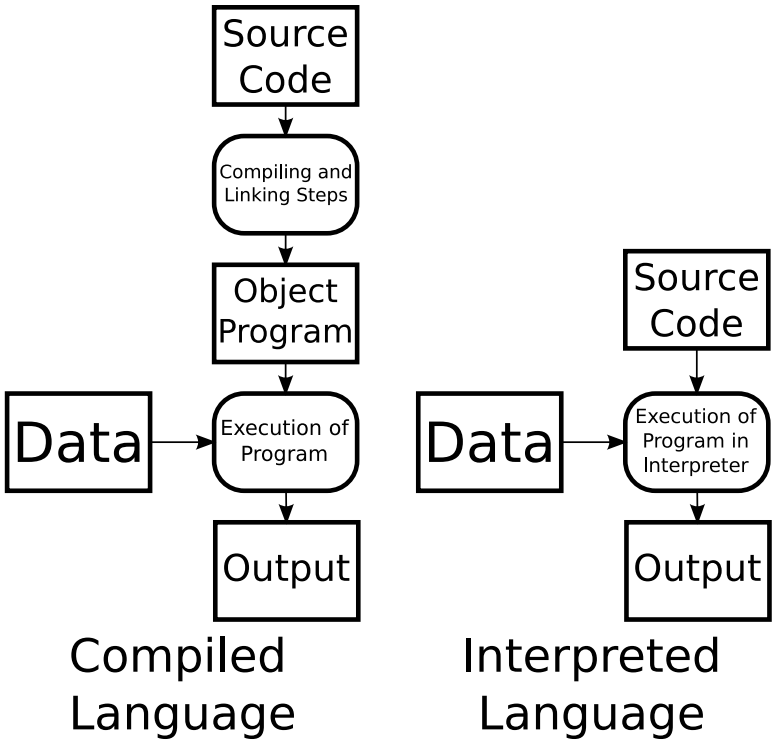

Figure F.1: Flow chart of the programming process for compiled languages and interpreted languages.

must be written and compiled before program execution. A flow chart of this procedure can be seen on the left in figure F.1.

Under certain circumstances Fortran is still the language of choice for scientific computing; however, these circumstances are becoming more and more limited. The main functional difference between a compiled language, such as Fortran, and a much higher-level interpreted programming language, such as Python (see F.3), is program execution speed. When this is of concern, it is possible to find the particular algorithm that is temporally costly, rewrite it in Fortran, and connect it to the existing Python code. There are therefore two reasons why a "modern" practitioner of scientific computing needs to understand a compiled language such as Fortran. The first reason is that much of the existing code from the last 60 years is written in Fortran, and it may be necessary in the future to interface with this code. The second reason is that despite the benefits of more modern interpreted programming languages (as will be described below), compiled languages still vastly outperform interpreted languages in terms of execution time.

Many excellent books about programming in Fortran have been written over the years. The two that I have found to be most helpful are "Structured Fortran 77 for Engineers and Scientists" [209] and "Classical Fortran" [210]. These two books are excellent for beginners who wish to learn both the Fortran language syntax and the basic ideas of computer science in general.

F.3 Python

F.3.1 The Core Python Programming Language

Python is a general-purpose, high-level, object-oriented, interpreted programming language. Its main focus is to give the programmer remarkable power with clear language syntax. Also included in the core programming language is a very large set of libraries that exposes essentially all of the capabilities of a computer running any of the main operating systems (Windows, Linux, and Mac OSX). The core Python programming language is in fact, often referred to as having "batteries included".

Interpreted languages, such as Python, require a separate program called the interpreter, which translates Python source code into something that a computer processor can understand (see figure F.1). This process means that programming can be interactive, where the programmer puts in one line of code into the interpreter and the results are immediately shown. Programming through an interpreter is immensely helpful to the novice programmer, who is immediately able to see the results of new code without the need to compile and link the source code into an executable file. However, this convenience comes at a price in program execution speed. This reduction in speed is often times unnoticeable because most simple scientific computing programs are not very processor intensive. For those programs that are processor intensive there are Python libraries available that offer functions written in a compiled language (such as C++ or Fortran). These functions perform at the speed of compiled languages, but with the convenience of Python functions. For very specialized cases it is possible to write C, C++, or Fortran functions and link them directly to Python functions to achieve the same speed up and convenience for personalized functions.

Python uses whitespace (spaces or tabs) as delimiters for code blocks. This forces the programmer to properly indent source code, making it more readable to the human user. Examples can be seen throughout the code listings section (F.4) of this appendix.

The cross-platform capabilities of Python are important because of the diversity of operating systems being currently used in the scientific community. For in-house code that is meant for personal use, cross-platform capabilities are much less important, but if one is attempting to make a usable piece of software that will be disseminated throughout the community, it is essential that it be able to run on Windows, Linux, and Mac OSX machines. Often times Python code written in a Linux environment can simply be copied over to a Windows machine and immediately be ready for use.

Python is a very young language, first implemented in a usable form in 1989 [155]. The current version of Python (Python 2.0 series) that is being used most often in a production setting was released in 2000. Because Python is still so young, tools and functionality will continue to be added as the language itself grows and changes. Textbooks therefore tend to not be entirely up-to-date when it comes to all the features available in the latest version of Python, and the best place to look for up-to-date information is the Internet. The 2nd edition of "Learning Python" [211] is an excellent guide for the beginning programmer. The 3rd and 4th edition have since been released. However, the 4th edition covers Python 3.0, a newer version of Python that has not seen sufficient support from the scientific community to be used for scientific computing quite yet. Those who are familiar with computer programming already may benefit more from the advanced text "Programming Python" [212]. Finally,

there is a text available specifically for those wishing to use Python for scientific computing entitled "Python Scripting for Computational Science" [213].

F.3.2 SciPy

SciPy is a library of algorithms and mathematical tools for Python. It takes advantage of the NumPy library (see F.3.3) and the Matplotlib library (see F.3.4) to produce an environment very similar to MATLAB in execution, but entirely built on open source software.

F.3.3 NumPy

NumPy is a library extension to Python that supports the use of large, multi-dimensional arrays and matrices. It includes a large library of high-level mathematical functions, such as least-squares minimization, parameter optimization; numerical methods; Fast Fourier Transforms (FFT), and other signal processing functions. These array objects and libraries are written in a compiled language and then attached to Python. In this way the user is able to use the convenience of Python with roughly the same speed of a compiled language. NumPy arrays and functions are used extensively in the code presented in section F.4 below.

F.3.4 Matplotlib

Matplotlib is a plotting library for Python. It has its own application programming interface (API), which allows the programmer to embed plot objects directly into GUI objects such as wxPython (see F.3.5). Matplotlib was developed to be an open source option to MATLAB and has very similar plotting functionality. Currently it supports many different 2D plot options, and is beginning to support 3D plotting as well. Matplotlib has excellent documentation and extensive examples for incorporating plotting objects into GUIs. A good book to get started with Matplotlib is "Matplotlib for Python Developers" [214].

F.3.5 wxPython

wxPython is a wrapper around the cross-platform GUI API known as wxWidgits (written in the C++ programming language). It is a very similar library to Tkinter, PyQt, and PyGTK. The choice of a particular GUI library is a fairly personal preference. Here, wxPython is chosen because of its compatibility with the Matplotlib (see F.3.4) plotting libraries and because of its extensive documentation. The purpose of writing a GUI is to present a "pretty" interface to the user. Many computational scientists believed that the time investment necessary to produce a robust GUI on top of programs is not commensurate with the resultant time savings for the user. However, this is not necessarily true. The total time savings for a well-designed program with a GUI could greatly outweigh the initial time investment spent programming if there is a large enough user base wanting to use the software. In a positive feedback fashion, the user is more likely to use a program that is easier to use. This often requires the program to have a GUI in the first place.

GUI programming is a very different beast from normal procedural programming, which usually requires an input file and produces an output file. In GUI programming the programmer must anticipate all possible routes that a user can travel through the program. An excellent resource to start learning about wxPython and GUI programming in general can be found in the book "WxPython in action" [214].

F.4 Code Listings

F.4.1 Introduction

Below are the listings for the major data analysis programs written for this project. The full code listings are presented with contextual formatting to guide the eye. Detailed information about each program is presented in the documentation located in the body of the listing.

F.4.2 SIMERAD

The purpose of this program is to generate simulated stochastic noise on top of calculated EXAFS spectra from the *ab initio* program FEFF7. The program expects to receive an input file defining the amount of error to add to the calculated spectrum, the number of simulated error files to make and a FEFF7 *.dat output file.

```
#!/usr/bin/env python
################################################################################
#simErAd.py
#Written by : Yung-Jin Hu
#Last updated: August 22, 2008
#
#This program has the form:
#simErAd -p <error file prefix> -n <number of files to make> <FEFF7 outputFile>
#
#Dependencies:
#feffExt.py
#errForm.py
#averrExt.py
#
#This program takes a ".dat" output file from FEFF7 and adds error to the
#calculated chi data. This program uses feffExt to extract out the k and chi.dat
#files calculated from FEFF7. A file named stats.out is also made by this
#program, documenting the average SD (sigma) error added to each file. The
#functional form of the added error can be adjusted in the definition module
#errForm.py
#
#Version        Description
#0.01           started version numbering and changed program from simErrAdd to
#               simErAd. Implemented use of feffExt for parsing FEFF7 output
#               file and removed all the hard coded parsing code sections.
#0.02           documented code and removed code lines that were made obsolete by
#               using feffExt. Also added the ability to plot all of the error
#               files on top of each other. This should be made into an option in
#               later versions.
#0.03           Added ability to fit sigma error to an error file, or to some
#               functional fit of the error file through the use of
#               errFuncForm.py
#0.04           Added subroutine to make an aPyErr.inp file after finishing with
#               making the error simulation files to help speed up getting the
#               stats out of the files.
```

```
#0.05          added code to calculate chi^2 value from the simulated average
#              and standard deviation compared to the parent FEFF7 file
#0.06          Added chiConst, chikConst, chikCubeConst as options for error
#              output. This correlates with the errFuncForm.py file
#0.07          Added ability to use bin2gnu files as input for error addition
#              instead of just FEFF7 output files
#0.08          Turned off plotting and made sure that -s is optional not
#              mandatory
#0.09          Cleaned up sorce code
#
#FUTURE ADDITIONS:
#-correct functional form testing should be done in errFuncForm and not here!
#-functional form should be passed to errFuncForm directly and let it handle
#checking
#-data output should be handled by the *Ext modules and not in here! That will
#minimize output writing errors. Should I rename them averrIo, feffIo, etc?
##############################################################################
#for parsing and regular expression matching
import string, re
#for math functions
import math
import numpy
#for plotting and figure generation
from pylab import *
#for random number generation and error addition
import random
#allow for command line arguments
import sys
#takes care fo parsing options
from optparse import OptionParser

#used to extract k and chi data from FEFF7 files
import feffExt
#defines the functional form of the error function
import errFuncForm
#used to extract averaged k and chiK data from AVERR averaged real data files
import averrExt
import kBinExt

versionNumber = 0.09

def addError(feffFile, simErNum, outFilePrefix, sigmaFile, sigmaFuncForm,
      scaleFactor, gnuFile):
   #DECLARATIONS
   ############################################################################
   #array to hold filename for each file generated
   fileNameArray = []
   ############################################################################

   parsedFile = []
   if gnuFile:
      parsedFile = kBinExt.extractKBin(feffFile)
#      print "DEBUG: parent file data length", parsedFile.dataLen
   else:
      #parse feffFile with feffExt and save to parsedFile
      parsedFile = feffExt.extractFeff7(feffFile)

   #parse averr with averrExt and save to averrFile if sigmaFile is defined
   if sigmaFile != 'NONE':
      averrFile = averrExt.extractAverr(sigmaFile)
      #print averrFile.k

   #fitting error file to some functional form
   ############################################################################
   if sigmaFuncForm in ['c','l','e','o']:
      sdChiOnGrid = errFuncForm.fitSigmaData(parsedFile.k, averrFile.k,
            averrFile.sdChi, sigmaFuncForm)
   elif sigmaFuncForm in ['r']:
```

```
        sdChiOnGrid = errFuncForm.interpolateSigmaData(parsedFile.k, averrFile.k,
            averrFile.sdChi)
    elif sigmaFuncForm in ['chiConst','chikConst','chikCubeConst']:
        sdChiOnGrid = errFuncForm.calculateSigmaData(parsedFile.k, sigmaFuncForm,
            scaleFactor)

#   #start plotting data
#   ###########################################################################
#   figure(1)
#   plot(parsedFile.k, parsedFile.chi, linewidth = 10)

    #start collecting data for chiSq test
    ###########################################################################
    #form zero arrays that are the length of the FEFF7 parent file
    simAveChi = numpy.zeros(parsedFile.dataLen)
    simSdChi = numpy.zeros(parsedFile.dataLen)

    #calculates new FEFF files with error added
    ###########################################################################
    for i in range(int(simErNum)):
        #DECLARATIONS
        ###########################################################################
        #array to house string lines of the new spectra data after addition of
        #error and reformatting to match original FEFF7 output
        newCalcSpectra = []
        ###########################################################################

        #setup output error file and copy over header from original file
        ###########################################################################
        #pointer to output file for new FEFF error file
        outputFile = open(outFilePrefix + '%03d' % (i+1),'w')
        #appends new filename to fileNameArray
        fileNameArray.append(outFilePrefix + '%03d' % (i+1))

        #write header information into error output file
        for line in parsedFile.header:
            outputFile.write(line)

        #add error to calculated input spectra
        ###########################################################################
        aNewChi = errFuncForm.addErrFunc(parsedFile.chi, sdChiOnGrid)

        #sum up simulated error data for chiSq test
        ###########################################################################
#       print "DEBUG: simAveChi length:", simAveChi.size
#       print "DEBUG: aNewchi length:", aNewChi.size
        simAveChi = simAveChi + aNewChi

#       plot(parsedFile.k, aNewChi)

        #change the numpy array aNewChi to python list newListChi
        newListChi = aNewChi.tolist()
        #print newListChi

        if gnuFile:
            #change all the other numpy array columns in the kBinOutfile instance
            #to to python list
            listK = parsedFile.k.tolist()

            for x in range(len(listK)):
                #NOTE: because this file is gnu formatted it needs to be output with
                #k*Chi weighting so that RSFIT knows what to do with it.
                newLine = '%12E   %12E\n' % (listK[x], listK[x]*newListChi[x])
                #a new formated line is formed with the first column 12 wide, the
                #second 12 wide. All types are exponential numbers (with capital E).
                outputFile.write(newLine)

        else:
```

```
            #change all the other numpy array columns in the feff7Outfile instance
            #to to python list
            listK = parsedFile.k.tolist()
            listMag = parsedFile.mag.tolist()
            listPhase = parsedFile.phase.tolist()

            for x in range(len(listK)):
            #length of listK used to make list with from 0 to 1-number of entries
            #in listK for use in the for loop. It is assumed that the lengths of
            #all column lists are the same
               newLine = '%11E%16E%14E%14E\n' % (listK[x], newListChi[x],
                     listMag[x], listPhase[x])
               #a new formated line is formed with the first column 11 wide, the
               #second 16 wide, the third 14 wide, and the fourth 14 wide followed
               #by a newline character. All types are exponential numbers (with
               #capital E).

               #the formated line is appended to the end of newCalcSpectra array
               newCalcSpectra.append(newLine)

            for line in newCalcSpectra:
               #takes contents of newCalcSpectra and writes to the output file
               outputFile.write(line)

         #clean up file handlers
         outputFile.close()

      #calculate average of the simulated data and reloop through the simulated
      #data files to calculate residuals and standard deviation of data
      ###############################################################################
      simAveChi = simAveChi/float(simErNum)
      #print "DEBUG: ",simErNum

      for errFile in fileNameArray:
         simErrfile = []
         if gnuFile:
            simErrFile = kBinExt.extractKBin(errFile)
         else:
            simErrFile = feffExt.extractFeff7(errFile)
#        print "DEBUG: data file", simErrFile.chi.size
#        print "DEBUG: calculated average data length ", simAveChi.size
         residual = (simErrFile.chi - simAveChi)**2.
         simSdChi = simSdChi + residual

      simSdChi = sqrt(simSdChi/(float(simErNum)-1.))

      #calculate chiSq value from the above information
      ###############################################################################
      chiSqArray = ((simAveChi-parsedFile.chi)/(simSdChi/sqrt(float(simErNum))))**2
      #print "DEBUG: number of elements summed up for chiSq", chiSqArray.size
      chiSqValue = sum(chiSqArray)

#     #show plots that have been accumulating
#     xlabel(r'k', size=20)
#     ylabel(r'$\chi(k)$', size=20)
#     title(r'Simulated Error with Parent File' + feffFile, size=20)
#     show()

      aPyErrInputMaker(fileNameArray)
#     print "all done"
      return chiSqValue

   def aPyErrInputMaker(nameArray):
      aPyErrInput = open("aPyErr.inp", 'w')
      for line in nameArray:
         aPyErrInput.write(line + '\n')
      aPyErrInput.close()
```

```
#start of main program
#############################################################################
#when executed as main, executes the main program
if __name__ == "__main__":
    print "Using simErrAdd version:", versionNumber

    usage = "usage: %prog [options]"
    version="%prog "+str(versionNumber)
    parser = OptionParser(usage=usage,version=version)
    #help message is automatically provided

    parser.add_option('-p', '--pre', dest='outFilePrefix', default='ERRORFILE',
        help='prefix for simulated error output files [DEFAULT: %default]')

    parser.add_option('-n', '--num', dest='simErNum', default='10',
        help='number of error files to be simulated [DEFAULT: %default]')

    parser.add_option('-s', '--sigma', dest='sigmaFile', default='NONE',
        help='AVERR output file which contains SDOM values for non-constant ' +\
             'sigma error addition [DEFAULT: %default]')

    parser.add_option('-k', '--kScaleFactor', dest='scaleFactor', default='0.05',
        help='Scale factor for errors constant in Chi*k^n [DEFAULT: %default]')

    parser.add_option('-f', '--func', dest='sigmaFuncForm', default='chiConst',
        help='functional form of error to be added [DEFAULT: %default]: ' +\
             'chiConst = constant sigma as a function of k; chikConst = ' +\
             'constant sigma as a function of k*chi; chikCubeConst = ' +\
             'constant sigma as a function of k^3*chi; l = linear fit to ' +\
             'AVERR error file; e = exponential decay fit to AVERR error ' +\
             'file; o = lorentzian fit to AVERR error file; r = use cubic ' +\
             'interpolation of real error')

    parser.add_option('-g', '--gnu', action = 'store_true', dest='gnuFile',
        help='is input file a bin2gnu file? (instead of FEFF7). Used to put ' +\
             'sigma^2 values in through RSFIT [DEFAULT: %default]')

    #to add new options to the parser include use the line below
    #parser.add_option('','',dest='',help='')

    #assigns defined options above to a dictionary called options and any
    #leftover arguments to a list args. To get an option back out just use
    #options.<optionName>
    options, args = parser.parse_args(sys.argv[1:])

    #program should take one argument. If number of arg is wrong send an error
    #and offer help
    if len(args) != 1:
        parser.error("This program takes only one argument. Please use " +\
             "simErAd -h for more help.")

    #get option variables out of optionParse namespace
    outFilePrefix = options.outFilePrefix
    simErNum = options.simErNum
    scaleFactor = options.scaleFactor
    sigmaFile = options.sigmaFile
    gnuFile = options.gnuFile
    if options.sigmaFuncForm in ['chiConst', 'chikConst', 'chikCubeConst', 'l',
            'e', 'o', 'r']:
        sigmaFuncForm = options.sigmaFuncForm
    else:
        parser.error(options.sigmaFuncForm + " is not a valid option for -f")

    feffFile = args[0]

#   print "DEBUG: feffFile: ", feffFile
#   print "DEBUG: simErNum: ", simErNum
#   print "DEBUG: outFilePrefix: ", outFilePrefix
```

```
#    print "DEBUG: sigmaFile: ", sigmaFile
#    print "DEBUG: sigmaFuncForm: ", sigmaFuncForm

   #send options and arguments to addError for further processing
   chiSq = addError(feffFile, simErNum, outFilePrefix, sigmaFile, sigmaFuncForm,
         scaleFactor, gnuFile)
   print "DEBUG: chi^2 value: ", chiSq
```

F.4.3 SPECIATE

The purpose of this program is to run take an input PHREEQC file and associated PHREEQC thermodynamic database and use these files to repeatedly run PHREEQC to calculated a speciation diagram with error bars. Currently the available species are hard-coded into the program. Adjustments also must be made to the PHREEQC thermodynamic database to include the associated errors for thermodynamic constants.

```
#!/usr/bin/env python
###############################################################################
#species.py
#Written by: Yung-Jin Hu
#Written on: September 15, 2009
#Last updated: October 08, 2009
#
#This program has the form:
#
#This program has the options:
#
#Version Date     Description
#0.01    09/15/09 Initial writing of program.
#0.02    09/16/09 Starting to document code. Included ability to select PHREEQC
#                 database. Now searches for plutonium hydroxide species
#0.03    09/24/09 Added "calculations" folder to put all Monte Carlo calculation
#                 files into. Implemented search on database file to look for
#                 entries with ERROR associated and parses out information which
#                 is sent to random.gauss() to pick random values.
#0.04    09/26/09 Now takes the thermodynamic information and rewrites the
#                 PHREEQC database with new MC picked random values. PHREEQC
#                 still runs and the output data looks to reflect the new
#                 database values. Code parses PHREEQC.out data and outputs to
#                 data.dat file. This is done with re.compile() calls which
#                 significantly speeds up this step. Incorperated fitting of
#                 histograms, first with beta function and then using the
#                 estimates for SD from the shape parameters. The second method
#                 is significantly faster and more robust than attempting to
#                 numerically integrate the beta function, however both come at
#                 quite a computational cost. Hacked together a method for
#                 smoothing by cubic-spline interpolation.
#0.05    09/27/09 Added a genState file to the random number generator to ensure
#                 that random numbers continue to be picked according to the
#                 last number picked not the system seed. Tried to implement
#                 fitting of beta function and numerical integration for
#                 asymetric error bars. Seems to be working so far with a
#                 comprable hit to computation time as the PHREEQC calculations.
#                 Clipping the first and last data points in the distribution to
#                 keep numeric integrals from blowing up to inf. The errors
#                 introduced should be quite small considering the bin size.
#                 Smoothing by cubic-spline interpolation has been depreciated
#                 and may be removed depending on the robust-ness of the beta
#                 fitting algorithm.
#0.06    10/02/09 Tightened up code. Random PHREEQC database now moved instead
#                 of copied to the correct location. Trying to integrate all
#                 data at the same time so that individual calculations don't
#                 need to be conducted for each species. This has proven to be
#                 difficult due to a memory leak somewhere that is causing the
```

```
#                   program to die before geting through the second species.
#0.07     10/05/09 Using pdb I've found the problem is when the histogram is
#                   being formed. Using hist() from the matplotlib libraries seems
#                   to cause problems with memory leakage. I've switched over to
#                   numpy.histogram() which doesn't have the problem, but there is
#                   an integration problem now. The problem with the integration
#                   is that using "normed=True" in numpy.histogram() is causing
#                   problems because the assumption is that the histogram then
#                   becomes normalized to 1 upon integration. The code works if I
#                   don't make this assumption, run integrate.cumtrap() on the
#                   histogram and then normalize integrate.cumtrap() with the last
#                   element of the integrate.cumtrap() array. The integration
#                   process is now incredibly fast. This is because using
#                   numpy.histogram() instead of hist() from the matplotlib
#                   library means I don't have the overhead of setting up a
#                   plotting environment each time I call hist(). This was the
#                   problem before and the reason why so much computer memeory was
#                   being used.
#0.08     10/06/09 Added more printout information for final output files.
#0.09     10/08/09 Fixed a bug that would accidnetally add error to lines that
#                   were commented out in the PHREEQC database file.
#
#TO DO LIST:
#-check calculations are proceeding correctly. What's up with the pKa? Do I
#     need inert species like in Lungeskile?
#-extraction of solutions species needs to be more elegant. No way to code
#regular expressions for each possible case. Problem is better now, but not
#perfect...
#-implement Latin Hypercube sampleing into the code.
#-split up integration step more specifically. Taking the concMatrix as a
#stopping point so that integration at 1 sigma, 2 sigma, and 3 sigma can be
#achieved without having to redo the computation step. This will involve
#outputing concMatrix as a real self-aware object and not just a simple matrix.
##############################################################################
from numpy import *
from scipy import optimize, special, stats, integrate, interpolate
from pylab import *
import subprocess
import time
import re
import os
import shutil
import random
import decimal
import pickle
import pdb

__version__ = 0.09

def regularExpressionMaker(text):
    text = text.replace('+','\+')
    text = text.replace('.','\.')
    text = text.replace('*','\*')
    return text

#declare certain running paramerters
##############################################################################
maxIterations = 10000
simulationNumber = 1000
cwd = os.getcwd()
phreeqcInputFilename = "phreeqc.in"
phreeqcOutputFilename = "phreeqc.out"
phreeqcDatabaseFilename = "actinides.dat"
pHRange = arange(3,11.1,0.1)
#a tuple containing all of the terms that I want to search and its associated
#name
expn = "[-+]?[0-9]*\.?[0-9]+([eE][-+]?[0-9]+)?"
```

```
searchList = (
      ("pH", re.compile("pH\s*=\s*([-+]?[0-9]*\.?[0-9]+)")),

      ("Pu(6)", re.compile("Pu\(6\)\s*("+expn+')')),

      ("PuO2+2", re.compile("PuO2\+2\s*("+expn+')\s+('+expn+')')),

      ("PuO2OH+", re.compile("PuO2OH\+\s*("+expn+')\s+('+expn+')')),

      ("(PuO2)2(OH)2+2",
         re.compile("\(PuO2\)2\(OH\)2\+2\s*("+expn+')\s+('+expn+')')),

      ("PuO2(OH)2", re.compile("PuO2\(OH\)2\s*("+expn+')\s+('+expn+')')),

      ("PuO2CO3", re.compile("PuO2CO3\s*("+expn+')\s+('+expn+')')),

      ("PuO2(CO3)2-2", re.compile("PuO2\(CO3\)2-2\s*("+expn+')\s+('+expn+')')),

      ("PuO2(CO3)3-4", re.compile("PuO2\(CO3\)3-4\s*("+expn+')\s+('+expn+')')),

      )

def writePhreeqcInp():
   #write out PHREEQC input file
   ###############################################################################
   phreeqcInputFile = open(phreeqcInputFilename,'w')
   phreeqcInputFile.write("KNOBS\n")
   phreeqcInputFile.write("\t-iterations " + str(maxIterations) + '\n')

   for i in range(len(pHRange)):
      phreeqcInputFile.write("\nSOLUTION " + str(i) + '\n')
      phreeqcInputFile.write("\tpH " + str(pHRange[i]) + '\n')
      phreeqcInputFile.write("\tC(4) 1 CO2(g) -3.5\n")
      phreeqcInputFile.write("\tPu 0.000250\n")
      phreeqcInputFile.write("END\n")

   phreeqcInputFile.close()

def prepSimulation(calcFolder):
   #Prepare simulation files
   ###############################################################################
   totalMakeInputFileTime = 0
   os.mkdir(calcFolder)
   #copy PHREEQC input file to calculation subfolder
   shutil.copy(cwd + r'/' + phreeqcInputFilename, calcFolder)
   writeRandomDatabase(calcFolder)

def writeRandomDatabase(calcFolder):
   phreeqcRandDatabaseFile = open(phreeqcDatabaseFilename,'r').readlines()
   tempPhreeqcDatabase = open("tempPhreeqcDatabase", 'w')

   pattern = """
   ^                       #line has to start with...
   \s*                     #some amount of white space (i.e. not just '#')
   log_k                   #looking for lines with "log_k"
   \s+                     #with as much whitespace as can fit
   ([-+]?[0-9]*\.?[0-9]+)  #with some value of log_k
   \s*                     #with as much whitespace as can fit
   \#ERROR                 #with the keyword "#ERROR"
   \s+                     #with as much whitespace as can fit
   ([0-9]*\.?[0-9]+)       #with some value of ERROR (1sigma conf)
   """
   errorPattern = re.compile(pattern, re.VERBOSE)
   for line in phreeqcRandDatabaseFile:
      errorVal = errorPattern.search(line)
      if errorVal:
         logK = map(decimal.Decimal, errorVal.groups())
         thermoConstant = float(logK[0])
```

```
            thermoConstantError = float(logK[1])
            #get random number generator state from file 'genstate if it exists
            if os.path.exists('genState'):
                inputGenState = open('genState','r')
                generatorState = pickle.load(inputGenState)
                random.setstate(generatorState)
            #or seed using the system clock
            else:
                random.seed()
            thermoConstantPlusError = random.gauss(float(logK[0]),float(logK[1]))
            #save current random number generator state
            genState = random.getstate()
            outputGenState = open('genState', 'w')
            pickle.dump(genState, outputGenState)
            outputGenState.close()
            newline = '\tlog_k\t%6.3f\t#ERROR\t%6.3f\tERR_ADDED_species_v.%3.2f\n'\
                  % (thermoConstantPlusError, thermoConstantError, __version__)
            tempPhreeqcDatabase.write(newline)
        else:
            tempPhreeqcDatabase.write(line)
    tempPhreeqcDatabase.close()
    #take the randomly written database and move it into the correct calculation
    #folder
    shutil.move(cwd + r'/tempPhreeqcDatabase' , calcFolder + r'/' +\
            phreeqcDatabaseFilename)

def runPhreeqc(calcFolderList):
    #run PHREEQC in separate terminal
    ##############################################################################
    phreqcStart = time.time()
    cwd = os.getcwd()
    print "leaving: ", cwd
    for folder in calcFolderList:
        os.chdir(folder)
        preeqcTerm = subprocess.call('phreeqc ' + phreeqcInputFilename + ' ' +
                phreeqcOutputFilename + ' ' + phreeqcDatabaseFilename, shell=True)
    os.chdir(cwd)
    print "back to: ", cwd

def extractPhreeqcOutput(calcFolder):
    #read and extract pertanant data from PHREEQC output file
    ##############################################################################
    phreeqcOutputFileLines = open(calcFolder + r'/' +\
            phreeqcOutputFilename,'r').readlines()

    #initial search through the phreeqc.out file to get everything that is
    #associated with Pu(6)
    ##############################################################################
    puSpeciesList = []
    puSpecies = False
    for line in phreeqcOutputFileLines:
        puSpeciesSearchComp = searchList[1][1]
        blankLineSearchComp = re.compile("^$")
        puSpeciesSearchResult = puSpeciesSearchComp.search(line)
        blankLineSearchResult = blankLineSearchComp.search(line)
        if puSpeciesSearchResult:
#           print "found Pu(6)"
            puSpecies = True
        if blankLineSearchResult:
#           print "found blank line"
            puSpecies = False
        if puSpecies:
            puSpeciesList.append(line)
#   print "********"
#   print puSpeciesList
#   print "********"

    #formation of the parsedData list with species information
```

```
    ##########################################################################
    parsedData = []
    #get the pH information and Pu(6) values
    ##########################################################################
    for columnName, searchComp in searchList[:2]:
        columnList = []
        for line in phreeqcOutputFileLines:
            searchResult = searchComp.search(line)
            if searchResult:
                columnList.append(searchResult.group(1))
        parsedData.append((columnName, columnList, searchComp))
    #get Pu species values
    ##########################################################################
    for columnName, searchComp in searchList[2:]:
        columnList = []
        for line in puSpeciesList:
            searchResult = searchComp.search(line)
            if searchResult:
                columnList.append(searchResult.group(1))
        parsedData.append((columnName, columnList, searchComp))

    ##########################################################################
    #export parsed data to file
    dataOutput = open(calcFolder + r'/' + "data.dat", 'w')

    #write a header line
    line = ''
    for i in range(len(parsedData)):
        line = line + parsedData[i][0] + '\t\t'
    dataOutput.write('#' + line[:-2] + '\n')

    #write out all the data
    for j in range(len(parsedData[0][1])):
        line = ''
        for i in range(len(parsedData)):
#           print parsedData[i][1][j]
            line = line + parsedData[i][1][j] + '\t\t'
        dataOutput.write(line[:-2] + '\n')
    dataOutput.close()

def calculateErrorBars(calcFolderList):
    #go through all the data, normalize, create histogram, fit beta function to
    #data and integrate to get asymetric error bars
    ##########################################################################
    #make a 3D matrix with all simulated data
    matrix = loadMatrix(calcFolderList[0])
    #stack simulation data on to initial 2D matrix to make a 3D matrix
    for calcFolder in calcFolderList[1:]:
        matrix = dstack([matrix, loadMatrix(calcFolder)])

    concMatrixState = open('concMatrix', 'w')
    concMatrixState.write(matrix.dumps())
    concMatrixState.close()

    for k in range(len(searchList[2:])):
        speciesList = searchList[2:]
        species = speciesList[k]
        print "working on species: " + species[0]
        errorData = open(cwd + r'/' + species[0] + ".dat", 'w')
        errorData.write("#Output written by species v. %7.4f\n" % __version__)
        errorData.write("#for species: %s\n" % species[0])
        errorData.write("#Fitted Mean\t\tLow Error Bar\t\tHigh Error Bar\n")

        print "loading concMatrix"
        inputConcMatrixState = open('concMatrix', 'r')
        concMatrix = pickle.load(inputConcMatrixState)
        inputConcMatrixState.close()
        print "concMatrix loaded"
```

```
        for j in range(concMatrix.shape[0]):
            print "k: ",k
            print "j: ",j
            (EBLow, fittedMean, EBHigh) = integrator(concMatrix[j,k,:])
            errorData.write("%7.4f\t\t%7.4f\t\t%7.4f\n" % (fittedMean, EBLow,\
                  EBHigh))
        errorData.close()

def loadMatrix(calcFolder):
    print calcFolder
    data = loadtxt(calcFolder + r'/data.dat', comments='#')
    numberOfColumns = data.shape[1]
    numberOfSpeciesColumns = data.shape[1] - 2
    pH = data[:,0]
    normalization = data[:,1]
    broadcastNorm = normalization
    while numberOfSpeciesColumns - 1 > 0:
        broadcastNorm = vstack([broadcastNorm, normalization])
        numberOfSpeciesColumns = numberOfSpeciesColumns - 1
    broadcastNorm = broadcastNorm.T
    concentration = data[:,2:]/broadcastNorm
    return concentration

def rescaleBins(bins):
    x = array(())
    for i in range(len(bins[:-1])):
        newXvalue = (bins[i]+bins[(i+1)])/2.0
#       print newXvalue
        x = append(x, newXvalue)
#       print x
    return x

def integrator(matrixColumn):
    #declare the number of bins for a histogram
    numOfBins = 2000

#    (n,bins,patches) = hist(matrixColumn, numOfBins, range=(0,1),\
#          align="mid")

    n,bins = histogram(matrixColumn, numOfBins, range=(0,1), normed=False,\
          new=True)

#    x = arange(0, 1., 1./numOfBins)
#    halfStep = (1./numOfBins)/2
#    xCorr = x + halfStep
#    x = xCorr
    ###############################################################################
    #HACK!!! To do this right you just need to average the two adjacent values in
    #the bins to get the middle...
    ###############################################################################
    x = rescaleBins(bins)
    y = n
#    print "finished calculating x!"
#    print "len(x)", len(x)
#    print "len(y)", len(y)
#    print "DEBUG: bins", len(x)
#    print "DEBUG: nvalues in bins", len(y)

#    #fit to beta function
#    ###############################################################################
#    #functional form of the beta distribution. NOTE: v is a list of
#    #variables used to fit the function. v[0] = shape parameter alpha, v[1]
#    #= shape parameter beta, v[2] = normalization constant
#    fp = lambda v, x: v[2]*stats.beta.pdf(x,v[0],v[1])
#
#    e = lambda v,x,y: (fp(v,x) - y)
#
```

```
#   #initial guess, up-side-down parabola normalized to 1
#   v0 = [2, 2, 1]
#   v, success = optimize.leastsq(e, v0, args=(x,y), maxfev=1000)
#
#   fitData = fp(v,x)
#   fitX = x
#   fittedMean = v[0]/(v[0]+v[1])
#   fittedSD = sqrt((v[0]*v[1])/((v[0]+v[1])**2*(v[0]+v[1]+1.)))
#   highRes = arange(0,1,0.0001)
##   highResBeta = v[2]*stats.beta.pdf(highRes,v[0],v[1])
#   highResBeta = stats.beta.pdf(highRes,v[0],v[1])
#
#   TotalDistributionArea = integrate.trapz(y,x)
#
##  print "Total distribution area High res:", TotalDistributionArea
#   normalizedHighResBeta = highResBeta
##   cumInt = integrate.cumtrapz(normalizedHighResBeta[1:-1],highRes[1:-1])
#   cumInt = integrate.cumtrapz(normalizedHighResBeta,highRes)
    cumInt = integrate.cumtrapz(y,x)
    print "normalization constant:", cumInt[-1]
    cumInt = cumInt/cumInt[-1]
    #triming the first and last datapoints MAY keep the normalization
    #factor from going to inf, or the left and right distribution factors
    #from going to inf which will cause issues withi integration
#   highResTrim = highRes[1:-1]

    for z in range(len(cumInt)):
        if cumInt[z] > 0.159:
            print z
            break
    EBLow = x[z]

    for z in range(len(cumInt)):
        if cumInt[z] > 0.5:
            print z
            break
    mean = x[z]

#   for z in range(len(normalizedHighResBeta[1:-1])):
    for z in range(len(cumInt)):
        if cumInt[z] > 0.841:
            print z
            break
    EBHigh = x[z]
#   print "%7.4f\t\t%7.4f" % (EBLow, EBHigh)
    return (EBLow, mean, EBHigh)

################################################################################
################################################################################
#make a calculation directory to house all MC calculations
wallTimeStart = time.time()
print "current working directory:", cwd
makeInputFileStart = time.time()
writePhreeqcInp()
makeInputFileStop = time.time()
print "making calculations folder"
calcDir = cwd + r'/calculations'
if os.path.isdir(calcDir):
    print "folder exists, removing"
    shutil.rmtree(calcDir)
os.mkdir(calcDir)

#create a nice list of folder numbers with attached full path and make the
#folders in the calculations directory
print "making simulation subfolders and copying in database and phreeqc input\
files!"
calcFolderList = [calcDir + r'/sim%04d' % i for i in range(simulationNumber)]
#prepare simulation files for the whole list of folders
```

```
prepSimFileStart = time.time()
map(prepSimulation, calcFolderList)
prepSimFileStop = time.time()
#run PHREEQC in all the folders
phreqcStart = time.time()
runPhreeqc(calcFolderList)
phreeqcStop = time.time()
#go through all the PHREEQC output files and extract pertanant data
extractPhreeqcOutputStart = time.time()
map(extractPhreeqcOutput, calcFolderList)
extractPhreeqcOutputStop = time.time()
#calculate error bars from historgram data
#pdb.set_trace()
calculateErrorStart = time.time()
calculateErrorBars(calcFolderList)
calculateErrorStop = time.time()

wallTimeStop= time.time()


print 80*"*"
print 80*"*"
print "Total PHREEQC input formation time: %05.2f s" %\
      (makeInputFileStop-makeInputFileStart)
print "Total MC simulation file formation time: %05.2f s" %\
      (prepSimFileStop-prepSimFileStart)
print "Total PHREEQC Calculation time: %05.2f s" % (phreeqcStop-phreqcStart)
print "Total PHREEQC output extraction time: %05.2f s" %\
      (extractPhreeqcOutputStop-extractPhreeqcOutputStart)
print "Total Error Calculation time: %05.2f s" %\
      (calculateErrorStop-calculateErrorStart)
print "Total wall time: %05.2f s" % (wallTimeStop-wallTimeStart)
################################################################################
################################################################################

print "done with species"
```

F.4.4 GFITES

This program is a GUI front end to the RSXAP [78] program FITES, used to conduct least-squares fitting of XANES edge spectra. Running the command "gfites" in a linux terminal with the appropriately installed libraries will bring up a menu driven system for XANES fitting. Help with the program can be found under the "Help" menu.

```
#!/usr/bin/env python
################################################################################
#gfites.py
#Written by: Yung-Jin Hu
#Written on: December 03, 2009
#Last updated: July 10, 2010
#
#This program has the form:
#
#>gfites
#
#This program has the options:
#
#
#The purpose of this program is to display a frontend GUI interface for fites.
#The options are then written into a file called inparam.dat and the fites
#routine is called.
#
#Version Date      Description
#0.01    12/03/09 Initial writing of program.
```

```
#0.02    12/09/09 GUI working with all the plumbing in place. Currently output
#                 goes directly to the terminal instead of calling fites. Logic
#                 checking still needs to be implemented.
#0.03    02/05/10 Output sent to inparam.dat and fites is running through a
#                 subprocess.
#0.04    02/06/10 Initial trial to set up a plotting system using matplotlib
#                 libraries. Reorganized GUI sizers to look cleaner. Added plot
#                 button for standard files.
#0.05    02/07/10 Customizing plotter to take axis labels, title, and changing
#                 colors. Plots now have status bars which displays current
#                 position of curser in the plot area.
#0.06    02/11/10 Implemented ListBox for standards with multiple selections
#                 for selecting standard files for fitting and the ability to
#                 add and remove standards from that ListBox. Implemented
#                 ListBox for fit files as well, but have not yet setup
#                 multiple fits through the GUI.
#0.07    02/12/10 Implemented bin2Ascii python module to do fortran binary file
#                 conversion for plotting instead of using bin2gnu. Fixed
#                 plotting for Fit Files. Added menubar with File -> Exit and
#                 Help -> About gfites.
#0.08    02/15/10 Implemented default directories and saved default directories
#                 state in binary file gFitesComData. Fixed problem with
#                 plotter windows still hanging around after main frame closes.
#                 Added legends to plots.
#0.09    02/16/10 Aligned default directory frame items. Implemented frame
#                 which holds data from fites standard output and a button ready
#                 for parsing text and moving it to a data grid.
#0.10    02/21/10 Implemented the data grid window which allows the user to
#                 send results from the fites output window for perminant
#                 storage and side-by-side comparison. Reimplemented About
#                 gfites as a frame with HTML so that it is similar to the
#                 previous ones written using then Qt libraries. This allows
#                 more standard integration with the rest of the program.
#0.11    02/22/10 Refactored inparam.dat file writing to allow for saved
#                 sessions and fit history tracking. Implemented session saves
#                 into python binary file with the extension *.gfe for GFitEs.
#0.12    02/23/10 Fixed two bugs in pushing data to the GUI when opening saved
#                 *.gfe files. Fixed a bug when loading *.gfe files to the GUI.
#                 now both the contents of the list boxes (fit and standards)
#                 and the specific file selections are saved in the binary
#                 file.  Implemented history window which saves previous fit
#                 instences so that you can go back and see previous fit
#                 parameters. Manages multi-file fitting by looping the single
#                 file fitting. When doing multi-file fitting data is
#                 automatically sent to the grid and plotting of fits is turned
#                 off. Fixed bug where multi-file fitting followed by
#                 single-file fitting would cause the program to stop fitting.
#0.13    03/05/10 Fit and standard directories now update automatically  when
#                 opening adding files ot the file list. Moved output filename
#                 and results filename onto one line at the top of the main GUI
#                 panel. Added full support for fitting linear terms. Added icon
#                 as a large image in the help window. Added Windows section in
#                 menubar. Now when child windows (i.e. not the main window) are
#                 closed they are actually hidden. The Windows menu allows for
#                 these windows to be shown again in case you accidentally close
#                 them (ahem... Wayne). All the child windows (except plot
#                 windows live until the main frame window closes.
#0.14    06/09/10 Added support for putting in initial parameters for the
#                 standards before they are fit (through the use of a model
#                 dialog. This functionallity simply writes the appropriate
#                 lines in the input file that is fed to fites. Currently this
#                 information is only saved while the program is running.
#0.15    07/10/10 Hacked a way to get multi-fit output data to be printed out as
#                 a text file. This is temporary since the ideal way would be to
#                 allow copy and paste from the grid. However, this involves
#                 alot of coding concerning the system clipboard and the grid
#                 which I'm not interested in doing right now.
#
```

```
#TO DO LIST:
#-write a script to read in data from "inparam.dat" files into the GUI and save
#data back out into inparam.dat style formats??
#-display data in the fit as 'o' not lines
#-add fitrange guessing??
#-allow initial input parameters to be saved to *.gfe saved files.
##############################################################################
import os
import platform
import glob
import re
import shutil
import time, datetime
import pickle
import subprocess
import scipy.io
import webbrowser

import wxversion
wxversion.ensureMinimal('2.8')

import matplotlib
matplotlib.use('WXAgg')
from matplotlib.backends.backend_wxagg import FigureCanvasWxAgg as FigureCanvas
from matplotlib.backends.backend_wx import NavigationToolbar2Wx
from matplotlib.figure import Figure
import wx
import wx.grid
import wx.html
from numpy import *
from pylab import *
from bin2Ascii import rsxapBinOpen

__version__ = 0.15

class stdIniParamDialog(wx.Dialog):
   def __init__(self):
      wx.Dialog.__init__(self, None, -1, 'Std Files Initial Params',
            size=(-1,-1))
      self.SetIcon(wx.Icon(os.environ['PYTHONPATH']+'/icons/gfitesIcon.png',\
            wx.BITMAP_TYPE_PNG))

      #accessing the filenames located in the stdListBox on the main frame.
      #Notice that we do this through the use of the variable
      #frame.stdListBox.GetString()
      self.allStdFiles = []
      print "#####################"
      print "#####################"
      print frame.stdListBox.GetCount()
      print "#####################"
      print "#####################"
      for i in range(frame.stdListBox.GetCount()):
         self.allStdFiles.append(frame.stdListBox.GetString(i))
      print "#####################"
      print "#####################"
      print self.allStdFiles
      print "#####################"
      print "#####################"
      print frame.stdDic
      self.localStdList = []

      okButton = wx.Button(self, wx.ID_OK, "OK", pos=(15,15))
      okButton.SetDefault()
      cancelButton = wx.Button(self, wx.ID_CANCEL, "Cancel", pos=(115,15))

      def stdIniParamInputLine(fileName, ampValue, shiftAmp, eValue, shiftE):
         line = wx.BoxSizer(wx.HORIZONTAL)
```

```
            line_l = wx.StaticText(self, -1, fileName + ':')
            shiftAmp_t = wx.TextCtrl(self, -1, str(ampValue), size=(100,-1))
            checkShiftAmp = wx.CheckBox(self, -1, "Shift_Amp?")
            checkShiftAmp.SetValue(bool(shiftAmp))
            shiftE_t = wx.TextCtrl(self, -1, str(eValue), size=(100,-1))
            checkShiftE = wx.CheckBox(self, -1, "Shift_E?")
            checkShiftE.SetValue(bool(shiftE))

            line.Add(line_l, 0, wx.ALIGN_CENTER_VERTICAL|wx.ALL, 5)
            line.Add(shiftAmp_t, 0, wx.ALIGN_CENTER_VERTICAL|wx.ALL, 5)
            line.Add(checkShiftAmp, 0, wx.ALIGN_CENTER_VERTICAL|wx.ALL, 5)
            line.Add(shiftE_t, 0, wx.ALIGN_CENTER_VERTICAL|wx.ALL, 5)
            line.Add(checkShiftE, 0, wx.ALIGN_CENTER_VERTICAL|wx.ALL, 5)

            print (fileName, shiftAmp_t.GetValue(), checkShiftAmp.IsChecked(),
                   shiftE_t.GetValue(), checkShiftE.IsChecked())

            return (line, (fileName, shiftAmp_t, checkShiftAmp, shiftE_t,
               checkShiftE))

        sizer = wx.BoxSizer(wx.VERTICAL)
        iniParamInputLines = []
        for key in sorted(frame.stdDic.keys()):
            standard = frame.stdDic[key]
            print "DEBUG:", (standard.name, standard.ampValue, standard.shiftAmp,
            standard.eValue, standard.shiftE)

            lineElement = stdIniParamInputLine(standard.name, standard.ampValue,
               standard.shiftAmp, standard.eValue, standard.shiftE)
            iniParamInputLines.append(lineElement[0])
            self.localStdList.append(lineElement[1])

        for horizontalLine in iniParamInputLines:
            sizer.Add(horizontalLine, 1, wx.EXPAND)

        buttons = wx.StdDialogButtonSizer()
        buttons.AddButton(okButton)
        buttons.AddButton(cancelButton)
        buttons.Realize()
        sizer.Add(buttons, 0, wx.EXPAND|wx.ALL, 5)

        self.SetSizer(sizer)
        sizer.Fit(self)

class xyPlotterFrame(wx.Frame):
    def __init__(self):
#       wx.Frame.__init__(self,frame,-1, 'Plotter', size=(350,350))
        wx.Frame.__init__(self,frame,-1, 'Plotter', size=(-1,-1))

        self.SetIcon(wx.Icon(os.environ['PYTHONPATH']+'/icons/gfitesIcon.png',\
              wx.BITMAP_TYPE_PNG))

#       self.SetBackgroundColour(wx.NamedColor("BLACK"))

        self.figure = Figure(figsize=(6,6))
        self.axes = self.figure.add_subplot(111)
#       self._resizeflag = False

        self.axes.grid(True, color='black')
        self.axes.set_axis_bgcolor('gray')
#       self.axes.set_aspect('equal')

        self.canvas = FigureCanvas(self, -1, self.figure)

        #note this event is a MplEvent. It is going to update the curser position
        #in the status bar and change the cursor icon when it enters the plot area
#       self.canvas.Bind(wx.EVT_ENTER_WINDOW, self.ChangeCursor)
        self.canvas.mpl_connect('motion_notify_event', self.UpdateStatusBar)
```

```
        self.sizer = wx.BoxSizer(wx.VERTICAL)
        self.sizer.Add(self.canvas, 1, wx.LEFT | wx.TOP | wx.GROW)
        self.SetSizer(self.sizer)

        self.add_toolbar()
        self.add_statusbar()
        #fit after toolbar and status bar to make sure everything fits
        self.Fit()

    def add_toolbar(self):
        self.toolbar = NavigationToolbar2Wx(self.canvas)
        self.toolbar.Realize()
        self.SetToolBar(self.toolbar)
        self.toolbar.update()

#subroutines needed for status bar at the bottom of the graphs and updates of
#data as you move the mouse
################################################################################
    def add_statusbar(self):
        self.statusBar = wx.StatusBar(self, -1)
        self.statusBar.SetFieldsCount(1)
        self.SetStatusBar(self.statusBar)

    #changes curser icon when entering plotting area. Never did work exactly
    #correctly...
#    def ChangeCursor(self, event):
#        self.canvas.SetCursor(wx.StockCursor(wx.CURSOR_CROSS))

    def UpdateStatusBar(self, event):
        if event.inaxes:
            x, y = event.xdata, event.ydata
            self.statusBar.SetStatusText("(%+.3f, %+.3f)" % (event.xdata,
                event.ydata), 0)
################################################################################

    def plot(self, dataToPlot, axesTitle='', axesLabels=()):
        for data in dataToPlot:
            self.axes.plot(data[0], data[1], label=data[2])
        if len(axesLabels) == 2:
            self.axes.set_title(axesTitle, size=14)
            self.axes.set_xlabel(axesLabels[0])
            self.axes.set_ylabel(axesLabels[1])
        self.axes.legend(loc='best')
################################################################################
################################################################################

class dirExistsValidator(wx.PyValidator):
    def __init__(self, dir, key):
        wx.PyValidator.__init__(self)
        self.dir = dir
        self.key = key

    def Clone(self):
        return dirExistsValidator(self.dir, self.key)

    def Validate(self, win):
        textCtrl = self.GetWindow()
        text = textCtrl.GetValue()

        if not os.path.isdir(text):
            wx.MessageBox("Directory does not exist. Try again!", "Error")
            textCtrl.SetBackgroundColour("pink")
            textCtrl.SetFocus()
            textCtrl.Refresh()
            return False
        else:
            textCtrl.SetBackgroundColour(
```

```
                wx.SystemSettings_GetColour(wx.SYS_COLOUR_WINDOW))
            textCtrl.Refresh()
            return True

    def TransferToWindow(self):
        textCtrl = self.GetWindow()
        textCtrl.SetValue(self.dir.get(self.key,""))
        return True

    def TransferFromWindow(self):
        textCtrl = self.GetWindow()
        self.dir[self.key] = textCtrl.GetValue()
        return True
################################################################################
################################################################################

class defaultDirsDialog(wx.Dialog):
    def __init__(self, dic):
        wx.Dialog.__init__(self, None, -1, "Set Default Directories",\
                size=(500,100))

        FitDir_l = wx.StaticText(self, -1, "Fit Directory:")
        self.FitDir_t = wx.TextCtrl(self,\
                validator=dirExistsValidator(dic, "fit"), size=(350,-1))
        FitDir_b = wx.Button(self, -1, "Browse")
        self.Bind(wx.EVT_BUTTON, self.onFitDirBrowse, FitDir_b)

        StdDir_l = wx.StaticText(self, -1, "Standard Directory:")
        self.StdDir_t = wx.TextCtrl(self,\
                validator=dirExistsValidator(dic, "std"), size=(350,-1))
        StdDir_b = wx.Button(self, -1, "Browse")
        self.Bind(wx.EVT_BUTTON, self.onStdDirBrowse, StdDir_b)

        okay = wx.Button(self, wx.ID_OK)
        okay.SetDefault()
        cancel = wx.Button(self, wx.ID_CANCEL)

        sizer = wx.BoxSizer(wx.VERTICAL)

        horzSizer1 = wx.BoxSizer(wx.HORIZONTAL)
        horzSizer1.Add(FitDir_l, 0, wx.ALIGN_CENTER_VERTICAL|wx.ALL, 5)
        horzSizer1.Add(self.FitDir_t, 1, wx.ALIGN_CENTER_VERTICAL|wx.ALL, 5)
        horzSizer1.Add(FitDir_b, 0, wx.ALIGN_CENTER_VERTICAL|wx.ALL, 5)
        horzSizer2 = wx.BoxSizer(wx.HORIZONTAL)
        horzSizer2.Add(StdDir_l, 0, wx.ALIGN_CENTER_VERTICAL|wx.ALL, 5)
        horzSizer2.Add(self.StdDir_t, 1, wx.ALIGN_CENTER_VERTICAL|wx.ALL, 5)
        horzSizer2.Add(StdDir_b, 0, wx.ALIGN_CENTER_VERTICAL|wx.ALL, 5)

        sizer.Add(horzSizer1, 1, wx.EXPAND)
        sizer.Add(horzSizer2, 1, wx.EXPAND)

        buttons = wx.StdDialogButtonSizer()
        buttons.AddButton(okay)
        buttons.AddButton(cancel)
        buttons.Realize()
        sizer.Add(buttons, 0, wx.EXPAND|wx.ALL, 5)

        self.SetSizer(sizer)
        sizer.Fit(self)

    def onFitDirBrowse(self, event):
        fitDirDialog = wx.DirDialog(frame, "Choose a Standards Directory:",
                style=wx.DD_DEFAULT_STYLE)
        if fitDirDialog.ShowModal() == wx.ID_OK:
            self.FitDir_t.SetValue(fitDirDialog.GetPath())
        fitDirDialog.Destroy()

    def onStdDirBrowse(self, event):
```

```
        stdDirDialog = wx.DirDialog(frame, "Choose a Standards Directory:",
                style=wx.DD_DEFAULT_STYLE)
        if stdDirDialog.ShowModal() == wx.ID_OK:
            self.FitDir_t.SetValue(stdDirDialog.GetPath())
        stdDirDialog.Destroy()
################################################################################
################################################################################

class wxHTML(wx.html.HtmlWindow):
    """Allows links in HTML windows to be clikced on and opened using the native
    webbrowser."""
    def OnLinkClicked(self, link):
        webbrowser.open(link.GetHref())
################################################################################
################################################################################

class AboutDlg(wx.Frame):
    def __init__(self, parent):
        wx.Frame.__init__(self, frame, wx.ID_ANY, title="About gFites",
                size=(-1,800))
        self.SetIcon(wx.Icon(os.environ['PYTHONPATH']+'/icons/gfitesIcon.png',\
                wx.BITMAP_TYPE_PNG))

        #go through the trouble of running fites once just to get the version
        #number
        fitesProcess = subprocess.Popen("fites", stdout=subprocess.PIPE)
        (stdoutdata, stderrdata) = fitesProcess.communicate()
        stdoutdata = ''.join(stdoutdata)
        #take stdOut and split along lines, take first line and split along
        #spaces, take the last value of the first line = fites version number!
        #What a HACK!
        stdoutLines = stdoutdata.split('\n')
        fitesVersion = float(stdoutLines[0].split()[-1])

        html = wxHTML(self)
        html.SetPage("<h2><center>About gFites %.2f</center></h2>" %
                (__version__) +
        "<center><IMG SRC=" + os.environ['PYTHONPATH']+'/icons/gfitesIcon.png' +\
        "></center>"

        """<p><b>gFites</b> version %.2f using <b>fites</b> version %.2f, part of
            the RSXAP package managed by <a href="mailto:CHBooth@lbl.gov">Corwin H.
            Booth</a>.

            <p>RSXAP is available from
            <b><a href="http://lise.lbl.gov/RSXAP/index.html">
            http://lise.lbl.gov/RSXAP/index.html</a></b>.

            <p>The full power of fites is exposed through the GUI interface,
            along with various convenience widgets, such as instant plotting of
            sample(s)/standard(s), session saves, result parsing, etc...

            <p>You are free to use, modify, and redistribute the source code and
            documentation. There is no charge for their use. The main
            limitations are that you cannot claim you wrote the program or
            documentation and cannot prevent other people from using them.
            <p>THE SOFTWARE IS PROVIDED "AS IS", WITHOUT WARRANTY OF ANY KIND,
            EXPRESS OR IMPLIED, INCLUDING BUT NOT LIMITED TO THE WARRANTIES OF
            MERCHANTABILITY, FITNESS FOR A PARTICULAR PURPOSE AND
            NONINFRINGEMENT. IN NO EVENT SHALL THE AUTHORS OR COPYRIGHT HOLDERS
            BE LIABLE FOR ANY CLAIM, DAMAGES OR OTHER LIABILITY, WHETHER IN AN
            ACTION OF CONTRACT, TORT OR OTHERWISE, ARISING FROM, OUT OF OR IN
            CONNECTION WITH THE SOFTWARE OR THE USE OR OTHER DEALINGS IN THIS
            SOFTWARE.

            <p>For comments and bug reports please send an email to:
            <a href="mailto:YHu@lbl.gov">YHu@lbl.gov</a>
```

```
        <p>Python %s - wxPython %s on %s""" % (__version__, fitesVersion,
        platform.python_version(), wx.__version__, platform.system()))
##############################################################################
##############################################################################

class fitHistoryFrame(wx.Frame):
    def __init__(self):
        wx.Frame.__init__(self, frame, -1, 'Fit History',
                pos=(wx.DisplaySize()[0],0))
        panel = wx.Panel(self, -1)
        self.SetIcon(wx.Icon(os.environ['PYTHONPATH']+'/icons/gfitesIcon.png',\
                wx.BITMAP_TYPE_PNG))

        self.Bind(wx.EVT_CLOSE, self.onCloseWindow)

        self.fitNamehistoryList = []
        self.fitInstanceHistoryList = []

        self.historyListBox = wx.ListBox(panel, -1, (-1,-1), (200,250),
                self.fitNamehistoryList, wx.LB_SINGLE)
        self.Bind(wx.EVT_LISTBOX, self.onInstanceSelection, self.historyListBox)

        sizer = wx.BoxSizer(wx.VERTICAL)
        sizer.Add(self.historyListBox, 0, wx.ALIGN_CENTER_HORIZONTAL| wx.ALL, 5)
        sizer.Fit(self)
        sizer.SetSizeHints(self)
        panel.SetSizer(sizer)

    def addFitInstance(self, fitInstanceName):
        self.historyListBox.Append(fitInstanceName)
        self.historyListBox.SetSelection(self.historyListBox.GetCount()-1)

    def onInstanceSelection(self, event):
        print "you selected a new history item!!! Loading..."
        i = self.historyListBox.GetSelection()
        frame.pushFitInstanceToGui(self.fitInstanceHistoryList[i])

    def onCloseWindow(self, event):
        self.Show(False)

##############################################################################
##############################################################################

class stdFile():
    """defining a type of data structure called stdFile to store
    information about standard files used for fitting"""
    def __init__(self, fileName, ampValue='1', shiftAmp=True, eValue='0',
            shiftE=True):
        self.name = fileName
        self.shiftAmp = shiftAmp
        self.ampValue = ampValue
        self.shiftE = shiftE
        self.eValue = eValue

class gFitesMainFrame(wx.Frame):
    def __init__(self):
        wx.Frame.__init__(self, None, -1, 'gFites', pos=(0,0))
        panel = wx.Panel(self, -1)
        self.SetIcon(wx.Icon(os.environ['PYTHONPATH']+'/icons/gfitesIcon.png',\
                wx.BITMAP_TYPE_PNG))

        ##########################################################################
        #make menu bar
        ##########################################################################
        self.menuBar = wx.MenuBar()
        self.SetMenuBar(self.menuBar)

        self.fileMenu = wx.Menu()
```

```
self.menuBar.Append(self.fileMenu, "&File")
fileSaveFit = self.fileMenu.Append(-1, "Save Fit...")
self.Bind(wx.EVT_MENU, self.onFileSaveFit, fileSaveFit)
fileOpenFit = self.fileMenu.Append(-1, "Open Fit...")
self.Bind(wx.EVT_MENU, self.onFileOpenFit, fileOpenFit)
fileDefaultDirs = self.fileMenu.Append(-1, "Default Directories...")
self.Bind(wx.EVT_MENU, self.onDefaultDirs, fileDefaultDirs)
fileExit = self.fileMenu.Append(-1, "&Exit")
self.Bind(wx.EVT_MENU, self.onFileClose, fileExit)

self.windowsMenu = wx.Menu()
self.menuBar.Append(self.windowsMenu, "&Windows")
historyWindow = self.windowsMenu.Append(-1, "Show History")
self.Bind(wx.EVT_MENU, self.onWindowsShowHistory, historyWindow)
stdOutWindow = self.windowsMenu.Append(-1, "Show Standard Output")
self.Bind(wx.EVT_MENU, self.onWindowsShowStdOut, stdOutWindow)
fitesGridWindow = self.windowsMenu.Append(-1, "Show Grid")
self.Bind(wx.EVT_MENU, self.onWindowsShowFitesGrid, fitesGridWindow)

self.helpMenu = wx.Menu()
self.menuBar.Append(self.helpMenu, "&Help")
helpAbout = self.helpMenu.Append(-1, "&About gfites")
self.Bind(wx.EVT_MENU, self.onHelpAbout, helpAbout)
#############################################################################

self.defaultDirDic = {"fit":"", "std":""}
self.unpickleDefaultDirDic()

fitDirLabel = wx.StaticText(panel, -1, "Fit Directory:")
self.fitDirText = wx.TextCtrl(panel, -1, self.defaultDirDic['fit'])
self.fitDirText.SetInsertionPoint(0)

#############################################################################
#############################################################################
fitFileLabel = wx.StaticText(panel, -1, "Fit File(s):")
fitList = ["003SumG_preg_shifted"]
self.fitListBox = wx.ListBox(panel, -1, (-1,-1), (200,150), fitList,
      wx.LB_MULTIPLE)

#define and standard file add, remove, and plot buttons
self.fitAdd= wx.Button(panel, -1, "Add")
self.Bind(wx.EVT_BUTTON, self.onClickFitAdd, self.fitAdd)
self.fitRemove= wx.Button(panel, -1, "Remove")
self.Bind(wx.EVT_BUTTON, self.onClickFitRemove, self.fitRemove)
self.fitPlot = wx.Button(panel, -1, "Plot")
self.Bind(wx.EVT_BUTTON, self.onClickFitPlot, self.fitPlot)
#############################################################################
#############################################################################
#define and browse button for fit file and directory
self.fitFileBrowse = wx.Button(panel, -1, "Browse")
self.Bind(wx.EVT_BUTTON, self.onClickFitDirBrowse, self.fitFileBrowse)

fitFileModeLabel = wx.StaticText(panel, -1, "Column:")
columnList = ['1', '2']
self.fitFileModeChoice = wx.Choice(panel, -1, (85,18), choices=columnList)
self.fitFileModeChoice.SetSelection(0)

stdDirLabel = wx.StaticText(panel, -1, "Standards Directory:")
self.stdDirText = wx.TextCtrl(panel, -1, self.defaultDirDic['std'],
      size=(350,-1))
self.stdDirText.SetInsertionPoint(0)

#define and browse button for standards directory
self.stdDirBrowse = wx.Button(panel, -1, "Browse")
self.Bind(wx.EVT_BUTTON, self.onClickStdDirBrowse, self.stdDirBrowse)

#############################################################################
#############################################################################
```

```
stdFileLabel = wx.StaticText(panel, -1, "Standard File(s):")
self.stdDic = {}
fileNameList = ["pu4Stde_pre_shifted", "pu5Stde_pre_shifted",
      "pu6Stde_pre_shifted"]
for name in fileNameList:
   self.stdDic[name] = stdFile(name)

nameList = sorted(self.stdDic.keys())
print "DEBUG!!!:", nameList

self.stdListBox = wx.ListBox(panel, -1, (-1,-1), (200,100), nameList,
      wx.LB_MULTIPLE)

#define and standard file add, remove, and plot buttons
self.stdAdd= wx.Button(panel, -1, "Add")
self.Bind(wx.EVT_BUTTON, self.onClickStdAdd, self.stdAdd)
self.stdRemove= wx.Button(panel, -1, "Remove")
self.Bind(wx.EVT_BUTTON, self.onClickStdRemove, self.stdRemove)
self.stdInitParam = wx.Button(panel, -1, "Initial Parameters")
self.Bind(wx.EVT_BUTTON, self.onClickInitParam, self.stdInitParam)
self.stdPlot = wx.Button(panel, -1, "Plot")
self.Bind(wx.EVT_BUTTON, self.onClickStdPlot, self.stdPlot)
##############################################################################
##############################################################################

stdFileModeLabel = wx.StaticText(panel, -1, "Column:")
columnList = ['1', '2']
self.stdFileModeChoice = wx.Choice(panel, -1, (85,18), choices=columnList)
self.stdFileModeChoice.SetSelection(0)

fitOutNameLabel = wx.StaticText(panel, -1, "Output Filename:")
self.fitOutNameText = wx.TextCtrl(panel, -1, "fitesOut.dat",
      size=(200,-1))
self.fitOutNameText.SetInsertionPoint(0)

fitResultNameLabel = wx.StaticText(panel, -1, "Results Filename:")
self.fitResultNameText = wx.TextCtrl(panel, -1, "fitesResults.dat",
      size=(200,-1))
self.fitResultNameText.SetInsertionPoint(0)

self.e0SameCheck = wx.CheckBox(panel, -1, "Set E0 to be the same?")
self.e0SameCheck.SetValue(True)

self.linTermCheck= wx.CheckBox(panel, -1, "Add linear term to the fit?")
self.linTermCheck.SetValue(False)

self.energyResolutionCheck = wx.CheckBox(panel, -1, "Energy Resolution"
      " (eV):")
self.Bind(wx.EVT_CHECKBOX, self.onEnergyResolutionCheck,
      self.energyResolutionCheck)
self.energyResolutionText = wx.TextCtrl(panel, -1, "", style=wx.TE_RIGHT)
self.energyResolutionText.SetInsertionPoint(0)
self.energyResolutionText.Enable(False)

fitRangeLabel = wx.StaticText(panel, -1, "Fit Range:")
self.fitRangeLow = wx.TextCtrl(panel, -1, "-30", style=wx.TE_RIGHT)
self.fitRangeLow.SetInsertionPoint(0)
self.fitRangeHigh= wx.TextCtrl(panel, -1, "30", style=wx.TE_RIGHT)
self.fitRangeHigh.SetInsertionPoint(0)

#define and bind a button to start the fit
self.fitesButton = wx.Button(panel, -1, "Run FITES")
self.Bind(wx.EVT_BUTTON, self.onClickFites, self.fitesButton)

#define and implement all the widgits into a sizer
sizer = wx.BoxSizer(wx.VERTICAL)

itemSet = [[(fitOutNameLabel, 0), (self.fitOutNameText, 0),
```

```
                (fitResultNameLabel, 0), (self.fitResultNameText, 0)],

            [(fitDirLabel, 0), (self.fitDirText, 1), (fitFileModeLabel, 0),
                (self.fitFileModeChoice, 0), (self.fitFileBrowse, 0)],

            [(fitFileLabel, 0), (self.fitListBox, 0), (self.fitPlot, 0)],

            [(self.fitAdd,0), (self.fitRemove,0)],

            [(stdDirLabel, 0), (self.stdDirText, 1), (stdFileModeLabel, 0),
                (self.stdFileModeChoice, 0), (self.stdDirBrowse, 0)],

            [(stdFileLabel, 0), (self.stdListBox, 0), (self.stdPlot, 0)],

            [(self.stdAdd,0), (self.stdRemove,0), (self.stdInitParam, 0)],

            [(self.e0SameCheck, 0)],

            [(self.linTermCheck, 0)],

            [(self.energyResolutionCheck, 0), (self.energyResolutionText, 0)],

            [(fitRangeLabel, 0), (self.fitRangeLow, 0), (self.fitRangeHigh, 0)],

            [(self.fitesButton, 0)]]

        sizerLineList = []
        #take the lists in itemSet list and add to a horizontal BoxSizer
        for itemLine in itemSet:
            sizerLine = wx.BoxSizer(wx.HORIZONTAL)
            sizerHorizontalList = []
            for item in itemLine:
                sizerHorizontalList.append((item[0], item[1],
                    wx.ALIGN_CENTER_VERTICAL | wx.ALL, 5 ))
            sizerLine.AddMany(sizerHorizontalList)
            #append horizontal BoxSizers to a list to send to vertical BoxSizer
            sizerLine.Fit(self)
            sizerLineList.append((sizerLine, 0, wx.GROW | wx.ALL, 2))

        #add horizontal BoxSizers to a vertical BoxSizer
        sizer.AddMany(sizerLineList)
        sizer.Fit(self)
        sizer.SetSizeHints(self)

        panel.SetSizer(sizer)
        self.Bind(wx.EVT_CLOSE, self.onCloseWindow)


    def onClickInitParam(self, event):
        self.openInitParamDialog()

    def openInitParamDialog(self):
        stdIniParamDialogInstance = stdIniParamDialog()
        result = stdIniParamDialogInstance.ShowModal()
        if result == wx.ID_OK:
            print "writing parameters"
            #clear out stdDic
            self.stdDic = {}
            #repopulate stdList with new input parameters
            for item in stdIniParamDialogInstance.localStdList:
                self.stdDic[item[0]] = stdFile(str(item[0]),
                    str(item[1].GetValue()), bool(item[2].IsChecked()),
                    str(item[3].GetValue()), bool(item[4].IsChecked()))

            stdIniParamDialogInstance.Destroy()
#           for line in self.stdList:
#               print (line.name, line.shiftAmp, line.ampValue, line.shiftE,
#                   line.eValue)
```

```
        else:
            print "canceled and not writing parameters"
        stdIniParamDialogInstance.Destroy()

    def pickleDefaultDirDic(self):
        pickleOutput = open("gFitesComData", 'wb')
        pickle.dump(self.defaultDirDic, pickleOutput)
        pickleOutput.close()

    def unpickleDefaultDirDic(self):
        if os.path.isfile("gFitesComData"):
            pickleInput = open("gFitesComData", 'rb')
            self.defaultDirDic = pickle.load(pickleInput)
            pickleInput.close()

    def onHelpAbout(self, event):
        gfitesAbout = AboutDlg(None)
        gfitesAbout.Show()

    def onFileClose(self, event):
        self.Close()
        self.Destroy()

    def onDefaultDirs(self, event):
        defaultDirsDialogInstance = defaultDirsDialog(self.defaultDirDic)
        defaultDirsDialogInstance.ShowModal()

        self.stdDirText.SetValue(self.defaultDirDic['std'])
        self.stdDirText.Refresh()
        self.fitDirText.SetValue(self.defaultDirDic['fit'])
        self.fitDirText.Refresh()
        self.pickleDefaultDirDic()

    def fitInputExtractor(self):
        """function that extracts important values from the GUI interface instance
        into class variables"""
        self.fitDir = self.fitDirText.GetValue()
        if self.energyResolutionCheck.IsChecked():
            self.energyResolution = self.energyResolutionText.GetValue()
        else:
            self.energyResolution = False

        if self.linTermCheck.IsChecked():
            self.linTerm = True
        else:
            self.linTerm = False

        if self.fitFileModeChoice.GetStringSelection() == "1":
            self.fitFileMode = "transmission"
        else:
            self.fitFileMode = "reference"
        self.fitRange = (self.fitRangeLow.GetValue(),
              self.fitRangeHigh.GetValue())
        self.fitOutName = self.fitOutNameText.GetValue()
        self.fitResultName = self.fitResultNameText.GetValue()
        self.stdDir = self.stdDirText.GetValue()
        #pull out the selected standard files in the list box
        self.selectedStdFiles = []
        for i in self.stdListBox.GetSelections():
            self.selectedStdFiles.append(self.stdListBox.GetString(i))
        numStdFiles = len(self.stdListBox.GetSelections())
        if numStdFiles == 0:
            print "no standard files selected!!! Please try again."
        #pull out all the standard files in the list box
        self.allStdFiles = []
        for i in range(self.stdListBox.GetCount()):
            self.allStdFiles.append(self.stdListBox.GetString(i))
```

```
        print self.selectedStdFiles

        self.fracAmpsList = [str(self.stdDic[self.selectedStdFiles[0]].ampValue),]
        self.shiftsList = [str(self.stdDic[self.selectedStdFiles[0]].eValue),]
        if self.stdDic[self.selectedStdFiles[0]].shiftAmp:
            self.varAmpsList = ['1',]
        else:
            self.varAmpsList = ['0',]
        if self.stdDic[self.selectedStdFiles[0]].shiftE:
            self.varShiftList = ['1',]
        else:
            self.varShiftList = ['0',]

#       self.shiftAmp = shiftAmp
#       self.ampValue = ampValue
#       self.shiftE = shiftE
#       self.eValue = eValue

        if numStdFiles > 1:
            for key in self.selectedStdFiles[1:]:
                self.fracAmpsList += [self.stdDic[key].ampValue,]
                self.shiftsList += [self.stdDic[key].eValue,]
                if self.stdDic[key].shiftAmp:
                    self.varAmpsList += ['1',]
                else:
                    self.varAmpsList += ['0',]
                if self.stdDic[key].shiftE:
                    self.varShiftList += ['1',]
                else:
                    self.varShiftList += ['0',]

        print self.fracAmpsList
        print self.shiftsList
        print self.varAmpsList
        print self.varShiftList

#       except ArithmeticError:
#           self.fracAmpsList = ''
#           self.shiftsList = ''
#           self.varAmpsList = ''
#           self.varShiftList = ''

        if self.stdFileModeChoice.GetStringSelection() == "1":
            self.stdFileMode = "transmission"
        else:
            self.stdFileMode = "reference"

        if self.e0SameCheck.GetValue():
            self.e0Same = True
        else:
            self.e0Same = False

        #pull out the selected fit files in the list box
        self.selectedFitFiles = []
        for i in self.fitListBox.GetSelections():
            self.selectedFitFiles.append(self.fitListBox.GetString(i))
        #pull out all the fit files in the list box
        self.allFitFiles = []
        for i in range(self.fitListBox.GetCount()):
            self.allFitFiles.append(self.fitListBox.GetString(i))

    def onFileSaveFit(self, event):
        self.fitInputExtractor()

        fitInstanceData = (self.fitDir, self.energyResolution, self.fitFileMode,
                self.fitRange, self.fitOutName, self.fitResultName, self.stdDir,
                self.selectedStdFiles, self.allStdFiles, self.fracAmpsList,
```

```
            self.shiftsList, self.varAmpsList, self.varShiftList,
            self.stdFileMode, self.e0Same, self.selectedFitFiles,
            self.allFitFiles, self.linTerm)

        fitInstance = formFitInstance(fitInstanceData)

        wildcard = "gfites fit files (*.gfe)|*.gfe| All files (*.*)|*.*|"

        saveFitDialog = wx.FileDialog(frame, "Save Fit:", os.getcwd(), ".gfe",
            wildcard, wx.SAVE)
        if saveFitDialog.ShowModal() == wx.ID_OK:
            pickleOutput = open(saveFitDialog.GetPath(), 'wb')
            pickle.dump(fitInstance, pickleOutput)
            pickleOutput.close()
        saveFitDialog.Destroy()

    def pushFitInstanceToGui(self, instance):
        #pushing loaded file back into the GUI interface
        self.fitDirText.SetValue(instance.fitDir)
        if instance.energyResolution:
            self.energyResolutionCheck.SetValue(True)
            self.energyResolutionText.Enable(True)
            self.energyResolutionText.SetValue(instance.energyResolution)
        else:
            self.energyResolutionCheck.SetValue(False)
            self.energyResolutionText.SetValue('')
            self.energyResolutionText.Enable(False)
        if instance.fitFileMode == 'transmission':
            self.fitFileModeChoice.SetSelection(0)
        else:
            self.fitFileModeChoice.SetSelection(1)
        self.fitRangeLow.SetValue(instance.fitRange[0])
        self.fitRangeHigh.SetValue(instance.fitRange[1])
        self.fitOutNameText.SetValue(instance.fitOutName)
        self.fitResultNameText.SetValue(instance.fitResultName)
        self.stdDirText.SetValue(instance.stdDir)

        #remove everything in the stdListBox before adding the new standard files
        #and then selecting the ones that were previously selected
        self.stdListBox.Clear()
        for file in instance.allStdFiles:
            self.stdListBox.Append(file)
        for selectedFile in instance.selectedStdFiles:
            selectedFilePos = self.stdListBox.FindString(selectedFile)
            if selectedFilePos != -1:
                self.stdListBox.SetSelection(selectedFilePos)
            else:
                print "DEBUG: This standard file was in the selected list, but"\
                      "not the full list:", selectedFile

        if instance.stdFileMode == 'transmission':
            self.stdFileModeChoice.SetSelection(0)
        else:
            self.stdFileModeChoice.SetSelection(1)

        if instance.e0Same:
            self.e0SameCheck.SetValue(True)
        else:
            self.e0SameCheck.SetValue(False)

        if instance.linTerm:
            self.linTermCheck.SetValue(True)
        else:
            self.linTermCheck.SetValue(False)

        #remove everything in the fitListBox before adding the new fit files
        self.fitListBox.Clear()
        for file in instance.allFitFiles:
```

```
            self.fitListBox.Append(file)
        for selectedFile in instance.selectedFitFiles:
            selectedFilePos = self.fitListBox.FindString(selectedFile)
            if selectedFilePos != -1:
                self.fitListBox.SetSelection(selectedFilePos)
            else:
                print "DEBUG: This fit file was in the selected list, but"\
                      "not the full list:", selectedFile

    def onFileOpenFit(self, event):
        """function that shows open file dialog. The file is then reloaded into
        the man GUI interface in the gFitesMainFrame."""
        #open file dialog and unpickling of *.gfe file
        wildcard = "gfites fit files (*.gfe)|*.gfe| All files (*.*)|*.*|"
        openFitDialog = wx.FileDialog(frame, "Open Previously Saved Fit:",
                os.getcwd(), "", wildcard, wx.OPEN)
        if openFitDialog.ShowModal() == wx.ID_OK:
            pickleInput = open(openFitDialog.GetPath(), 'rb')
            self.openFitInstance = pickle.load(pickleInput)
            pickleInput.close()
        openFitDialog.Destroy()
        self.pushFitInstanceToGui(self.openFitInstance)

    def onClickFitRemove(self, event):
        #while loop is used here since the GetSelections() command updates in a
        #for loop as it deletes through the list. Here we're just looping as long
        #as there is something being returned from GetSelections() and deleting
        #the first entry in the list.
        while self.fitListBox.GetSelections():
            self.fitListBox.Delete(self.fitListBox.GetSelections()[0])

    def onClickFitAdd(self, event):
        fitFileDialog = wx.FileDialog(frame, "Choose Fit File(s):",
                self.fitDirText.GetValue(), "", "*", wx.MULTIPLE)
        if fitFileDialog.ShowModal() == wx.ID_OK:
            for path in fitFileDialog.GetPaths():
                filename = os.path.basename(path)
                directory = os.path.dirname(path)
                self.fitListBox.Append(filename)
                self.fitDirText.SetValue(directory)
        fitFileDialog.Destroy()

    def onClickFitPlot(self, event):
        cwd = os.getcwd()
        os.chdir(self.fitDirText.GetValue())

        dataToPlot = []
        for i in self.fitListBox.GetSelections():
            (header, xData, yDataMatrix) =\
                    rsxapBinOpen(self.fitListBox.GetString(i))
            #WARNING! Hack here to just take care of es binary files. This should
            #be fixed in the future incase someone wants to fit ks or rs files
            dataToPlot.append((xData, yDataMatrix[:,0],\
                    self.fitListBox.GetString(i)))
        os.chdir(cwd)

        plotter = xyPlotterFrame()
        plotter.plot(dataToPlot, "Plot of Fit File(s)", ("Energy (eV)",\
                "Relative Absorption (a.u.)"))
        plotter.Show()
################################################################################
################################################################################

    def onClickStdRemove(self, event):
        #while loop is used here since the GetSelections() command updates in a
        #for loop as it deletes through the list. Here we're just looping as long
        #as there is something being returned from GetSelections() and deleting
        #the first entry in the list.
```

```
        while self.stdListBox.GetSelections():
            self.stdListBox.Delete(self.stdListBox.GetSelections()[0])

    def onClickStdAdd(self, event):
        stdFileDialog = wx.FileDialog(frame, "Choose Standard File(s):",
                self.stdDirText.GetValue(), "", "*", wx.MULTIPLE)
        if stdFileDialog.ShowModal() == wx.ID_OK:
            for path in stdFileDialog.GetPaths():
                filename = os.path.basename(path)
                directory = os.path.dirname(path)
                self.stdListBox.Append(filename)
                self.stdDirText.SetValue(directory)
        stdFileDialog.Destroy()

    def onClickStdPlot(self, event):
        cwd = os.getcwd()
        os.chdir(self.stdDirText.GetValue())

        dataToPlot = []
        for i in self.stdListBox.GetSelections():
            (header, xData, yDataMatrix) =\
                    rsxapBinOpen(self.stdListBox.GetString(i))
            #WARNING! Hack here to just take care of es binary files. This should
            #be fixed in the future incase someone wants to plot ks or rs files
            dataToPlot.append((xData, yDataMatrix[:,0],\
                    self.stdListBox.GetString(i)))

        plotter = xyPlotterFrame()
        plotter.plot(dataToPlot, "Plot of Standard(s)", ("Energy (eV)",\
                "Relative Absorption (a.u.)"))
        plotter.Show()

        os.chdir(cwd)

    def onClickFitDirBrowse(self, event):
        fitDirDialog = wx.DirDialog(frame, "Choose a Fit Directory",
                self.fitDirText.GetValue(), style=wx.DD_DEFAULT_STYLE)
        if fitDirDialog.ShowModal() == wx.ID_OK:
            self.defaultDirDic['fit'] = fitDirDialog.GetPath()
            self.fitDirText.SetValue(fitDirDialog.GetPath())
        fitDirDialog.Destroy()

    def onClickStdDirBrowse(self, event):
        stdDirDialog = wx.DirDialog(frame, "Choose a Standards Directory:",
                self.stdDirText.GetValue(), style=wx.DD_DEFAULT_STYLE)
        if stdDirDialog.ShowModal() == wx.ID_OK:
            self.defaultDirDic['std'] = stdDirDialog.GetPath()
            self.stdDirText.SetValue(stdDirDialog.GetPath())
        stdDirDialog.Destroy()

    def onCloseWindow(self, event):
        self.Destroy()

    def onEnergyResolutionCheck(self, event):
        if self.energyResolutionCheck.IsChecked():
            self.energyResolutionText.Enable(True)
        elif not self.energyResolutionCheck.IsChecked():
            self.energyResolutionText.Enable(False)

    def writeInparamFile(self, fitFile):
        """function that writes the file inparam.dat to be used as the input file
        for fites"""
        if os.path.exists("inparam.dat"):
            print "inparam.dat already exists!"
            inputFileList = glob.glob("inparam*.dat")
            print inputFileList
            inputFileList = sorted(inputFileList)
            lastInputFile = inputFileList[-1]
```

```
    number = re.search('inparam(\d*)\.dat', lastInputFile)
    if number:
        newFileNumber = 1
        if number.group(1) != '':
            newFileNumber = int(number.group(1)) + 1
        print "renaming current inparam.dat file to inparam" +\
              str(newFileNumber) +".dat"
        shutil.move("inparam.dat", "inparam%05d.dat" % newFileNumber)
inputFile = open("inparam.dat", 'w')
#write Header lines to document automated program writing and time

inputFile.write("#This fites input file was automatically written " +\
      "using gfites version " + str(__version__) + '\n')

inputFile.write("#On " + time.strftime("%a, %b %d %Y %H:%M:%S",\
    time.localtime()) + '\n')
#write FITDIR line
inputFile.write("FITDIR " + self.fitDir + '\n')
#write resolution line
if self.energyResolution:
    inputFile.write("RESOLUTION " + self.energyResolution + '\n')
#write FITFILEMODE
inputFile.write("FITFILEMODE " + self.fitFileMode + '\n')
#write FITRANGE
inputFile.write("FITRANGE " + self.fitRange[0] + " " + self.fitRange[1] +\
      '\n')
#write OUTFITFILE line
inputFile.write("OUTFITFILE " + self.fitOutName + '\n')
#write FITRESULTS line
inputFile.write("FITRESULTS " + self.fitResultName + '\n')
#write STDDIR line
inputFile.write("STDDIR " + self.stdDir + '\n')

#write STDFILE line(s)
for i in self.selectedStdFiles:
    inputFile.write("STDFILE " + i + '\n')

#write AMPS line
ampsLine = "AMPS"
for i in self.fracAmpsList:
    ampsLine = ampsLine + " %s" % i
inputFile.write(ampsLine + '\n')
#write SHIFTS line
shiftsLine = "SHIFTS"
for i in self.shiftsList:
    shiftsLine = shiftsLine + " %s" % i
inputFile.write(shiftsLine + '\n')
#write VARAMPS line
varAmpsLine = "VARAMPS"
for i in self.varAmpsList:
    varAmpsLine = varAmpsLine + " %s" % i
inputFile.write(varAmpsLine + '\n')
#write VARSHIFTS line
varShiftsLine= "VARSHIFTS"
for i in self.varShiftList:
    varShiftsLine = varShiftsLine + " %s" % i
inputFile.write(varShiftsLine + '\n')

#write STDFILEMODE line
inputFile.write("STDFILEMODE " + self.stdFileMode + '\n')
#write E0 same line
if self.e0Same:
    inputFile.write("E0SAME\n")
#write linear term line
if self.linTerm:
    inputFile.write("LIN\n")
#write FITFILE line
inputFile.write("FITFILE " + fitFile + '\n')
```

```
        inputFile.close()

    def onClickFites(self, event):
        self.fitInputExtractor()

        if len(self.fitListBox.GetSelections()) > 1:

            outputFile = open("textOutput.dat", 'w')
            #write Header lines to document automated program writing and time
            outputFile.write("#This output data was automatically written using "
                  "gfites version " + str(__version__) + '\n')
            outputFile.write("#On " + time.strftime("%a, %b %d %Y %H:%M:%S",\
                time.localtime()) + '\n')

            for i in self.fitListBox.GetSelections():
                print "Fitting These Files:", self.fitListBox.GetString(i)
                self.writeInparamFile(self.fitListBox.GetString(i))

                fitInstanceData = (self.fitDir, self.energyResolution,
                      self.fitFileMode, self.fitRange, self.fitOutName,
                      self.fitResultName, self.stdDir, self.selectedStdFiles,
                      self.allStdFiles, self.fracAmpsList, self.shiftsList,
                      self.varAmpsList, self.varShiftList, self.stdFileMode,
                      self.e0Same, self.selectedFitFiles, self.allFitFiles,
                      self.linTerm)

                fitInstance = formFitInstance(fitInstanceData)

                fitHistoryFrameInstance.addFitInstance(
                      self.fitListBox.GetString(self.fitListBox.GetSelections()[i]))
                fitHistoryFrameInstance.fitInstanceHistoryList.append(fitInstance)

                runFites(self,
                      self.fitListBox.GetString(self.fitListBox.GetSelections()[i]),
                      plot=False)

                fitResult = fitesStdOutFrameInstance.sendDataToGrid()
#               print "#####################################################"
#               print "DEBUG HERE:"
                print fitResult
                outputLine = ""
                for item in fitResult:
                    if isinstance(item, float) or isinstance(item, unicode) or\
                          isinstance(item, str):
                        outputLine = outputLine + str(item) + '\t'
#                       print item
                    else:
#                       print "classInstance:"
#                       print item
                        outputLine = outputLine + str(item.amp) + '\t'
                        outputLine = outputLine + str(item.ampErr) + '\t'
                        outputLine = outputLine + str(item.eShift) + '\t'
                        outputLine = outputLine + str(item.eShiftErr) + '\t'
                outputFile.write(outputLine.strip() + '\n')
                outputLine = ""

            outputFile.close()
#           print "#####################################################"

        else:
            i = self.fitListBox.GetSelections()[0]
            print "Fitting This ONE File:", self.fitListBox.GetString(i)
            self.writeInparamFile(self.fitListBox.GetString(i))

            fitInstanceData = (self.fitDir, self.energyResolution,
                  self.fitFileMode, self.fitRange, self.fitOutName,
                  self.fitResultName, self.stdDir, self.selectedStdFiles,
```

```
                self.allStdFiles, self.fracAmpsList, self.shiftsList,
                self.varAmpsList, self.varShiftList, self.stdFileMode,
                self.e0Same, self.selectedFitFiles, self.allFitFiles,
                self.linTerm)

        fitInstance = formFitInstance(fitInstanceData)

        fitHistoryFrameInstance.addFitInstance(
                self.fitListBox.GetString(self.fitListBox.GetSelections()[0]))
        fitHistoryFrameInstance.fitInstanceHistoryList.append(fitInstance)

        runFites(self,
                self.fitListBox.GetString(self.fitListBox.GetSelections()[0]),
                plot=True)

    def onWindowsShowHistory(self, event):
        showHistoryWindow()

    def onWindowsShowStdOut(self, event):
        showStdOutWindow()

    def onWindowsShowFitesGrid(self, event):
        showFitesGridWindow()

def showStdOutWindow():
    fitesStdOutFrameInstance.Show(True)

def showHistoryWindow():
    fitHistoryFrameInstance.Show(True)

def showFitesGridWindow():
    fitesStdOutFrameInstance.fitesGridFrameInstance.Show(True)

################################################################################
################################################################################

class fitesResult():
    def __init__(self, amp, ampErr, eShift, eShiftErr):
        self.amp = amp
        self.ampErr = ampErr
        self.eShift = eShift
        self.eShiftErr = eShiftErr
################################################################################
################################################################################

class fitesStdOutFrame(wx.Frame):
    def __init__(self):
        wx.Frame.__init__(self, frame, -1, 'fites output', pos=wx.DisplaySize())

        self.Bind(wx.EVT_CLOSE, self.onCloseWindow)

        self.residual = ''
        self.freeParameters = ''
        self.NIndep = ''
        self.ySquared = ''
        self.fitFileName = ''

        fitesStdOutPanel = wx.Panel(self, -1)
        fitesStdOutPanel.SetBackgroundColour('dark gray')
        self.SetIcon(wx.Icon(os.environ['PYTHONPATH']+'/icons/gfitesIcon.png',\
              wx.BITMAP_TYPE_PNG))

        #WARNING! This is a hack to give the StdOutFrame a minimum size to begin
        #with before placing data into it. I'm just making it display 80 spaces.
        #There must be a way to require a minimum window size but still allow the
        #window to dynamically adjust as new StdOut data comes into the frame, but
        #I can't get it working quite yet.
#       self.stdoutText = wx.StaticText(fitesStdOutPanel, -1, "", size=(350,100))
```

```
        self.stdoutText = wx.StaticText(fitesStdOutPanel, -1, 80*"_",
              size=(-1,-1))

        self.toGrid_b = wx.Button(fitesStdOutPanel, -1, "Send To Grid")
        self.Bind(wx.EVT_BUTTON, self.onToGrid, self.toGrid_b)

##############################################################################
##############################################################################
        self.sizer = wx.BoxSizer(wx.VERTICAL)
        self.sizer.Add(self.stdoutText, 1, wx.ALIGN_CENTER_VERTICAL|wx.ALL, 5)
        self.sizer.Add(self.toGrid_b, 0, wx.ALIGN_CENTER_VERTICAL|wx.ALL, 5)
        self.sizer.Fit(self)

        #take the sizer and apply it to the panel being housed in the frame
        fitesStdOutPanel.SetSizer(self.sizer)

        ##########################################################################
        #Start an instance of fitesGrid as part of the initialization of the
        #fitesStdOutFrame
        ##########################################################################
        self.fitesGridFrameInstance = fitesGrid()
        self.fitesGridFrameInstance.Show(True)

    def showStdOut(self, textData, fitFileName):
        self.fitFileName = fitFileName
        self.stdoutText.SetLabel(textData)
        self.sizer.Fit(self)
        self.stdoutText.Refresh()

    def onToGrid(self, event):
        result = self.sendDataToGrid()

    def sendDataToGrid(self):
        toGridStdResult = []
        rawOutput = self.stdoutText.GetLabel()
        rawOutput = rawOutput.split('\n')
        for line in rawOutput:
            fitMetrics = re.search('^'+self.fitFileName+'(.*)', line)
            statsMatch = re.search(' resid,free,Nind,ysq,amps2one,e0same=(.*)',\
                  line)
            if fitMetrics:
                rawFitMetrics = fitMetrics.group(1).split()
                #handling fits with linear terms (HACK!)
                if rawFitMetrics[1] != '+/-':
                    self.constant = rawFitMetrics[0]
                    self.slope = rawFitMetrics[1]
                    rawFitMetrics = rawFitMetrics[2:]
                else:
                    self.constant = "0.0"
                    self.slope = "0.0"
                NumberOfStandards = len(rawFitMetrics)/6
                for i in range(NumberOfStandards):
                    oneStdResult = fitesResult(rawFitMetrics[0+(i*6)],
                          rawFitMetrics[2+(i*6)], rawFitMetrics[3+(i*6)],
                          rawFitMetrics[5+(i*6)])
                    toGridStdResult.append(oneStdResult)
            if statsMatch:
                rawStats = statsMatch.group(1).split()
                self.residual = float(rawStats[0])
                self.freeParameters = float(rawStats[1])
                self.NIndep = float(rawStats[2])
                self.ySquared = float(rawStats[3])
        toGrid = [self.fitFileName, self.residual, self.freeParameters,
              self.NIndep, self.ySquared]
        toGrid = toGrid + [self.constant, self.slope] + toGridStdResult

        self.fitesGridFrameInstance.AppendRows()
        self.fitesGridFrameInstance.addDataToRows(toGrid)
```

```
        return toGrid

    def onCloseWindow(self, event):
        self.Show(False)

###########################################################################
###########################################################################

class fitesGrid(wx.Frame):
    def __init__(self):
        wx.Frame.__init__(self, frame, -1, 'gFites Data Grid',
                size=(wx.DisplaySize()[0],200), pos=(0,0))
        self.SetIcon(wx.Icon(os.environ['PYTHONPATH']+'/icons/gfitesIcon.png',\
                wx.BITMAP_TYPE_PNG))

        self.Bind(wx.EVT_CLOSE, self.onCloseGridWindow)

        self.grid = wx.grid.Grid(self)
        self.table = fitesGridTable()
        self.grid.SetTable(self.table, True)
        #autosize all the columns so that the lables can be fully read and set
        #that as the minimum size for the columns
        self.grid.AutoSizeColumns(setAsMin=True)

    def addDataToRows(self, newGridData):
        print "DEBUG:", newGridData
        rowIndex = self.grid.GetNumberRows()-1
        self.table.data[(rowIndex, 0)] = newGridData[0]
        self.table.data[(rowIndex, 1)] = newGridData[1]
        self.table.data[(rowIndex, 2)] = newGridData[2]
        self.table.data[(rowIndex, 3)] = newGridData[3]
        self.table.data[(rowIndex, 4)] = newGridData[4]
        self.table.data[(rowIndex, 5)] = newGridData[5]
        self.table.data[(rowIndex, 6)] = newGridData[6]

        self.table.data[(rowIndex, 7)] = newGridData[7].amp
        self.table.data[(rowIndex, 8)] = newGridData[7].ampErr
        self.table.data[(rowIndex, 9)] = newGridData[7].eShift
        self.table.data[(rowIndex, 10)] = newGridData[7].eShiftErr
        try:
            self.table.data[(rowIndex, 11)] = newGridData[8].amp
            self.table.data[(rowIndex, 12)] = newGridData[8].ampErr
            self.table.data[(rowIndex, 13)] = newGridData[8].eShift
            self.table.data[(rowIndex, 14)] = newGridData[8].eShiftErr
        except IndexError:
            print "no second standard!"
        try:
            self.table.data[(rowIndex, 15)] = newGridData[9].amp
            self.table.data[(rowIndex, 16)] = newGridData[9].ampErr
            self.table.data[(rowIndex, 17)] = newGridData[9].eShift
            self.table.data[(rowIndex, 18)] = newGridData[9].eShiftErr
        except IndexError:
            print "no third standard!"
        try:
            self.table.data[(rowIndex, 19)] = newGridData[10].amp
            self.table.data[(rowIndex, 20)] = newGridData[10].ampErr
            self.table.data[(rowIndex, 21)] = newGridData[10].eShift
            self.table.data[(rowIndex, 22)] = newGridData[10].eShiftErr
        except IndexError:
            print "no fourth standard!"
        self.grid.AutoSizeColumns(setAsMin=True)

    def AppendRows(self, numRows=1):
        self.table.numOfRows = self.table.numOfRows + numRows

        #sending a message to the grid object and then processing that message to
        #tell it that things have changed. This will cause the grid to be
        #refreshed and the new data will show up
```

```
        msg = wx.grid.GridTableMessage(self.table,
                wx.grid.GRIDTABLE_NOTIFY_ROWS_APPENDED, 1)
        self.grid.ProcessTableMessage(msg)

    def onCloseGridWindow(self, event):
        self.Show(False)
################################################################################
################################################################################

class fitesGridTable(wx.grid.PyGridTableBase):
    """fites version of a grid table which will be put into an instance of
    wx.grid.Grid()."""
    def __init__(self):
        wx.grid.PyGridTableBase.__init__(self)
        self.colLabels = ['Filename', 'Residual', 'Free Param', 'Indep Points',
                'y^2', 'constant', 'slope',
                'Std1 Amp', 'Std1 Amp Err', 'Std1 eShift', 'Std1 eShift Err',
                'Std2 Amp', 'Std2 Amp Err', 'Std2 eShift', 'Std2 eShift Err',
                'Std3 Amp', 'Std3 Amp Err', 'Std3 eShift', 'Std3 eShift Err',
                'Std4 Amp', 'Std4 Amp Err', 'Std4 eShift', 'Std4 eShift Err']

        self.data = {   (1,1): "Here",
                        (2,2): "is",
                        (3,3): "some",
                        (4,4): "data"}

        self.odd = wx.grid.GridCellAttr()
        self.odd.SetBackgroundColour("light blue")
        self.odd.SetFont(wx.Font(10, wx.SWISS, wx.NORMAL, wx.BOLD))
        self.even = wx.grid.GridCellAttr()
        self.even.SetBackgroundColour("goldenrod")
        self.even.SetFont(wx.Font(10, wx.SWISS, wx.NORMAL, wx.BOLD))

        self.numOfRows = 0
        self.numOfCols = 23

    def GetNumberRows(self):
        return self.numOfRows

    def GetNumberCols(self):
        return self.numOfCols

    def IsEmptyCell(self, row, col):
        return self.data.get((row, col)) is not None

    def GetValue(self, row, col):
        value = self.data.get((row, col))
        if value is not None:
            return value
        else:
            return ''

    def SetValue(self, row, col, value):
        self.data[(row,col)] = value

    def GetAttr(self, row, col, kind):
        attr = [self.even, self.odd][row % 2]
        attr.IncRef()
        return attr

    def AppendRows(self, numRows=1):
        return True

    def GetColLabelValue(self, col):
        return self.colLabels[col]

    def ForceRefresh():
        return True
```

```
##############################################################################
##############################################################################

def formFitInstance(fitInstanceData):
    fitInstance = fitInstanceClass(fitInstanceData)
    return fitInstance

class fitInstanceClass():
    def __init__(self, Data):
        self.fitDir, self.energyResolution, self.fitFileMode, self.fitRange,\
                self.fitOutName, self.fitResultName, self.stdDir,\
                self.selectedStdFiles, self.allStdFiles, self.fracAmpsList,\
                self.shiftsList, self.varAmpsList, self.varShiftList,\
                self.stdFileMode, self.e0Same, self.selectedFitFiles,\
                self.allFitFiles, self.linTerm = Data
##############################################################################
##############################################################################

def runFites(self, fitFileName, plot=True):
    fitesProcess = subprocess.Popen("fites", stdout=subprocess.PIPE)
    (stdoutdata, stderrdata) = fitesProcess.communicate()

    if plot:
        plotDataArray = loadtxt("fitesOut.dat")

        energy = plotDataArray[:,0]
        data = plotDataArray[:,1]
        totalFit = plotDataArray[:,2]
        std1 = plotDataArray[:,3]
        std2 = plotDataArray[:,4]
        std3 = plotDataArray[:,5]
        std4 = plotDataArray[:,6]

        dataToPlot = [(energy, data, "Data"),
                (energy, totalFit, "Total Fit"),
                (energy, std1, "Standard 1"),
                (energy, std2, "Standard 2"),
                (energy, std3, "Standard 3"),
                (energy, std4, "Standard 4")]

        plotter = xyPlotterFrame()
        plotter.plot(dataToPlot, "gFites Fit Results",\
                ("Energy (eV)","Relative Absorption (a.u.)"))

        plotter.Show()

    print "BAM!!! Done with Fit!"


    stdoutdata = ''.join(stdoutdata)
    fitesStdOutFrameInstance.showStdOut(stdoutdata, fitFileName)
##############################################################################
##############################################################################

if __name__ == '__main__':
    app = wx.PySimpleApp()
    frame = gFitesMainFrame()
    fitesStdOutFrameInstance = fitesStdOutFrame()
    fitesStdOutFrameInstance.Show(True)
    ##########################################################################
    #Start an instance of fitHistory if it does not exist when starting the
    #first fit
    ##########################################################################
    fitHistoryFrameInstance = fitHistoryFrame()
    fitHistoryFrameInstance.Show(True)
    frame.Show()

    app.MainLoop()
```

Appendix G

Tips and Tricks

> Make it idiot proof, and someone will make a better idiot
>
> *Anonymous*

G.1 Introduction

The scientific process is often based on trial and error. In the previous sections I have made every effort to show only the successes throughout this endeavor. However, research is marked as much (if not more so) by failures as it is by successes. Often these failures arise from a lack of a refined technique or experimental "experience." Below are some important tips and tricks that I have learned during my time in graduate school, which may save those who come after me some time and effort.

G.2 A Liquid Helium Cryostat for Bulk XAS Measurements

Figures G.1 and G.2 show the manufacturing drawings of a specially engineered liquid helium cryostat and transfer line for conducting bulk XAS measurements at cryogenic temperatures. Measuring XAS samples at cryogenic temperatures helps to mitigate possible X-ray beam-induced chemistry in certain sample matrices (see section 7.3). This system can achieve temperatures of less than 5 K.

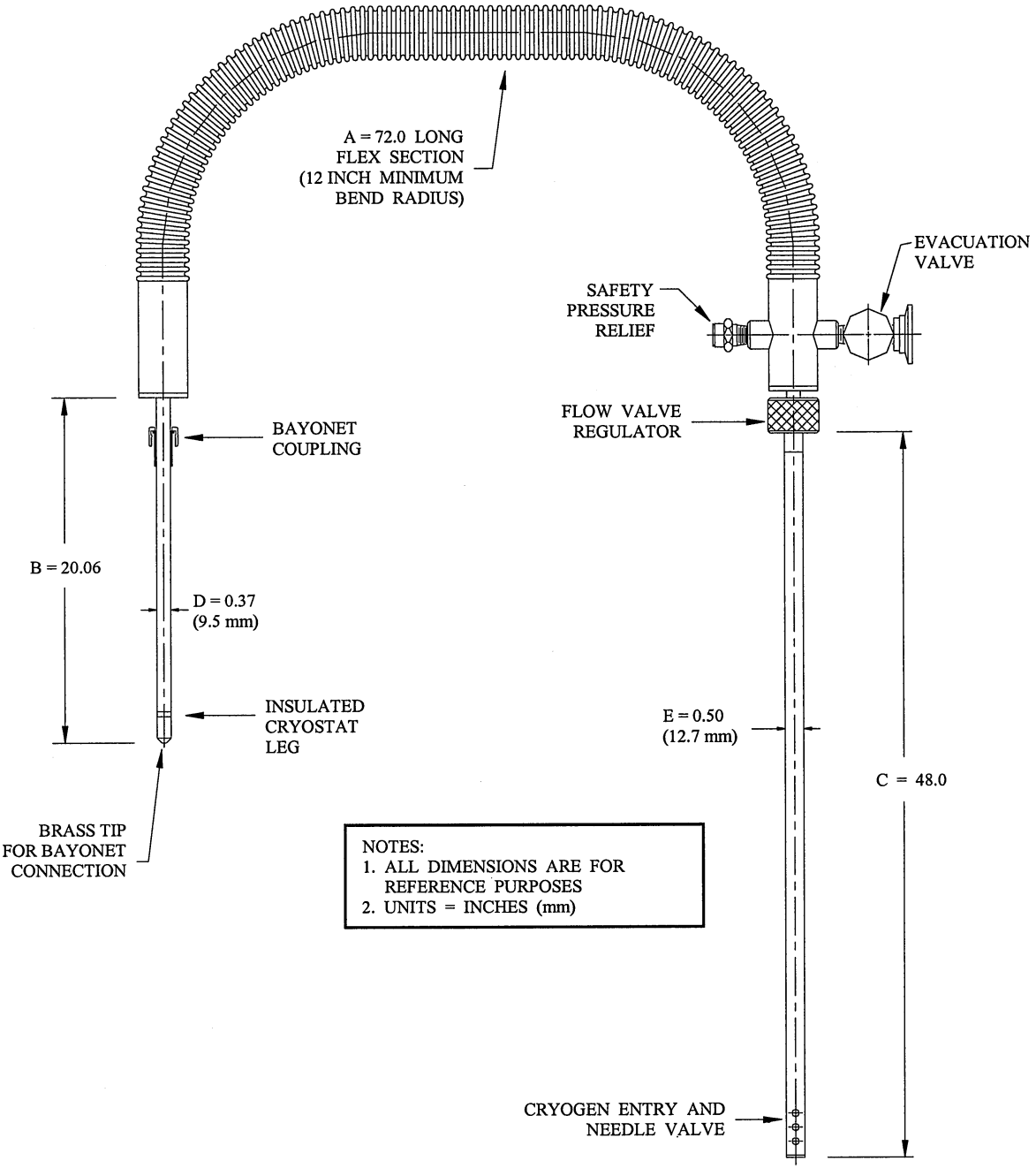

Figure G.1: Manufacturing drawing of the Janus liquid helium cryostat transfer line.

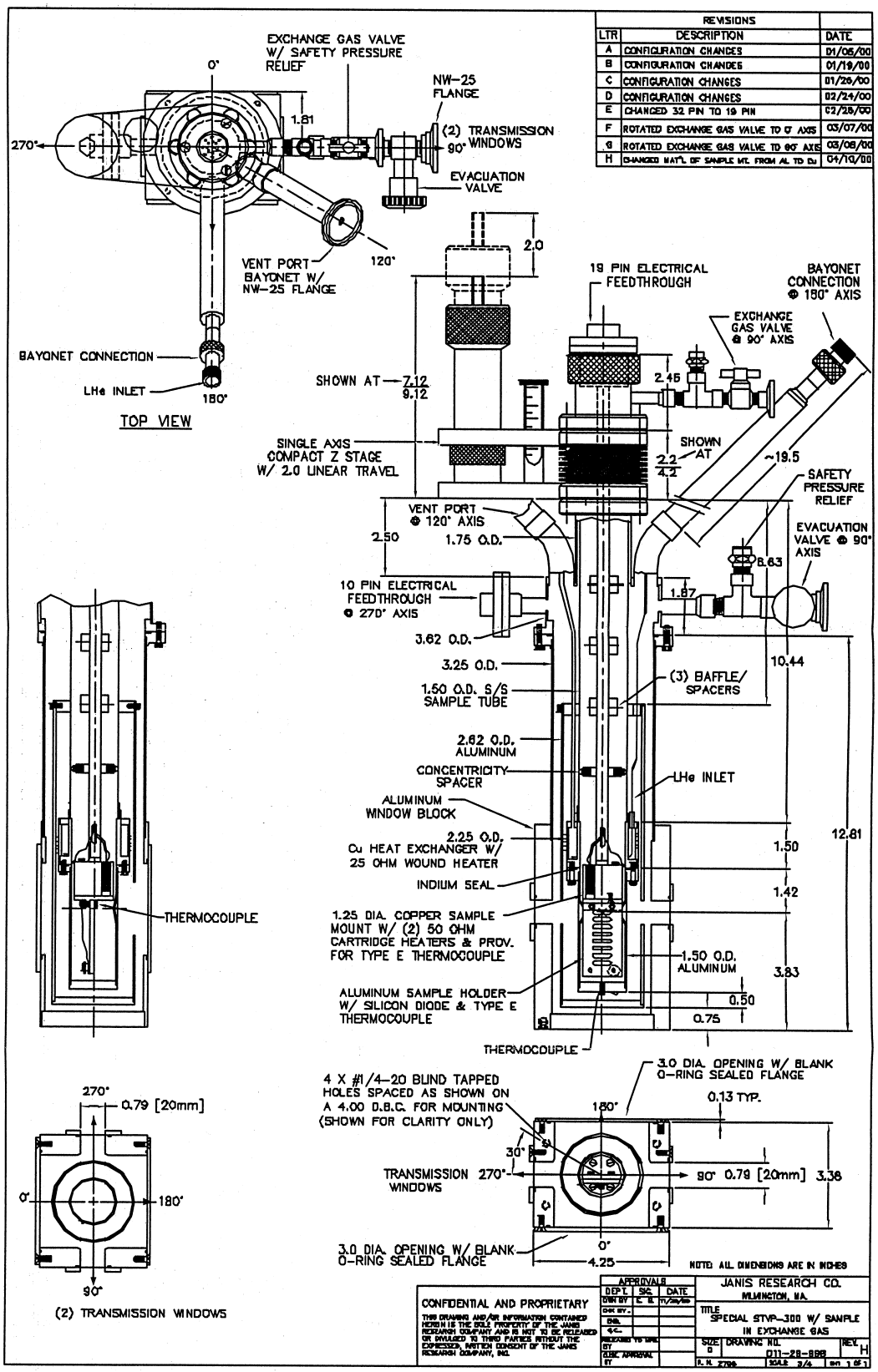

Figure G.2: Manufacturing drawing of the Janus liquid helium cryostat.

G.3 Packaging Transuranic Samples for Bulk XAS and Micro-XAS Measurements

G.3.1 Introduction

The major difficulty of working with transuranic elements is the issue of sample containment. Each facility has its own specific restrictions and protocols concerning how to handle such radioactive materials, and it is best to check with the specific user-facility about containment requirements for the specific isotope that will be used in an experiment. For experiments run at SSRL with ^{239}Pu, samples must have three layers of containment. Be aware that if a new type of sample holder is to be used, it must first go through a review and approval process by the Radiation Protection Group (RPG) at SSRL. The final approval process may take as long as 30 days, not including initial safety meetings and presentations.

G.3.2 Bulk XAS Sample Loading

Bulk XAS samples in this study (see section 7.4) are measured at low temperatures (30-50 K) to minimize possible beam-induced chemistry that could occur (see section 7.3). Samples therefore needed to be prepared for packaging in specially designed cryogenic sample holders able to withstand extremely cold temperatures. For our studies, the SSRL type "1g" holder, designed by Dr. Corwin Booth of LBNL Chemical Sciences Division, is used. This holder provides three layers of Kapton containment with indium gasket seals. Schematics for the holder design are available from Dr. Booth as well as the RPG at SSRL.

Because we are working with wet paste samples it is best to load our samples in some kind of pseudo-container before placing it into a type "1g" holder. This will allow us to load the "1g" holder much more easily than if we directly load the wet paste into the holder itself. Also, this pseudo-container isolates the sample from the aluminum holder body, thus minimizing any possible contamination of the sample.

Figure G.3 a-d shows schematics of the sample loader. Polyimide (Kapton) tubing (Cole-Parmer part number: 95820-13, ID: 0.0710", OD: 0.0750") is cut to a length of approximately 11.5 mm, as shown in figure G.3 a. One end is stuffed with a small wad of Parafilm (gray) and sealed with quick-drying epoxy (olive). After the epoxy is dried, the end is checked to see that it will fit into the type "1g" sample holder. The tip of a 1000 μL pipet tip is then cut to approximately 23 mm. The open sample cells (figure G.3 a) are then epoxied to the smaller end of the pipet tip (figure G.3 b). The completed sample loader is then placed into a 1.5 mL microtube with a snap cap. The mineral sample is loaded into the pipet tip and the whole sample loader is centrifuged (figure G.3 c). During this step the mineral wet paste will be centrifuged into the Kapton tube portion of the sample loader. Centrifuging at too high of a speed may cause the Kapton tube to bend at the attachment to the pipet tip. This may cause solution from the pipet to spill out. Once the tube is sufficiently loaded with sample (red) it is cut from the sample loader, the tube is capped with another wad of Parafilm and epoxied at the other end (figure G.3 d). These samples are then ready to be loaded into the type "1g" sample holder.

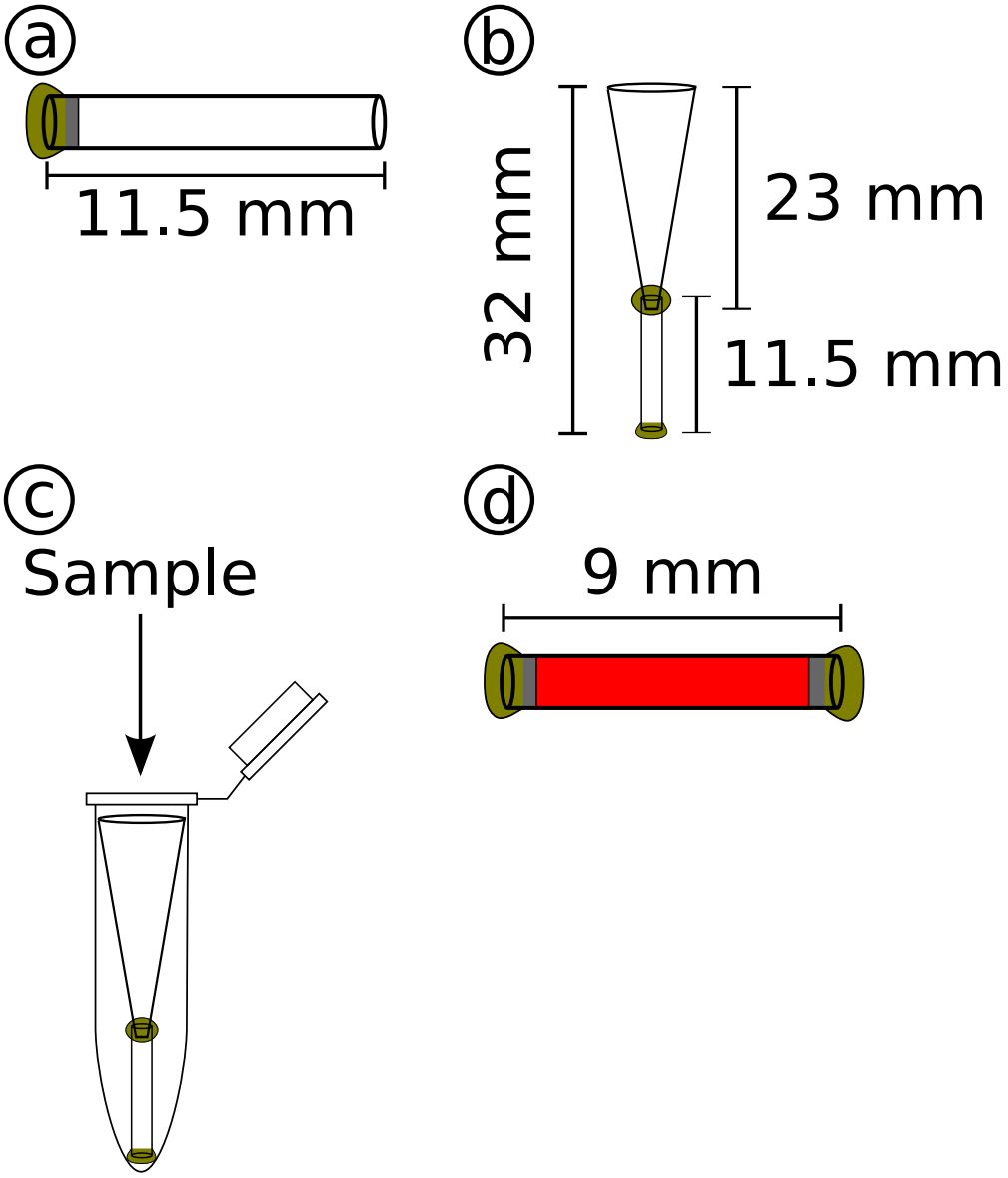

Figure G.3: Sample loader schematics for bulk XAS samples.

G.3.3 Micro XAS Sample Loading

Micro XAS samples in this study are measured at room temperature because of experimental constraints. However, the data collection parameters (see section 7.5) are adjusted to minimize possible beam-induced chemistry that could occur (see section 7.3). All samples are be held within a triply-contained sample holder as required for samples containing ^{239}Pu at room temperature. The sample containment schematic and procedure is shown in figure G.4 and G.5 below.

A small amount of the mineral solution sample is pipetted onto a piece of Parafilm inside the glovebox. Another layer of Parafilm is placed over the sample and sealed by applying pressure around the sides of the Parafilm. Although this is not considered a layer of containment, samples appear to be stable visually in this type of containment for up to two weeks. Specifically, there does not appear to be any loss of moisture after transporting samples to the beamline and back. Scotch tape is placed on one side of the Parafilm-encapsulated sample and double-sided tape is placed on the other side. The sample is then mounted on a plastic washer. The purpose of the plastic washer is to add rigidity to the sample. The sample is then further contained in two layers of heat-sealed polyethylene bags. SSRL RPG has designated this type of sample holder as their "1o" sample holder.

The sample holder design is very similar in containment design to the SSRL "1a" holder. Kapton tape is avoided due to metal contaminants in the tape that can not be tolerated in microprobe experiments. Polyethylene is used for its high tensile strength and because it has been successfully used at SSRL for containment purposes in the past. Furthermore, polyethylene is heat-sealable. Measurements on these samples are only to be conducted under ambient temperatures and pressures.

Figure G.6 a and b shows pictures of the front (labeled "F" on the washer) and back (labeled "B" on the washer) of a fully assembled sample holder, as described above. The mineral sample contained in the holder is light brown.

G.4 A Sample Mount for Transuranic Micro XAS

Figure G.7 shows the manufacturing drawing of a specially engineered sample mount for transuranic μ-XAS samples. All the corners on this sample mount are beveled to remove sharp edges that could potentially compromise the sample containment. The sample, as prepared in subsection G.3.3, is attached to the sample mount using double-sided tape. This sample mount is then fitted into the sample positioner on the beamline.

G.5 Running Beamtime Experiments

G.5.1 Introduction

Below is a set of notes and instructions that have been collected over the years during beamtime experiments. They by no means represent an exhaustive list of instructions for every possible experimental situation. However, they do represent much of what is easily forgotten between beamtime runs.

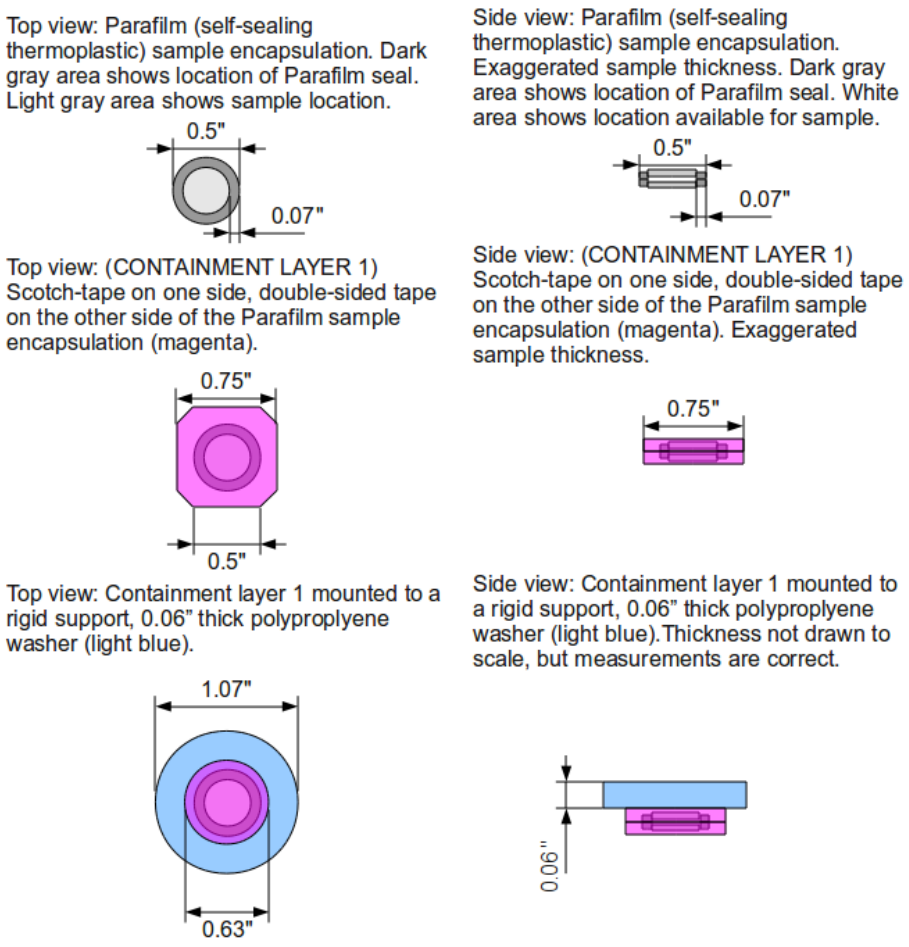

Figure G.4: Schematic of the first containment layer of the X-ray microprobe sample holder.

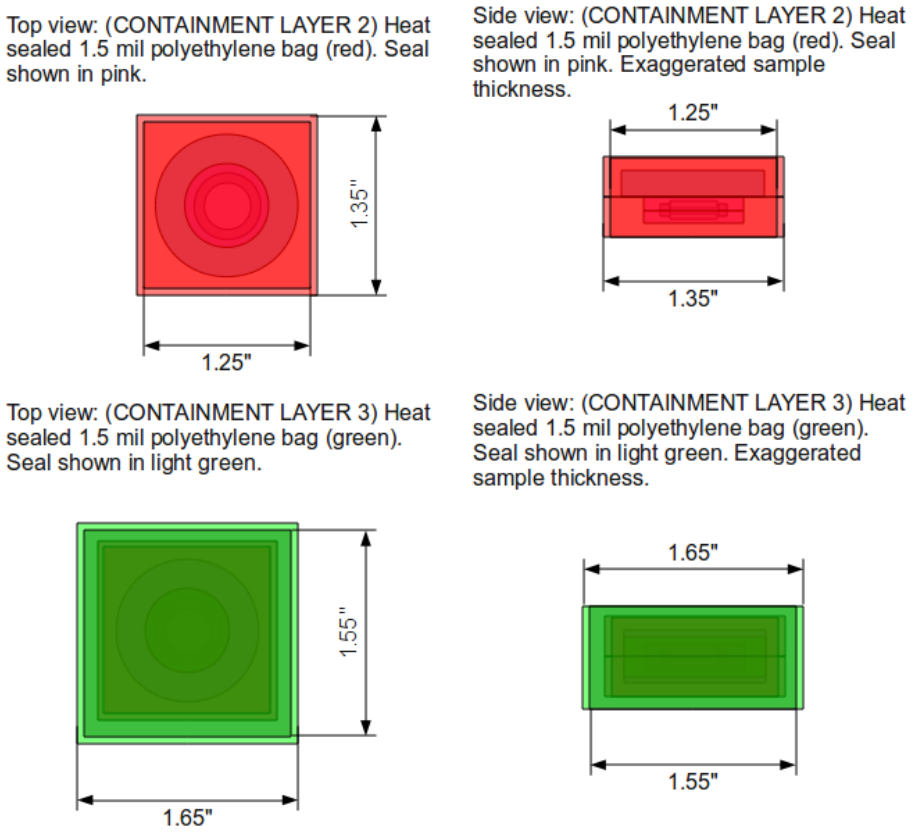

Figure G.5: Schematic of the second and third containment layers of the X-ray microprobe sample holder.

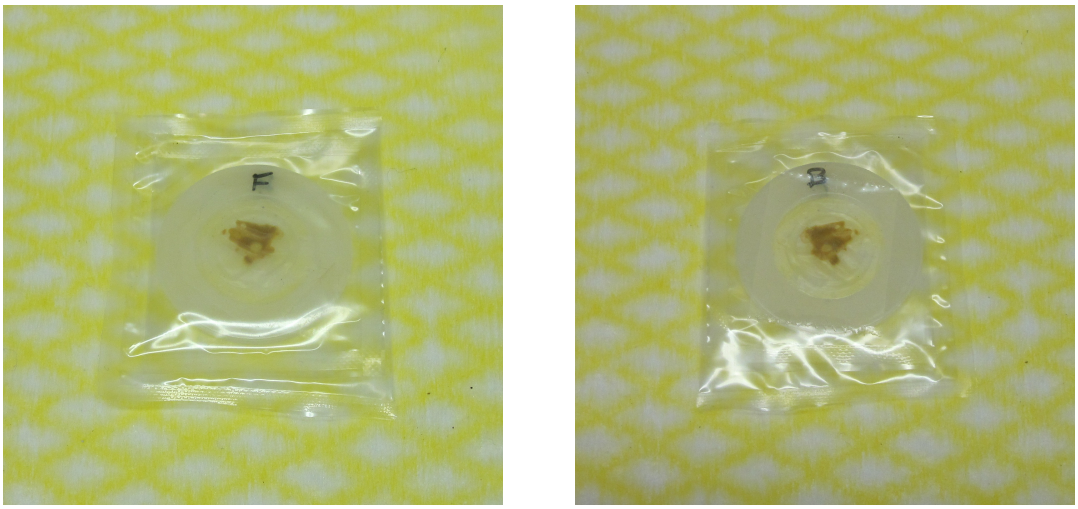

(a) Front (b) Back

Figure G.6: Photographs of the (a) front and (b) back of the X-ray microprobe sample holder for radioactive samples.

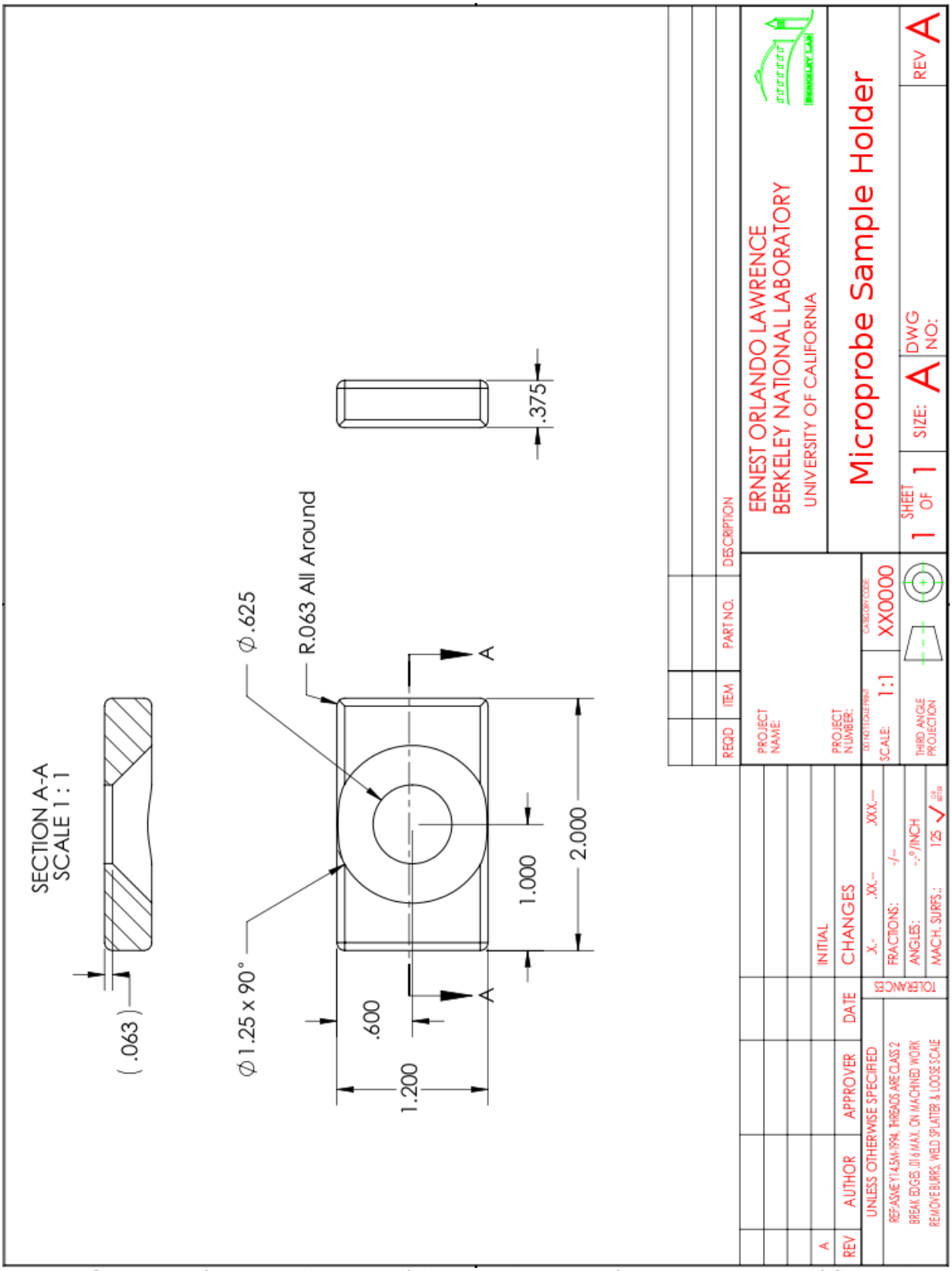

Figure G.7: Manufacturing drawing of the sample mount for transuranic μ-XAS samples.

G.5.2 Logging In and Preparing for Runs

Start by logging into the main beamline computer. To turn on the gain controller program type:

```
SR112>sr570 <RETURN>
```

To turn on the XAS collect program type:

```
SR112>xas <RETURN>
```

Before taking data be sure to:

- Ask the beamline scientists to help you drop the curtain in the hutch. It's easy to work around the curtain, but if you need to drop it yourself there's a bunch of electronic equipment that may need to be unplugged, and that could be a problem.
- Change the data directory in the directory listing to something descriptive of the experimental run (e.g. hu01, hu02,...). Run directories that use MonthYear (i.e. Jan02) as a naming scheme end up being confusing because file directories are sorted alphabetically in the computer.
- Load the correct detector file under the detector list for the 32-element Ge detector. Ask if you don't know which file is the correct one. **Also ask even if you do know because they change it all the time, so it's better just to be sure!**
- Measure an offset spectrum with the beam off when you are using the Ge detector. This is the dark current of the detector and will be subtracted from the spectrum when collecting in fluorescence mode. To do this go into the "Detectors" menu and select "Current" from the list. Click on "Collect Offsets" and a message should appear, telling you that the shutters should be closed. Click "OK" and wait 10 seconds as the offsets collect.
- After collecting offsets, confirm that the detector is set up to stop when there is a "Low Signal Level." Adjust the settings so that the scan is restarted from the beginning 5 minutes after the beam comes back on. This will allow you to sleep through beam fills with minimal delay in sample collection time.
- The energy should already be calibrated to some source that is close to the ionization energy of the element of interest. Full-tune and do a table scan on table2vert, monitoring I_0 to check for the optimum table position, then detune.
- Go below the edge and detune some percentage. 25-50% detuning is usual. The plot on beamline 11-2 shows that it is slightly better to detune to the low energy side. An argument can be made (and it's a good one) that you should detune at higher energies (i.e. detune at the point where you plan on stopping your scan).

- If you are measuring only in fluorescence mode, be sure to take a fluorescence spectrum of your standard to window the fluorescence detector with. This may take some complex sample hanging, and needs to be done before the cryostat is put in-line with the ion chamber detectors, otherwise the cryostat will have to be moved out to get the standard positioned correctly.

- Remember to take a deadtime scan of the fluorescence detector. This can be done before or after the run, but is difficult to do while the cryostat is in place. The best way to take a deadtime scan is to place a standard sample at 45 degrees with respect to the beam, and scan the monochromator slits from 0 (closed) to whatever value is fully open. Start off by closing the slits on I_0 until they are fairly small (0.5 mm x 1.0 mm) and continue to open them up symmetrically until the fluorescence detector is sufficiently saturated. Depending on the detector file being used on the fluorescence computer, this number can be anywhere from 250 k counts in the ICR to 350 k counts in the ICR. Ideally, you want to collect a deadtime scan going out to $\sim$500 k counts to ensure that you are over the deadtime hump. After the I_0 slits are properly set, select the correct detector file and region file on the data collection computer. The region file should have one line of even steps going from 0 to whatever value is fully open for the monochromator slits. The correct detector file will have a line in it that tells the data collection computer to drive the monochromator slits for deadtime collection (normally this line tells the computer to drive the monochromator for XAS collection). Check with the beamline scientist to make sure the correct detector file is being used.

- Line up the cryostat without a sample inside and find the center of the transmission window by scanning vertically (vert) and horizontally (horz) while monitoring I_1. **BE SURE TO WRITE THESE NUMBERS DOWN!**

- Place your sample into the cryostat and line up on a sample.

- Go below the edge and check that your ion chamber gains are not set so high that you max out the ion chambers (MAX VOLTAGE = 5.0 V). You shouldn't be going above 2-3 V though. If the detector voltages are maxed out below the edge it will be difficult, or impossible, to do a proper background subtraction of the data.

- Go just slightly above the edge and check that your ion chamber gains are set high enough that they produce a signal (i.e. don't register 0.0 V). A voltage of 0.200 V is probably as low a signal as you want to collect.

G.5.3 Working with X-ray Mirrors

BL 11-2

On special occasions the need may arise to run low energy edges (5-10 keV) on beamline 11-2. The problem is that in this energy region there is a lot of harmonic content in the beam, so much so that detuning will not remove it. To correct for this effect use harmonic rejection mirrors.

Harmonic rejection mirrors work on the principle that each type of material has a special angle at which total internal reflection occurs. These angles are different for the fundamental and the harmonic, so in theory all of the harmonic content can be removed by using an X-ray mirror.

Mirrors have two degrees of movement: pitch (the tilt of the mirror) and bend (the curvature of the mirror). The pitch of the mirror controls the harmonic rejection, as well as the direction of the beam, while the bend of the mirror controls the focusing of the beam. Beam focusing is used to increase photon flux. Beware that all the flux hitting the X-ray mirror will be focused on some point, which means that energy resolution must be controlled (using upstream slits) before your beam hits the mirror. After it hits the mirror all of the flux will be "mixed together" and directed towards a focal point. For high energy resolution we should therefore set the bend to be as flat as possible, so that the mirror only acts as a harmonic rejector.

BL 10-2

On beamline 10-2 we sometimes want to run both low and high energy samples. This can be done with Matt Latimer's harmonic rejection mirrors. These mirrors were specifically made for measuring manganese on beamlines with high harmonic content. The energy cut-off is approximately 8-9 keV depending on the angle of the rack that the mirror sits on.

G.5.4 Common Rookie Mistakes

- **Never assume the parameters of your experiment are correct, especially right after changing shifts. Check to ensure that monochromator energy, gains, slit dimensions, and detune are all correct *before* taking data!**
- **Before starting a scan (especially if you've moved the configuration of the sample) take a second to imagine the beam coming off of the storage ring and hitting the sample, going through each point where the beam is modified (storage ring, monochromator slit, mirror, monochromator, mirror, hutch slits, I_0, sample holder, I_1, standard, I_2, beamstop).**
- Do not move the mono inside the monochromator menu. Move the mono in the motors and then calibrate the energy in the monochromator menu. The reason is that when moving the mono in the move motors menu the table will track with the mono position, while this does not happen when moving directly in the monochromator menu. In the extreme case the beam, without table tracking, may wander off the slits entirely, which should be accompanied with a suspicious 0.000 V in I_0 when the beam is on.
- When setting proper windows in the fluorescence detector it is a good idea to use fluorescence from a standard to set the windows, and then keep the windows the same when measuring the sample. This is extremely helpful if the sample contains a very small fraction of the element you are trying to detect.
- If all you can get is fluorescence from the sample (i.e. the sample is too thick to collect in transmission mode), line up the sample using the fluorescence line of the major

component of the sample. Trying to line up on plutonium with only 0.01% plutonium in your sample is a futile effort.

- Be sure to align horizontally and vertically after sample rotation to 45 degrees when switching from transmission to fluorescence mode. Samples will shift in both directions when rotated because the sample probe is not perfectly centered. Also since the solid angle at 45 degrees is smaller, be sure to neck down the slits in the horizontal direction.

- Sometime glitches happen. Keep an eye on **I0/RTC** to make sure you know where they are. If they show up in the data then there is a possibility of a pinhole in the sample. If beam is going through and a glitch suddenly causes beam flux to increase then the increase in flux is passed directly to I_1 through the pinhole and the glitch shows up in the data. Move to a spot where there are no holes and the glitch should ratio out. RTC = Real Time Counts, and is simply the timer on the system that gives the total counting time. This value is used in calculating the count rate.

- **I0/RTC** can show you other stuff as well. Normally, you expect the functions to be slowly decaying from left to right (ignoring glitches). As you go from one scan to the next the ratio should drop due to the decay of the electron beam in the synchrotron as time goes on. On BL 11-2 we have experienced, in the past, issues with the monochromator cooling system, which causes the incident beam to fluctuate. This will cause the beam going through I_0 to change. You can see these effects in a **I0/RTC** plot as random jumps in the decay. This is different from glitches which occur at the same point in each crystal, but like glitches, they should ratio out properly as long as high quality samples have been prepared.

- **Be aware of what you are plotting.** Most importantly, don't accidentally plot the wrong thing! "**log(I0/I1)**" will give you the sample XAS in transmission, "**log(I1/I2)**" will give you the standard XAS in transmission, and "**Sum (SCA1/I0)**" will give you the sample XAS in fluorescence from all of the fluorescence channels summed together.

- Be sure to collect offsets for the detector when you change energy. This is essentially zeroing out the dark current in the detectors. To do this turn off the beam and go into Detectors → Current → Offsets. **This should also be done every time you change the gains on the ion chambers.**

- Sometimes the beam slits need to be reset. This mostly likely will happen when one accidentally scans the slit motors instead of some other motor (like vertical). The best way to fix this problem is to move all the problem motors to the zero position using the data collection software. Then unplug the controller cable to the slit motors. The left/right motor controller cable is on the side of the slits, the top/bottom motor controller cable is on the top of the slits. Once the controller cable is unplugged the slits can be closed by hand until they won't turn anymore. The controller cable should then be plugged in and your slits should be reset to zero. It would be prudent to check if this is actually true.

- On beamline 11-2 there are two tables, the front table and the back table. Each one has a set of beam slit motors. Often times when the previous users were working on the front table, the front slit motors will be activated in the data collection computer. To activate the back slit motors go to Motors → Setup Motors and select the appropriate slit. Click on the "Edit" button and then on the "Add" button. In the text entry area, edit the name of the slit so that it ends with the number "2" for table 2. Finally, click on "Add Motor" and the new motor will be added to the list.

G.5.5 Transferring Data Back to the Ranch

BL 2-3

Data from beamline 2-3 is written by the data acquisition program in ASCII format. The easiest way to transfer data back to an LBNL server is to copy the data in the directory:

```
C:\Documents and Settings\<user name>\My Documents\UXAS\data\<data folder>
```

into a pen drive and then take it back home by hand and place it in the appropriate folders on the server. You could also immediately copy the files to a laptop and SSH it back to LBNL, but both involve manually copying the files from the data acquisition computer.

BL 10-2 and 11-2

Dr. Booth's code does not work with the SSRL binary type files so they first need to be translated into ascii type files using the beamline program XAS_ASCII. This needs to be done **BEFORE** leaving the beamline. To do this you need to use the commands:

```
S112>set def $data1:[b_booth.<directory>]
```

or

```
S112>set def $data:[b_booth.<directory>]
S112>dir
S112>xas_ascii

enter file specification:hu01*.*
```

where <directory> is the directory where the data is saved. In my case it will be "hu##" starting from "hu01" and increasing for each beamtime run. Notice here that you need the "." between *.* because the main computer on 11-2 does not count "." in the wildcard expansion. The wildcard for matching any one character is %, not ? like in Unix operating systems. For example, the specification "hu01_00%.*" will translate the first 9 data scans. As written, the above file specification takes all the data in run "hu01" and translates it to ASCII format.

On the general use computer, open the "Reflection FTP Client" program and in the menu click on "Connection → Connect...". Make a connection name, or change an existing one to access the current data directory. The data computer address is S112.slac.stanford.edu and the data directory is $DATA1:[B_BOOTH.<directory>]. The data then needs to be transferred to a pen drive or some other suitable memory device and moved to a computer that can SSH the data back to the ranch, or the data must be moved back manually.

XAS Data Conversion

Once the data is on the home server we need to convert it from the SSRL ASCII format into Dr. Booth's RSXAP binary format (yuck!). This will take all the transmission data and convert it from a "data space" file to an "energy space" file in addition to the binary data space file. That means the files will be found in /es and /ds. Also since these are transmission files they will not have "G" (for germanium) appended to the end of the file. Note, if either I_1 or I_2 contained negative values (possibly from offsets being selected to be too negative) then those files will not be converted because the logarithm of a negative number is not defined. We want to run the code in the"/exafs/exdata/" data directory. The conversion process is done using the following code:

```
>convgerm

input subdir for exafs data files: <directory>
Save Lytle (Iff) fluorescence data [RET=N]? <return>
Keep reference file data? [RET=y] <return>

input-file PREFIX name?    i.e. input sc6 for sc6_***.
<directory>
Input the start number
 1
Input the stop number
 <max sample number>
```

Usually we want to have the input-file PREFIX name to be the same as the run name that was given to it, in our case "hu##" is used. For the stop number you can put a number larger than the maximum number of scans and the code will simply convert all of the files.

To extract the fluorescence data out of the raw data, we first go into the data space directory /ds and then run SUG:

```
>sug -d BL112 ???b*
```

This translates all the "data space" files into "energy space" files with a "G" appended to the end of the file to signify that it is fluorescence data. If some of the data has already been translated into "energy space," it is usually easier to just delete all the files and run SUG again instead of running SUG and manually ignoring each of the files that were already translated. This can be done from the "data space" folder by using the command:

```
>rm ../es/*G*
```

Sometimes you want to be able to select exactly which fluorescence channels you want to add together to get the total fluorescence file. This can be done with:

```
>sug -h BL112
```

More information about the programs CONVGERM, SUG, and other codes in RSXAP can be found in the RSXAP instruction manual [78].

G.5.6 Temperature Controlling Notes

- When working down at around 30 K you should be able to regulate the temperature fairly well with the 20 W heater setting. At above 100 K you will want to switch over to the 50 W setting.
- Very little helium is needed to cool things. However, there is a delay between dropping the stick and seeing a significant change in the temperature.
- Realize that dropping the stick will raise the pressure in the tank, but the only way to lower the pressure is for it to flow out through the cryostat or one of the pressure release valves on the tank.
- Stop and think, is exact temperature control essential? If ± 1 °C is tolerable then take it easy on the temperature controlling. You'll save quite a lot of helium.

G.5.7 Data Collection Notes

- The $^{242}PuO_2$ standard (although it looks to be very big) is actually contained in a very small sample holder. It only looks big because the sample has shifted in the sample holder slightly since it was first prepared. There are two red lines on either side of the sample that shows the exact position of the sample. The standard gives an edge step of $\sim$0.3 in transmission mode.
- When collecting data in fluorescence mode, using the SSRL "1g" type sample holders, no beam will pass through to I_1. This means that we are unable to collect a standard in the I_2 position. To fix this problem, we need to collect standards of the PuO_2 by taping the standard on the front of the cryostat (over the transmission windows) at least at the beginning and at the end of the beamtime run. Ideally more scans should be done to verify that there is no drifting in delivered X-ray energy from the monochromator between each sample or each scan. In reality, the stability of the monochromator crystals is very good and PuO_2 standard scans only need to be run when the monochromator is moved a long distance, or if the table is scanned.
- When collecting XANES data it is a good idea to collect out to a k-range of 10 $Å^{-1}$ anyways. This is important when trying to do an accurate post-edge background subtraction and normalization. The counts out at high k-space don't need to be very long or have very fine spacing since we're not trying to collect EXAFS information.